Title

Effects of Composition and Structure on Metal Oxide Catalysts for Hydrocarbon Oxidation and Oxidative Dehydrogenation

Permalink

https://escholarship.org/uc/item/7c04m1r1

Author

Zhai, Zheng

Publication Date

2014

Peer reviewed|Thesis/dissertation

Effects of Composition and Structure on Metal Oxide Catalysts for Hydrocarbon Oxidation and Oxidative Dehydrogenation

By

Zheng Zhai

A dissertation submitted in partial satisfaction of the

requirements for the degree of

Doctor of Philosophy

in

Chemical Engineering

in the

Graduate Division

of the

University of California, Berkeley

Committee in charge:

Professor Alexis T. Bell, Chair
Professor David B. Graves
Professor T. Don Tilley

Fall 2014

Effects of Composition and Structure on Metal Oxide Catalysts for Hydrocarbon
Oxidation and Oxidative Dehydrogenation

by

Zheng Zhai

Abstract

Effects of Composition and Structure on Metal Oxide Catalysts for Hydrocarbon Oxidation and Oxidative Dehydrogenation

by

Zheng Zhai

Doctor of Philosophy in Chemical Engineering

University of California, Berkeley

Professor Alexis T. Bell, Chair

The selective oxidation and ammoxidation of light alkenes underpins the 10 billion pounds per year acrylics industry, and is among the essential processes for preparing monomers and intermediates. The most effective catalysts known are multi-component oxides based on bismuth molybdate, and were first patented in the 1950s. A significant body of research has been done since then to understand the mechanism, yet a surprising number of questions remain unanswered. The aim of this thesis is to identify "*descriptors*" relating the activity of i) different catalysts to their material properties and ii) different reactants to their physical properties in order to systematically guide catalyst design for greater activity for oxidation reactions.

A systematic investigation of the kinetics of propene oxidation to acrolein was carried out over $Bi_{1-x/3}V_{1-x}Mo_xO_4$ (x = 0 − 1). X-ray absorption near edge spectroscopy (XANES) was used to determine the oxidation state of Bi, Mo, and V before and after exposure of the catalyst to propene at 713 K. It was established that, contrary to previous discussions of the mechanism of propene oxidation on $Bi_{1-x/3}V_{1-x}Mo_xO_4$, Bi remains in the 3+ state and only V and Mo undergo reduction and oxidation during reaction. The kinetics of propene oxidation were investigated to establish the activation barrier for acrolein formation and determine how the partial pressure dependences on propene and oxygen change with the value of x. The data obtained from this study were then used to propose a generalized model for the kinetics of propene oxidation over $Bi_{1-x/3}V_{1-x}Mo_xO_4$. This model is fully consistent with our findings regarding the reducibility of the metallic elements in the oxide. According to this model, vanadium and molybdenum are randomly distributed to form three types of sites each associated with its own rate parameters. Mo-V sites are found to exhibit the highest activity. The proposed model provides a good description of the experimental data for all catalyst formulations examined, for a range of propene and oxygen partial pressures, and for temperatures above 653 K.

UV-Vis spectroscopy revealed that the rate of propene oxidation to acrolein correlates with the rate of catalyst reduction, suggesting that absorption edge energy or catalyst band gap might be a good descriptor of activity. Further work demonstrated that the apparent activation energy for the oxidation of propene over scheelite-structured,

multicomponent mixed metal oxides ($Bi_3FeMo_2O_{12}$, $Bi_2Mo_{2.5}W_{0.5}O_{12}$, and $Bi_{1-x/3}V_{1-x}Mo_xO_4$) correlates with the band gap of the catalyst measured at reaction temperature. The relationship between band gap of the oxide and the activation energy for propene activation can be rationalized by examining a Born-Haber cycle relating the electronic excitation observed during the band gap measurement to an electronic excitation taking place in the transition state for propene activation. We also found that the change in band-gap energy with composition arises from the interplay between the sizes and energies of the V 3d, Fe 3d, Mo 4d, and W 5d orbitals, which give rise to the lowest unoccupied crystal orbitals. Subsequent work showed that the correlation of the apparent activation energy with the catalyst band gap also holds for metal oxides having an aurivillius structure, $Bi_4V_{2-x}Mo_xO_{11+x/2}$ ($x = 0 - 1$). The band gap was also found to be a good descriptor of acrolein selectivity. Catalysts with band gaps above ~ 2.1 eV exhibit intrinsic selectivities of ~ 75%, whereas the intrinsic acrolein selectivity rapidly decreases for catalysts with band gaps below ~ 2.1 eV. Catalysts with band gaps below ~ 2.1 eV also promote acrolein combustion, whereas catalysts with higher band gaps do not.

A systematic investigation of the oxidative dehydrogenation of propane to propene, 1- and 2-butene to 1,3-butadiene and the selective oxidation of isobutene to methacrolein was carried out over $Bi_{1-x/3}V_{1-x}Mo_xO_4$ ($x = 0-1$) with the aim of defining the effects of catalyst and reactant composition on the reaction kinetics. This work revealed that the reaction kinetics can differ significantly depending on the state of catalyst oxidation, which in turn depends on the catalyst composition and the reaction conditions. When the catalyst is fully oxidized, the kinetics for the oxidation of propene to acrolein and isobutene to methacrolein, and the oxidative dehydrogenation of propane to propene, 1-butene and trans-2-butene to butadiene are very similar - first order in the partial pressure of the alkane or alkene and zero order in the partial pressure of oxygen. These observations, together with XANES and UV-Vis data, suggest that all these reactions proceed via a Mars van Krevelen mechanism involving oxygen atoms in the catalysts and that the rate-limiting step involves cleavage of the weakest C-H bond in the reactant. Consistent with these findings, the apparent activation energy and preexponential factor for both oxidative dehydrogenation and selective oxidation correlate with the dissociation energy of the weakest C-H bond in the reactant. As the reaction temperature is lowered, catalyst reoxidation becomes rate-limiting, and the transition to this regime depends on the ease of catalyst reduction and effectiveness of the reacting hydrocarbon as a reducing agent. A third regime is observed for isobutene oxidation at lower temperatures, in which the catalyst is more severely reduced and oxidation now proceeds via reaction of molecular oxygen, rather than catalyst lattice oxygen, with the reactant.

This thesis is dedicated to
    my parents,
          who have supported me all the way,
    my husband Zhenhua,
          whose love made this possible,
    and our beloved daughter, Junyi.

Table of Contents

List of Figures

List of Tables

List of Schemes

List of Abbreviations and Symbols

$\mathring{A}$	angstrom (10^{-10} m)
A_{app}	apparent preexponential factor in Arrhenius equation, $k_{app} = A_{app} \exp(-E_{app}/RT)$
BET	Brunauer-Emmett-Teller theory of gas adsorption
DFT	density functional theory
DFT+U	density functional theory containing a Hubbard term to correct coulombic interaction
DOE	United States Department of Energy
EA	electron affinity
E_{app}	apparent activation energy
E_{int}	intrinsic activation energy
eV	electron volt, a unit of energy equivalent to 96.485 kiloJoules per mol
EXAFS	extended X-ray absorption fine structure
FID	flame ionization detector
FTIR, IR	fourier transform infrared spectroscopy
GC	gas chromatograph
HOMO	highest occupied molecular orbital
IE	first ionization energy
K_i	equilibrium constant for reaction i
k_{app}	apparent rate constant
k_i	rate coefficient for reaction i
M06-L	a density functional developed by Zhao and Truhlar
LMCT	ligand-to-metal charge transfer
LUMO	lowest unoccupied molecular orbital
PBE	a density functional named for Perdew, Burke, and Ernzerhof
P_i	partial pressure of reactant i
QM	quantum mechanics
R	molar gas constant
RDS	rate determining step, the kinetically relevant step in a catalytic reaction
r_i	reaction rate for reaction i
TCD	thermal conductivity detector
UV-VIS	ultraviolet and visible light
VASP	Vienna Ab initio simulation program, a quantum chemistry package used for carrying out density functional theory calculations
XANES	X-ray absorption near edge structure
XPS	X-ray photoelectron spectroscopy
XRD	X-ray diffraction
ΔH_{ads}	enthalpy of activation
θ	angle, in degrees, of X-ray beam with respect to the sample in XRD
σ	symmetry number

Acknowledgements

During the past five years, I have been always grateful for the extreme fortune to be advised by Prof. Alexis Bell. It is really a luxury and indeed an honor, working with him at this early stage of my career, and learning from him from critical thinking, clear writing, effective presentations, time management, positive attitude, and many others. His thoughtful guidance, continuing support without reservation, and cheerful encouragement accompanied me to hurdle all the obstacles during the past years. He did motivate and nurture me so much that I feel even stronger than I ever imagined. In my mind, he is the best advisor and excellent role model.

I sincerely enjoyed studying in the Department of Chemical Engineering at Berkeley, in which students rarely have to worry about anything other than our research. I owe a huge thank you to Kristin Stangl, who helped me a lot for my orders, travel arrangements, etc., and always there to help. I would also like to thank Rocio Sanchez, Fred Deakin and Carlet Altamirano, for keeping everything working in our favor.

Within the Bell research group, many of my lab-mates have helped me with various aspects of my projects and graduate school. I cannot thank them enough for their support. I must especially acknowledge Bean Getsoian for his mentorship and exceptional collaboration, and for providing countless hours of his time to discuss the metal oxides and explain the theoretic results he got. I can truly say that I would not be where I am today without him. I also would like to thank Anton Mliner, who guided me in how to carefully design experiments and build up the hood, and provided a lot of very useful discussions about kinetics. All of these helped me immensely in keeping my research moving, and for that, I am forever grateful. Additionally, I had a great time collaborating with Rachel Licht, and I appreciate everything she did for the lab to make it like a big family. When I first joined the lab, the mentorship of Fuat Celik and Will Vining proved to be indispensible in helping me get familiar with catalysis, and get acquainted with life in the Bell lab. They acted as examples for me to emulate as I grew in seniority within the lab. In addition, I need to thank Joe Gomes, Shannon Klaus, Sankaranarayanapillai Shylesh, David Hanna, Amber Janda, Eric Sacia, Greg Johnson, Jason Wu, Lin Louie, Shaama M S, Yi-pei Li, Sebastian Werner, Zhenmeng Peng, Vlad Shapovalov, Jennifer Strunk and John Howell. They have made working in the Bell lab the pleasure that it has been over the past five years. I am also grateful to the two outstanding students I mentored, Xuan Wang and Maïté Wütschert, for their help in the experimental work and the friendship. Much of the work presented in this dissertation was only possible because of their time and effort on the project.

I would like to thank those who helped me get to Berkeley. I am thankful to my former advisor, Prof. Guangsheng Luo for his guidance during my master's study in Tsinghua University. He is always supportive and helped me a lot until right now. I also want to thank my parents for providing a loving, nurturing environment for me. They have selflessly sacrificed to give me every opportunity growing up, a debt that I can truly never repay.

Another thing that I already feel so comfortable and accustomed to is the lasting understanding, support, and love from my husband, Zhenhua Liu. He flies back and forth

every week from Caltech to Berkeley to meet me for the last five years and he has been my companion every step since we met ten years ago. It is so ordinary in my daily life that I do not remember how scarce it is and how much I have been blessed! It has been a great journey, and I can't wait to take the next steps down the road with him.

Chapter 1

Introduction

A wide variety of commodity and specialty chemicals required by modern society are produced via the selective oxidation of hydrocarbons. For example, the selective oxidation and ammoxidation of light alkenes underpins the 10 billion pounds per year acrylics industry [1]. Because of the magnitude of this production, even small improvements in catalyst activity and selectivity can result in significant economic and environmental gains by preserving a nonrenewable resource (e.g., petroleum and natural gas). Hence, it is not surprising that a large amount of research and development has been undertaken to improve the performance of catalysts used for the selective oxidation of hydrocarbons [2-9].

In Chapter 2, we first focus on the selective catalytic oxidation of propene to acrolein, a commodity chemical produced at the scale of 10^8 kg/year [10]. The most commonly used catalysts for selective oxidation of light alkenes are based on bismuth molybdate, first patented in the late 1950s [11]. Since then, a large number of studies have been published dealing with the characterization of bismuth molybdates and the mechanism of propene oxidation over these oxides [12-16]. While it is known that bismuth and molybdenum must both be present in the same phase to observe significant catalytic activity, the particular role of bismuth has not been clearly defined. In this chapter, the mechanism by which propene is oxidized on $Bi_2Mo_3O_{12}$ is investigated. XANES spectra revealed that Mo^{6+} is reduced while Bi^{3+} is not during catalyst exposure to propene at 713K. This observation contradicts the widely accepted mechanism proposed by Grasselli [1,8], which envisions that both Bi and Mo undergo reduction and re-oxidation. We have used the results of our studies to propose an alternative mechanism that is fully consistent with all experimental observations. The first step in this sequence is the physical absorption of propene on the catalyst. It is followed by the rate-determining step: the activation of the propene at one of the Mo=O bonds, during which a hydrogen atom is abstracted from a methyl group and the molybdenum center is reduced. Oxygen insertion then follows, after which a second hydrogen atom is abstracted to produce acrolein. Finally, the catalyst is re-oxidized by the gas phase oxygen. The presence of a nearby bismuth that interacts with the frontier orbitals of the active Mo=O group facilitates the promotion of an electron into a Mo−O π^* orbital that must accompany the abstraction of hydrogen from propene.

Industrial catalysts used for propene oxidation to acrolein are based on bismuth molybdate, to which many other metals are added to improve activity and selectivity [17-19]. However, the exact function of each additional element is poorly understood and very few systematic studies on the effects of an added metal have been reported due to the complex structure of the multicomponent metal oxides. A single-phase bismuth molybdate catalyst system with only one additional element is needed to simplify the problem. The remainder of Chapter 2 describes the preparation and investigation of a series of scheelite-type bismuth vanadium molybdates, $Bi_{1-x/3}V_{1-x}Mo_xO_4$ (x = 0 − 1).

XRD data shows that a solid solution is formed for all compositions of $Bi_{1-x/3}V_{1-x}Mo_xO_4$. Rate data for a range of reaction conditions were obtained and interpreted on the basis of a generalized model for the kinetics of propene oxidation over $Bi_{1-x/3}V_{1-x}Mo_xO_4$. According to this probabilistic model, vanadium and molybdenum are uniformly distributed to form three types of sites, each associated with its own rate parameters. Mo-V sites are found to exhibit the highest activity. The proposed model provides a meaningful description of the experimental data for all catalyst formulations examined.

As noted above, industrial catalysts contain many other metals in addition to Bi, Mo, and O. A fundamental question is to understand how the metals affect the activity of the host material, i.e., $Bi_2Mo_3O_{12}$. To this end, it would be beneficial to identify one or more descriptors that relates observed catalytic activity and selectivity to a physico-chemical properties of the catalyst [20-24]. This is the topic taken up in Chapters 3-5.

Chapter 3 investigates the relationship between the band gap of scheelites with compositions of $Bi_3FeMo_2O_{12}$, $Bi_2Mo_{2.5}W_{0.5}O_{12}$, and $Bi_{1-x/3}V_{1-x}Mo_xO_4$ (x = 0 − 1) and the activity of these materials for propene oxidation to acrolein. The band gaps of these oxides were found to correlate with the activation energies for propene oxidation. This relationship can be understood by examining a Born-Haber cycle relating the electronic excitation observed during the band gap measurement to an electronic excitation taking place in the transition state for propene activation. For mixed metal oxides, the band-gap energy can be thought of as the energy difference between the highest occupied crystal orbital (HOMO, which is typically oxygen-centered) and the lowest unoccupied crystal orbital (LUMO, which is transition metal centered). During the rate-determining step (hydrogen abstraction which leads to a reduction of the metal center), the energy needed to rearrange electron density within the Mo-O bond, from singlet M=O to triplet •M—O•, is the reaction barrier. This process is what the ligand-metal charge transfer (LMCT) describes, and therefore explains why the intrinsic activation energy can be related to the band gap for catalysts with the same structure that follow the same mechanism. We also demonstrate that the change in band-gap energy with composition arises from the interplay between the sizes and energies of the V 3d, Fe 3d, Mo 4d, and W 5d orbitals, which gives rise to the lowest unoccupied crystal orbitals.

The findings of Chapter 3 for scheelite-structured oxides are extended in Chapter 4 to aurivillius-structured oxides. To this end, we synthesized a set of materials with the general stoichiometry of $Bi_4V_{2-x}Mo_xO_{11+x/2}$ (x = 0 − 1) and investigated their activity for propene oxidation. It was found that the kinetics of propene oxidation over aurivillius-structured oxides are identical to those found for scheelite structures. It was also found that the apparent activation energy for propene oxidation correlates with the band gap energy for aurivillius-structured mixed metal oxides. There is however a difference of 1.5 kcal/mol between the aurivilius and scheelite catalysts that could be attributed to the difference in heat of propene adsorption on the two types of materials. The results of this work lead us to the conclusion that the use of the band-gap energy as a descriptor for catalytic activity is likely to be general feature in mixed metal oxide oxidation catalysts.

In Chapter 5, we broaden the scope of oxidation reactions to include the oxidative dehydrogenation of propane to propene and 1- and 2-butene to 1,3-butadiene, and the

oxidation of isobutene to methacrolein. This work reveals that the kinetics of these reactions change with the extent of catalyst oxidation. If the catalyst is maintained in its fully oxidized state, the kinetics for both types of reactions and all hydrocarbons are identical – first order in hydrocarbon partial pressure and zero order in oxygen partial pressure. In situ UV-Vis studies show that the rate of reaction is proportional to the rate of catalyst reduction, indicating that both oxidative dehydrogentation and oxidation proceed via a Mars van Krevelen mechanism. This observation combined with the observed first-order kinetics in hydrocarbon partial pressure can be rationalized by the same mechanism as that used for the oxidation of propene to acrolein, in which the rate-limiting step is the cleavage of the weakest C-H bond in the reacting hydrocarbon. Consistent with this interpretation, the apparent activation energy on each catalyst is found to increase with the strength of the weakest C-H bond of the reactant. This trend also follows the pattern that would be expected on the basis of the theoretical work presented in Chapter 2. The pre-exponential factor also shows a positive correlation with the apparent activation energy for the main product formation. Such a correlation suggests that the transition state for hydrogen abstraction is more tightly bound to the catalyst surface with the lower activation barrier reactant, and, hence, that the entropy of activation is more negative.

References

[1] Grasselli R.K. Top. Catal. 2002, 21 (1-3), 79-88.
[2] C.C. McCain, G. Gough, G.W. Godin, *Nature*. 198 (1963) 989-990.
[3] C.R. Adams, H.H. Voge, C.Z. Morgan, W.E. Armstrong, *J. Catal.* 3 (1964) 379-386.
[4] J. Haber, B. Grzybowska, *J. Catal.* 28 (1973) 489-505.
[5] K. Aykan, D. Halvorson, A.W. Sleight, D.B. Rogers, *J. Catal.* 35 (1974) 401-406.
[6] L.D. Krenzke, G.W. Keulks, *J. Catal. 61* (1980) 316-325.
[7] I. Matsuura, R. Schut, K. Hirakawa, *J. Catal.* 63 (1980) 152-166.
[8] R.K. Grasselli, J.D. Burrington, *Ind. Eng. Chem. Prod. Res. Dev.* 23 (1984) 393-404.
[9] T.A. Hanna, *Coord. Chem. Rev.* 248 (2004) 429-440.
[10] G. Ertl, H. Knozinger, F. Schuth, J. Weitkamp (Eds.) Handbook of Heterogeneous Catalysis, Wiley-VCH, Weinheim, 2008, pp. 3481.
[11] J.D. Idol (to Sohio), U.S. Patent 2,094,580 (September 15, 1959)
[12] H.H. Voge, C.D. Wagner, D.P. Setvenson, J. Catal. 2 (1963) 58-62.
[13] W.M.H. Sachtler. Rec. Trav. Chim. 82 (1963) 243-245.
[14] W. Ueda, K. Asakawa, C.L. Chen, Y. Moro-Oka, T. Ikawa, J. Catal. 101 (1986) 360-368.
[15] G.W. Keulks, J. Catal. 19 (1970) 232- 235.
[16] B. Grzybowska, J. Haber, J. Janas, J. Catal. 49 (1977) 150-163.
[17] Y. Moro-Oka, W. Ueda, Adv. Catal. 40 (1994) 233-273.
[18] J.M.M. Millet, H. Ponceblanc, G. Coudurier, J.M. Herrmann, J.C. Vedrine, J. Catal. 142 (1993) 381-391.
[19] D. Carson, G. Coudurier, M. Forissier, J.C. Vedrine, J. Chem. Soc. Faraday Trans. I. 79 (1983) 1921-1929.
[20] B. Hammer, J.K. Nørskov, *Adv. Catal.* 45 (2000) 71.

[21] Y.-L. Lee, J. Kleis, J. Rossmeisl, Y. Shao-Horn, D. Morgan. *Energy Environ. Sci.* 4 (2011) 3966.
[22] P. Moriceau, A. Lebouteiller, E. Bordes, P. Courtine, *Phys. Chem. Chem. Phys.* 1 (1991) 5735.
[23] P. Moriceau, B. Tauok, E. Bordes, P. Courtine, *Catal. Today* 61 (2000) 197.
[24] E. Bordes-Richard, *Top. Catal.* 50 (2008) 82.

Chapter 2

The Kinetics of Selective Oxidation of Propene on Bismuth Vanadium Molybdenum Oxide Catalysts

Abstract

We report the results of a systematic investigation of the kinetics of propene oxidation to acrolein over $Bi_{1-x/3}V_{1-x}Mo_xO_4$. BET isotherms were measured to determine catalyst surface area and powder x-ray diffraction was used to characterize the bulk structure. Further characterization by x-ray absorption near edge spectroscopy (XANES) was used to determine the oxidation states of Bi, Mo, and V before and after exposure of the catalyst to propene at 713 K. We find that, contrary to previous discussions of the mechanism of propene oxidation on $Bi_{1-x/3}V_{1-x}Mo_xO_4$, Bi remains in the 3+ state and only V and Mo undergo reduction and oxidation during reaction. The kinetics of propene oxidation were examined to establish the activation barrier for acrolein formation and how the partial pressure dependences on propene and oxygen change with the value of x. The data obtained from this study were then used to propose a generalized model for the kinetics of propene oxidation over $Bi_{1-x/3}V_{1-x}Mo_xO_4$ that is consistent with our findings about the reducibility of the three metallic elements in the oxide. According to this model, vanadium and molybdenum are randomly distributed to form three types of sites each associated with its own rate parameters. Mo-V sites are found to exhibit the highest activity. The proposed model provides a good description of the experimental data for all catalyst formulations examined, for a range of propene and oxygen partial pressures, and for temperatures above 653 K.

2.1 Introduction

The catalytic oxidation of low molecular weight alkenes to produce α,β-unsaturated aldehydes is widely used industrially. Among the most successful of these reactions is the selective oxidation of propene to acrolein [1], a commodity chemical produced at the level of 10^8 kg/year [2]. While the first catalysts used for propene oxidation to acrolein were based on cuprous oxide [3], several other systems have also been studied [4-8]. Subsequent work demonstrated that higher acrolein yields could be obtained using catalysts based on bismuth molybdates [9,10]. Since their first introduction into commercial use, a large number of studies have been published dealing with the characterization of bismuth molybdates and the mechanism propene oxidation over these oxides [11-17]. These efforts have shown that the oxidation of propene involves consumption of oxygen from the oxide lattice and its subsequent replacement by gas phase O_2, i.e, via a Mars van Krevelen mechanism [18]. The rate-limiting step is abstraction of an H atom from the methyl group of propene to form an allyl intermediate. Acrolein is then produced by the abstraction of a second H atom from the allyl species. While not demonstrated experimentally, it has been suggested that in the course of the reaction, both Bi and Mo undergo reduction and re-oxidation.

Catalysts employed industrially are multicomponent metal oxides in which bismuth molybdate is the main component. Such catalysts exhibit much higher yields of acrolein than can be attained using bismuth molybdate alone [19-21]. The exact function of the added elements is only poorly understood, and very few systematic studies of the effects of an added metal have been reported. One system that has been investigated more extensively than others is bismuth vanadium molybdate, $Bi_{1-x/3}V_{1-x}Mo_xO_4$ ($x = 0 - 1$) [22]. This material has a scheelite-type structure. The ideal scheelite ($CaWO_4$) structure has the stoichiometry ABO_4, where the B cation is tetrahedrally coordinated by oxygen and the A cation is coordinated to eight O atoms from eight different MO_4 tetrahedra. In the case of $Bi_{1-x/3}\square_{x/3}V_{1-x}Mo_xO_4$ ($\square$ = cation vacancy), $x/3$ cation deficiencies exist. X-ray diffraction studies of these compounds show that the lattice parameter of the crystal changes systematically and that the replacement of vanadium by molybdenum results in random bismuth cation vacancies in order to balance the difference in charges between $(VO_4)^{3-}$ and $(MoO_4)^{2-}$ anions [23,24].

Ueda et al. [14] and Sleight et al. [24,25] have reported that $Bi_{1-x/3}V_{1-x}Mo_xO_4$ is more active for the oxidation of propene and butene than either bismuth molybdate ($x = 1$) or bismuth vanadate ($x = 0$). Ueda et al. [14] have also noted a correlation between the catalytic activity and the mobility of lattice oxide ions. However, the reason for such a correlation is not apparent, because at elevated temperatures, the rate of propene oxidation is zero order in oxygen partial pressure, and the rate-determining step – abstraction of hydrogen from the olefin – does not involve lattice oxygen diffusion. Sleight et al. [24,25] have argued that both defects and bismuth have dramatic effects on the activity and selectivity of olefin oxidation reactions. They propose that the role of the defect appears to be to promote the formation of the allyl radical, while bismuth serves to promote rapid reoxidation of the catalyst. However, no experimental evidence is given to support these suggestions. Therefore, the exact roles of Bi and V in affecting the activity and selectivity of the $Bi_{1-x/3}V_{1-x}Mo_xO_4$ catalysts remain unclear.

We report here the results of a systematic study aimed at understanding the trends in activity and selectivity of $Bi_{1-x/3}V_{1-x}Mo_xO_4$ catalysts for propene oxidation to acrolein. Powder x-ray diffraction was used to obtain bulk structural information, and the oxidation states of Bi, Mo, and V were characterized by x-ray absorption near edge spectroscopy (XANES) before and after exposure of the catalyst to propene. The kinetics of propene oxidation were examined to establish how the activation barrier to acrolein formation and the partial pressure dependences on propene and oxygen change with the value of x. The data obtained from this study was then used to propose a generalized model for the kinetics of propene oxidation over $Bi_{1-x/3}V_{1-x}Mo_xO_4$.

2.2 Methods

2.2.1 Catalyst Preparation

$Bi_{1-x/3}V_{1-x}Mo_xO_4$ catalysts were prepared by complexation using citric acid [26,27]. This method allows for good mixing of the precursor materials and produces a solid product with a more uniform distribution of the metallic elements and a higher surface area than can be achieved by co-precipitation [28].

The precursors used in the catalyst preparation were ammonium molybdate tetrahydrate ($(NH_4)_6Mo_7O_{24} \cdot 4H_2O$) (99.98%, Sigma-Aldrich), bismuth(III) nitrate pentahydrate ($Bi(NO_3)_3 \cdot 5H_2O$) (99.98%, Sigma-Aldrich), and ammonium metavanadate (NH_4VO_3) (99%, Sigma-Aldrich). The metal precursors were added to the preparation solutions at the atomic ratios of Bi:V:Mo = (1-x/3):(1-x):x, (x = 0 to 1) in order to produce materials with the stoichiometry $Bi_{1-x/3}V_{1-x}Mo_xO_4$. The precursor solutions were $Bi(NO_3)_3 \cdot 5H_2O$/citric acid with molar ratio of 1:1 dissolved in 2M HNO_3 (solution A), $((NH_4)_6Mo_7O_{24} \cdot 4H_2O)$/citric acid prepared with molar ratio of (1/7):1 (solution B) dissolved in water, and NH_4VO_3/citric acid prepared with molar ratio of 1:1 (solution C) dissolved in water. 2M HNO_3 was used in place of water in solution A in order to prevent precipitation of bismuth hydroxides. Solution B was slowly added to solution A, followed by addition of solution C. The resulting mixture was placed in an oven at 60 °C for about 24 h in air until it formed a gel. The gel was then dried at 120 °C for 2 h and calcined in air at 600°C for 6 h.

2.2.2 Catalyst Characterization

Powder X-ray diffraction patterns were obtained with a Siemens D5000 diffractometer using Cu Kα radiation. Data were collected in the range 5°<2θ <70° with a step size of 0.02°.

X-Ray absorption spectroscopy (XAS) measurements were performed at the Advanced Photon Source at Argonne National Laboratory (ANL) on beam line 10-BM. Measurements were performed at the Bi L_3-edge, and at the Mo and V K-edges. The energy for each element was referenced to that for the pure metal, as determined by placing a metal foil between two ionization chambers located after the sample. The metal edge energy was taken as the first inflection point of the main absorption peak. Sample quantities were calculated to obtain an absorbance of ~2.5, and boron nitride, an inert and relatively x-ray transparent material, was added to make a self-supporting pellet. An absorbance of 2.5 provides optimal signal to noise ratio [29]. Samples were placed in a controlled-atmosphere cell that allowed for heating to 713K in the presence of flowing gas [30], and then cooled to ambient conditions before collecting the XAS data. The XAS data were analyzed with the IFEFFIT software and its complementary Athena GUI [31,32].

2.2.3 Catalyst Activity and Selectivity

Measurements of reaction rates and product distributions were performed using a packed bed quartz tube reactor (10 mm in diameter) loaded with 100-500 mg of catalyst. Reactions were carried out between 573 K and 713 K. This temperature range assured that no bulk phase changes occurred in the catalysts. Prior to starting a reaction, the catalyst was preheated to the reaction temperature in air in order to remove residual moisture. All experiments were carried out at atmospheric pressure with 3.3-16.7% propene (99.9%, Praxair) and 3.3-16.7% oxygen (supplied from 20% oxygen in helium, Praxair), balanced as needed with additional helium (99.995%, Praxair). Flow rates and catalyst loadings were chosen to maintain propene conversion around 1% so that the intrinsic kinetics could be measured under conditions of differential conversion. Data

were collected after steady-state conditions were achieved. Products were analyzed using a gas chromatograph (GC) equipped with a 30 m HP-PLOT Q column and a flame ionization detector (FID), for analyzing propene, acrolein, ethene and acetaldehyde. An Alltech Hayesep DB packed column was used to analyze for oxygen, carbon mono- and di-oxides, and these products were detected by a thermal conductivity detector (TCD).

Conversion was calculated on the basis of products formed (since conversions were below 5%). Selectivity to acrolein was defined as moles of propene converted to acrolein over moles of propene converted to all products, based on a carbon balance.

2.3 Results

2.3.1 Catalyst Characterization

2.3.1.1 Structure of $Bi_{1-x/3}V_{1-x}Mo_xO_4$ Catalysts from XRD

Powder X-ray diffractograms for different compositions of $Bi_{1-x/3}V_{1-x}Mo_xO_4$, shown in Figure 2.1, exhibit similar features as the value of x changes, indicating that the crystal structure changes only slightly with composition.

In general, $Bi_{1-x/3}\square_{x/3}V_{1-x}Mo_xO_4$ ($\square$ - cation vacancy) solid solutions have a tetragonal scheelite structure in which xMo^{6+} cations replace an equivalent number of V^{5+} cations at the tetrahedral sites, leaving x/3 eight-coordinated cation vacancies [33]. High vacancy content leads to the monoclinic distortion observed for x > 0.75, evidenced by the splitting of the peaks at $2\theta \sim 28º$, 47°, and 53°.

2.3.1.2 Oxidation State Change of Different Element in $Bi_{1-x/3}V_{1-x}Mo_xO_4$ Catalysts from XANES

In situ XANES spectra of $Bi_{1-x/3}V_{1-x}Mo_xO_4$ were acquired during exposure to propene at 713 K, with the aim of establishing which elements are reduced and to what extent. Figure 2.2 shows XANES spectra for the L_3-edge of Bi and the K-edge of Mo before and after exposure of $Bi_2Mo_3O_{12}$ (x = 1) to propene for 24 h. The Bi L_3-edge (13429 ev) does not change with time and remains identical to that for Bi_2O_3, indicating that Bi remains in the 3+ state and is not reduced. By contrast, the initial Mo K-edge (20017 ev) is identical to that of $CaMoO_4$, indicating that Mo is in the 6+ state. After reduction, the Mo K-edge shifts to lower energy (20008 eV), becoming identical to that of MoO_2. This means that after extended reduction, all of the Mo is in the 4+ state.

The pre-edge feature seen in the XANES spectrum of Mo is due to a 1s to 4d transition (allowed by 4d-5p orbital hybridization) [29,30] the height of which indicates the oxidation state and coordination of Mo. $CaMoO_4$ contains isolated tetrahedral molybdate units, and the high degree of p-d hybridization in tetrahedral coordination environments is responsible for the strong pre-edge feature observed for this compound. The lower pre-edge height of oxidized $Bi_2Mo_3O_{12}$ has been ascribed to a distortion in the geometry of the tetrahedral molybdate [22], which lowers the extent of p-d hybridization.

For MoO_2, Mo^{4+} cations occur as nearly octahedral molybdate units, and in this case there is almost no p-d hybridization, and consequently no pre-edge feature.

Figure 2.3 shows XANES spectra for the L_3-edge of Bi, the K-edge of Mo, and the K-edge of V before and after exposure of $Bi_{0.85}V_{0.55}Mo_{0.45}O_4$ (x = 0.45) to propene for 24 h. Here bismuth is not reduced after exposure to propene, but molybdenum is reduced from Mo^{6+} to Mo^{4+}. For vanadium, the V K-edge energy (5480 ev) observed in the oxidized catalyst is identical to that of $NaVO_3$ (V^{5+}), indicating that V is initially in the 5+ state. After reduction, the edge shifts (5478 ev) and pre-edge feature height decreases indicating a reduction of V to the 4+ oxidation state. For vanadium, the pre-edge feature is a 1s to 3d transition (allowed by 3d-4p orbital hybridization). After reduction, the increase in d-orbital occupancy leads to a decrease in hybridization. Consequently, fewer states are available for the transition from the 1s orbital and the pre-edge peak intensity decreases.

Figure 2.4 shows XANES spectra for the L_3-edge of Bi and the K-edge of V before and after exposure of $BiVO_4$ (x = 0) to propene at 713 K. Bismuth is not reduced, but vanadium is reduced from V^{5+} to V^{4+}. To summarize, for all compositions of $Bi_{1-x/3}V_{1-x}Mo_xO_4$, only molybdenum and vanadium are reduced by propene.

2.3.2 Kinetics of Propene Oxidation over $Bi_{1-x/3}V_{1-x}Mo_xO_4$

The main product of propene oxidation over $Bi_{1-x/3}V_{1-x}Mo_xO_4$ is acrolein, and the principle byproducts are CO_2, CO, acetaldehyde, and ethylene. The influence of vanadium content on catalyst activity for acrolein formation is presented in Figure 2.5. At 673 K, the activity passes through a well-defined maximum for x = 0.45, in a manner similar to that reported by Ueda et al [14].

The influence of propene conversion on the selectivity to acrolein is illustrated in Figure 2.6. In each case, the propene conversion was increased by reducing the space time. With the exception of $BiVO_4$, acrolein selectivity did not change with propene conversion. This indicates that acrolein and the other byproducts are produced in parallel on $Bi_{1-x/3}V_{1-x}Mo_xO_4$, but on $BiVO_4$ secondary oxidation of acrolein to CO_x also occurs. Flow rates and catalyst loadings were chosen to maintain conversion around 1%, and the intrinsic selectivity was determined by extrapolating data taken as a function of space velocity to zero conversion. The intrinsic selectivity for oxidation of propene over the $Bi_{1-x/3}V_{1-x}Mo_xO_4$ catalysts at 400ºC is presented in Figure 2.7. The selectivity to acrolein increases from 75% at x = 0 to a maximum of 85% at x = 0.15 and then decreases to 68% for x = 1.

The selectivity to byproducts is also presented in Figure 2.7. $BiVO_4$ has a noticeably higher selectivity to CO_2 than the other catalyst compositions. On $BiVO_4$, acrolein can be further oxidized to produce CO_2, consisted with the observation that selectivity to CO_2 increases and electivity to acrolein decreases with increasing conversion. For x = 0.15 catalyst, the selectivity to CO and CO_2 reached a minimum, consistent with the observation of the highest selectivity to acrolein for this value of x.

9

2.3.2.1 Temperature Dependence

Arrhenius plots for propene oxidation to acrolein over bulk $Bi_{1-x/3}V_{1-x}Mo_xO_4$ are shown in Figure 2.8 for the temperature range 573 K - 713 K. A single linear relationship was obtained for $Bi_2Mo_3O_{12}$ and $BiVO_4$, with apparent activation energies of 19.9 ± 0.3 kcal/mol and 14.5 ± 0.1 kcal/mol, respectively. However, when both V and Mo were present in the catalyst (0 < x < 1), the apparent activation energy was higher at low temperatures (573 K - 653 K) and lower at high temperatures (653 K - 713 K). Values of the apparent activation energy are listed in Table 2.1 for each temperature range. In the high temperature range, the apparent activation energies for intermediate compositions are similar to that for $BiVO_4$. The results show that adding moderate amounts of V decreases E_{app}, relative to that for $Bi_2Mo_3O_{12}$. The results obtained at temperatures above 653 K are similar to those reported by Ueda et al [14], who observed no change in the apparent activation energy with the value of x for temperatures in the range of 673 K - 743 K.

2.3.2.2 Pressure Dependence

Table 2.2 shows how the reaction orders for C_3H_6 and O_2 are affected by changing composition, x, at 673 K (in the high temperature range) and 613 K (in the low temperature range) for $Bi_{1-x/3}V_{1-x}Mo_xO_4$. In all cases the rate of acrolein formation can be represented by:

$$rate_{acrolein} = k_{app}P_{C_3H_6}^m P_{O_2}^n \qquad (1)$$

where m and n are the apparent reaction orders of propene and oxygen.

For $BiVO_4$ and $Bi_2Mo_3O_{12}$, the data show that for both the high and low temperature regimes, the rate of propene oxidation to acrolein is nearly first-order with respect to the partial pressure of C_3H_6 and nearly zero-order with respect to the partial pressures of O_2.

However, for intermediate compositions (0 < x < 1), the reaction orders vary with temperature. The dependence on partial pressure of C_3H_6 increased from nearly zero order at low temperature (613 K) to nearly first order at high temperature (673 K). The reaction order with respect to O_2 decreased from a positive fractional order at lower temperatures to zero order at higher temperatures.

Previous studies have found a kinetic isotope effect for H- vs. D-labeled propene, and an isotope distribution in the oxidation products of ^{13}C-labeled propene consistent with a π-allyl intermediate [34,35]. These studies have argued that the rate-determining step (RDS) is the abstraction of an α-methyl hydrogen to form a π-allyl intermediate. The reaction orders observed at higher temperatures (673 K) in the present study are consistent with previous results, and suggest that the measured apparent activation energies can be related to the abstraction of H atoms from the methyl group of propene in the RDS.

In contrast to the first order dependence on C_3H_6 and zero order dependence of O_2 found at 673 K, the nearly zero order dependence on C_3H_6 and the positive order

dependence on O_2 found at 613 K suggest a change in the RDS from abstraction of the H atom to a step that is related to lattice re-oxidation.

Ueda et al. [14] observed that propene oxidation is first order with respect to propene and independent of the oxygen pressure for all x values at 673 K - 743 K, consistent with what we observe in the high temperature regime (653 K - 713 K). A change in reaction order for propene and oxygen at different temperatures has also been reported previously by Keulks et al. [36] for β-$Bi_2Mo_2O_9$.

Reaction orders for C_3H_6 and O_2 were also measured for the main byproducts CO_2 and CO at 673 K on $BiVO_4$, $Bi_2Mo_3O_{12}$ and $Bi_{0.95}V_{0.85}Mo_{0.15}O_4$ (x = 0.15), and the results are shown in Table 2.3. For all of the catalysts, the rate of CO_2 production is nearly first order in C_3H_6. For $BiVO_4$, a nearly zero order dependence on O_2 is observed, but for $Bi_2Mo_3O_{12}$ and $Bi_{0.95}V_{0.85}Mo_{0.15}O_4$, the dependence on O_2 is slightly positive order. The rate of CO production, however, exhibited a nearly first order dependence on both C_3H_6 and O_2. The selectivity dependence on partial pressure of C_3H_6 and O_2 for these three catalysts is shown in Figure 2.9. For all three catalysts, the selectivity to acrolein, CO and CO_2 remains almost constant due to the nearly first order dependence on C_3H_6 for all the three products. However, the selectivity to acrolein increases with decreasing O_2 concentration, a consequence of the positive dependence on O_2 for CO_2 and CO formation and the zero order dependence on O_2 for acrolein formation.

2.4 Discussion

2.4.1 Mechanism and Kinetics of Propene Oxidation to Acrolein

The mechanism of propene oxidation to acrolein over $Bi_2Mo_3O_{12}$ has been discussed extensively by Grasselli and coworkers [37-40], and is summarized in Scheme 2.1. The following steps are involved:

1.Coordination of propene to the catalyst.

2.Activation of propene at a bismuth site to form a π-allyl species, during which a hydrogen atom is abstracted and a metal center is reduced. Adams et al. [41] have shown that this is the rate determining step in the reaction at 723 K.

3.C-O bond formation or lattice oxygen insertion.

4.A second hydrogen abstraction to form acrolein and a reduced site.

5.Re-oxidation of the active site, either by oxygen migration from the bulk or by gas phase O_2.

Grasselli et al. [37-39] proposed that an oxygen bridging between Bi and Mo in $Bi_2Mo_3O_{12}$ is responsible for H-abstraction. The occurrence of this step is hypothesized to result in reduction of Bi^{3+} to Bi^{2+}. An oxygen double-bonded to Mo is proposed to react with the allylic intermediate in step 3. Since propene oxidation to acrolein is a four-electron process, molybdenum is assumed to reduce from Mo^{6+} to Mo^{3+}.

In Grasselli's mechanism, Bi^{3+} is assumed to be reduced before Mo^{6+}. However, Mo^{6+} should be easier to reduce than Bi^{3+} due the lower energy of a Mo 4d orbital

compared with a Bi 6p orbital [42,43]. XANES data reported here (see Figure 2.2) show that bismuth is not reduced, but molybdenum is reduced from Mo^{6+} to Mo^{4+}. This suggests that two Mo^{6+} centers must be involved in the redox reaction in order for the four-electron process of oxidation of propene to acrolein to take place. The overall process on $Bi_2Mo_3O_{12}$ is hypothesized to follow steps as shown in Scheme 2.2. One active site involves two adjacent molybdenum centers. The structure depicted in Scheme 2.2 represents the low energy (010) surface [22, 44]. However, any surface of the catalyst containing neighboring Mo sites should be competent to carry out the reaction. The reaction mechanism involves the following steps:

1. Physical adsorption of propene onto the catalyst.

2. Hydrogen abstraction from the methyl group of propene by one of the Mo=O bonds and reduction of Mo^{6+} to Mo^{5+}. The reaction passes through a barrierless π-allyl radical step, O insertion follows immediately, and another Mo^{6+} center is reduced to Mo^{5+}. This step is still believed to be the rate determining step in the reaction. Two adjacent molybdenum centers are required and two electrons are transferred in this step, resulting in the formation of Mo-OH and Mo-OCH$_2$CH=CH$_2$ species.

3. A second hydrogen is abstracted to produce acrolein and another hydroxyl group, resulting in further reduction of two Mo centers to Mo^{4+}.

4. Water is formed and desorbed reversibly, producing oxygen vacancies. According to XANES data, a fully reduced site with two Mo^{4+} centers is formed.

5. Re-oxidation of the active site by gas phase oxygen.

2.4.2 Rate Expression Based on Kinetics Data

All the steps, together with pseudo-steady-state assumptions for the intermediate compositions, lead to the rate expression shown in Eqn. 2. (See Supporting Information for the derivation.)

$$rate = \frac{k_1 k_2 P_{C_3H_6}[S]}{(k_2 + k_{-1})\left[1 + \dfrac{k_1 P_{C_3H_6}}{k_2 + k_{-1}} + \dfrac{k_1 k_2 P_{C_3H_6}}{k_3(k_2 + k_{-1})} + \left(\dfrac{k_1 k_2 P_{C_3H_6}}{k_4(k_2 + k_{-1})} + \dfrac{k_1 k_2 k_{-4} P_{C_3H_6} P_{H_2O}}{k_4 k_5 P_{O_2}(k_2 + k_{-1})}\right) + \dfrac{k_1 k_2 P_{C_3H_6}}{k_5 P_{O_2}^n(k_2 + k_{-1})}\right]} \quad (2)$$

For temperatures in the range 653 K - 713 K, the rate of propene oxidation to propene is first-order in propene and zero order in oxygen (see Table 2.2). These kinetics are consistent with Eqn. 3 when the fully oxidized active site (the "1" term in the denominator in Eqn. 2) is taken to be the most abundant surface intermediate:

$$rate_{acrolein} = \frac{k_1 k_2 [S]}{(k_{-1} + k_2)} P_{C_3H_6} = k_{app} P_{C_3H_6} \quad (3)$$

In this case, the apparent rate constant k_{app} is given by $\dfrac{k_1 k_2 [S]}{(k_{-1} + k_2)}$. By contrast, in the low-temperature regime (573 K - 653 K) for $0 < x < 1$, the rate of propene oxidation to acrolein is nearly zero-order in C_3H_6 and positive-order in O_2. This dependence implies

that the last term in the denominator of Eqn. 2 is dominant, i.e., the most abundant surface intermediates are reduced centers, and in this case, the rate of acrolein formation is given by:

$$rate_{acrolein} = k_5 P_{O_2}^n \tag{4}$$

The next challenge is to develop an expression for k_{app} that accounts for the effects of catalyst composition. This will be done for the case of reaction carried out in the high temperature regime (653 K - 713 K), for which the first H abstraction is the RDS.

In the absence of V we assume that an active site involves two adjacent molybdenum centers, as is shown in Scheme 2.2. As the value of x increase in $Bi_{1-x/3}V_{1-x}Mo_xO_4$, Mo^{6+} cations substitute for V^{5+} cations, creating three different types of sites as shown in Scheme 2.3. Sleight et al. have proposed that disordered cation vacancies are introduced randomly into the lattice [24], so we have assumed that vanadium and molybdenum are randomly distributed.

According to the formula $Bi_{1-x/3}V_{1-x}Mo_xO_4$, x is equal to the molybdenum content over the sum of the molybdenum and vanadium content in the catalyst. Therefore, the probabilities of finding different types of active sites are:

Mo-Mo: $P_{Mo} = x^2$

Mo-V: $P_{mix} = 2x(1-x)$ $\tag{5}$

V-V: $P_V = (1-x)^2$

Giving the total probability of different types of active sites as:

$$P_{Mo} + P_{mix} + P_V = x^2 + 2x(1-x) + (1-x)^2 = 1 \tag{6}$$

Therefore the total rate constant for all compositions can be expressed as:

$$k_{app} = k_{Mo} x^2 + k_{mix} 2x(1-x) + k_V(1-x)^2 \tag{7}$$

Eqn. 7 contains three unknowns, one for each of the rate constants for the three different types of sites. Values for k_V and k_{Mo} can be obtained directly from the experimental data for $BiVO_4$ and $Bi_2Mo_3O_{12}$ (673 K data see Figure 2.8). For k_{mix}, we analyzed values of k_{app} for x = 0.15, 0.30, 0.45, 0.60, 0.75 using Eqn. 7 and found that k_{mix} is independent of the value of x. Values of k at 673 K are given in Table 2.4.

Figure 2.10 demonstrates that Eqn. 5 together with the parameters shown in Table 2.4 provides a good description of the experimental data. We can extend the model to describe all of the data taken in the high temperature regime (653 K - 713 K). To do so, we assume that k_V, k_{Mo} and k_{mix} can each be expressed as an Arrhenius expression, Eqn. 8:

$k_{Mo} = A_{Mo}exp(-E_{Mo}/RT)$

$k_V = A_V exp(-E_V/RT)$ $\tag{8}$

$k_{mix} = A_{mix}exp(-E_{mix}/RT)$

Here the A_i is the pre-exponential factor and E_i is the apparent activation energy for site type i.

The six unknowns (appearing in Eqn. 8), A_{Mo}, E_{Mo}, A_V and E_V can be obtained from experimental data for $BiVO_4$ and $Bi_2Mo_3O_{12}$. For A_{mix} and E_{mix}, we used k_{app} values for x = 0.15, 0.30, 0.45, 0.60, 0.75 and calculated all k_{mix} values using Eqn. 9, which is derived from Eqn. 7.

$$k_{mix} = [k_{app} - k_{Mo} x^2 - k_V(1-x)^2]/[2x(1-x)] \tag{9}$$

From Arrhenius plots of k_{mix} for different values of x, we can determine A_{mix} and E_{mix}. The A_i and E_i values are listed in Table 2.5. Figure 2.11 shows that the model for k_{app} given by Eqn. 10 describes all of the data taken in the high temperature regime (653 K - 713 K) quite effectively.

$$k_{app} = A_{Mo}exp(-E_{Mo}/RT)x^2 + A_{mix}exp(-E_{mix}/RT)2x(1-x) + A_Vexp(-E_V/RT)(1-x)^2 \tag{10}$$

A parity plot comparing values of k_{app} obtained from the data and from Eqn. 10 is shown in Figure 2.12. The data presented in this plot were taken at different temperatures and different partial pressures of propene and oxygen. The slope of the plot is 0.964 ± 0.013, with R = 0.9777, indicating a good description of data by the model.

Using the data in Table 2.5, we can also verify the relationship of E_{app} vs. x determined from Eqn. 10. The comparison of experimental data to the model is shown in Figure 2.13. The values of E_{app} from the model are calculated by picking a value of x, and then calculating k_{app} for different temperatures. E_{app} is then determined from the slope of a plot of (ln k_{app}) v.s. (1/T).

The agreement between experiment and model indicate that the assumptions made in developing the model are reasonable. Vanadium and molybdenum are randomly distributed to form three types of sites with different reaction properties. There are no interactions between different types of sites. Table 2.5 lists the rate parameters for each of the three sites. The apparent activation energy E_{app} actually includes physical adsorption from step 1 and the intrinsic activation energy of H abstraction from the RDS, step 2 in Scheme 2.2.

The lowest activation barrier is for V-V sites (14.5 kcal/mol). The activation barrier for Mo-V sites, E_{app} (16.0 kcal/mol) is higher, but closer to that for V-V sites than to that for the Mo-Mo sites (19.9 kcal/mol). The lower barrier for V-containing sites can be attributed to the greater ease of reduction of V^{5+} than Mo^{6+} [42,43]. Therefore, activation of propene occurs more rapidly on V=O than Mo=O. On both V-V and Mo-V sites, vanadium is responsible for the first H abstraction. However, on Mo-V sites, Mo-$OCH_2CH=CH_2$ is formed and both V and Mo are reduced, but on V-V sites, two V are reduced and V-$OCH_2CH=CH_2$ is produced.

Table 2.5 shows that there is a positive correlation between the pre-exponential factor, A, and the activation barrier. Such a correlation suggests that the transition state for hydrogen abstraction from the methyl group of propene is more tightly bound to the catalyst surface with the lower activation barrier and, hence, that the entropy of activation is more negative.

In the low-temperature regime (573 K - 653 K), for $0 < x < 1$, the RDS becomes the re-oxidation of the catalyst, a process for which the order in the partial pressure of oxygen is about 0.5. This rate expression can be rationalized in terms of the following mechanism [45]:

$$M + O_2 \longleftrightarrow M - O_2$$
$$M - O_2 + V \longleftrightarrow O_L + M - O$$
$$M - O + V \longrightarrow O_L + M$$
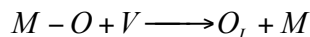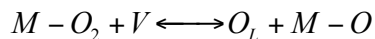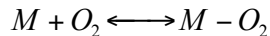
M represents a surface site where gaseous oxygen can chemisorb and dissociate, and V represents an anion vacancy located either on the surface or in the bulk. The first step is reversible adsorption of di-oxygen followed by step 2, oxygen dissociation. Because of half order dependence in oxygen, the third step is rate-determining.

Grasselli et al. [45] observed two re-oxidation processes which are a function of the initial degree of catalyst reduction, proved by a pulse microreactor method on $Bi_2Mo_3O_{12}$. At low degrees of reduction, re-oxidation of proceeds with an activation energy of 1.2 kcal/mol and re-oxidation is confined primarily to the surface of the catalyst. The activation energy is low since only surface diffusion of oxygen is required to fill oxygen vacancies. This is the case for $BiVO_4$ and $Bi_2Mo_3O_{12}$ in the low-temperature regime in our study, in which reduction is the RDS and fully oxidized sites are the most abundant surface species, indicating a low degree of reduction and a low activation energy for re-oxidation. However, for high extents of reduction, Grasselli et al. found that the activation energy for re-oxidation increases to about 26.0 kcal/mol, a value similar to that reported here (see Table 2.1). In this case, re-oxidation involves subsurface vacancies and not just those on the surface. So the re-oxidation rate is limited by oxygen mobility, the ability to transport the newly incorporated surface oxygen to the bulk vacancies. This is the case for intermediate compositions in the low-temperature regime, for which fully reduced sites are the most abundant surface intermediates, and the catalysts exhibit a high activation energy for re-oxidation.

2.4.3 Product Selectivity

The byproducts of propene oxidation over $Bi_{1-x/3}V_{1-x}Mo_xO_4$ catalysts are CO, CO_2, CH_3CHO, and C_2H_4. The pathways to these byproducts are not well understood. Keulks et al. [36,46] have reported $^{18}O_2$ labeling studies aimed at elucidating the reaction pathways to acrolein and CO_2 on $Bi_2Mo_3O_{12}$. At low conversions, it is believed that CO_2 is formed from an adsorbed precursor to acrolein or from a stable surface intermediate produced after the formation of the allylic species [47]. Green et al. [48] have also proposed surface reaction mechanisms for the products formation, in which CO and CO_2 originate from an acrolein precursor. The results presented in Figure 2.6 demonstrate that on $Bi_2Mo_3O_{12}$, all byproducts are formed in parallel with acrolein and that there is no evidence for the further oxidation of acrolein. This suggests that CO_2 is formed from a surface intermediate produced after the formation of allylic species in agreement with prior studies. We also note that the partial pressure dependence on O_2 for CO_2 formation is 0.4 on $Bi_2Mo_3O_{12}$, and is first order for CO formation. This suggests that the oxygen

atoms in CO_2 come from both gas phase oxygen and lattice oxygen; however, the oxygen atom in CO only comes from gas phase oxygen, and not from lattice oxygen.

A possible mechanism for forming CO, CO_2, CH_3CHO, and C_2H_4 on $Bi_2Mo_3O_{12}$ is shown in Scheme 2.4. The reaction sequence begins with the allyl species formed in the RDS. Reaction of an adsorbed O_2 with the adsorbed acrolein is proposed to form an intermediate leading to CO and CO_2. Cleavage of the C-C bond in this species can result in formation of acetaldehyde, and CO or CO_2. In this mechanism, the oxygen in CO comes from O_2, whereas one of the oxygen atoms in CO_2 comes from O_2 and the other from lattice oxygen.

For both $Bi_{0.95}V_{0.85}Mo_{0.15}O_4$ and $Bi_2Mo_3O_{12}$ the partial pressure dependencies for CO and CO_2 production are very similar (see Table 2.3), and Figure 2.9 shows that CO and CO_2 are formed in a 1:1 ratio on both catalysts. This suggests that the pathways leading to CO and CO_2 formation on $Bi_{0.95}V_{0.85}Mo_{0.15}O_4$ and $Bi_2Mo_3O_{12}$ are similar, and likewise for other catalysts with the general stoichiometry of $Bi_{1-x/3}V_{1-x}Mo_xO_4$. The exception is for $BiVO_4$ (x = 0) for which the rate of CO_2 production exhibits a zero-order dependence on O_2, which means that all the oxygen in CO_2 come from lattice oxygen. We note further that this is the only catalyst for which acrolein can undergo secondary oxidation to CO_2. We hypothesize that this distinctive behavior may be a direct consequence of the greater ease with which V, as compared to Mo, can undergo oxidation.

2.5 Conclusions

The activity and selectivity of $Bi_{1-x/3}V_{1-x}Mo_xO_4$ for the oxidation of propene to acrolein changes in a systematic manner with the value of x = Mo/(Mo+V). The maximum activity for acrolein formation occurs at x = 0.45, whereas the maximum in the selectivity to acrolein occurs at x = 0.15. At temperatures above 653 K, the rate of acrolein formation is first order in the partial pressure of propene and zero order in the partial pressure of oxygen for all values of x between 0 and 1, suggesting that the catalyst is fully oxidized and that the formation of acrolein does not involve gas-phase O_2. Below 653 K, the rate of acrolein formation becomes zero order in the partial pressure of propene and positive order in the partial pressure of oxygen for catalyst compositions with 0 < x < 1. The two exceptions are $BiVO_4$ (x = 0) and $Bi_2Mo_3O_{12}$ (x = 1), for which the dependencies on propene and oxygen partial pressures remain the same as those observed for temperatures below 653 K. These trends suggest that at low temperatures and catalyst compositions for which 0 < x < 1, the formation of acrolein is rate-limited by catalyst re-oxidation. Further evidence for a change in the rate-limiting step with temperature is seen in the activation energies. Above 653 K, the activation energy for acrolein formation is about 16 kcal/mol for catalyst compositions for which 0 < x < 1. However, the activation energy is the same as that measured at temperatures above or below 653 K for x = 0 and x = 1. The reason why the rate-limiting step does not change with temperature for $BiVO_4$ (x = 0) and $Bi_2Mo_3O_{12}$ (x = 1) is not apparent and requires further investigation.

The primary byproducts of propene oxidation are CO and CO_2. These products are produced in parallel to acrolein on all catalysts except for $BiVO_4$, for which CO_2 also forms via the combustion of acrolein. The kinetics of both CO and CO_2 formation are

first order in the partial pressure of propene, and are first order in the partial pressure of oxygen for CO formation and between zero and 0.4 order in the partial pressure of oxygen for CO_2 formation. These observations suggest that the formation of CO and CO_2 occur via the reaction of molecularly or atomically adsorbed oxygen with a precursor to acrolein. For $BiVO_4$ the re-adsorption of acrolein leads to its combustion to form CO_2.

Powder x-ray diffraction demonstrates that the crystal structure of $Bi_{1-x/3}V_{1-x}Mo_xO_4$ varies only slightly with composition. XANES data reveal that Bi^{3+} is not reduced, but that Mo^{6+} is reduced to Mo^{5+} and V^{5+} is reduced to V^{4+} upon reaction with propene. Based on these observations and the measured kinetics for acrolein formation, we have proposed a mechanism for acrolein formation on $Bi_2Mo_3O_{12}$. This reaction sequence (Scheme 2.2) builds on that originally envisioned by Grasselli and coworkers but takes into to account the observed reducibility of Mo^{6+} cations and the irreducibility of Bi^{3+} cations. The rate-limiting step in this scheme involves abstraction of a hydrogen atom from the methyl group of propene to form an allylic species, which then rapidly reacts with a Mo=O group to form a $Mo-OCH_2-CH=CH_2$ group. Acrolein is then formed upon abstraction of a second hydrogen atom from the α carbon atom of this species. The resulting rate expression is fully consistent with the reaction kinetics measure at low and high temperatures.

A model for the dependence of catalyst activity on catalyst composition was developed that correctly describes the experimental results, seen in Figure 2.10. According to this model, vanadium and molybdenum are randomly distributed to form three types of sites (Mo-Mo, Mo-V, and V-V) each associated with its own set of rate parameters. Mo-V sites exhibit the highest activity. Since vanadium affects the ease of H abstraction, V-V and Mo-V sites are characterized by lower apparent activation energies compared to Mo-Mo sites. The proposed model gives a very good description of the effects of catalyst composition on the rate of acrolein formation as a function of catalyst composition, and reactant partial pressures for temperatures above 653 K.

2.6 Supplemental Information

2.6.1 Derivation of Eqn. 2

$$rate = \frac{k_1 k_2 P_{C_3H_6}[S]}{(k_2 + k_{-1})\left[1 + \dfrac{k_1 P_{C_3H_6}}{k_2 + k_{-1}} + \dfrac{k_1 k_2 P_{C_3H_6}}{k_3(k_2 + k_{-1})} + \left(\dfrac{k_1 k_2 P_{C_3H_6}}{k_4(k_2 + k_{-1})} + \dfrac{k_1 k_2 k_{-4} P_{C_3H_6} P_{H_2O}}{k_4 k_5 P_{O_2}(k_2 + k_{-1})}\right) + \dfrac{k_1 k_2 P_{C_3H_6}}{k_5 P_{O_2}^n(k_2 + k_{-1})}\right]}$$

In the derivation, [O*] represents a fully oxidized active site that is shown in Scheme 2.2. [O*•••C_3H_6] is a fully oxidized sites with propene molecule physically adsorbed on the surface. [O*-C_3H_5] represents an adsorbed species after first H abstraction and O insertion, with two electron transferred as a half reduced site. [*-OH] denotes a hydroxyl group on a fully reduced site. [*] represents a fully reduced center with oxygen vacancies.

Assuming step 2 in Scheme 2.2 to be the rate-determining step (RDS), the rate of acrolein formation is:

$$rate = k_2[O^* \cdots C_3H_6]$$

The concentration of the reactive intermediates can be determined using the quasi-equilibrium assumptions for all the steps:

$$\frac{d[O^* \cdots C_3H_6]}{dt} = k_1 P_{C_3H_6}[O^*] - k_2[O^* \cdots C_3H_6] - k_{-1}[O^* \cdots C_3H_6] = 0$$

$$[O^* \cdots C_3H_6] = \frac{k_1 P_{C_3H_6}[O^*]}{k_2 + k_{-1}}$$

$$\frac{d[O^* - C_3H_5]}{dt} = k_2[O^* \cdots C_3H_6] - k_3[O^* - C_3H_5] = 0$$

$$[O^* - C_3H_5] = \frac{k_2}{k_3}[O^* \cdots C_3H_6] = \frac{k_1 k_2 P_{C_3H_6}[O^*]}{k_3(k_2 + k_{-1})}$$

$$\frac{d[* - OH]}{dt} = k_3[O^* - C_3H_5] + k_{-4}[*]P_{H_2O} - k_4[* - OH] = 0$$

$$[* - OH] = \frac{k_1 k_2 P_{C_3H_6}[O^*]}{k_4(k_2 + k_{-1})} + k_{-4}[*]P_{H_2O}$$

$$\frac{d[*]}{dt} = k_4[* - OH] - k_{-4}[*]P_{H_2O} + k_5[*]P_{O_2}^n = 0$$

$$[*] = \frac{k_1 k_2 P_{C_3H_6}[O^*]}{k_5 P_{O_2}^n (k_2 + k_{-1})}$$

Plug back into $[* - OH]$:

$$[* - OH] = \frac{k_1 k_2 P_{C_3H_6}[O^*]}{k_4(k_2 + k_{-1})} + \frac{k_1 k_2 k_{-4} P_{C_3H_6} P_{H_2O}[O^*]}{k_4 k_5 P_{O_2}^n (k_2 + k_{-1})}$$

The concentration of fully oxidized sites $[O^*]$ can be eliminated using a site balance:

$$[S] = [O^*] + [O^* \cdots C_3H_6] + [O^* - C_3H_5] + [* - OH] + [*]$$

$$[O^*] = \cfrac{[S]}{1 + \cfrac{k_1 P_{C_3H_6}}{k_2 + k_{-1}} + \cfrac{k_1 k_2 P_{C_3H_6}}{k_3(k_2 + k_{-1})} + \left(\cfrac{k_1 k_2 P_{C_3H_6}}{k_4(k_2 + k_{-1})} + \cfrac{k_1 k_2 k_{-4} P_{C_3H_6} P_{H_2O}}{k_4 k_5 P_{O_2}(k_2 + k_{-1})} \right) + \cfrac{k_1 k_2 P_{C_3H_6}}{k_5 P_{O_2}^n (k_2 + k_{-1})}}$$

Now the rate of propene consumption per site can be rewritten (Eqn. 2 in the text)

$$rate = k_2[O^* \cdots C_3H_6] = \frac{k_1 k_2 P_{C_3H_6}[O^*]}{k_2 + k_{-1}}$$

$$= \cfrac{k_1 k_2 P_{C_3H_6}[S]}{(k_2 + k_{-1})\left[1 + \cfrac{k_1 P_{C_3H_6}}{k_2 + k_{-1}} + \cfrac{k_1 k_2 P_{C_3H_6}}{k_3(k_2 + k_{-1})} + \left(\cfrac{k_1 k_2 P_{C_3H_6}}{k_4(k_2 + k_{-1})} + \cfrac{k_1 k_2 k_{-4} P_{C_3H_6} P_{H_2O}}{k_4 k_5 P_{O_2}(k_2 + k_{-1})} \right) + \cfrac{k_1 k_2 P_{C_3H_6}}{k_5 P_{O_2}^n (k_2 + k_{-1})} \right]}$$

2.7 References

[1] G.W. Keulks, L.D. Krenzke, T. M. Notermann, Adv. Catal. 27 (1978) 183-225.
[2] G. Ertl, H. Knozinger, F. Schuth, J. Weitkamp (Eds.) Handbook of Heterogeneous Catalysis, Wiley-VCH, Weinheim, 2008, pp. 3481.
[3] G.W. Hearne, M.L. Adams, U.S. Patent 2, 451, 485 1948.
[4] R. Haggblad, J.B. Wagner, B. Deniau, J.M.M. Millet, J. Holmberg, R.K. Grasselli, S. Hansen, A. Andersson, Top. Catal. 50 (2008) 52-65.
[5] M. Carbucicchio, G. Centi, P. Forzatti, F. Trifirò, P.L. Villa, J. Catal. 107 (1987) 307-316.
[6] T. Ono, K.W. Hillig II, R.L. Kuczkowski, J. Catal. 123 (1990) 236-244.
[7] R. Nilsson, T. Lindblad, A. Andersson, Catal. Lett. 29 (1994) 409-420.
[8] R.K. Grasselli, G. Centi, F. Trifirò, Appl. Catal. 57 (1990) 149-166.
[9] J.D. Idol. U.S. Patent 2, 904, 580, 1959.
[10] J.L. Callahan, R.W. Foreman, F. Veatch, U.S. Patent 3, 044, 966, 1962.
[11] H.H. Voge, C.D. Wagner, D.P. Setvenson, J. Catal. 2 (1963) 58-62.
[12] W.M.H. Sachtler. Rec. Trav. Chim. 82 (1963) 243-245.
[13] L.D. Krenzke, G.W. Keulks, J. Catal. 61 (1980) 316-325.
[14] W. Ueda, K. Asakawa, C.L. Chen, Y. Moro-Oka, T. Ikawa, J. Catal. 101 (1986) 360-368.
[15] G.W. Keulks, J. Catal. 19 (1970) 232- 235.
[16] B. Grzybowska, J. Haber, J. Janas, J. Catal. 49 (1977) 150-163.
[17] J. Haber, W. Turek, J. Catal. 190 (2000) 320-326.
[18] P. Mars, D.W. van Krevelen, Chem. Eng. Sci. 3 (1954) 41-59.
[19] Y. Moro-Oka, W. Ueda, Adv. Catal. 40 (1994) 233-273.
[20] J.M.M. Millet, H. Ponceblanc, G. Coudurier, J.M. Herrmann, J.C. Vedrine, J. Catal. 142 (1993) 381-391.
[21] D. Carson, G. Coudurier, M. Forissier, J.C. Vedrine, J. Chem. Soc. Faraday Trans. I. 79 (1983) 1921-1929.
[22] M. Cesari, G. Perego, A. Zazzetta, G. Manara, B. Notari, J. Inorg. Nucl. Chem. 33 (1971) 3595-3597

[23] A.W. Sleight, J. Burton, Advanced materials in catalysis, Academic Press, New York, 1977, pp. 181-208.

[24] A.W. Sleight, K. Aykan, D.B. Rogers, J. Solid State Chem. 13 (1975) 231-236.

[25] A.W Sleight, W.J Linn. Ann. N. Y. Acad. Sci. 272 (1976) 22-44.

[26] H.P. Yang, Y.N. Fan, L.Y. Feng, J.H. Qiu, M. Lin, B.L. Xu, Y. Chen, Acta Chimica Sinica. 60 (2002) 1006-1010.

[27] J.A. Schwarz, C. Contescu, A. Contescu, Chem. Rev, 95 (1995) 477-510.

[28] M.T. Le, W.J.M. Van Well, I. Van Driessche, S. Hoste, Appl. Catal. A: Gen. 267 (2004) 227-243.

[29] S.D. Kelly, D. Hesterberg, B. Ravel, in: A.L. Ulery, L.R. Drees, (Eds.), Methods of Soil Analysis. Soil Science Society of America, Madison, WI, 2008.

[30] R.E. Jentoft, S.E. Deutsch, B.C. Gates, Rev. Sci. Instrum. 67 (1996) 2111-2112.

[31] B. Ravel, M. Newville, J. Synchrotron Radiat. 12 (2005) 537-541.

[32] M. Newville, J. Synchrotron Radiat. 8 (2001) 96-100.

[33] M. Hartmanova, M.T. Le, M. Jergel, V. Smatko, F. Kundracik, Russ. J. Electrochem. 45 (2009) 621-629.

[34] C.C. McCain, G. Gough, G.W. Godin, Nature. 198 (1963) 989-990.

[35] J.D. Burrington, C.T. Kartisek, R.K. Grasselli, J. Catal. 63 (1980) 235-254.

[36] J.R. Monnier, G.W. Keulks, J. Catal. 68 (1981) 51-66.

[37] R.K. Grasselli, Top. Catal. 21 (2001) 79-88.

[38] R.K. Grasselli, J. Chem. Educ. 63 (1986) 216-221.

[39] L.C. Glaeser, J.F. Brazdil, M.A. Hazle, M. Mehicic, R.K. Grasselli, J. Chem. Soc., Faraday Trans. I 81 (1985) 2903-2912.

[40] T.A. Hanna, Coord. Chem. Rev. 248 (2004) 429-440.

[41] C.R. Adams, T.J. Jennings, J. Catal. 3 (1964) 549-558.

[42] R.H. Summerville, R. Hoffmann, J. Am. Chem. Soc. 98 (1976) 7240-7254.

[43] L.A. Bengtsson, R. Hoffmann, J. Am. Chem. Soc. 115 (1993) 2666-2676.

[44] S.V. Yanina, R.L. Smith, J. Catal. 13 (2003) 151-162.

[45] J.F. Brazdil, D.D. Suresh, R.K. Grasselli, J. Catal. 66 (1980) 347-367.

[46] D. Krenzke, G.W. Keulks, J. Catal. 64 (1980) 295-301.

[47] D. Krenzke, G.W. Keulks, J. Catal. 61 (1980) 316-325.

[48] H.W Wong, M.C. Cesa, J.T. Golab, J.F Brazdil, W.H. Green, Appl. Catal. A-Gen. 303 (2006) 177-191.

Figure 2.1 XRD patterns of $Bi_{1-x/3}V_{1-x}Mo_xO_4$ catalysts.
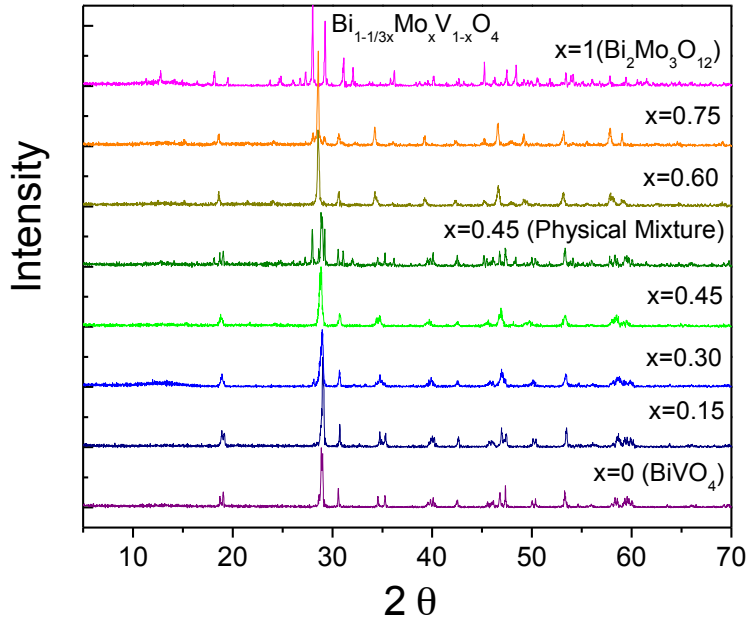
Figure 2.2 Normalized Bi L_3-edge and Mo K-edge XANES scans of $Bi_2Mo_3O_{12}$. Samples were treated in air to 713 K for oxidized sample and in pure propylene (1 atm) for 24 hours for reduced samples.
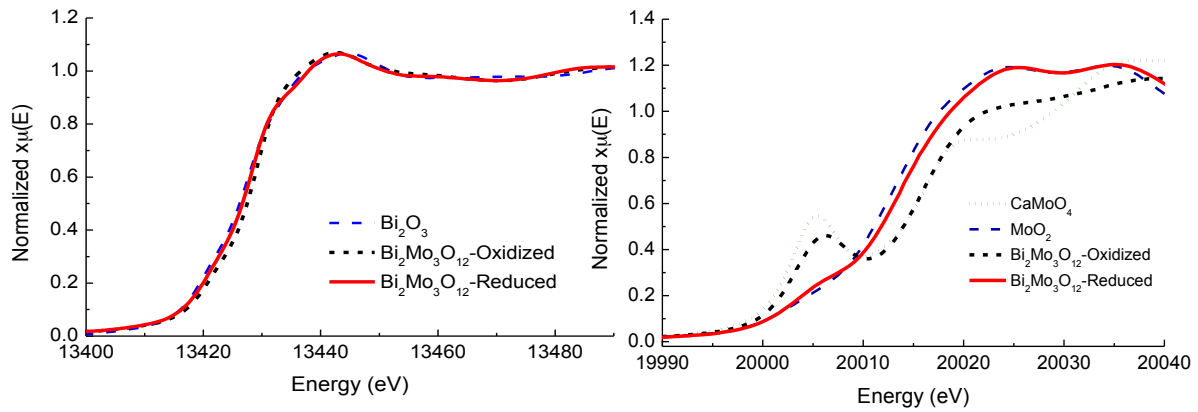
Figure 2.3 Normalized Bi L_3-edge, Mo K-edge and V K-edge XANES spectra of $Bi_{0.85}Mo_{0.45}V_{0.55}O_4$. Samples were treated in air to 713 K for oxidized sample and in pure propylene (1 atm) for 24 hours for reduced samples.
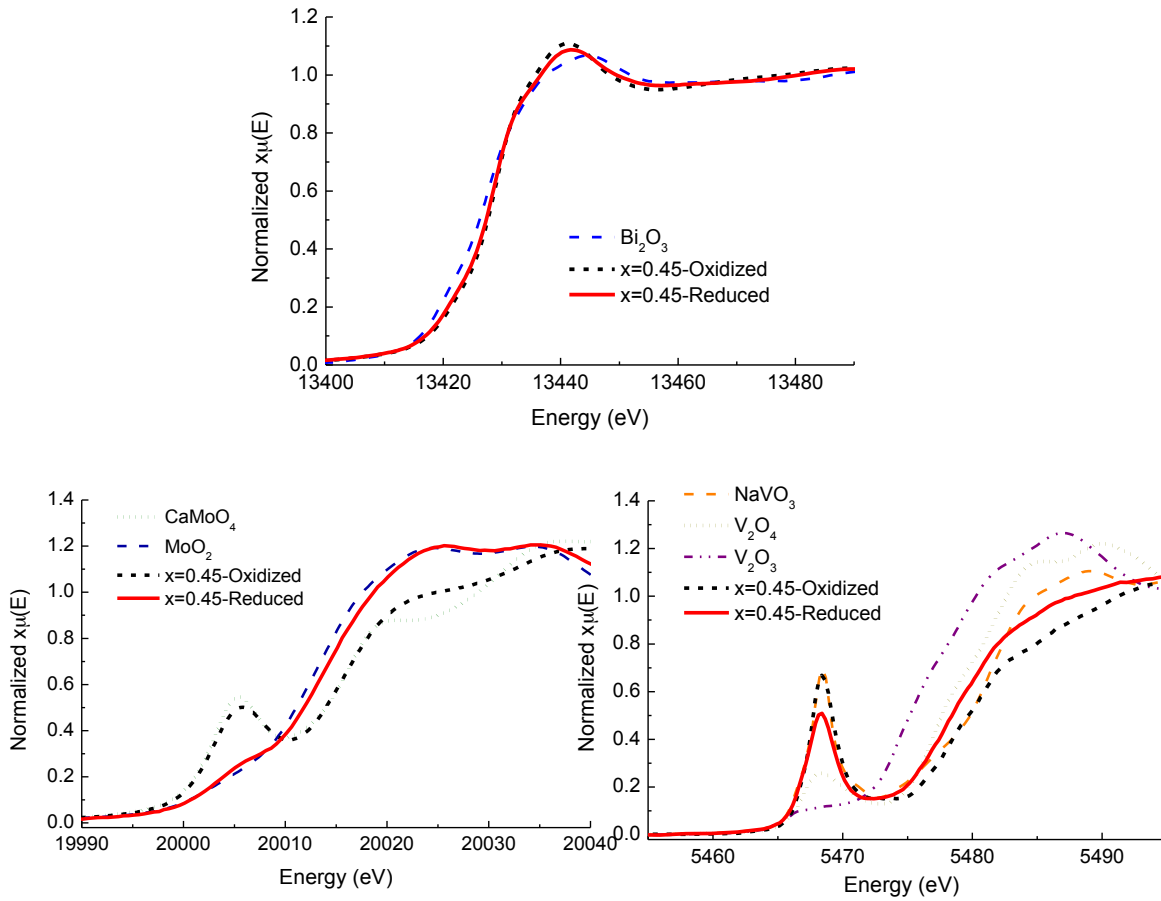
Figure 2.4 Normalized Bi L_3-edge and V K-edge XANES scans of BiVO$_4$. Samples were treated in air to 713 K for oxidized sample and in pure propylene (1 atm) for 24 hours for reduced samples.
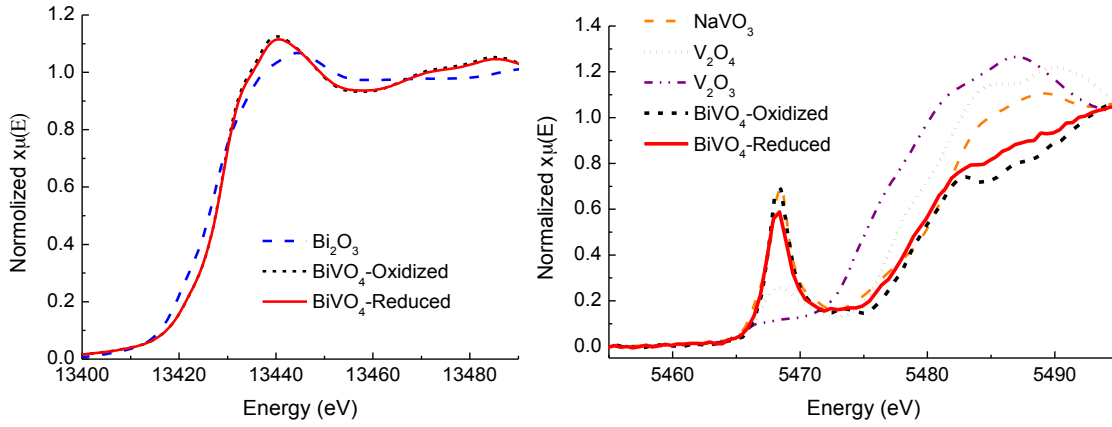
Figure 2.5 Variation in the rate of propene oxidation to acrolein Bi$_{1-x/3}$V$_{1-x}$Mo$_x$O$_4$ with x at 673 K and $P_{C3H6} = P_{O2} = 0.167$ atm.
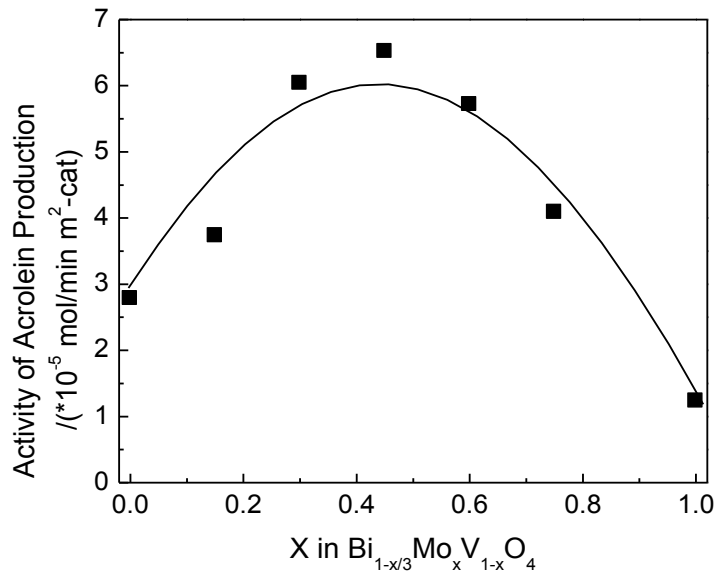
Figure 2.6 Variation in the selectivity of $Bi_{1-x/3}V_{1-x}Mo_xO_4$ for propene oxidation to acrolein at 673 K and $P_{C3H6} = P_{O2} = 0.167$ atm measured as a function of propene conversion.
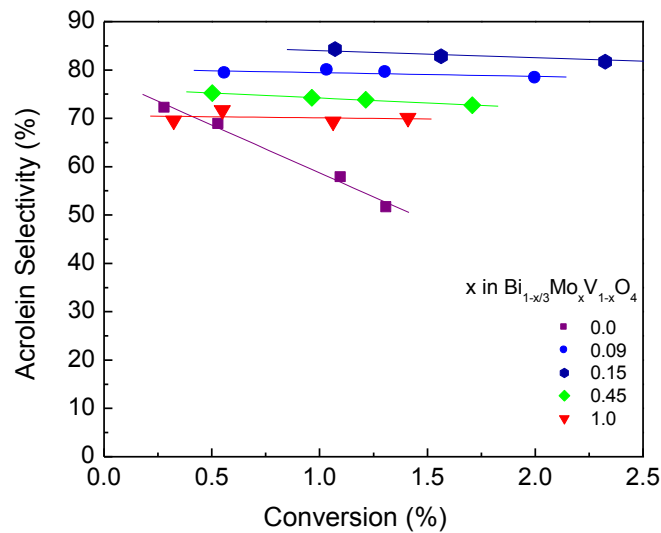
Figure 2.7 Dependence of the intrinsic selectivity of $Bi_{1-x/3}V_{1-x}Mo_xO_4$ for the oxidation of propene at 673 K and $P_{C3H6} = P_{O2} = 0.167$ atm.
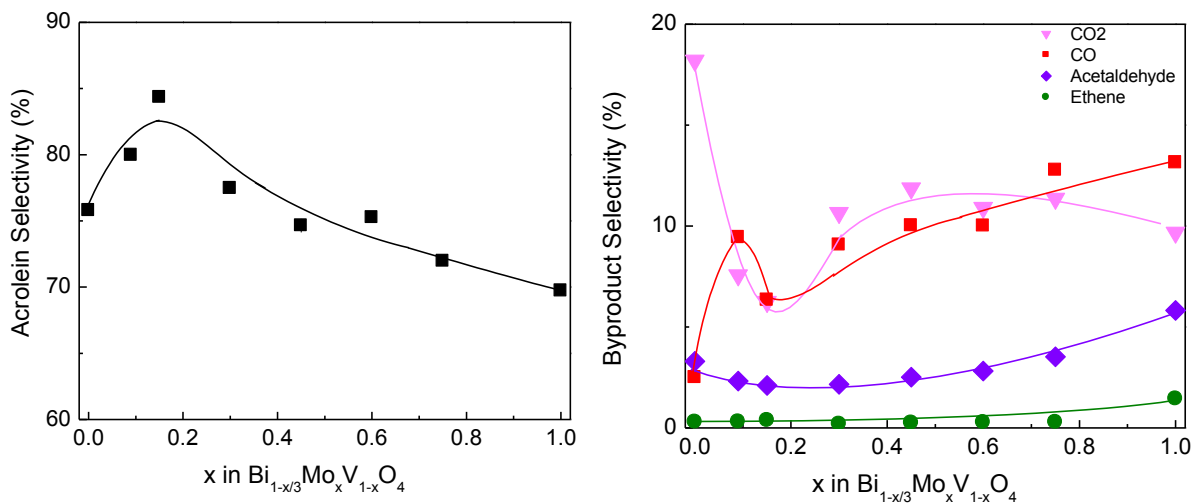
Figure 2.8 Arrhenius plot for propene oxidation to acrolein over $Bi_{1-x/3}V_{1-x}Mo_xO_4$ catalysts at 573 K - 713 K and $P_{C3H6} = P_{O2} = 0.167$ atm.
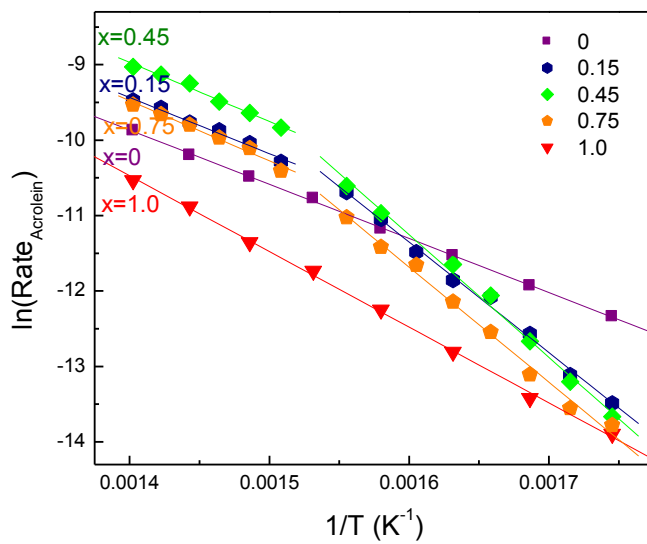
Figure 2.9 Effect of propene and oxygen partial pressure on the selectivities to acrolein, CO, and CO_2 formed during propene oxidation on $Bi_2Mo_3O_{12}$, $BiVO_4$, and $Bi_{0.95}V_{0.85}Mo_{0.15}O_4$ at 673 K. The partial pressures of propene and oxygen were fixed at 0.067 and 0.167 atm while the partial pressure of the other reactant was varied.
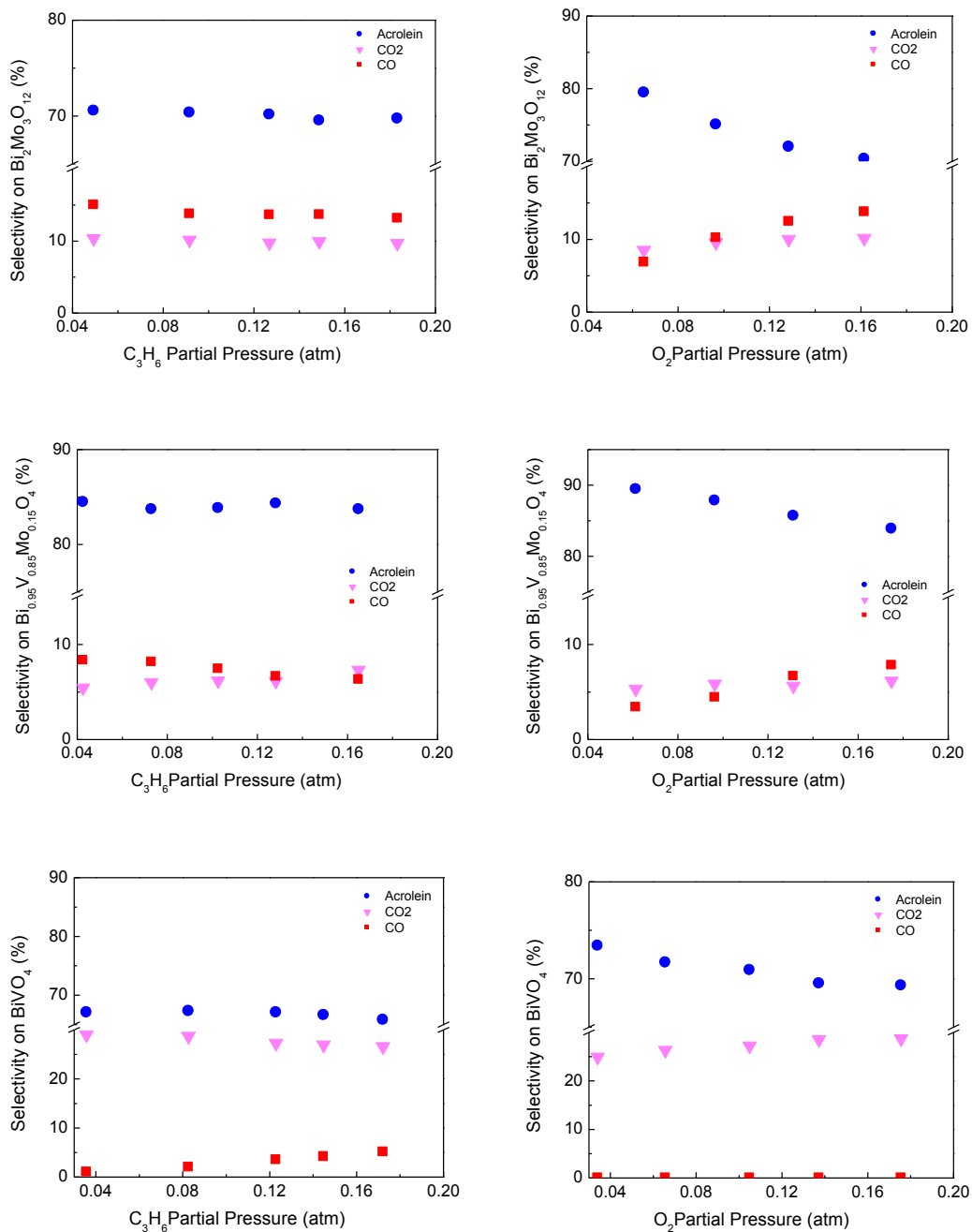
Figure 2.10 Comparison of the apparent rate coefficient k_{app} for propene oxidation to acrolein determined from Eqn. 7 and from experiments carried out at 673 K.
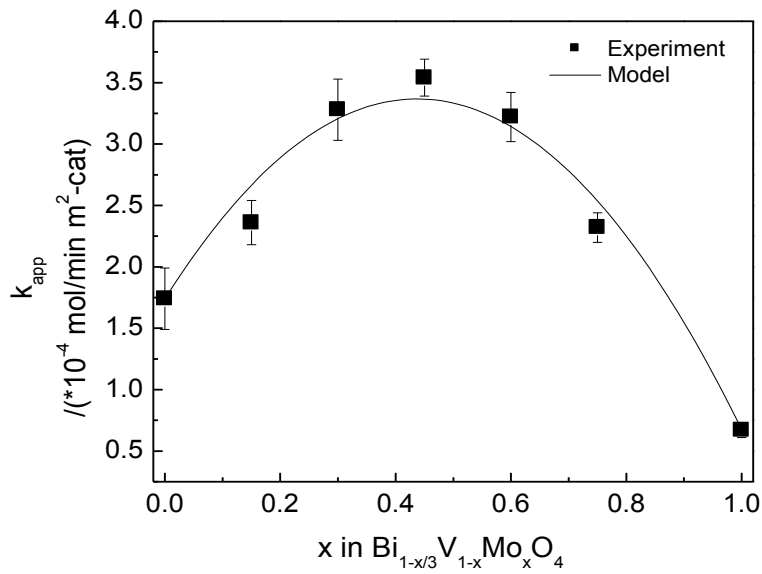
Figure 2.11 Comparison of the apparent rate coefficient k_{app} for propene oxidation to acrolein determined from Eqn. 10 and from experiments carried out at temperatures between 663 K and 713 K.
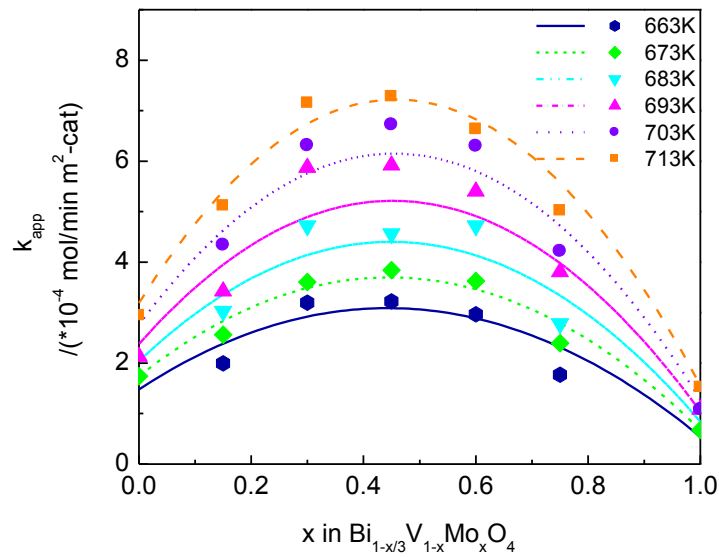
Figure 2.12 Parity plot of rates of acrolein formation deduced from Eqns. 3 and 10 and from experiments conducted at temperatures of 653 K to 713 K, partial pressures of propene between 0.067 and 0.167 atm, and partial pressures of oxygen between 0.067 and 0.167 atm over $Bi_{1-x/3}V_{1-x}Mo_xO_4$ (x = 0 to 1).
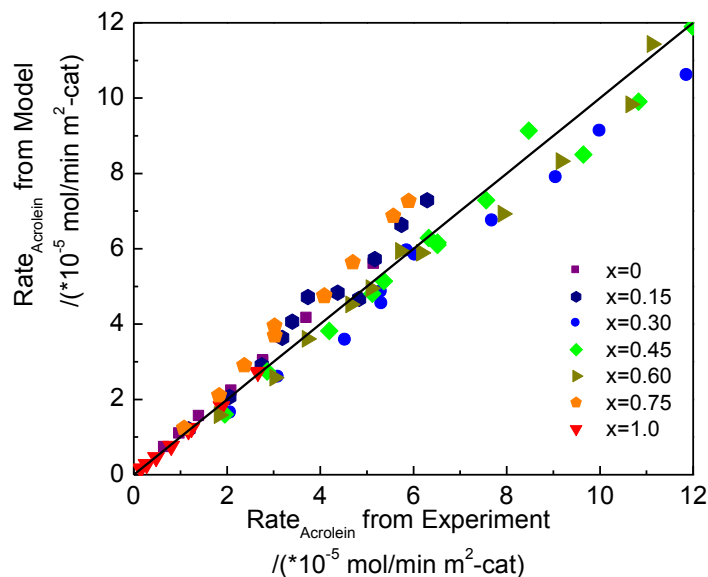
Figure 2.13 Comparison of the apparent activation energy for propene oxidation to acrolein from Eqn. 10 and those determined from and experiments conducted at temperatures of 653 K to 713 K and $P_{C3H6} = P_{O2} = 0.167$ atm on $Bi_{1-x/3}V_{1-x}Mo_xO_4$ (x = 0 to 1).
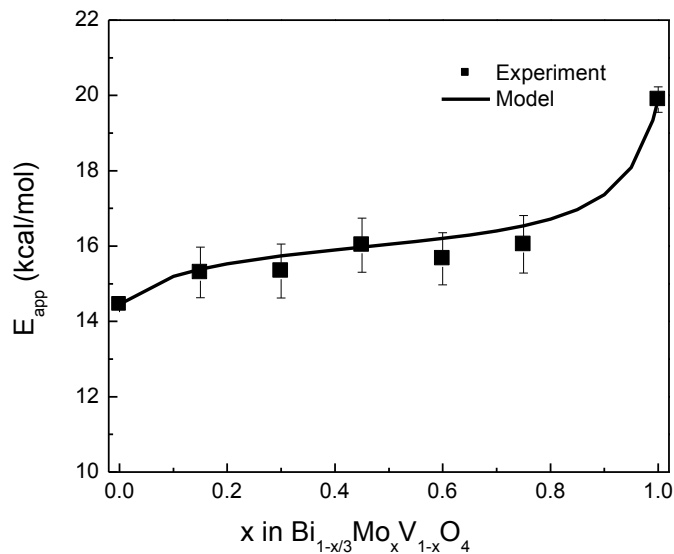
Scheme 2.1 Reaction sequence for the oxidation of propene to acrolein on $Bi_2Mo_3O_{12}$ proposed by Grasselli and coworkers [37-39].
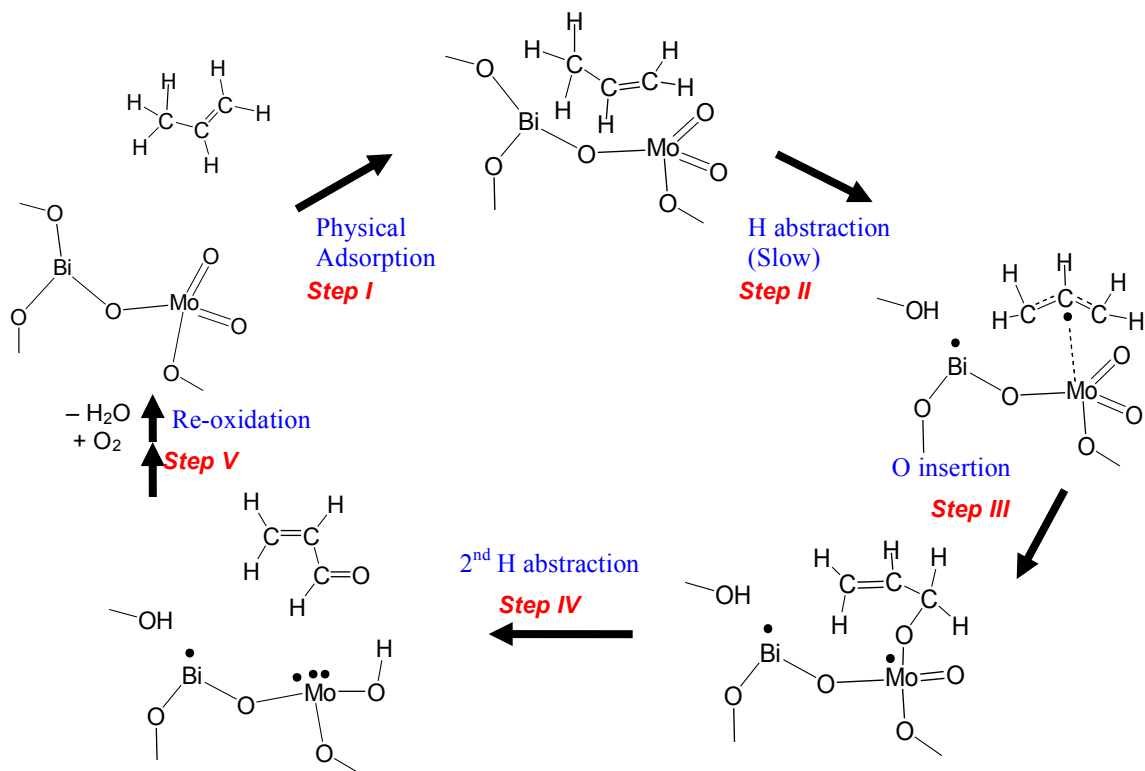
Scheme 2.2 The mechanism for the oxidation of propene to acrolein over $Bi_2Mo_3O_{12}$ proposed on the basis of data reported in this study.

Scheme 2.3 Three different types of active sites produced when vanadium is added to bismuth molybdate.
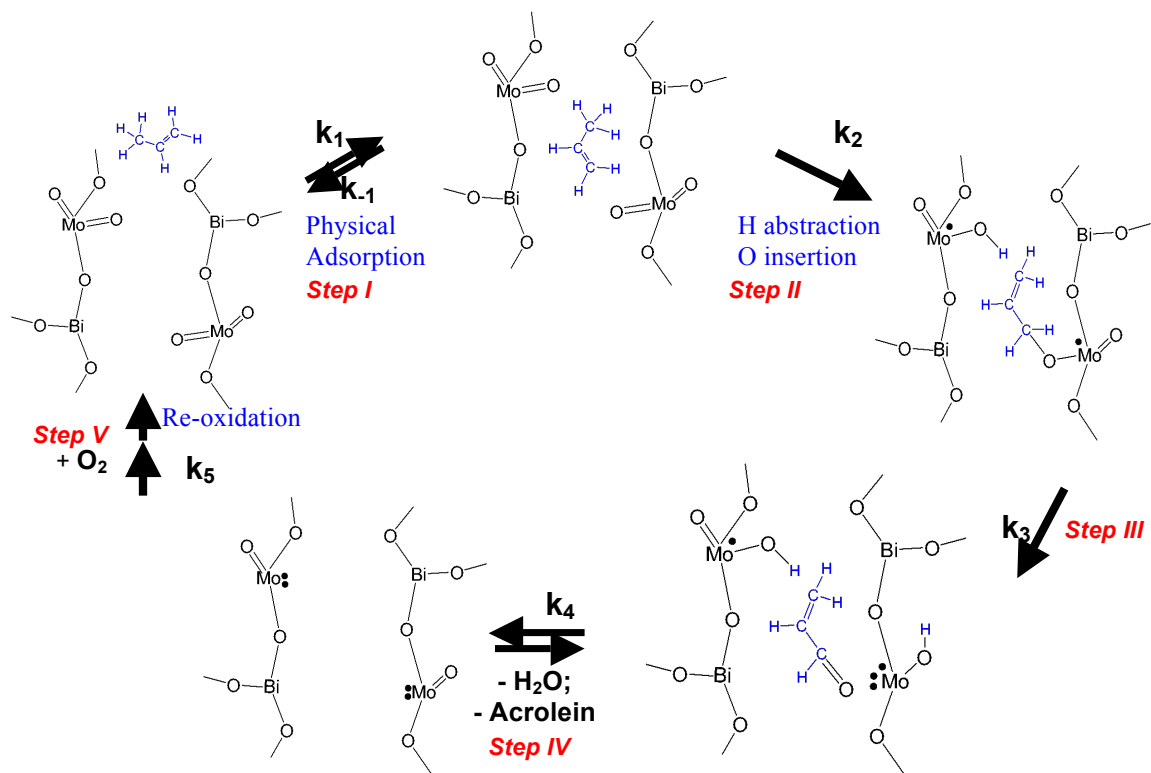
Scheme 2.4 Possible pathway for byproduct formation on $Bi_2Mo_3O_{12}$ during the oxidation of propene.
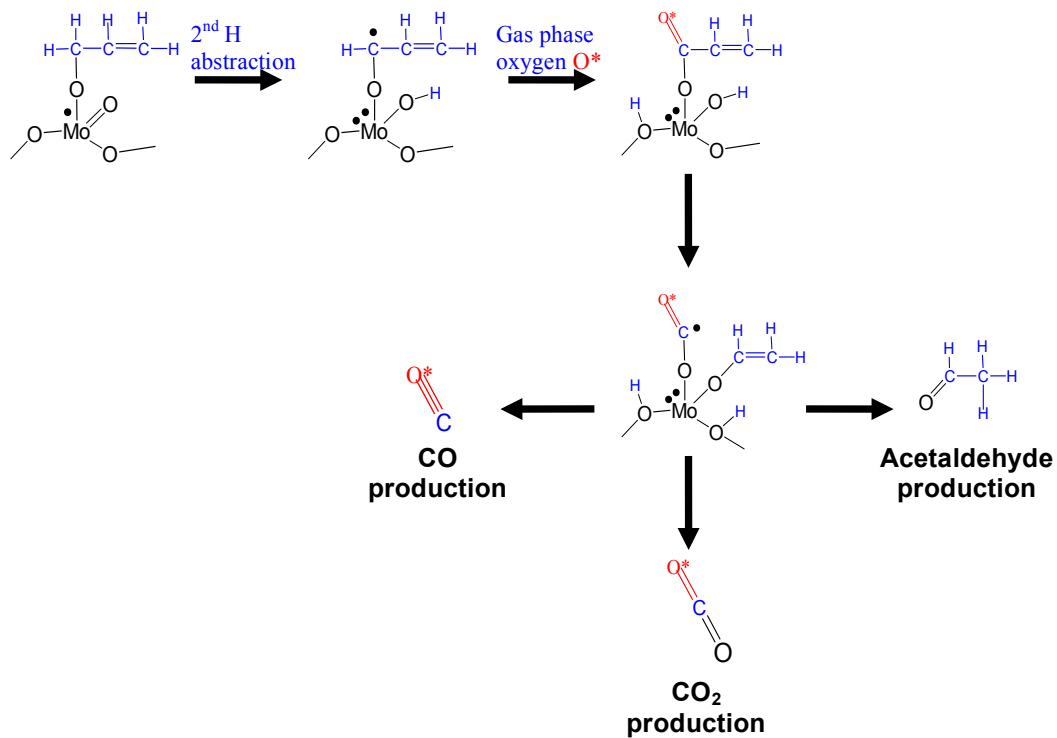
Table 2.1 Apparent activation energies for propene oxidation to acrolein in the temperarure ranges of 653 - 713 K and 573 - 653 K on $Bi_{1-x/3}V_{1-x}Mo_xO_4$. $P_{C3H6} = P_{O2} = 0.167$ atm.

Composition	E_{app} (kcal/mol)	
	653K-713K	573K-653K
0	14.5	
0.15	15.3	29.2
0.30	15.3	30.8
0.45	16.0	31.3
0.60	15.8	30.8
0.75	16.0	29.9
1	19.9	

Table 2.2 Reaction orders in propene and oxygen measure at 673 K and 613 K for propene oxidation to acrolein on $Bi_{1-x/3}V_{1-x}Mo_xO_4$. The partial pressures of propene or oxygen were fixed at 0.067 or 0.167 atm, respectively, while the other one was varied.

Composition(x)	673 K		613 K	
	Propene	Oxygen	Propene	Oxygen
0	1.1±0.2	0.0±0.0	1.0±0.0	0.1±0.1
0.15	1.0±0.1	0.1±0.1	0.1±0.0	0.8±0.1
0.30	0.9±0.1	0.0±0.0	0.0±0.0	0.6±0.0
0.45	0.9±0.1	0.1±0.0	0.0±0.0	0.5±0.0
0.60	0.9±0.1	0.0±0.0	0.0±0.1	0.5±0.1
0.75	1.0±0.1	0.1±0.0	0.0±0.1	0.6±0.0
1	1.0±0.0	0.0±0.0	1.0±0.1	0.0±0.1

Table 2.3 Reaction orders in propene and oxygen measured at 673 K for propene oxidation to CO and CO_2 on $Bi_{1-x/3}V_{1-x}Mo_xO_4$. The partial pressures of propene or oxygen were fixed at 0.067 or 0.167 atm, respectively, while the other one was varied.

Composition	CO_2		CO	
	Propene	Oxygen	Propene	Oxygen
$BiVO_4$ (x = 0)	1.1±0.1	0.1±0.0	1.5±0.37	1.0±0.0
$Bi_{0.95}V_{0.85}Mo_{0.15}O_4$ (x = 0.15)	1.0±0.1	0.3±0.1	0.8±0.1	1.0±0.1
$Bi_2Mo_3O_{12}$ (x = 1)	1.0±0.0	0.4±0.0	0.9±0.0	1.0±0.1

Table 2.4 Apparent reaction rate coefficients for propene oxidation to acrolein on Mo-Mo, Mo-V, and V-V sites at 673 K.

k	Value ($*10^{-4}$ mol/min m^2-cat)
k_{Mo}	0.68
k_{mix}	6.13
k_V	1.74

Table 2.5 Pre-exponential factors and apparent activation energies for propene oxidation to acrolein on Mo-Mo, Mo-V, and V-V sites at 653K - 713K.

Types of sites	Value	
	A($*10^{-4}$ mol/min m^2-cat atm)	E (kcal/mol)
Mo-Mo (Mo)	195	19.9
Mo-V (mix)	97	16.0
V-V (V)	9	14.5

Chapter 3

Band-Gap Energy as a Descriptor of Catalytic Activity for Propene Oxidation over Mixed Metal Oxide Catalysts

Abstract

The development of a descriptor or descriptors that can relate the activity of catalysts to their physical properties is a major objective of catalysis research. In this study we have found that the apparent activation energy for propene oxidation to acrolein over scheelite-structured, multicomponent mixed metal oxides ($Bi_3FeMo_2O_{12}$, $Bi_2Mo_{2.5}W_{0.5}O_{12}$, and $Bi_{1-x/3}V_{1-x}Mo_xO_4$, where $0 \leq x \leq 1$) correlates with to the band-gap of the catalyst measured at reaction temperature. We show through theoretical analysis of the energy components comprising the activation energy why the band-gap energy is the primary component dependent on catalyst composition and, hence, why one should expect the activation energy for propene oxidation to correlate with the band-gap energy. We also demonstrate that the change in band-gap energy with composition arises from the interplay between the sizes and energies of the V 3d, Fe 3d, Mo 4d, and W 5d orbitals that give rise to the lowest unoccupied crystal orbitals. Both the utility of the band gap energy as a descriptor for catalytic activity and the role of orbital overlap in determining the band gap are likely to be general features in mixed metal oxide oxidation catalysts, enabling the rational design of catalysts with greater activity for oxidation reactions.

3.1 Introduction

There has been a long-standing interest in the field of catalysis to identify descriptors that relate observed catalytic activity and selectivity to physico-chemical properties of the catalyst. Having such descriptors should enable the rational design of catalysts with superior catalytic performance by specifying the material properties responsible for such performance, and thereby guiding the development of materials with the requisite properties. Insights from theory have proven particularly fruitful in developing such descriptors. For example, Hammer and Nørskov and co-workers have developed the "d-band model" to describe the adsorption of reactants and intermediates on metal surfaces [1]. This model relates the strength of adsorption of a molecule on a metal surface to the energy of the center of the d band of electronic states in the metal. This model has been refined and extended by a number of researchers [2-6], and has proven useful for predicting the catalytic activity of alloys [7] and metal-overlayers [4,8] for a number of reactions, such as CO oxidation, Fischer-Tropsch synthesis, and the electrochemical evolution of oxygen from water [9].

The success of the d-band model for metals motivates the development of a comparable set of descriptors for the catalytic properties of metal oxides. Metal oxides comprise a large family of catalysts that are used for selective oxidation of alkanes [10-13], olefins [14], alcohols [15,16], and aromatics [17], selective reduction of nitrogen

oxides [18-20], and oxidation of hydrogen sulfide [21]. Moreover, the most active and selective metal oxides involve successful mixtures of multiple metal oxides (e.g., BiMoO [22], USbO [23], VMoNbTeO [24], VMoO [25], FeSbO [26], and FeMoO [27]), the performance of which is typically quite different from that of the component oxides. In mixed oxide systems, both the stoichiometry and the surface structure of the working catalyst may determine the catalytic activity [28,29]. A great deal is known about the chemical reactivity of individual oxide systems [30,31], and rationales have been proposed for changes in reactivity with composition in the case of a few mixed metal oxide systems [32-34]. In particular, the effect of doping on the catalytic performance of metal oxides has been reviewed in detail by McFarland and Metiu [35]. However, development of a general model by which the effects of composition on catalyst performance in mixed metal oxide systems can be rationalized remains an open challenge.

The desire to establish such a model has led to several alternative approaches. For example, Rossmeisl and coworkers [36] have found that the strength of adsorption of oxygen-containing species O, OH, and OOH on transition metal oxides is related to the number of outer sphere electrons on the transition metal center. The authors examined substitution of transition metal oxides into cubic MO and perovskite AMO_3 structures, where $A = Sr^{2+}$, Ba^{2+}, La^{3+}, or Y^{3+}, and M is any first row transition metal Sc – Cu. Using density functional theory, linear correlations were found between the strength of adsorption of O, OH, and OOH species and the number of electrons occupying d orbitals on the transition metal to which these species were bound. Such correlations suggest that the d orbital occupancy reflects the number of electrons available to participate in bonding between the metal center and the adsorbate. This model represents a significant step towards understanding the reactivity of oxygen species on transition metal oxide surfaces.

A further significant step toward relating the reactivity of mixed metal oxides to fundamental physico-chemical properties has been taken by Morgan and collaborators [37]. In a study also focusing on multicomponent perovskite-structured oxides, they demonstrate that oxygen vacancy formation energy closely correlates to catalytic activity toward solid oxide fuel cell autothermal reforming reactions. The relevance to catalysis of oxygen vacancy formation energy arises from the importance of oxygen diffusion through the perovskite lattice during autothermal reforming. The authors further show that the oxygen vacancy formation energy can be directly related to the oxygen p-band center energy for a wide range of solid oxide compositions, thus enabling catalytic activity to be predicted from a first-principles descriptor. However, the authors also show that this descriptor fails for the composition family $(La,Sr)MnO_3$, for which bulk oxygen diffusion is known not to be rate determining. Thus, there remains a need for a model applicable to oxidation reactions over mixed metal oxides in which bulk oxygen diffusion does not determine catalytic rates.

In attempting to develop new models in one field, it is often useful to consider models that have already proven successful in other fields. A notable example of such an attempt directed at providing a set of descriptors for metal oxide catalysts has been reported by Bordes-Richard and Courtine [38-40]. These researchers used the concept of "optical basicity," first developed by Duffy [41] in the 1970s for rationalizing the glass-

forming properties of main group oxides, and adapted it to catalysis. They showed that for a variety of catalysts, the optical basicity of the catalyst correlates with the product selectivity for the oxidation reactions of alkanes, alkenes, and alcohols. However, there are problems in the general application of this method to metal oxide catalysts. Optical basicity, Λ, is derived by experimentally measuring the energy of the 6s $\rightarrow$ 6p excitation on Pb^{2+} or Bi^{3+} ions doped in low concentration into the oxide of interest. Unfortunately, this measurement cannot be conducted in transition metal oxides, as light absorption from the transition metal overwhelms the signal from the probe cation, necessitating the use of scaling relationships to determine optical basicity values. Unfortunately, major contradictions arise in such scaling relationships for catalytically important ions such as V^{5+}: the optical basicity assigned using band gap correlations [42] is $\Lambda = 1.04$ (more basic than Ca^{2+}); using the iono-covalent parameter [43] yields $\Lambda = 0.63$-0.69 (acid-base properties similar to Al^{3+}); and using Brønsted acidity [44] gives $\Lambda = 0.49$ (as acidic as P^{5+}). The value of optical basicity is also likely limited to systems in which acid-base properties are important for catalysis. Therefore, the concept of optical basicity is not applicable to systems such as bismuth molybdates, which are known to oxidize olefins via a radical mechanism.

For catalysis over transition metal sulfides, the metal-sulfur (M-S) bond strength has been proposed as a descriptor for catalytic activity [45]. In a series of studies [46-49], Toulhoat, Raybaud, and collaborators demonstrate the utility of this descriptor in accounting for both adsorption and activation enthalpies in catalytic hydrogenation, hydrogenolysis, and hydrodesulfurization reactions. However, analysis by Wachs and co-workers has determined that an analogous relationship between metal-oxygen bond strength and the activities of transition metal oxides toward oxidation reactions does not exist [50]. That such a descriptor succeeds for sulfides but fails for oxides may be a consequence of structural differences between oxide and sulfide phases: the surfaces of transition metal oxides often contain metal-oxygen bonds with significant double bond character, with the degree of double bond character differing for different surface terminations and between surface and bulk. By contrast, transition metal sulfide surfaces typically contain metal-sulfur single bonds, the character of which differs much less between surface and bulk. The bulk M-S bond strength is therefore more relevant to the description of bond-breaking and bond-forming processes occurring during catalysis on transition metal sulfide surfaces than the bulk M-O bond strength is to such processes occurring on the surfaces of transition metal oxides.

Idress and Seebauer [51] have proposed that the catalytic reactivity of oxides is related to the polarisability of oxygen. They have shown that the rates of ethanol dehydrogenation to acetaldehyde and isopropanol oxidation to acetone over a series of binary oxides correlate very closely with the polarisability of the oxygen atoms in each oxide lattice. A similar trend was found for the rate of the Tishchenko reaction over alkali earth oxides. Since lattice oxygen is involved in the rate determining steps of these reactions, it is reasonable to connect catalyst reactivity to a physical characteristic of the reacting oxygen atoms. However, this approach has not been extended to mixed metal oxide systems, so it is not possible to comment on the utility of oxygen polarisability as a predictive descriptor for rational catalyst design.

Another model that has shown substantial explanatory power is the band-edge model widely used in semiconductor physics and photocatalysis. In the design of semiconductor systems such as light-harvesting diodes, the band-edge model provides key information about the electronic properties produced by the interface between materials of differing composition [52]. In photocatalysis, the same model provides information about the electronic properties (and therefore catalytic properties) of the interface between a semiconducting catalyst and an aqueous reactant [53]. Whether a material is a potentially suitable catalyst for photo(electro)chemical production of hydrogen, for example, can be determined directly from an inspection of conduction band edge energy of the material [54,55].

In attempting to identify descriptors of catalytic activity for mixed metal oxide oxidation catalysts, it is helpful to recognize that the chemical properties of both the metal and oxygen centers will contribute to catalytic performance of the oxide. In particular, oxidation of hydrocarbons is often understood to proceed via the interaction of surface oxygen atoms with carbon or hydrogen atoms of adsorbed reactants, in conjunction with electron transfer from the adsorbate to reducible transition metal centers in the catalyst. A simple descriptor that captures both the nature of the reactive oxygen centers and the tendency of adjacent transition metal centers to gain electron density is the ligand-to-metal charge transfer (LMCT) excitation energy. For metal oxides containing transition metal centers in their highest oxidation states, the LMCT excitation energy typically corresponds to the band gap energy. In chemical terms, the band-gap energy can be thought of as the energy difference between the highest occupied crystal orbital (which is typically oxygen-centered) and the lowest unoccupied crystal orbital (which is transition metal centered). The band-gap energy therefore contains information about the frontier molecular orbitals in a crystalline material. The relative energies of frontier molecular orbitals have long been used to rationalize reactivity in molecular systems [56,57]. The character of the frontier crystal orbitals is also an important descriptor for the catalytic activity of transition metal sulfides toward hydrodesulfurization reactions [58]. It is therefore of interest to determine whether the energy difference between frontier crystal orbitals in a mixed metal oxide can be used as a descriptor of catalytic activity.

The objective of the present work is to determine the extent to which it is possible to explain trends in activation energy with composition for a family of oxidation catalysts in terms of the LMCT excitation energy or band gap. To decouple differences in observed band gap due to composition from differences due to changes in crystal structure, only catalysts with the scheelite crystal structure were considered. In particular, attention was focused on $Bi_3FeMo_2O_{12}$, $Bi_2Mo_{2.5}W_{0.5}O_{12}$, and solid solutions of composition $Bi_{1-x/3}V_{1-x}Mo_xO_4$, where $0 \leq x \leq 1$. The reaction chosen for investigation was the oxidation of propene to acrolein because the mechanism and kinetics of this reaction has been investigated extensively over $Bi_2Mo_3O_{12}$ and related oxides [59-65]. The principal findings are that the rate of the reaction is first order in propene and zero order in oxygen. Consistent with these kinetics, H/D isotopic labeling indicates that the rate-limiting step is the cleavage of one a C-H bond in the methyl group of propene [59,60]. [13]C labeling studies have shown that this step produces a symmetric allyl radical [61]. The initial C-H bond cleavage and the subsequent insertion of oxygen to produce acrolein involve oxygen in the catalyst lattice, indicating that propene oxidation proceeds via a

Mars-van Krevelen mechanism [62,66]. Kinetics identical to those for $Bi_2Mo_3O_{12}$ have been reported for other scheelites with the composition $Bi_{1-x/3}V_{1-x}Mo_xO_4$ [67]. That work has also demonstrated that in contrast to earlier proposals, only Mo and V cations undergo reduction and oxidation, but not Bi. The mechanism of propene oxidation proposed for $Bi_2Mo_3O_{12}$ has also been the subject of several theoretical studies [68-74]. Detailed density functional theory calculations performed within our group have revealed that the lone pair of Bi interacts with an equatorial Mo=O bond, thereby making the O atom in this bond significantly more active than Mo-O-Bi or axial Mo=O bonds [73,74]. A similar conclusion regarding the active site for propene oxidation on $Bi_2Mo_3O_{12}$ had previously been reached by the Goddard group in a modeling study employing the ReaxFF reactive force field [72].

As stated above, the objective of the present work is to develop a first-principles descriptor explaining the composition dependence of activation energy for propene oxidation over mixed metal oxides. In order to develop a complete understanding of the factors determining observed reaction rates, descriptors accounting for contributions to the pre-exponential factor must also be developed. Such contributions include the entropy of adsorption of propene on the catalyst surface, the intrinsic activation entropy for C-H bond activation at the active site(s), and the number and distribution of active sites. Evaluation of these contributions is, however, beyond the scope of the present work.

3.2 Methods

3.2.1 Experimental Methods

Catalysts with the generic composition $Bi_{1-x/3}V_{1-x}Mo_xO_4$ were prepared by the complexation procedure using citric acid [67]. Citric acid was added to aqueous solutions of the metal precursors bismuth(III) nitrate pentahydrate, ammonium molybdate tetrahydrate, and ammonium metavanadate. Solutions were then mixed in the atomic ratios of Bi:V:Mo = (1-x/3):(1-x):x, (x = 0 to 1.0). To prepare $Bi_2Mo_{2.5}W_{0.5}O_{12}$, ammonium molybdate tetrahydrate, bismuth(III) nitrate pentahydrate, and ammonium tungstate, with citric acid, were mixed at the atomic ratios of Bi:Mo:W = 2:2.5:0.5. $Bi_3FeMo_2O_{12}$ was prepared by mixing ammonium molybdate tetrahydrate, bismuth(III) nitrate pentahydrate, and iron(III) nitrate, with citric acid in the atomic ratios of Bi:Mo:Fe = 3:2:1. Each of the resulting solution was dried at 60 °C for about 24 h in air to form a gel. The gel was then dried further at 120 °C and calcined in flowing air at 600°C for 6 h. The phase purity of the catalysts formed was confirmed by x-ray diffraction (see Supporting Information).

Diffuse reflectance UV-VIS-NIR spectra were acquired using a Fischer Scientific EVO 300 spectrometer equipped with a Praying Mantis reflectance chamber and an *in situ* high pressure cell (Harrick Scientific, Inc), fitted with quartz windows. Spectra were referenced to the diffuse reflectance spectrum of a Teflon reference tile. The procedure used to extract band gap energies from absorption edge data is discussed in the Supporting Information.

XANES scans were taken at the Mo and V K edges and Bi L_3 edge at beamline 10-BM at the Advanced Photon Source at Argonne National Laboratory. Experimental details are provided in the Supporting Information.

3.2.2 Theoretical Methods

Bulk and slab density functional theory calculations were carried out using VASP [75] 5.3.3. Projector augmented wave cores [76,77] containing kinetic energy density information were used to represent core electrons, while plane wave basis sets [78] with cutoff energies of 450 eV were used to represent valence electrons. Electron exchange and correlation was modeled using the M06-L density functional [79,80]. Successful use of this functional within VASP requires non-default values of several input parameters; these are provided in the Supporting Information.

Crystal structures taken from the literature [81-83] were used for $BiVO_4$ (minimal unit cell $Bi_4V_4O_{16}$), $Bi_2Mo_3O_{12}$ (minimal unit cell $Bi_8Mo_{12}O_{48}$), and $Bi_3FeMo_2O_{12}$ (minimal unit cell $Bi_{12}Fe_4Mo_8O_{48}$), and lattice constants and atomic positions allowed to relax to minimize the total energy within the M06-L functional. Relaxed lattice constants differed from experimental values by < 0.5% in all cases. To model the $Bi_{1-x/3}V_{1-x}Mo_xO_4$ phase [34] with an intermediate value of x, the smallest possible mixed vanadate-molybdate structure was constructed. This minimal model, of formula $Bi_7V_5Mo_3O_{12}$, was built from a $Bi_8V_8O_{32}$ supercell by substitution of three V sites by Mo, and removal of one Bi to form a charge-compensating cation vacancy. $Bi_2Mo_{2.5}W_{0.5}O_{12}$ was modeled by replacing two molybdenum atoms in a $Bi_8Mo_{12}O_{48}$ unit cell with W atoms to yield a model of stoichiometry $Bi_8W_2Mo_{10}O_{48}$. Details of the construction of these models can be found in the Supporting Information. While these minimal models cannot fully account for the experimentally observed random substitution of V or W for Mo, they nevertheless provide useful insights into the electronic consequences of substitution at transition metal centers.

Band structures (crystal orbitals) were obtained by calculating the site projected density of states. By default, the zero of energy in a VASP-generated density of states calculation is the energy of the highest occupied state. In this work, it was desirable to instead choose the reference zero energy to be the energy of the vacuum state (i.e. the energy of electrons and nuclei separated at infinity). With this choice of reference state, Koopmans' theorem [84] states that the energy of the highest occupied state is an approximation of the first ionization energy (IE) of the material, and the energy of the lowest unoccupied state is an approximation of the electron affinity (EA). The procedure used to adjust the zero energy in density of states plots is described in the Supporting Information.

3.3 Results and Discussion

3.3.1 Kinetics of Propene Oxidation

The kinetics of propene oxidation to acrolein were measured in a fixed bed reactor operating at atmospheric pressure and temperatures between 633 K and 713 K.

Conversion was maintained below 1% in order to minimize the effects of secondary reactions. For all of the materials investigated, the selectivity to acrolein was greater than 65%. Table 3.1 lists the reaction orders in propene and oxygen, apparent rate constant at 673 K, the apparent activation energy, and the apparent pre-exponential factor for each catalyst. For the temperature range chosen, the rate of acrolein formation is essentially first order in propene and zero order in oxygen (reaction order plots are shown in the Supporting Information). The latter result indicates that under the conditions chosen, the catalyst is saturated with oxygen. The production rate of acrolein does not change when the conversion increases, demonstrating no inhibition by acrolein under experimentally relevant low conversion conditions. (Plots are shown in the Supporting Information).

3.3.2 UV-VIS-NIR and XANES Spectroscopy

Figure 3.1 shows the absorption edges for a series of solid solutions having the stoichiometry $Bi_{1-x/3}V_{1-x}Mo_xO_4$. The absorption edges determined for bismuth vanadate and bismuth molybdate are consistent with those reported previously [85,86]. Each material exhibits only a single absorption edge, with the position of the edge shifting monotonically with the relative proportions of vanadium and molybdenum. This result indicates that vanadate and molybdate ions are not electronically independent, but, rather, the electronic properties of the mixed metal oxide depends upon the relative proportions of vanadate and molybdate ions present in the material. By contrast, a physical mixture of bismuth vanadate and bismuth molybdate exhibits two separate absorption edges (see Supporting Information).

The diffuse reflectance spectra of $Bi_3FeMo_2O_{12}$ and $Bi_2Mo_{2.5}W_{0.5}O_{12}$ are shown in Figure 3.2. The absorption edge of $Bi_3FeMo_2O_{12}$ is lower in energy than that of $Bi_2Mo_3O_{12}$, indicating that Fe substitution, like V substitution, reduces the band gap energy. The spectrum of $Bi_3FeMo_2O_{12}$ also exhibits absorption features at energies below the edge, attributable to the presence of occupied d orbitals on Fe^{3+} ions. These absorption features may arise from d-d excitations on individual Fe atoms (which, however, are both spin and Laporte forbidden for the d^5 high spin tetrahedral Fe^{3+} ion), or they may arise from the charge transfer excitation process $2\ Fe^{3+} \rightarrow Fe^{2+} + Fe^{4+}$ between neighboring Fe ions. In either case, the spectrum in Figure 3.2 indicates that (1) the band gap in $Bi_3FeMo_2O_{12}$ is lowered relative to that in $Bi_2Mo_3O_{12}$, presumably via coupling between Mo and Fe electronic states; and (2) there exist additional Fe electronic states in $Bi_3FeMo_2O_{12}$ which are not coupled to Mo states and which give rise to additional features in the absorption spectrum. As discussed below, both points (1) and (2) are relevant to understanding the impact of Fe substitution on the catalytic performance of bismuth molybdate. The diffuse reflectance UV-Visible spectrum of $Bi_2Mo_{2.5}W_{0.5}O_{12}$ closely resembles that of $Bi_2Mo_3O_{12}$.

Heating bismuth molybdate-based catalysts in non-reducing atmospheres (e.g. helium or air) caused a shift in the absorption edge to lower energies (see Supporting Information). This shift is attributable to strong coupling between electronic states and lattice vibrations (phonons), together with a smaller effect due to thermal expansion of the lattice. The relationship between band gap and temperature is almost perfectly linear across the temperature range studied (298 - 713 K), as expected from theory [87,88]. Thermal effects on band gaps are qualitatively similar across all catalysts studied, with

the magnitude of the decrease in band gap varying from 0.1 - 0.2 eV upon heating from ambient conditions to 713 K, depending on catalyst composition. The band gaps for all materials studied, as measured at 673 K, are given in Table 3.2.

Heating $Bi_{1-x/3}V_{1-x}Mo_xO_4$ at 673 K in an oxidizing atmosphere and then exposing it to 20% propene in helium caused a time-dependent shift in the baseline UV-Vis absorbance (e.g. the absorbance at all energies below the edge), indicating reduction of the catalyst (see Supporting Information). This observation is consistent with a Mars-van Krevelen mechanism in which propene is oxidized by lattice oxygen, leading to reduction of the catalyst. In fact, the initial rate of catalyst reduction determined from UV-Vis data is proportional to the measured rate of propene oxidation. However, these data do not reveal which element(s) undergo reduction. For this reason, *in situ* XANES experiments were carried out in order to determine extent to which Bi, Mo, and V are reduced by propene and whether reduction of all elements occurs concurrently or sequentially.

Figures 3.3 and 3.4 show *in situ* XANES spectra collected during reduction of $Bi_{0.85}V_{0.55}Mo_{0.45}O_4$ at 713 K in propene flowing at 100 mL/min. Reduction was initiated after pre-treatment in air at 713 K to ensure a fully oxidized initial state prior to reduction. While experimental details preclude rigorous investigation of reduction kinetics (see Supporting Information), observation of the qualitative features of the reduction process is sufficient for the present investigation. Under reducing conditions, a decrease in the pre-edge peak intensity and an edge shift to lower energy begin immediately upon exposure to reducing conditions, as seen in Figure 3.3a. Both changes are consistent with reduction of vanadium. Figure 3.3b shows that the initial pre-edge peak height and edge position are consistent with tetrahedrally coordinated V^{5+}, as expected from the stoichiometry and known crystal structure of $Bi_{1-x/3}V_{1-x}Mo_xO_4$. After 5 min exposure to propene, reduction is essentially complete. Figure 3.3c shows that after reduction, the V K edge position is consistent with that for V^{4+}; however, the pre-edge peak height is much larger than that for VO_2. The pre-edge feature arises from a $1s \rightarrow 3d$ transition, which is formally prohibited by the selection rule for photon absorption ($\Delta L = \pm 1$). It is therefore only observed for coordination environments in which mixing of 3d and 4p orbitals is allowed by symmetry. Such mixing is strong in tetrahedral coordination such as that in NH_4VO_3 and the as-prepared $Bi_{0.85}V_{0.55}Mo_{0.45}O_4$, but becomes weaker as the coordination environment becomes more octahedral. Vanadium in VO_2 sits in a distorted octahedral environment with weak $3d - 4p$ mixing, resulting in a weak pre-edge peak. The much greater pre-edge peak height in the reduced x = 0.45 catalyst indicates that the vanadium centers in the reduced catalyst retain their nearly tetrahedral coordination.

The Mo K edge XANES shown in Figure 3.4a show trends in qualitative agreement with those seen in the V K edge XANES in Figure 3.3a: a decrease in pre-edge peak intensity and a shift of the absorption edge to lower energies. Although the reduction conditions (100 mL/min 99% propene at 713 K) are the same as in the vanadium case, the catalyst loading required to obtain good XANES signal is different, resulting in a different timescale for reduction. Nevertheless, these results show that Mo reduction begins immediately upon exposure to reducing conditions, identical to the case for vanadium. The XANES spectrum of the as-prepared $Bi_{0.85}V_{0.55}Mo_{0.45}O_4$ contains tetrahedrally coordinated Mo^{6+} sites similar to those present in $CaMoO_4$. Exposure to

reducing conditions leads to a pre-edge feature height and an edge position midway between those expected for Mo^{6+} and Mo^{4+}. This observation is consistent with formation of either Mo^{5+} sites or with a mixture of both Mo^{4+} and Mo^{6+} sites. Investigations using XPS and EPR have detected both Mo^{4+} and Mo^{5+} in reduced bismuth molybdate [89-91], and DFT calculations suggest that both Mo^{4+} and Mo^{5+} are formed during reduction of bismuth molybdate by propene. No stoichiometric Mo^{5+} oxide phase is known, and in mixed-valence oxides such as Mo_4O_{11}, extensive delocalization of Mo d electrons [92,93] precludes the assignment of integral oxidation states to individual molybdenum centers. While the relative concentrations of formally Mo^{6+}, Mo^{5+}, and Mo^{4+} sites cannot be assessed from the data in Figure 3.4, it is evident that reduction of molybdenum begins immediately upon exposure to propene. It can therefore be concluded that during reduction of $Bi_{0.85}V_{0.55}Mo_{0.45}O_4$, vanadium and molybdenum undergo reduction simultaneously. This conclusion is extended to other catalysts with the composition $Bi_{1-x/3}V_{1-x}Mo_xO_4$ based on our earlier work [67], which showed that exposure of such materials to 100 mL/min of 99% propene at 713 K for 24h resulted in the reduction of V^{5+} to V^{4+} and Mo^{6+} to Mo^{4+}. That work also demonstrated that Bi^{3+} does not undergo reduction.

3.3.3 Band Gap Energy as a Descriptor of Activation Energy

Figure 3.5 shows the apparent activation energy for each catalyst plotted as a function of the band gap energy measured at 673 K. This relationship can be understood by relating the band gap to the elementary processes involved in attaining the transition state for the rate-limiting step of propene oxidation, the step which involves cleavage of a C-H bond in the methyl group of the reactant.

The band gap in a semiconductor separates the highest occupied and lowest unoccupied crystal orbitals. In bismuth molybdate, both the highest occupied and lowest unoccupied crystal orbitals are centered on the molybdate ions: the highest occupied states consist of O 2p lone pair orbitals of local t_1 symmetry, while the lowest unoccupied states consist of the Mo 4d orbitals of local e symmetry (the d_{z^2} and $d_{x^2-y^2}$). The band gap thus arises from a ligand-to-metal charge transfer (LMCT) process in which an excited electron is formally transferred from oxygen to molybdenum. This process can be represented in the following manner $Mo^{6+}=O^{2-} \rightarrow Mo^{5+}-O^{1-}$, and gives rise to the absorbance maximum near 380 nm for $Bi_2Mo_3O_{12}$ seen in Figure 3.1.

Likewise, for vanadate ions, the highest occupied states consist of O 2p lone pair orbitals of local t_1 symmetry, while the lowest unoccupied states consist of the V 3d orbitals of local e symmetry. The band gap in $BiVO_4$ thus arises from an LMCT process which can be written schematically as $V^{5+}=O^{2-} \rightarrow V^{4+}-O^{1-}$. The V3d($e$) $\leftarrow$ O2p(t_1) LMCT excitation in $BiVO_4$ gives rise to the absorbance maximum near 475 nm in Figure 3.1. (A second higher energy absorbance maximum arising from the V3d(t_2) $\leftarrow$ O2p(t_1) excitation is also visible near 390 nm.) As shown in Scheme 3.1, both LMCT excitation processes can be depicted as M=O $\rightarrow$ •M—O•.

Density functional theory calculations of propene activation over $Bi_2Mo_3O_{12}$ have been reported previously [69-74], and DFT calculations of the activation barrier for propene activation over $BiVO_4$ are given in the Supporting Information. This work

provides a generic picture of the transition state for C-H activation over a surface M=O structure (M = Mo, V). As shown in Figure 3.6, the transition state for C-H bond activation involves three simultaneous processes: dissociation of a C-H bond, formation of an O-H bond, and elongation and rehybridization of an M=O double bond to yield an M–O single bond. The sum of these three processes can be written as $M^{(n)+}=O^{2-} + C_3H_6 \rightarrow •M^{(n-1)+}–OH + •C_3H_5$.

Figure 3.7 demonstrates how the contributions from each of the three components to the overall reaction barrier can be represented in terms of a Born Haber cycle. The bond dissociation energy for a C-H bond in the methyl group of propene is 88.2 kcal/mol [94]. The remaining contributions are summarized in Table 3.3. The H bond formation energy E_{OH} was determined by calculating the energy released by the attachment of an H radical to •M—O•. A value of ΔE_{OH} of 117.9 kcal/mol was obtained for M = Mo, and 115.8 kcal/mol for M = V, suggesting that the O-H bond energy does not depend strongly on the identity of the nearest neighbor to oxygen. For comparison, the dissociation energy for the first O-H bond in water is 117.59 kcal/mol [95].

The value of $E_{stretch}$ was determined by subtracting the energy of the model catalyst surface with the active site M=O bond at the M-O bond distance of the initial state for C-H bond activation (1.60 Å for V=O, 1.74 Å for Mo=O; see Supporting Information) from the energy of the model catalyst surface with the active site M=O bond stretched to the M-O bond distance in the M-OH final state (1.74 Å for V-O, 2.00 Å for Mo-O). Again, the values of $E_{stretch}$ are similar for $BiVO_4$ and $Bi_2Mo_3O_{12}$. Remarkably, the 2.1 kcal/mol greater $E_{stretch}$ required to elongate the Mo=O bond is exactly matched by a 2.1 kcal/mol greater Mo-OH bond strength. This cancelation may indicate a compensation effect whereby the M-O bond will undergo a greater (more energetically costly) deformation in order to form a stronger M-OH bond.

E_{hyb} was calculated as the difference in energy between singlet M=O and triplet •M—O• orbital configurations for the M-O bond at the final state (M-OH) geometry (but with no H atom attached), and reflects only the energy required to rearrange electron density within the M-O bond [96]. As seen in Table 3.3, the largest difference between $BiVO_4$ and $Bi_2Mo_3O_{12}$ occurs for the E_{hyb} term. Furthermore, the compensation between $E_{stretch}$ and E_{OH} eliminates the composition dependence of the sum $E_{stretch} + E_{OH}$; as a result, almost the entire difference in E_{TS} between $BiVO_4$ and $Bi_2Mo_3O_{12}$ is due to the E_{hyb} term. Importantly, the metal-oxygen bond reorganization energy described by E_{hyb} — transfer of an electron from a non-bonding oxygen 2p-derived state into a metal d-derived state with $\pi^*(M=O)$ antibonding character — corresponds to an LMCT excitation. Both the M-O bond reorganization taking place at the C-H bond activation transition state and the LMCT excitation that gives rise to the band gap involve the M=O $\rightarrow$ •M—O• redistribution of electron density depicted in Scheme 3.1. It is for this reason that the band gap energy emerges as a descriptor of catalytic activity.

The excited state generated in an LMCT excitation has a sufficiently long enough lifetime to undergo vibrational relaxation. This is the reason why the band-gap energy is sensitive to temperature. Therefore, the band gap energy should contain contributions from both geometric and electronic rearrangement, and we expect $E_G \approx E_{stretch} + E_{hyb}$. Indeed, the sum $E_{stretch} + E_{hyb} = 51$ kcal/mol for $BiVO_4$ and 62 kcal/mol for $Bi_2Mo_3O_{12}$, nearly equal to the band gap energies of 2.28 eV = 52.6 kcal/mol for $BiVO_4$ and 2.80 eV

= 64.6 kcal/mol for $Bi_2Mo_3O_{12}$ determined from density of states calculations. The close agreement between E_G values obtained from two different calculations — a Born Haber cycle describing changes to the catalyst occurring during C-H bond activation, and a density of states calculation describing the states involved in a UV-Visible absorption experiment — reflects the commonality of the physics of these two processes.

The difference between E_{hyb} values for $BiVO_4$ and $Bi_2Mo_3O_{12}$ amounts to ~ 9 kcal/mol, consistent with the ~ 5 kcal/mol difference in observed activation energies for propene oxidation over these two catalysts. Even better agreement between theory and experiment could be obtained by including spin-orbit coupling effects in the calculation: previous analysis [73,74] found that spin-orbit coupling effects reduce the barrier to C-H activation on $Bi_2Mo_3O_{12}$ by 4.6 kcal/mol, whereas a much smaller 0.5 kcal/mol reduction in barrier occurs for $BiVO_4$ due to weaker spin-orbit coupling for V 3d vs. Mo 4d orbitals. However, incorporation of spin-orbit coupling effects requires detailed knowledge of the potential energy surface near the transition state for C-H bond activation, where these effects are manifest. By contrast, no transition state calculations are required to obtain the terms used in the Born-Haber cycle presented above. Rather, knowledge of the initial state and final state for C-H bond activation, and consideration of the bond-breaking and bond-forming processes linking these states, is sufficient not only to explain differences in catalytic performance between $BiVO_4$ and $Bi_2Mo_3O_{12}$, but further, to link these differences to a simple experimental observable: the band-gap energy.

The change in enthalpy upon adsorption needs to be considered in order to complete the discussion of the relationship of catalyst band gaps to apparent activation energies. Under the reaction conditions used in this work to extract apparent activation energies, the resting state of the catalyst is the bare, fully oxidized oxide surface. The oxidation of propene is initiated by reversible physisorption of propene gas to the active site, followed by rate-limiting activation of an allylic C-H bond. The apparent activation energy assessed by experiment comprises the sum of the energies of both of these steps, whereas the intrinsic activation energy estimated from Born Haber cycle analysis addresses only the C-H bond activation step. An estimate for the apparent activation energy can therefore be obtained by adding the adsorption enthalpy to the calculated intrinsic activation energy. The change in enthalpy upon adsorption of propene on bismuth molybdate has been measured experimentally at -7 to -8 kcal/mol [97,98]. Unfortunately, the enthalpies of adsorption of propene on bismuth vanadate or on V-, Fe-, or W-substituted bismuth molybdates have not been reported in literature to the best of our knowledge. However, given the purely van der Waals nature of the interaction between propene and support, and the structural similarity among the oxide phases under consideration, it is reasonable to expect the adsorption enthalpy to be relatively insensitive to composition. Support for this expectation is provided by DFT calculations, which yield adsorption enthalpies of -8.2 kcal/mol on $BiVO_4$, -7.8 kcal/mol on $Bi_7V_5Mo_3O_{32}$, and -6.4 kcal/mol on $Bi_2Mo_3O_{12}$ (taking adsorption enthalpy as the enthalpy of the adsorbed state minus the separate enthalpies of the model catalyst surface and propene). Calculated heats of adsorption are used with caution, as the M06-L functional employed here does not contain an explicit van der Waals interaction term. It is, however, parameterized using training sets including systems dominated by dispersive interactions, and has proven successful in capturing such interactions in a number of other systems [74,99-102]. It is therefore expected that the calculated heats of adsorption

presented here are of sufficient accuracy to provide useful estimates of propene adsorption enthalpies on the oxide phases examined. The estimated ~2 kcal/mol variation in heat of adsorption with composition is comparable in magnitude to the ~ 2 kcal/mol variations with composition in $E_{stretch}$ and E_{OH} in the Born Haber cycle, and remains significantly smaller in magnitude than the variation in E_{hyb}. Thus, even after accounting for adsorption enthalpy, the observed trends in apparent activation energy with composition are primarily attributable to changes in band gap energy.

Taking the change in enthalpy for propene adsorption on $BiVO_4$ to be -8 kcal/mol and adding it to the values of E_{C-H} (88.2 kcal/mol), $E_{stretch}$ (20.9 kcal/mol), E_{hyb} (30.1 kcal/mol), and E_{OH} (-115.8 kcal/mol) yields an estimated apparent activation barrier of 15.4 kcal/mol, in excellent agreement with the experimentally observed apparent activation energy of 14.5 kcal/mol. Likewise, taking the change in enthalpy for propene adsorption on $Bi_2Mo_3O_{12}$ to be -7 kcal/mol and adding it to the values of E_{C-H} (88.2 kcal/mol), $E_{stretch}$ (23.0 kcal/mol), E_{hyb} (39.0 kcal/mol), and E_{OH} (-117.9 kcal/mol) yields an estimated apparent activation barrier of 25.3 kcal/mol, which can be compared to the 19.9 kcal/mol measured experimentally. As noted above, inclusion of spin-orbit coupling effects would provide even closer agreement between estimate and experiment (i.e. estimated barriers of 14.9 kcal/mol for $BiVO_4$ and 20.7 kcal/mol for $Bi_2Mo_3O_{12}$). The close agreement between estimated and measured apparent activation barriers confirms that all of the physical processes contributing to the observed activation barrier have been accounted for in the Born Haber analysis. This analysis, in turn, provides a rationale for the observed lower barrier to propene activation over $BiVO_4$ as compared to $Bi_2Mo_3O_{12}$.

3.3.4 Density of States Calculations

To understand why the band-gap energy is a good descriptor of catalytic activity for mixed phases containing both Mo and V, Fe, or W, it is necessary to examine more closely how the electronic states involved in LMCT excitation are affected by composition. For all materials examined, the highest occupied crystal orbital involves the non-bonding O 2p states, which have t_1 symmetry with respect to the tetrahedral oxoanions. The character of the lowest unoccupied, metal-centered electronic states involved in the LMCT excitation, however, depends on the metal(s) present in the catalyst. To obtain a more complete understanding of the electronic structure of substituted bismuth molybdate-based catalysts, density functional theory calculations were carried out on five representative compositions. Crystal structures taken from the literature were used to generate models for $BiVO_4$, $Bi_2Mo_3O_{12}$, and $Bi_3FeMo_2O_{12}$. A single material of composition $Bi_7V_5Mo_3O_{32}$ (x = 0.375) was used to explore electronic effects in $Bi_{1-x/3}V_{1-x}Mo_xO_4$, and a single material of composition $Bi_8Mo_{10}W_2O_{48}$ was used to explore electronic effects in $Bi_2Mo_{3-y}W_yO_{12}$. We note that prior studies of the electronic structure of $BiVO_4$ have shown good agreement between theory and experiment [103-108]. To our knowledge, the present study represents the first investigation of the electronic structure of $Bi_2Mo_3O_{12}$, $Bi_3FeMo_2O_{12}$, $Bi_{1-x/3}V_{1-x}Mo_xO_4$, or $Bi_2Mo_{3-y}W_yO_{12}$ using density functional theory.

The density of states for $BiVO_4$, $Bi_7V_5Mo_3O_{32}$, $Bi_3FeMo_2O_{12}$, $Bi_2Mo_3O_{12}$, and $Bi_2Mo_{2.5}W_{0.5}O_{12}$ are presented in Figure 3.8. The bands centered at -25.3 eV and -15.9

eV correspond to O 2s and Bi 6s electrons, respectively. (Bi 5d core states, not explicitly modeled in these calculations, would appear below -28 eV; they have been shown to play no role in bonding in bismuth oxides [109]). Although O 2s and Bi 6s orbitals are treated as valence orbitals in the calculations, the narrow width of these bands and the lack of mixing with other orbitals suggest these states are essentially core-like and ionic in character. The core-like character of these states is further underscored by the finding that their energies do not vary with composition: the density-weighted average energy of the O 2s states is within 0.10 eV of -25.30 eV, and the density-weighted average energy of the Bi 6s states within 0.05 eV of -15.90 eV, in all compositions studied. For comparison, the energy of the O 2s orbital on an isolated O atom is calculated to be -25.2 eV.

The valence states run from near -13 eV to -7 eV, while the conduction band states begin near -4.5 eV and run past the vacuum level. $Bi_3FeMo_2O_{12}$ also contains two mid-gap states just below the conduction band; the significance of these states is discussed more fully below. The band gap is calculated as the difference in energy between the lowest energy conduction band state and the highest energy valence band state. As compiled in Table 3.1, the density of states calculations yielded band gaps in excellent agreement with those measured experimentally.

To determine the effect of V substitution on the electronic structure of $Bi_2Mo_3O_{12}$, the atom-projected density of states has been evaluated for $Bi_7V_5Mo_3O_{32}$. As shown in Figure 3.9, the valence states of $Bi_7V_5Mo_3O_{32}$ run from -12.5 eV to -6.8 eV, while the conduction band states begin near -4.5 eV and run up to the vacuum level. (Recall that the energy abscissa in Figure 3.9 has been referenced to the vacuum state energy.) The valence states can loosely be grouped into four regions. The region from -12.5 to -11 eV is comprised primarily of Mo-O σ and π bonding states built from Mo 4d and O 2p orbitals. This region also contains a smaller contribution from Bi 6p orbitals, which mix with O 2p orbitals to produce Bi-O σ bonds. The region from -11 eV to -9 eV is dominated by V-O σ and π bonds built from V 3d and O 2p orbitals. The region from -9 to -7 eV has primarily O 2p character, and is attributed to lone-pair-like states on oxygen. The narrow region from -7.1 eV to the valence band edge at -6.8 eV remains predominantly O 2p in character, but also contains an important contribution from Bi 6s states. These states have Bi-O σ* character, and are responsible for the existence of the "stereochemically active lone pair" on bismuth [110,111]. We have shown elsewhere that these lone pairs play an instrumental role in creating catalytically active sites on the surface of the $Bi_2Mo_3O_{12}$ catalyst [73,74].

The conduction band states can also be categorized according to the dominant character of the states in each energy region. The V 3d and Mo 4d states on tetrahedrally coordinated vanadate and molybdate ions are split by the local crystal field into lower energy e states (d_{z^2} and $d_{x^2-y^2}$ orbitals) and higher energy t_2 states (d_{xy}, d_{yz}, and d_{xz} orbitals). In $Bi_7V_5Mo_3O_{32}$, the e states run from the conduction band edge at -4.48 eV to -3.08 eV, while the t_2 states begin at -3.08 eV and run up to roughly -1.2 eV. The states above this energy are primarily derived from the empty Bi 6p orbitals, which also contribute slightly in the e and t_2 bands. Though none of the conduction band states have strong O 2p character, all of them have Mo-O, V-O, or Bi-O antibonding character.

In scheelite-structured materials, MO_4^{n-} ions are not perfectly tetrahedral, experiencing a small oblate tetragonal distortion. As a result, the d_{z^2} orbitals are lowered

in energy relative to the $d_{x^2-y^2}$ orbitals. Although the distortion is not large enough to split the e band in $Bi_7V_5Mo_3O_{32}$ into separate d_{z^2} and $d_{x^2-y^2}$ bands, the state right at the conduction band edge has almost purely d_{z^2} character. A map of the charge density distribution for this state is shown at right in Figure 3.9. In accordance with the presence of both V 3d and Mo 4d states at the bottom of the e band, significant charge density is present in d_{z^2} orbitals on both V and Mo centers. (The greater spatial extension of the larger Mo 4d orbitals compared to the smaller V 3d orbitals is also visible.) The mixing of V 3d and Mo 4d states in the e band, and the contribution of both V and Mo centers to the charge density shown in Figure 3.9, provide an explanation for the results seen in Figure 3.1: both V 3d and Mo 4d orbitals contribute to the character of the states into which electrons are excited during the band gap measurement. Increasing vanadium content in $Bi_{1-x/3}V_{1-x}Mo_xO_4$ increases the contribution from lower energy V 3d states to the e band, lowering the LMCT excitation energy. It is for this reason that only a single adsorption edge at a composition-dependent energy is observed in $Bi_{1-x/3}V_{1-x}Mo_xO_4$ solid solutions.

The effect of W substitution in $Bi_2Mo_{3-y}W_yO_{12}$ materials can be understood using the same analysis. The e band states at the bottom of the conduction band are comprised of both Mo 4d and W 5d orbitals, with the energy of the e band (and therefore the LMCT excitation energy) dependent upon the relative proportions of Mo and W present. In contrast to the case of vanadium substitution, however, tungsten substitution increases the LMCT excitation energy. This can be understood by examining the data in Table 3.4. The average energy of the V 3d orbitals is lower than the average energy of the Mo 4d orbitals, so V substitution tends to lower the e band energy. (Again, these energies are referenced to the vacuum state.) Conversely, the average energy of the W 5d orbitals is higher than that of the Mo 4d orbitals, so W substitution tends to increase the e band energy. In both cases, efficient mixing among d orbitals leads to a single, mixed-character e band and a single, composition-dependent LMCT absorption edge energy.

The results in Table 3.4 indicate that since the 3d orbitals in Fe are even lower in energy than the 3d orbitals in V, substitution of Fe into bismuth molybdate should have an even greater energy-lowering effect on the LMCT excitation energy than substitution with V. As shown in Figure 3.2, Fe substitution does indeed lower the LMCT excitation energy. However, a comparison between $Bi_3FeMo_2O_{12}$ and $Bi_{2.4}V_{1.2}Mo_{1.8}O_{12}$ ($x = 0.60$) reveals that the band gap in the Fe-substituted material is actually slightly larger than in a V-substituted material with a similar degree of substitution. The comparatively lower effectiveness of the Fe 3d orbitals in lowering the e band energy in $Bi_3FeMo_2O_{12}$ vs. that of the V 3d orbitals in $Bi_{1-x/3}V_{1-x}Mo_xO_4$ can be understood by examining the projected density of states for $Bi_3FeMo_2O_{12}$ presented in Figure 3.10. In $Bi_{1-x/3}V_{1-x}Mo_xO_4$, the states at the bottom of the conduction band arise from the overlap between Mo 4d states of e symmetry and lower energy V 3d states of e symmetry. (The Mo 4d and V 3d states of t_2 symmetry also overlap to create a higher energy t_2 band, which lies above -3.1 eV in Figure 3.9.) By contrast, in $Bi_3FeMo_2O_{12}$, the e symmetry Fe 3d states are too low in energy to overlap effectively with Mo 4d states. Instead, the Fe 3d e states form a pair of narrow, localized bands that lie below the conduction band edge energy. (These states are in fact so localized that the slight oblate tetragonal distortion of the nominally tetrahedral oxoanions in the scheelite crystal structure completely resolves the nominally e symmetry Fe 3d states into separate d_{z^2} and $d_{x^2-y^2}$ bands.) These are best considered mid-gap states;

excitation of occupied Fe 3d electrons into these states gives rise to the pre-edge absorption shown in Figure 3.2. The lowering of the conduction band edge energy in $Bi_3FeMo_2O_{12}$ relative to that in $Bi_2Mo_3O_{12}$ instead arises from mixing between Mo 4d states of e symmetry and Fe 3d states of t_2 symmetry. This mixing gives rise to the charge density shown in the upper right inset in Figure 3.10. While Fe 3d states of t_2 symmetry are still lower in energy than Mo 4d states of e symmetry, they are not as low in energy as Fe 3d states of e symmetry. It is for this reason that substitution with Fe lowers the LMCT excitation energy, but not as effectively as might have been expected from the results in Table 3.4.

The contrast between the mixing of Mo 4d states with V 3d states vs. with Fe 3d states illustrates that a metric attempting to predict the effect of cation substitution on the LMCT excitation energy that is based only on the average energy of the d states of the substituting atom (see Table 3.4) would be not be appropriate. Greater insight into the ability of a substituent cation to influence the LMCT excitation energy can be obtained by considering not only the average energies of the d states, but also their band widths. As shown in Table 3.5, the widths of the e band states in $BiVO_4$ and $Bi_2Mo_3O_{12}$ are 1.18 and 1.30 eV, respectively. The somewhat greater width of the e band in $Bi_2Mo_3O_{12}$ compared to $BiVO_4$ is a consequence of greater spatial overlap between the larger Mo 4d orbitals compared to the smaller V 3d orbitals (as seen in the inset in Figure 3.9). According to Table 3.4, the average V 3d and Mo 4d orbital energies differ by only ~ 0.5 eV, which is less than the width of the e bands arising from V 3d and Mo 4d orbitals. The result is effective overlap between V 3d and Mo 4d states in $Bi_{1-x/3}V_{1-x}Mo_xO_4$ solid solutions. The difference in average orbital energies between the Fe 3d and Mo 4d orbitals, however, is greater than 2 eV. In addition, the greater effective nuclear charge on Fe vs. V renders the Fe 3d orbitals even more compact than the V 3d orbitals, resulting in poorer through-space overlap and reduced band width: even including the gap between the Fe $3d_{z^2}$ and Fe $3d_{x^2-y^2}$ states, the e band width in $Bi_3FeMo_2O_{12}$ is only 0.46 eV. The widths of the Fe 3d and Mo 4d e bands are not great enough to span the > 2 eV difference in the energies between these orbitals, and as a result, the Fe 3d and Mo 4d e states do not mix.

Although not explored further in the present study, the orbital mixing effects observed here are likely to be general features in single phase metal oxides containing multiple transition metal species. With knowledge of the center and band width of the e band in tetrahedral systems, or the t_{2g} band in octahedral systems, it should be possible to systematically tune the LMCT excitation energy. For catalytic systems in which the activation of substrate bonds involves LMCT-like excited states, systematic tuning of the LMCT excitation energy should in turn provide a means for altering catalytic activity. Although only scheelite-structured materials have been examined here, these effects should be generally observable in other mixed metal oxide systems, including those based on zircons [112], perovskites [36-37,113-114], spinels [115,116], rutile [117], and other structures [118]. More work in this area is clearly required.

3.4 Conclusions

A model has been proposed to explain the observed correlation of the activation barrier propene oxidation to acrolein over a mixed metal oxide with the ligand-to-metal charge transfer (LMCT) excitation energy of the oxide. This excitation energy corresponds to the band-gap energy for metal oxides containing transition metals in their highest oxidations states. We note that this model should also apply to any oxidation reaction in which activation of the reactive substrate occurs through a transition state involving rehybridization of a catalyst M=O bond in the rate-controlling catalytic step. We have shown that the model successfully explains the variations in the apparent activation energy observed for the oxidation of propene to acrolein over catalysts based on bismuth molybdate, and containing varying proportions of vanadium, tungsten, or iron. Substitution of vanadium or iron for molybdenum reduces the apparent activation energy by lowering the LMCT energy. In bismuth molybdates, the LMCT excitation occurs between oxygen lone pair states at the top of the valence band and e symmetry Mo 4d states at the bottom of the conduction band. Substitution by vanadium lowers the LMCT excitation energy by mixing the e symmetry Mo 4d states with lower energy e symmetry V 3d states. Substitution by iron also lowers the LMCT excitation energy. However, in this case the e symmetry Mo 4d states mix instead with t_2 symmetry Fe 3d states; the e symmetry Fe 3d states are too low in energy to mix effectively and instead form a pair of mid-gap states. Substitution by tungsten increases the LMCT excitation energy, as e symmetry Mo 4d states mix with higher energy e symmetry W 5d states. In each case, the LMCT excitation energy can be rationalized by considering both the average energy and the band width of the metal d-orbital states. With knowledge of these orbital properties, it becomes possible to systematically tune the LMCT excitation energy in mixed metal oxides. Such tuning allows the rational formulation of more active mixed metal oxide oxidation catalysts in at least one family of materials, and it is believed that other systems are likely to exhibit similar effects.

3.5 Supplemental Information

3.5.1 Determination of the Band Gap from Absorption Edge Data

A standard formula for the relationship between the absorption coefficient and light frequency is

$$\alpha \propto \frac{(h v - E_g)^\eta}{h v}, \tag{1}$$

where α is the absorption coefficient, v is the frequency of light, h is Planck's constant, E_g is the band gap energy, and the value of η depends on the type of electronic transition involved. For an allowed, direct band gap transition, $\eta = 2$. The band gaps in bismuth vanadates and molybdates arise primarily from ligand-to-metal charge transfer excitations taking place on the vanadate and molybdate ions [119,120]. These LMCT excitations are symmetry-allowed and give rise to direct transitions: both the conduction band minimum and the valence band maximum occur at the same value of the wave vector $\mathbf{k}$. (Interestingly, the band gap minimum in these materials, while direct, occurs at $\mathbf{k} = (\pi/2,0,0)$ rather than at $\mathbf{k} = (0,0,0)$ as is more usual for direct band gap materials. This has consequences for calculation of the band gap within DFT, as discussed below.) If

equation (1) were exact, then plots of the product $(\alpha hv)^2$ vs. hv for $BiVO_4$ and $Bi_2Mo_3O_{12}$ would yield straight lines, with $E_g = hv$ when $\alpha = 0$.

In fact, as shown in Figure 3.S1, the suitably transformed absorbance data are indeed relatively linear over much of the energy range near the absorption edge. In order to best determine the value of E_g, it is desirable to fit a line to the largest possible portion of the edge data. Upon closer investigation of the plot of $(\alpha hv)^2$ vs. hv, however, it becomes apparent that the data deviate systematically from linearity, falling along an S-shaped curve. Consequently, the larger the range of data included in the fit, the shallower the slope of the resulting best fit line, and the lower the calculated edge energy. In order to make a fair comparison among absorption edges calculated for different materials (with potentially different degrees of deviation from linearity in the edge region), it is necessary to develop a consistent approach for determining which data points should be used in the construction of a linear fit which "best captures" the edge. Recognizing the S-shaped deviation from linearity in the plot of $(\alpha hv)^2$ vs. hv, least-squares regression was used to fit the data to a function of the form

$$(\alpha hv)^2 = a + \frac{b}{2}\left(1 + erf\left[\frac{hv-c}{d\sqrt{2}}\right]\right) \tag{2}$$

This function is an antiderivative of the standard Gaussian (bell) curve with center c and standard deviation d. In equation (2), a is the limiting value of $(\alpha hv)^2$ at energies below the edge, and should be very nearly zero. $a+b$ is the 'height' or upper asymptote of the sigmoid, and corresponds to the maximum absorbance that would be observed above the edge if there were no additional electronic transitions at higher energies. c is the value of hv at the center of the absorption edge, and d controls the 'steepness' of the absorption edge. Since d can be interpreted as a standard deviation, equation (2) gives a convenient and systematic method for determining which data to include in the best fit line used to determine E_g: the 'linear region' of the $(\alpha hv)^2$ vs. hv plot is taken as the region between $hv = c - d$ and $hv = c + d$, i.e. the data within one standard deviation of the center of the edge. Investigation revealed that the values of a, b, c and d (and therefore of E_g) produced by a least squares fit of equation (2) to a plot of $(\alpha hv)^2$ vs. hv were quite insensitive to the exact span of data used in the fitting procedure, so long as the data range used extended from below $hv < c - d$ to above $hv > c + d$. (In the present investigation, typically $d \sim 0.1$ – 0.2 eV.) The goodness-of-fit R^2 values describing the fit of equation (2) to the plot of $(\alpha hv)^2$ vs. hv typically exceeded 0.9995. Both results confirm the validity of the approach. Note also that once the values of a, b, c, and d in equation (2) were determined, a subsequent linear least squares fit to the data between $hv = c - d$ and $hv = c + d$ was not actually necessary, as E_g could be calculated directly from equation (3):

$$E_g = c - \frac{d}{erf(1/\sqrt{2})} \approx c - 1.465d \tag{3}$$

Application of this approach enabled band gap energies to be reliably determined to within 0.02 eV across a range of catalyst compositions and at a range of measurement temperatures.

3.5.2 Measurement of Catalyst Reduction by XANES

Samples were prepared by diluting the catalyst with an appropriate quantity of boron nitride or silica, then pressing a pellet into a specially designed sample holder and loading the holder into a reactor cell. The sample holder used, referred to as a "six-shooter" for its resemblance to the cylinder on a revolver handgun, enables up to six samples to be loaded into the reactor cell simultaneously. The reactor cell comprises a quartz tube equipped with UltraTorr fittings at each end allowing gas to be passed through the tube; the tube ends are capped with X-ray transparent Kapton tape. The quartz tube is then aligned parallel to the incident X-ray beam, and moved along the axes normal to the X-ray beam by worm gear motors to allow each of the six loaded samples to sequentially be moved into the beam path. A clamshell-style tube furnace placed around the quartz tube enables samples to be heated during analysis.

The six-shooter does not completely fill the cross-sectional area of the quartz tube, but instead sits loosely inside the tube. In following the path of least resistance, reactant gas will primarily flow around the sample holder rather than through the samples, and the gas in contact with each catalyst sample is nearly stagnant. As a result, the actual concentration and effective flow rate through the catalyst bed is unknown, a fact which precludes the quantitative evaluation of kinetic parameters during *operando* XANES experiments. Still, given the low mass of catalyst used (2-10 mg), and the high concentration of reductant present in the gas phase (pure propene was used), mass transfer limitations are not expected to arise, and reasonable kinetics could likely be obtained by treating the catalyst as though reacting with a constant concentration of propene at zero space velocity.

A target post-edge absorbance of 2.5 and an edge step of 1.0 absorbance units (a.u.) were sought; however, the large absorption cross-section for Bi limited the edge step at the V K edge to ~ 0.2 a.u. Energies were calibrated against reference foils: the edge energy for the V metal foil was set to 5465 eV, and that for the Mo metal foil set to 20000 eV. Data analysis was carried out using the Ifeffit software suite [121].

3.5.3 Theoretical Methods

Bulk and slab density functional theory calculations were carried out using VASP [75] version 5.3.3. Projector augmented wave cores [76,77] containing kinetic energy density information were used to represent core electrons, while plane wave basis sets [78] with cutoff energies of 450 eV were used to represent valence electrons. Electron exchange and correlation were modeled using the M06-L density functional [79,80]. Because the kinetic energy density component of the M06-L functional requires evaluation of the second derivative of electron density, a fine integration grid is required to achieve accurate results [122] (and in many cases, required to achieve convergence at all). In VASP 5.3.3, this was achieved by using the "Accurate" precision setting, such that forces and kinetic energies were evaluated on an integration grid twice as fine as that used for the electron density. In addition, the energy density grid was explicitly set to include 30-50% more points in each lattice direction than VASP uses by default (accomplished by setting NGX, NGY, and NGZ explicitly in the INCAR file). It was found that scaling the integration grid to provide 10 points per angstrom of lattice vector length proved sufficient to achieve good results, so e.g. for $Bi_4V_4O_{16}$ where a = 5.147 and

c = 11.722, we used NGX = NGY = 52 and NGZ = 120. We also note that initial convergence of the M06-L functional was greatly facilitated by first converging the energy of a structure using the PBE [123] functional, then reading the resulting PBE charge density and wavefunction as initial guesses in M06-L calculations. Bulk calculations performed with M06-L starting from a PBE initial guess typically converged within 20 iterations. Slab calculations were much more challenging, requiring as many as 500 iterations to achieve convergence. Pulay mixing is not implemented in VASP for the M06-L functional, so the all-band simultaneous minimization algorithm was used.

The minimum energy structures were obtained by allowing atomic positions to relax from their reported crystallographic positions in a set of calculations with fixed, differing unit cell volumes; the structure obtained at the minimum of the volume-vs-energy curve was used for subsequent calculations [124]. Crystal structures taken from the literature were used for $BiVO_4$ (minimal unit cell $Bi_4V_4O_{16}$), $Bi_2Mo_3O_{12}$ (minimal unit cell $Bi_8Mo_{12}O_{48}$), and $Bi_3FeMo_2O_{12}$ (minimal unit cell $Bi_{12}Fe_4Mo_8O_{48}$). The $Bi_2Mo_3O_{12}$ structure contains three crystallographically distinct Mo environments. $Bi_2Mo_{2.5}W_{0.5}O_{12}$ was modeled by replacing two molybdenum atoms at Mo(1) sites with W atoms. Given the similarity in size and coordination environments of Mo^{6+} and W^{6+} ions, the choice of alternate locations for Mo substitution by W is not expected to produce results substantially different from those obtained here.

To model the $Bi_{1-x/3}V_{1-x}Mo_xO_4$ phase with an intermediate value of x, the smallest possible mixed vanadate-molybdate structure was constructed. This minimal model, of formula $Bi_7V_5Mo_3O_{32}$, corresponding to $x = 0.375$, was obtained from a three step procedure. (1) A $Bi_8V_8O_{32}$ supercell was built from two $Bi_4V_4O_{16}$ unit cells by choosing new lattice vectors in the ab plane rotated with respect to the original a and b vectors by 45° and lengthened by √2. The resulting supercell contained two Bi and two V atoms in each of four layers stacked along the c lattice direction. This same $Bi_8V_8O_{32}$ supercell was used for slab calculations on the $BiVO_4$ phase. (2) One V atom from each of the top three layers was replaced by a Mo atom, and a Bi atom from the middle of these three layers was removed to form a cation vacancy. The symmetry of this minimal cell ensured that removing either Bi atom from this layer produced an identical structure once periodic boundary conditions were applied. Placing the cation vacancy in the middle layer ensured both local and global charge neutrality. (3) The atomic positions in the resulting structure were allowed to relax at a series of fixed volumes to determine the optimal lattice constants and atomic positions for the $Bi_7V_5Mo_3O_{32}$ structure.

Geometry optimizations were carried out at 4x4x2 k points for $Bi_4V_4O_{16}$, 3x3x2 k points for $Bi_7V_5Mo_3O_{32}$, 3x2x2 k points for $Bi_8Mo_{12}O_{48}$ and $Bi_8Mo_{10}W_2O_{48}$, and 2x2x5 k points for $Bi_{12}Fe_4Mo_8O_{48}$. Lattice constants thus obtained differed from crystallographic values by < 0.5%.

Site-projected density of states calculations were carried out on relaxed structures using doubled k point grids (e.g. 6x4x4 for $Bi_8Mo_{12}O_{48}$). It is preferable to carry out density of states calculations using a dense k point grid, with interpolation between k points achieved via the tetrahedral method with Blöchl corrections. In order to achieve accurate band structure calculations when employing the all-band simultaneous minimization algorithm, it is further necessary to diagonalize the orbital matrix at each self-consistent step. This is the default behavior in VASP, and can be chosen explicitly by

setting LSUBROT=TRUE. However, we found that attempts to combine the tetrahedral interpolation scheme with orbital diagonalization led to instability in the SCF algorithm when the M06-L density functional was employed. To overcome this instability, the structure was first converged using a k point grid sufficiently accurate for structural relaxation (e.g., a 4x4x2 grid was used for $Bi_4V_4O_{16}$), using Gaussian band blurring with SIGMA=0.05 for interpolation between bands and with orbital diagonalization suppressed via LSUBROT=FALSE. Once the geometry had been optimized, the k point grid was doubled along each axis (e.g. to 8x8x4 for $Bi_4V_4O_{16}$), and the wavefunction converged using the same Gaussian blurring and LSUBROT=FALSE. The converged wavefunction was then used to seed a subsequent calculation with LSUBROT=TRUE to properly optimize the orbitals, while the Gaussian blurring scheme was retained. Finally, the resulting wavefunction was again reconverged using the tetrahedral scheme with Blöchl corrections (and SIGMA=0) with LSUBROT=TRUE. Only by initializing this final calculation with a pre-converged wavefunction was it possible to obtain a converged result with properly optimized orbitals.

By default, the zero of energy in a VASP-generated density of states calculation is the energy of the highest occupied state. In this work, it was desirable to instead choose the reference zero energy to be the energy of the vacuum state (i.e. the energy of electrons and nuclei separated at infinity). With this choice of reference state, Koopmans' theorem [84] states that the energy of the highest occupied state is an approximation of the first ionization energy (IE) of the material, and the energy of the lowest unoccupied state is an approximation of the electron affinity (EA). The band gap energy can then be determined as E_g = EA – IP. The energy axis for density of states calculations was aligned using the following procedure. First, density of states calculations were carried out in VASP on bulk catalyst models. Next, bulk structures were converted to slab surface models by introducing ~11 Å of vacuum space between layers. The top two atomic layers of the slab were allowed to relax, while the bottom two layers were held fixed to bulk positions. Propene was then introduced above the slab and allowed to relax. A density of states calculation was carried out for a model of adsorbed propene, and a site-projection scheme was used to extract the energies of states involving carbon and hydrogen atoms. These states comprise the molecular orbitals in the adsorbed propene. (Note that k point grids were reduced to 6x6x1 ($Bi_8V_8O_{32}$ and $Bi_7V_5Mo_3O_{32}$), and 6x1x4 ($Bi_8Mo_{12}O_{48}$) for slab calculations.) Separately, a cluster calculation on propene was carried out in VASP in a large 12 Å x 13 Å x 14 Å box to determine the orbital eigenvalues for gas phase propene. The energy abscissae in the slab projected density of states calculations were then shifted so as to align the energies of the propene states in the propene-on- slab calculations with the orbital eigenvalues for propene in the gas phase. The densities of states from the bulk calculations were then aligned with their corresponding slab calculations. The procedure is illustrated in Figure 3.S2.

As noted above, bismuth vanadate and bismuth molybdate exhibit direct band gaps; however, the band gap minimum in k space occurs at the **X** point, $\mathbf{k} = (\pi/2,0,0)$ rather than at the **Γ** point $\mathbf{k} = (0,0,0)$. In order for the values of EA, IP, and E_g to be accurately determined from density of states calculations, it is therefore essential that the **X** point be included in the calculations. This was ensured by use of **Γ**-centered k point meshes with an even number of k points along the crystallographic a axis in all density of states calculations.

The $Bi_3FeMo_2O_{12}$ phase contains unpaired electrons on Fe atoms. Accurate evaluation of the density of states in this material therefore requires consideration of the possible impact of magnetic ordering among unpaired electrons. The magnetic properties of $Bi_3FeMo_2O_{12}$ do not appear to have been investigated in literature. In order to evaluate the impact of magnetic ordering on electronic structure, three possibilities were considered: ferromagnetic ordering (all Fe 3d electrons unpaired; 20 unpaired spins per $Bi_{12}Fe_4Mo_8O_{48}$ unit cell), antiferromagnetic ordering (5 up spins on one Fe atom paired with 5 down spins on the nearest Fe atom; zero net spin per unit cell), and non-magnetic (non-spin-polarized calculation). Note that both magnetically ordered phases contain high spin d^5 iron, as expected from crystal field theory for tetrahedral Fe^{3+} ions. It was found that the total energies of the ferromagnetic and antiferromagnetic calculations agreed to within 0.0001 eV, and both calculations yielded equivalent densities of states. It was thus concluded that no long range magnetic ordering exists in $Bi_3FeMo_2O_{12}$, a result consistent with the relatively long nearest Fe-Fe contact (3.84 Å) and lack of Fe-Fe or Fe-O-Fe linkages in the crystal structure. However, the total energy of the non-spin-polarized calculation exceeded that of the ferromagnetic and antiferromagnetic calculations by ~ 2 eV. The non-spin-polarized density of states also indicated metallic conductivity for $Bi_3FeMo_2O_{12}$, in clear disagreement with experimental observation. Evidently, spin-polarized calculations are required to obtain accurate results on $Bi_3FeMo_2O_{12}$ even in the absence of magnetic ordering in this phase. All results reported in the present work for $Bi_3FeMo_2O_{12}$ were obtained from calculations containing antiferromagnetically ordered high spin d^5 Fe^{3+} ions.

3.5.4 Kinetics Results

The production rate of acrolein does not change when the conversion increases, demonstrating no inhibition by acrolein under experimentally relevant low conversion conditions. Variation in the acrolein production rate at 673 K and $P_{C3H6} = P_{O2} = 0.167$ atm measured as a function of propene conversion is shown in Figure 3.S3.

Reaction orders in propene and oxygen measured at 673 K for propene oxidation to acrolein are shown in Figure 3.S3 as well. The partial pressures of propene or oxygen were fixed at 0.067 or 0.167 atm, respectively, while the other one was varied.

3.5.5 X-Ray Diffraction

Powder XRD spectra for catalysts of composition $Bi_{1-x/3}V_{1-x}Mo_xO_4$ are presented in Figure 2.1. All catalysts of composition $Bi_{1-x/3}V_{1-x}Mo_xO_4$ have crystal structures that can be formally derived from the scheelite structure [62,67], which has a tetragonal AMX_4 unit cell in which eight-coordinate A^{n+} cations are linked through X atoms to eight different tetrahedral MX_4^{n-} anions, and each X atom in a tetrahedral MX_4^{n-} anion is linked to two different A^{n+} cations. Pure $BiVO_4$ has the scheelite structure above 526 K [125]; below this temperature it exists as a monoclinic distortion driven by emergence of a stereochemically active lone pair on Bi^{3+} cations and the shortening of one V-O bond to produce asymmetric $V(=O)O_3^{3-}$ anions. This monoclinic distortion, which has been

observed by others [34] in $Bi_{1-x/3}V_{1-x}Mo_xO_4$ materials with $x \leq 0.04$, results in the splitting of peaks near 18°, 35°, and 47° 2θ into doublets. Materials for which $0.15 \leq x < 0.75$ show essentially identical XRD patterns consistent with a single phase material with an undistorted scheelite structure. Further confirmation that these materials are true solid solutions is evident in the comparison between the solid state solution material of composition x = 0.45 (light green) and the physical mixture of $BiVO_4$ and $Bi_2Mo_3O_{12}$ with the same vanadium to molybdenum ratio (dark green); the two spectra are clearly distinguishable.

Charge neutrality dictates that substitution of three V^{5+} centers by three Mo^{6+} centers requires removal of one Bi^{3+} center from the crystal, leaving a cation defect site. The absence of any indication of superstructure peaks in the XRD patterns in Figure 2.1 for $0.15 \leq x < 0.75$ shows that these cation defects are distributed randomly throughout the crystal lattice of $Bi_{1-x/3}V_{1-x}Mo_xO_4$, which in turn suggests that V^{5+} and Mo^{6+} centers are also probably distributed nearly randomly.

Pure $Bi_2Mo_3O_{12}$ has a monoclinic crystal structure which can be derived from a scheelite structure containing an ordered pattern of cation vacancy sites. This monoclinic distortion and vacancy ordering results in the emergence of new peaks near 14° and 25° 2θ and the splitting of peaks near 28°, 47°, and 53°. Such splitting is also evident in the XRD spectrum of the x=0.90 material and possibly the x=0.75 material, suggesting that ordering of cation vacancies begins to become important as the solid solution becomes molybdenum-rich.

The crystal structure of $Bi_3FeMo_2O_{12}$ can also be derived from the scheelite structure, with all A cation sites filled by Bi^{3+} ions, FeO_4^{5-} ions occupying one-third of the MX_4^{n-} sites, and MoO_4^{2-} ions occupying two-thirds of the MX_4^{n-} sites. The distributions of Fe and Mo across the M sites are not random, with Fe ions occurring in pairs. The ordered distribution of Fe and Mo ions gives rise to the peaks near 28° in Figure 3.S4.

For W concentrations below 25%, the $Bi_2Mo_{3-y}W_yO_{12}$ solid solution has the same crystal structure as its $Bi_2Mo_3O_{12}$ parent. In this structure, Mo and W ions are randomly distributed. As a result, the diffraction pattern is very nearly identical to that of $Bi_2Mo_3O_{12}$, as shown in Figure 3.S4.

3.5.6 Raman Spectroscopy

Raman spectra of the as-prepared $Bi_{1-x/3}V_{1-x}Mo_xO_4$ catalysts are presented in Figure 3.S5a. No features are visible above 1100 cm^{-1}. The spectra in Figure 3.S5a show a gradual evolution in vibrational features from vanadate-like to molybdate-like as the composition varies from x=0 to x=1. Figure 3.S5b shows that, as in the XRD data, the spectrum for x=0.45 is clearly distinguishable from a 55/45 mixture of the spectra of x=0 and x=1, providing further evidence that the mixed-composition materials are true solid solutions.

Figure 3.S5c shows a detail of the region from 700 – 1000 cm^{-1}. Raman scattering in this part of the spectrum is characteristic of V=O and Mo=O double bond stretching

modes. The prominent peak at 832 cm^{-1} in $BiVO_4$ (x=0) has been assigned to the symmetric stretching mode of the VO_4^{3-} ion in monoclinic $BiVO_4$ [126]. The analogous peak near 819 cm^{-1} in the 0.15≤x<0.75 samples can reasonably be assigned to the symmetric stretch of VO_4^{3-} ions in these mixed-composition materials. Two effects account for the change in position of this peak with composition. The largest change, from 832 cm^{-1} in x=0 to 823 cm^{-1} in x=0.15, is due to a loss of monoclinic distortion of the crystal lattice, as discussed above. The additional small shifts from 823 cm^{-1} in x=0.15 to 819 cm^{-1} in x=0.30 to 816 cm^{-1} in x=0.45 can be attributed to a slight expansion of the lattice of $Bi_{1-x/3}V_{1-x}Mo_xO_4$ with increasing proportions of larger molybdate in place of smaller vanadate. A similar effect is seen in lanthanoid vanadates: the position of the VO_4^{3-} symmetric stretch varies systematically with the size of the lanthanoid cation [127].

The growth in intensity of a peak near 877 cm^{-1} from nonexistent in x=0 to roughly half the size of the peak near 820 cm^{-1} in x=0.45 suggests that the former can be attributed to the symmetric stretch of the MoO_4^{2-} ion. For x=0.60 and x=0.75, at least four peaks can be distinguished, at 819, 859, 891, and 919 cm^{-1}, suggesting that ordering of cation vacancies gives rise to several distinguishable populations of vanadate and molybdate ions. This tendency reaches its culmination in the x=0.90 and x=1.00 materials, in which five peaks can be clearly distinguished at 817, 841, 859, 902, and 926 cm^{-1} (a sixth peak, at 958 cm^{-1}, is visible in Figure 3.S5a but not 3.S5b). The appearance of six Mo-O stretches is consistent with the presence of six crystallographically distinguishable Mo=O double bonds in the $Bi_2Mo_3O_{12}$ crystal structure.

The Raman spectra of $Bi_3FeMo_2O_{12}$ and $Bi_2Mo_{2.5}W_{0.5}O_{12}$ are provided in Figure 3.S6. The spectra of $Bi_2Mo_3O_{12}$ and $Bi_2W_3O_{12}$ are also provided for comparison. The prominent peak at 870 cm^{-1} in the spectrum of $Bi_3FeMo_2O_{12}$ can be assigned to the symmetric stretching mode of tetrahedral MoO_4^{2-} ions. This assignment is consistent with that made for the peaks at 877 cm^{-1} in Figure 3.S5. The spectrum for $Bi_2Mo_{2.5}W_{0.5}O_{12}$ in Figure 3.S6 exhibits peak positions and intensities nearly identical to those of $Bi_2Mo_3O_{12}$, but notably different from those of $Bi_2W_3O_{12}$. This result supports the conclusion that for y values at least as large as 0.5, the crystal structure of $Bi_2Mo_{3-y}W_yO_{12}$ solid solutions does not differ from that of the y = 0 endmember.

3.5.7 Diffuse Reflectance UV-Visible-Near IR Spectroscopy

As shown in Figure 3.S7, the diffuse reflectance UV-Vis spectrum of a physical mixture of bismuth vanadate and bismuth molybdate exhibits two separate absorption edges. This result contrasts with the spectra of bismuth vanadate-bismuth molybdate solid solutions, which show only a single absorption edge at a position dependent upon the relative proportions of vanadate and molybdate ions present in the solid solution.

When semiconductors are heated, their absorption edges typically broaden and shift to lower energies. Both changes arise primarily from coupling between electronic and vibrational excitations: higher temperatures lead to greater populations of vibrationally excited sub-states of the electronic ground state. Since these vibrationally excited sub-states are closer in energy to the electronic excited state, less energy is

required to excite electrons into the electronic excited state. A second, smaller change in the band gap also arises from dilation (usually expansion) of the lattice as the temperature increases. Theory predicts that the relationship between band gap and temperature obeys the relationship

$$E_g(T) = E_g(0) - \frac{\alpha T^2}{T + \beta} \qquad (4)$$

For $T \gg \beta$, equation (4) predicts that the band gap E_g will decrease linearly with temperature.

The diffuse reflectance spectra of $Bi_{0.85}V_{0.55}Mo_{0.45}O_4$ in air at temperatures between 298K – 713K are shown in Figure 3.S8a. The band gaps, extracted using equations (2) and (3), are plotted as a function of temperature in Figure 3.S8b. It is evident that the band gap does indeed decrease linearly with temperature over the range examined. The diffuse reflectance spectra of $BiVO_4$, $Bi_{0.85}V_{0.55}Mo_{0.45}O_4$, $Bi_3FeMo_2O_{12}$, $Bi_2Mo_3O_{12}$, and $Bi_2Mo_{2.5}W_{0.5}O_{12}$ under flowing oxygen at 673 K are presented in Figure 3.S9.

Exposure of bismuth molybdates heated to 673K in a non-reducing atmosphere to reducing conditions results in a time-dependent increase in absorbance at energies below the edge. This effect is illustrated for $Bi_2Mo_3O_{12}$ in Figure 3.S10. The increase in absorbance of the catalyst at energies below the absorption edge is indicative of reduction of the catalyst.

3.5.8 Propene Activation on BiVO₄

Previously [73,74], we have developed a mechanism for the oxidation of propene to acrolein on the $Bi_2Mo_3O_{12}(010)$ surface. We found that the initial, rate-determining activation of a methyl C-H bond on propene occurred at a Mo=O site on the catalyst surface. As shown in Figure 3.S11, the reaction path for C-H bond activation begins from an initial state involving propene physisorbed above the active site. It proceeds through a transition state involving concurrent C-H bond breakage, O-H bond formation, rehybridization of a Mo=O double bond to a Mo–O single bond, and transfer of one electron to the catalyst. A crossing between singlet and triplet spin potential energy surfaces, enabled by spin-orbit coupling, also occurs at the transition state. As discussed in greater detail in the reference [126], contributions from spin-orbit coupling reduce the maximum energy along the reaction path relative to the singlet-triplet crossing by 4.6 kcal/mol. The final state for C-H bond activation comprises an allyl radical physisorbed above the active site, which now consists of a hydroxyl group attached to a molybdenum center bearing a formal oxidation state of +5.

Although the mechanism for C-H bond activation on the surface of substituted molybdates has not been investigated via density functional theory, it is reasonable to propose that active sites similar to those identified for $Bi_2Mo_3O_{12}$ exist also on the surfaces of substituted bismuth molybdates. However, the $BiVO_4$ end-member of the $Bi_{1-x/3}V_{1-x}Mo_xO_4$ solid solution contains no molybdenum, and therefore no Mo=O active

sites. Since this phase is nevertheless active for propene oxidation, an examination of the mechanism for C-H bond activation over $BiVO_4$ becomes necessary. We report here the results of such an examination.

In our previous examination of propene oxidation on $Bi_2Mo_3O_{12}$, we examined several potential active sites on the (010) surface. The choice of this surface was motivated by the experimental observation that the (010) surface is the most abundant surface exposed by crystals of $Bi_2Mo_3O_{12}$ [73,74]. Comparison of the crystal structures of $BiVO_4$ and $Bi_2Mo_3O_{12}$ reveals that the (001) surface of $BiVO_4$ most closely corresponds to the (010) surface of $Bi_2Mo_3O_{12}$. Experimentally, it has been observed that $BiVO_4$ and $Bi_{1-/x3}V_{1-x}Mo_xO_4$ crystals are generally orthorhombic in shape, terminated by (100), (010), and (001) surfaces. A typical image of such crystals is presented in Figure 3.S12, which was collected in the preparation of reference [128] (see that reference for details). Given this observation, density functional theory was used to investigate the mechanism for C-H bond activation on the $BiVO_4(100)$ and $BiVO_4(001)$ surfaces. The $BiVO_4(100)$ and $BiVO_4(010)$ surfaces are crystallographically identical, so separate investigation of $BiVO_4(010)$ was not required.

The $BiVO_4$ (100) and (001) surfaces are illustrated in Figure 3.S13. Since the active site for C-H activation on $Bi_2Mo_3O_{12}$ involves a Mo=O double bond, it is reasonable to anticipate that the active site for C-H bond activation on $BiVO_4$ will involve a V=O double bond. The (001) surface exposes only a single type of lattice oxygen site comprised of an oxygen atom linked by single bonds to neighboring Bi and V atoms. The lack of V=O bond character on oxygen sites on the (001) surface suggests that sites on this surface are not likely to be involved in C-H bond activation. Consistent with this expectation, no transition state for C-H bond activation on the (001) surface could be located with an activation energy less than 2 eV ≈ 50 kcal/mol, far higher than the experimentally observed barrier of 16 kcal/mol.

In addition to sites with V-O single bond character, the (100) surface also contains sites with V=O double bond character. The reaction path for C-H bond activation at V=O sites on $BiVO_4(100)$ is presented in Figure 3.S14.

The reaction begins from an initial state comprised of propene physisorbed over the active site. At the transition state, the C-H bond length has increased from 1.10 Å to 1.52 Å, while the O-H distance of 1.19 Å is still significantly stretched from the 0.98 Å O-H bond distance found in the final state. These bond distances are consistent with abstraction of H from C by vanadyl O occurring in the transition state. These distances may be compared with the C-H bond distance of 1.60 Å and the O-H bond distance of 1.05 Å in the transition state for propene activation on Mo=O active sites presented in Figure 3.S11. The 1.60 Å V-O distance in the initial state is typical of a vanadyl V=O double bond, while the 1.74 Å V-O distance in the final state is indicative of a V-O single bond. This elongation is accompanied by a singlet-triplet transition in which the character of the V-O bond changes from V=O -like to •V—O• -like, again analogous to the singlet-triplet crossing and rehybridization from Mo=O to •Mo—O• character which occurs at the transition state for propene activation over bismuth molybdate. The intrinsic reaction barrier calculated for C-H bond activation at V=O sites on $BiVO_4$ (100) is 33.0 kcal/mol, essentially identical to the 32.3 kcal/mol barrier calculated for the Mo=O active sites on $Bi_2Mo_3O_{12}$ (010). The close similarity in the propene activation mechanisms on $BiVO_4$

and $Bi_2Mo_3O_{12}$ obtained within DFT supports the conclusion that propene activation proceeds through the same mechanism on both catalysts.

It should be stressed that the calculations reported here are meant only to capture the qualitative features of the propene activation mechanism at V=O sites on $BiVO_4$. In the absence of detailed experimental characterization of the structure and distribution of sites present on all of the experimentally relevant facets of $BiVO_4$, and exhaustive examination of each of these sites within density functional theory, it is not possible to draw definitive conclusions about the identity of the active site(s) at which $BiVO_4$ activates C-H bonds. Previous investigation has shown that even on the (010) surface of $Bi_2Mo_3O_{12}$, multiple potential active sites exist, with calculated activation barriers varying widely between sites. Qualitatively, however, the same mechanistic features were observed on all $Bi_2Mo_3O_{12}$ (010) sites: each transition state involved simultaneous C-H bond cleavage, O-H bond formation, and M=O to •M—O• bond rehybridization (with M = Mo). The present investigation demonstrates that these same qualitative features occur also in propene activation on $BiVO_4$ (with M = V), consistent with experimental observations which also suggest similar mechanisms occurring on both $BiVO_4$ and $Bi_2Mo_3O_{12}$ (as discussed in the main text). Thus, while experimental evidence suggests that the barrier to C-H activation on $BiVO_4$ should be quantitatively lower than that on $Bi_2Mo_3O_{12}$ (which itself is expected to exhibit a lower barrier than that found using the M06-L functional), the numerical results in Figures 3.S11 and 3.S14 are less important than the bond-breaking and bond-forming processes these figures describe.

3.6 References:

[1] B. Hammer, J.K. Nørskov, *Adv. Catal.* 45 (2000) 71.
[2] A. Ruban, B. Hammer, P. Stoltze, H.L. Skriver, J.K. Nørskov, *J. Molec. Catal.* 115 (1999) 421.
[3] C. Lu, I.C. Lee, R.I. Masel, A. Wieckowski, C. Rice, *J. Phys. Chem. A.* 106 (2002) 3084.
[4] J.R. Kitchin, J.K. Nørskov, M.A. Barteau, J.G. Chen, *J. Chem. Phys.* 120 (2004) 10240.
[5] V. Stamenkovic, B.S. Mun, K.J.J. Mayrhofer, P.N. Ross, N.M. Markovic, J. Rossmeisl, J. Greeley, J.K. Nørskov, *Angew. Chemie.* 118 (2006) 2963.
[6] H. Xin, S. Linic, *J. Chem. Phys.* 132 (2010) 221101.
[7] J. Greeley, I.E.L. Stephens, A.S. Bondarenko, T.P. Johansson, H.A. Hansen, T.F. Jaramillo, J. Rossmeisl, I. Chorkendorff, J.K. Nørskov, *Nature Chem.* 1 (2009) 552.
[8] J. Greeley, M. Mavrikakis, *Nature Materials,* 3 (2004) 810.
[9] C.-F. Huo, Y.-W. Li, J. Wang, H. Jiao, *J. Am. Chem. Soc.* 131 (2009) 14713.
[10] S. Albonetti, F. Cavani, F. Trifirò, *Cat. Rev.-Sci. Eng.* 38 (1996) 413.
[11] S. Albonetti, F. Cavani, F. Trifirò, P. Venturoli, G. Calestani, M. López Granados, J.L.G. Fierro, *J. Catal.* 160 (1996) 52.
[12] M.A. Bañares, *Catal. Today* 51 (1999) 319.
[13] B.K. Hodnet,. *Cat Rev.: Sci. Tech.* 27 (1985) 373.
[14] R.K. Grasselli, *Top. Catal.* 14 (2001) 93.
[15] W.C. Vining, A. Goodrow, J. Strunk, A.T. Bell, *J. Catal.* 270 (2010) 163.

[16] W. Zhang, A. Desikan, S.T. Oyama, *J. Phys. Chem.* 99 (1995) 11468.

[17] V. Nikolov, D. Klissurski, A. Anastasov, *Cat Rev.: Sci. Eng.* 33 (1991) 319.

[18] Z. Liu, F. Peng, X. Liu, *Adv. Mater. Res.* 119 (2012) 550.

[19] R.M. Heck, *Catal. Today* 53 (1999) 519.

[20] M. Kang, E.D. Park, J.M. Kim, J.E. Yie, *App. Cat A* 327 (2007) 261.

[21] K.-T. Li, M.-Y. Huang, W.-D. Cheng, *Ind. Eng. Chem. Res.* 35 (1996) 621.

[22] J.M. Peacock, A.J. Parker, P.G. Ashmore, J.A. Hockey, *J. Catal.* 15 (1969) 398.

[23] G.W. Keulks, Z. Yu, L.D. Krenzke, *J. Catal.* 84 (1983) 38.

[24] M. Baca, A. Pigamo, J.L. Dubois, J.M.M. Millet, *Top. Catal.* 23 (2003) 39.

[25] A. Bielański, M. Najbar, *App. Cat. A* 157(1997) 223.

[26] N. Burriesci, F. Garbassi, M. Petrera, G. Petrini, *J. Chem. Soc., Faraday Trans 1,* 78 (1982) 817.

[27] A.P. Vieira Soares, M. Farinha Portela, A. Kiennemann, *Cat. Rev.; Sci. Eng.* 47 (2005) 125.

[28] J.M. López Nieto, *Top. Catal.* 41 (2006) 3-15.

[29] I.E. Wachs, K. Routray, *ACS Catal.* 2 (2012) 1235.

[30] C.T. Campbell, J. Sauer, *Chem. Rev.* 113 (2013) 3859.

[31] C.T. Campbell, J.R.V. Sellers, *Chem. Rev.* 113 (2013) 4106.

[32] L.J. Burcham, L.E. Briand, I.E. Wachs, *Langmuir* 17 (2001) 6164.

[33] A. Goodrow, A.T. Bell, *J. Phys Chem. C* 112 (2008) 13204.

[34] A.W. Sleight, W.J. Linn, *Annals NY Acad. Sci.* (2006) 22.

[35] E.W. McFarland, H. Metiu, *Chem. Rev.* 113 (2013) 4391.

[36] F. Calle-Vallejo, N.G. Inoglu, H.-Y Su, J.I. Martínez, I.C. Man, M.T.M. Koper, J.R. Kitchin, J. Rossmeisl, *Chem. Sci. 4* (2013) 1245.

[37] Y.-L. Lee, J. Kleis, J. Rossmeisl, Y. Shao-Horn, D. Morga, *Energy Environ. Sci.* 4 (2011) 3966.

[38] P. Moriceau; A. Lebouteiller, E. Bordes, P. Courtine, *Phys. Chem. Chem. Phys.* 1 (1991) 5735.

[39] P. Moriceau, B. Tauok, E. Bordes, P. Courtine, *Catal. Today* 61 (2000) 197.

[40] E. Bordes-Richard, *Top. Catal.* 50 (2008) 82.

[41] J.A. Duffy, M.D. Ingram, *J. Am. Chem. Soc.* 24 (1971) 6448.

[42] V. Dimitrov, S. Sakka, *J. Appl. Phys.* 79 (1996) 1736.

[43] A. Lebouteiller, P. Courtine, *J. Solid State Chem.* 137 (1998) 94.

[44] J.A. Duffy, M.D. Ingram, *J. Inorg. Nuc. Chem.* 38 (1976) 1831.

[45] T.A. Pecoraro, R.R. Chiannelli, *J. Catal.* 67 (1981) 430.

[46] H. Toulhoat, P. Raybaud, S. Kasztelan, G. Kresse, J. Hafner. *Catal. Today* 50 (1999) 629.

[47] R.R. Chianelli, G. Berhault, P. Raybaud, S. Kasztelan, J. Hafner, H. Toulhoat, *Appl. Catal. A* 227 (2002) 83.

[48] H. Toulhoat, P. Raybaud. *J. Catal.* 216 (2003) 63.

[49] N. Guernalec, C. Geantet, T. Cseri, M. Vrinat, H. Toulhoat, P. Raybaud, *Dalton Trans.* 39 (2010) 8420.

[50] K. Routray, L.E. Briand, I.E. Wachs, *J. Catal.* 256 (2008) 145.

[51] H. Idriss, E.G. Seebauer, *Catal. Lett.* 66 (2000) 139.

[52] V.L. Rideout, *Solid State Electronics* 18 (1975) 541.

[53] A.J. Nozik, R. Memming, *J. Phys. Chem.* 100 (1996) 13061.

[54] X. Chen, S. Shen, L. Guo, S.S. Mao, *Chem .Rev.* 110 (2010) 6503.

[55] Y. Xu, M.A.A. Schoonen, *Amer. Minerol.* 85 (2000) 543.

[56] K. Fukui, Y. Teijiro, S. Haruo, *J. Chem. Phys.* 20 (1952) 722.

[57] E.V. Anslyn, D.A. Dougherty, *Modern Physical Organic Chemistry*. University Science Books: USA, 2006.

[58] P. Raybaud, J. Hafner, G. Kresse, H. Toulhoat, *J. Phys.: Condens. Matter* 9 (1997) 11107.

[59] C. R. Adams, T. J. Jennings, *J. Catal.* 2 (1963) 63.

[60] C. R. Adams, T. J. Jennings, *J. Catal.* 3 (1964) 549.

[61] C.C. McCain, G. Gough, G.W. Godin, *Nature.* 198 (1963) 989.

[62] W. Ueda, K. Asakawa, C.-L. Chen, Y. Moro-Oka, T. Ikawa, *J. Catal.* 101 (1986) 360.

[63] L.D. Krenzke, G.W. Keulks, *J. Catal.* 61 (1980) 316.

[64] G.W. Keulks, *J. Catal.* 19 (1970) 232.

[65] J.D. Burrington, C.T. Kartisek, R.K. Grasselli, *J. Catal.* 63 (1980) 235.

[66] P. Mars, D.W. van Krevelen, *Chem. Eng. Sci.* 3 (1954) 41.

[67] Z. Zhai, A. Getsoian, A. T. Bell, J. Catal. 308 (2013) 25-36.

[68] H.-W. Wong, M.C. Cesa, J.T. Golab, J.F. Brazdil, W.H. Green, *App. Catal. A* 303 (2006) 177.

[69] Y. Jang, W.A. Goddard, *Top. Catal.* 2001, *15*, 273.

[70] Y. Jang, W.A. Goddard, *J. Phys. Chem. B* 2002, *106*, 5997.

[71] S. Pudar, J. Oxgaard, K. Chenoweth, A.C.T. van Duin, W.A. Goddard. *J. Phys. Chem. C* 111 (2007) 16045.

[72] W.A. Goddard, A.C.T. van Duin, K. Chenoweth, M. J. Cheng, S. Pudar, J. Oxgaard, B. Merinov, T.H. Jang, P. Persson, *Top. Catal.* 38 (2006) 93.

[73] A. Getsoian, V. Shapovalov, A. T. Bell, J. Phys. Chem. C 117 (2013) 7123-7137.

[74] A. Getsoian, A. T. Bell, J. Phys. Chem. C 117(2013), 25562-25578.

[75] G. Kresse, J. Furthmüller, *Comput. Mat. Sci.* 6 (1996) 15.

[76] P.E. Blochl, *Phys. Rev. B* 50 (1994) 17953.

[77] G. Kresse, D. Joubert, *Phys. Rev. B* 59 (1999) 1758.

[78] G. Kresse, J. Furthmüller, *Phys. Rev. B* 54 (1996) 11169.

[79] Y. Zhao, D.G. Truhlar, *J. Chem. Phys.* 125 (2006) 194101.

[80] Y. Zhao, D.G. Truhlar, *Theor. Chem. Account* 120 (2008) 215.

[81] A.W. Sleight, H.-Y. Chen, A. Ferretti, D.E. Cox, *Mat. Res. Bull.* 14 (1979) 1571.

[82] F. Theobald, A. Laarif, A.W. Hewat. *Mat. Res. Bull.* 20 (1985) 653.

[83] W. Jeitschko, A.W. Sleight, W.R. McClellan, J.F. Weiher, *Acta Cryst.* B32 (1976) 1163.

[84] T. Koopmans, *Physica (Elsevier)*1 (1934) 104.

[85] S. Tokunaga, H. Kato, A. Kudo, *Chem. Mater.* 13 (2001) 4624.

[86] A.M. de la Cruz, S.O. Alfaro, *Solid State Sci.* 11 (2009) 829.

[87] H.Y. Fan, *Phys. Rev.* 82 (1951) 900.

[88] Y.P. Varshni, *Physica* 34 (1967) 149.

[89] A. Ayame, K. Uchida, M. Iwataya, M. Miyamoto, *App. Cat. A* 227 (2002) 7.

[90] J.M. Peacock, M.J. Sharp, A.J. Parker, P.G. Ashmore, J.A. Hockey, *J. Catal.* 15 (1969) 379.

[91] K.M. Sancier, T. Dozono, H. Wise, *J. Catal.* 23 (1971) 270.

[92] E. Canadell, M.-H. Whangbo, C. Schelnker, C. Escripe-Filippini, *Inorg. Chem.* 28 (1989) 1466.

[93] Z. Zhu, S. Chowdhary, V.C. Long, J.L. Musfeldt, H.-J. Koo, M.-H. Whangbo, X. Wei, H. Negishi, M. Inoue, J. Sarrao, Z. Fisk, *Phys. Rev. B* 61 (2000) 10057.

[94] *Comprehensive Handbook of Chemical Bond Energies*; Y.R. Luo, Ed.; CRC Press: Boca Raton, FL, 2003, 26.

[95] B. Ruscic, A.F. Wagner, L.B. Barding, R.L. Asher, D. Feller, D.A. Dixon, K.A. Peterson, Y. Song, X. Qian, C.-Y Ng, J. Liu, W. Chen, D.W. Schwenke, *J. Phys. Chem. A* 106 (2002) 2727.

[96] Note that because the electron assigned to the metal center in the •M—O• excited state enters the conduction band and becomes spatially delocalized over the crystal lattice, there is essentially zero exchange coupling between the metal-centered and oxygen-centered electrons in the excited state. The excited state energy is therefore independent of the net spin configuration (singlet or triplet). However, the DFT calculation on the •M—O• state is substantially more straightforward in the spin triplet case, so for convenience, excited states with triplet spin configurations were used in calculation of E_{hyb}.

[97] L. Stradella, G. Vogliolo, *Z. Phys. Chem.* 139 (1983) 99.

[98] M. Křivánek, P. Jírů, J. Strnad, *J. Catal.* 23 (1971) 259.

[99] L.F. Molnar, X. He, B. Wang, K.M. Merz Jr, *J. Chem. Phys.* 131 (2009) 065102.

[100] L. Ferrighi, G.K.H. Madsen, B. Hammer, *Chem. Phys. Lett.* 492 (2010) 183.

[101] G.K.H. Madsen, L. Ferrighi, B. Hammer, *J. Phys. Chem. Lett.* 1 (2010) 515-519.

[102] J. Cao, T. van Mourik, *Chem. Phys. Lett.* 485 (2010) 40.

[103] K. Sayama, A. Nomura, T. Arai, T. Sugita, R. Abe, M. Yanagida, T. Oi, Y. Iwasaki, Y. Abe, H. Sugihara, *J. Phys. Chem. B* 110 (2006) 11352.

[104] A. Walsh, Y. Yan, M.N. Huda, M.M. Al-Jassim, S.-H. Wei, *Chem. Mater.* 21 (2009) 547.

[105] M.W. Stoltzfus, P.M. Woodward, R. Seshadri, J.-H. Klepeis, B. Bursten, *Inorg. Chem.* 46 (2007) 3839.

[106] D.J. Payne, M.D.M. Robinson, R.G. Egdell, A. Walsh, J. McNulty, K.E. Smith, L.F.J. Piper, *App. Phys. Lett.* 98 (2011) 212110.

[107] Z. Zhao, Z. Li, Z. Zou, *Phys. Chem. Chem. Phys.* 13 (2011) 4746.

[108] K. Ding, B. Chen, Z. Fang, Y. Zhang, *Theor. Chem. Acc.* 132 (2013) 1352.

[109] W.L. Huang, Q. Zhu, *J. Comput. Chem.* 30 (2008) 183.

[110] D. J. Payne, R.G. Egdell, A. Walsh, G.W. Watson, J. Guo, P.-A. Glans, T. Learmonth, K.E. Smith, *Phys. Rev. Lett.* 96 (2006) 157403.

[111] A. Walsh, W.G. Watson, D.G. Payne, R.G. Egdell, J. Guo, P.-A. Glans, T. Learmonth, K.E. Smith, *Phys. Rev. B* 73 (2006) 235104.

[112] X. Gao, J.L.G. Fierro, I.E. Wachs, *Langmuir* 15 (1999) 3169.

[113] S.L. Cuffini, V.A. Macagno, R.E. Carbonio, A. Melo, E. Trollund, J.L. Gautier, *J. Solid State Chem.* 105 (1993) 161.

[114] F. Magalhaes, F.C. Camilo Moura, J.D. Ardisson, R.M. Lago, *Mater. Res.* 11 (2008) 307.

[115] W.Y. Ching, S-D. Mo, L. Ouyang, I. Tanaka, M. Yoshiya, *Phys. Rev. B*. 61 (2000) 10609.

[116] S.P. Ghorpade, V.S. Darshane, S.G. Dixit, *App. Cat. A* 166 (1998) 135.

[117] M.H. Harunsani, F.E. Oropeza, R.G. Palgrave, R.G. Egdell, *Chem. Mater.* 22 (2010) *22*, 1551.

[118] M.R. Pai, J. Majeed, A.M. Banerjee, A. Arya, S. Bhattacharya, R. Rao, S.R. Bharadwaj, *J. Phys. Chem. C* 116 (2012) 1458.

[119] M.R. Dolgos, A.M. Paraskos, M.W. Stolzfus, S.C. Yarnell, P.M. Woodward, *J. Solid State Chem.* 182 (2009) 1964.

[120] J.R. Winkler, H.B. Gray, Struct. *Bond.* 142 (2012) 17.

[121] M. Newville, *J. Synchrotron Rad.* 8 (2001) 322.

[122] S.E. Wheeler, K.N. Houk, *J. Chem. Theory Comput.* 6 (2010) 395.

[123] J.P. Perdew, K. Burke, M. Ernzerhof, *Phys. Rev. Lett.* 77 (1996) 3865.

[124] V.G. Tyuterev, N. Vast, *Comput. Mater. Sci.* 38 (2006) 350.

[125] A.W. Sleight, K. Aykan, D.B. Rogers, *J. Solid State Chem.* 13 (1975) 231.

[126] F.D. Hardcastle, I.E. Wachs, H. Eckert, D.A. Jefferson, *J. Solid State Chem.* 90 (1991) 194.

[127] N. Deligne, V. Gonze, D. Bayot, M. Devillers, *Eur. J. Inorg. Chem.* (2008) 896.

[128] A. Nell, A. Getsoian, S. Werner, L. Kiwi-Minsker, A.T. Bell, *Langmuir*, 30 (2014) 873.

Figure 3.1 Diffuse reflectance UV-Visible absorption spectra for catalysts with composition $Bi_{1-x/3}V_{1-x}Mo_xO_4$.
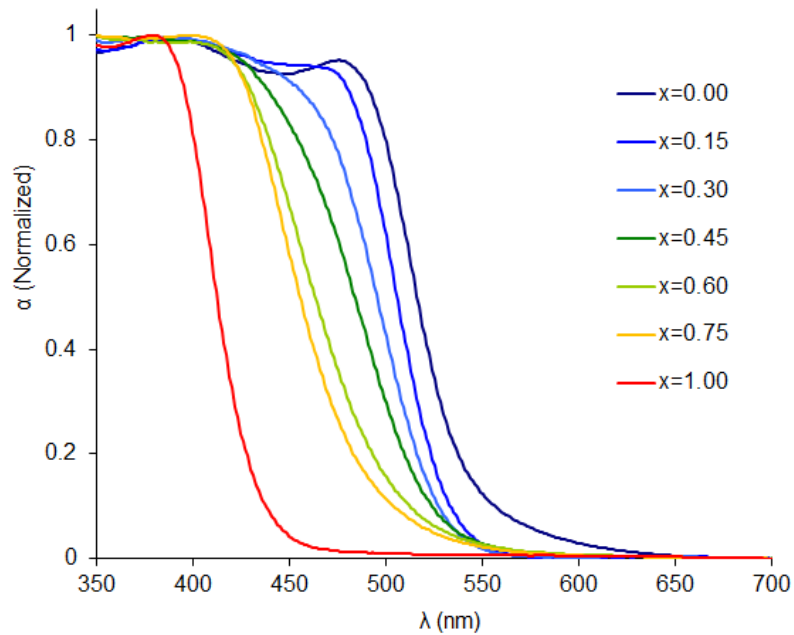
Figure 3.2 Diffuse reflectance UV-Visible absorption spectrum of $Bi_3FeMo_2O_{12}$ and $Bi_2Mo_{2.5}W_{0.5}O_{12}$. For $Bi_3FeMo_2O_{12}$, labels mark the principal LMCT absorption edge and the pre-edge absorption features arising from occupied Fe 3d orbitals.
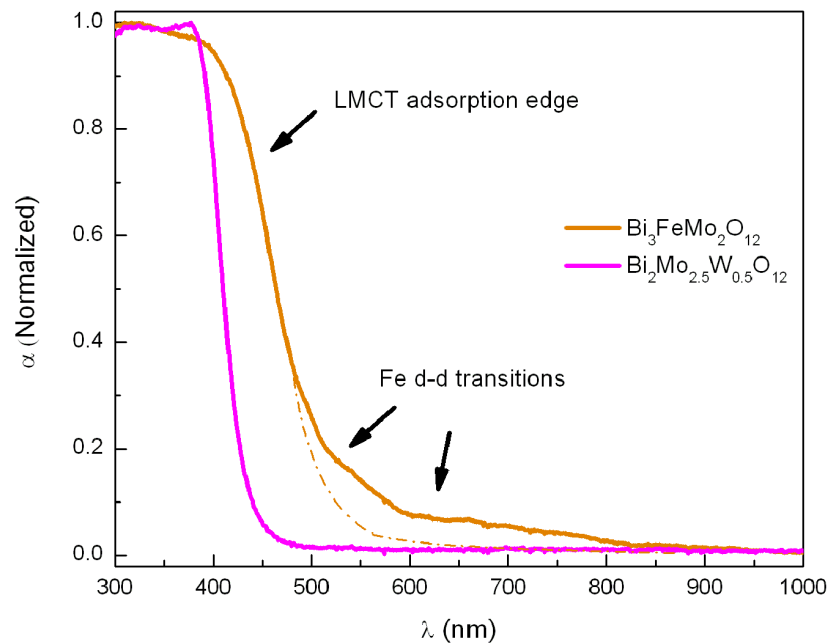
Figure 3.3 (a) Vanadium K edge XANES spectra for $Bi_{0.85}V_{0.55}Mo_{0.45}O_4$ (x=0.45) as a function of time of exposure to propene gas (99%, 100 mL/min) at 713K. The decrease in pre-edge peak height and redshift in edge energy have been magnified to illustrate spectral changes occurring during reduction. (b) Spectra of fully oxidized $Bi_{0.85}V_{0.55}Mo_{0.45}O_4$ and a reference compound, NH_4VO_3, containing tetrahedral V^{5+}. (c) Comparsion of the reduced catalyst to reference compounds containing pseudo-octahedral V^{4+} (VO_2) and V^{3+} (V_2O_3).
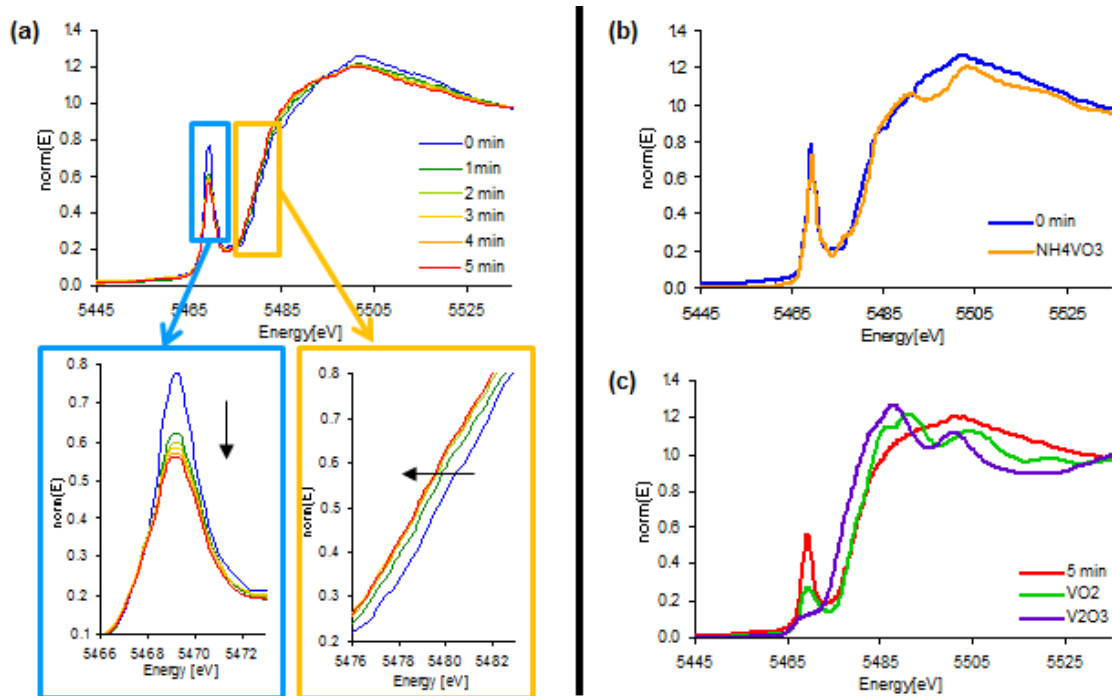
Figure 3.4 (a) Molybdenum K edge XANES spectra of $Bi_{0.85}V_{0.55}Mo_{0.45}O_4$ as a function of time of exposure to propene gas (99%, 100 mL/min) at 713K. (b) Comparison of the oxidized and reduced catalysts to reference compounds containing tetrahedral Mo^{6+} ($CaMoO_4$) and pseudo-octahedral Mo^{4+} (MoO_2).
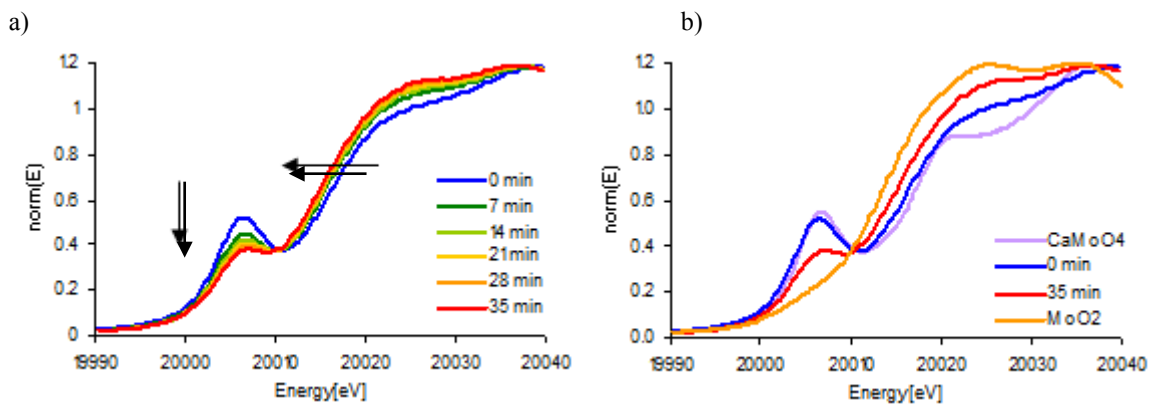
Figure 3.5 Apparent activation energies for oxidation of propene to acrolein over substituted bismuth molybdates.
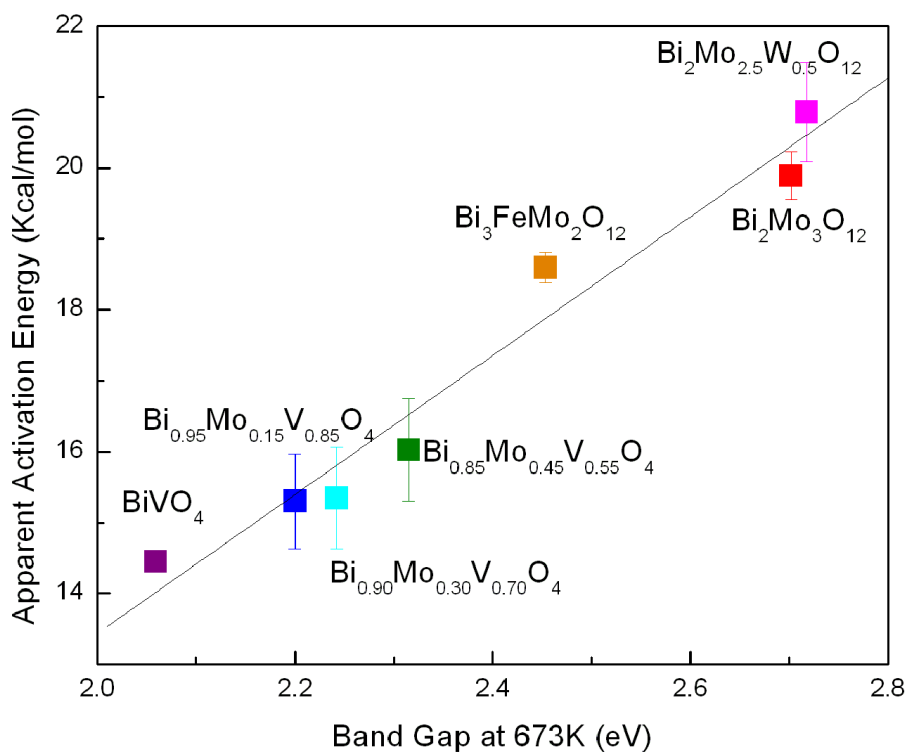
Figure 3.6 Generic mechanism for propene activation involving a catalyst M=O bond.
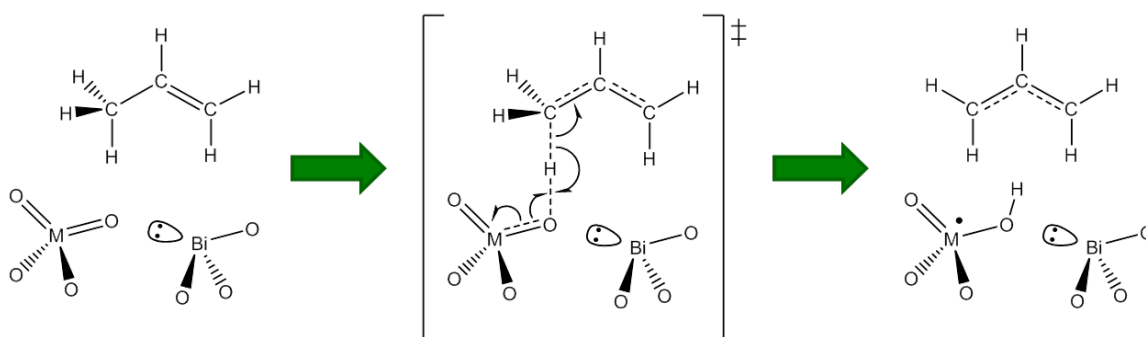
Figure 3.7 Born-Haber cycle decomposition of the transition state energy E_{TS} into contributions from C-H bond breaking E_{C-H}, M=O bond elongation $E_{stretch}$, M=O bond rehybridization E_{hyb}, and O-H bond formation E_{O-H}.
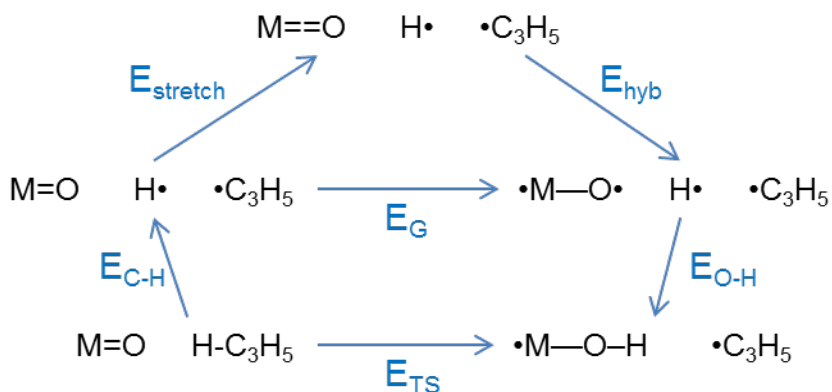
Figure 3.8 From left to right: calculated density of states for $BiVO_4$ (purple), $Bi_7V_5Mo_3O_{12}$ (green), $Bi_3FeMo_2O_{12}$ (orange), $Bi_2Mo_3O_{12}$ (red), and $Bi_2Mo_{2.5}W_{0.5}O_{12}$ (pink).
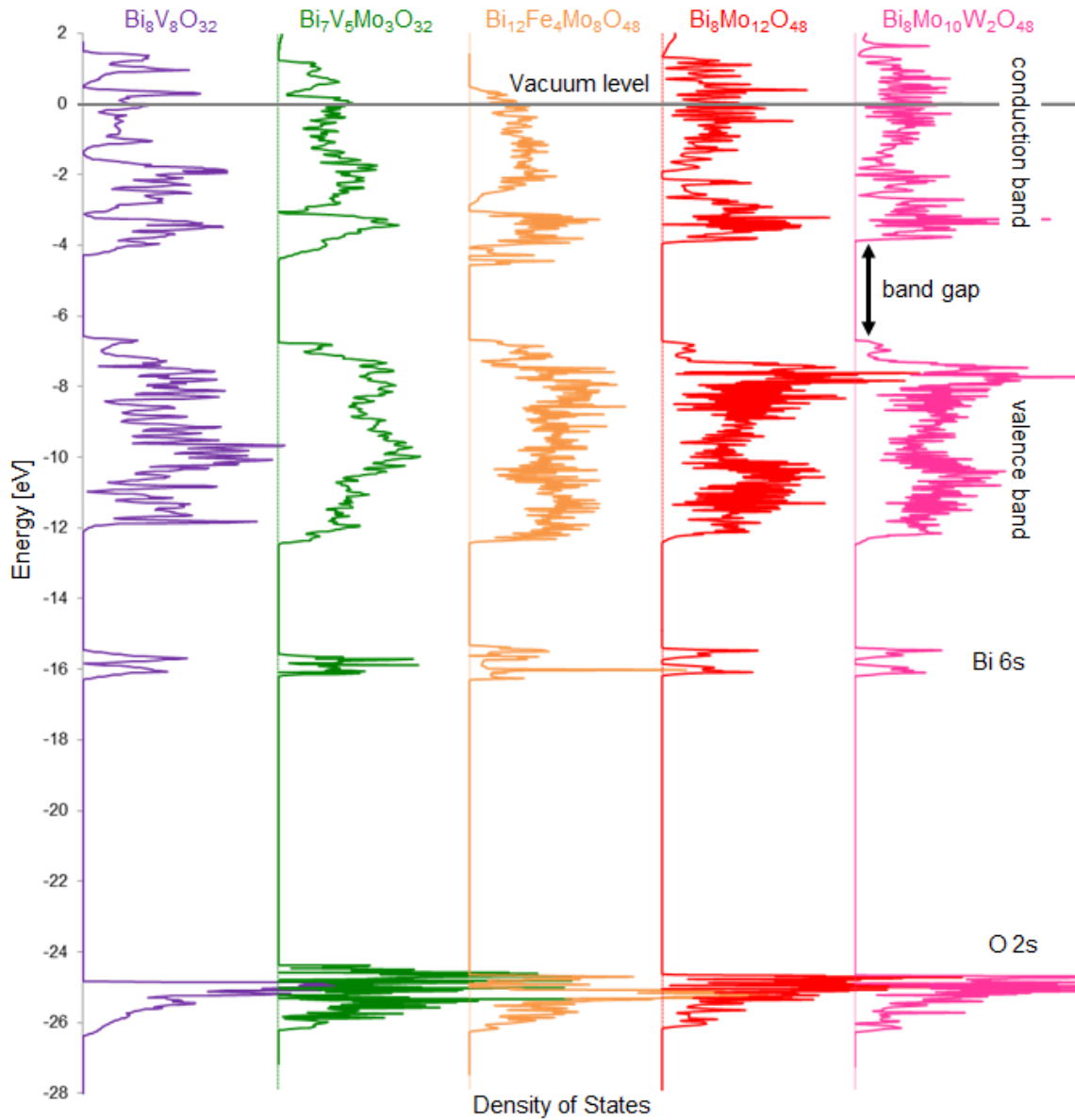
Figure 3.9 Atom-projected density of states for $Bi_7V_5Mo_3O_{32}$. A map of the charge density of the states from -4.5 to -4.0 eV is shown on the right.
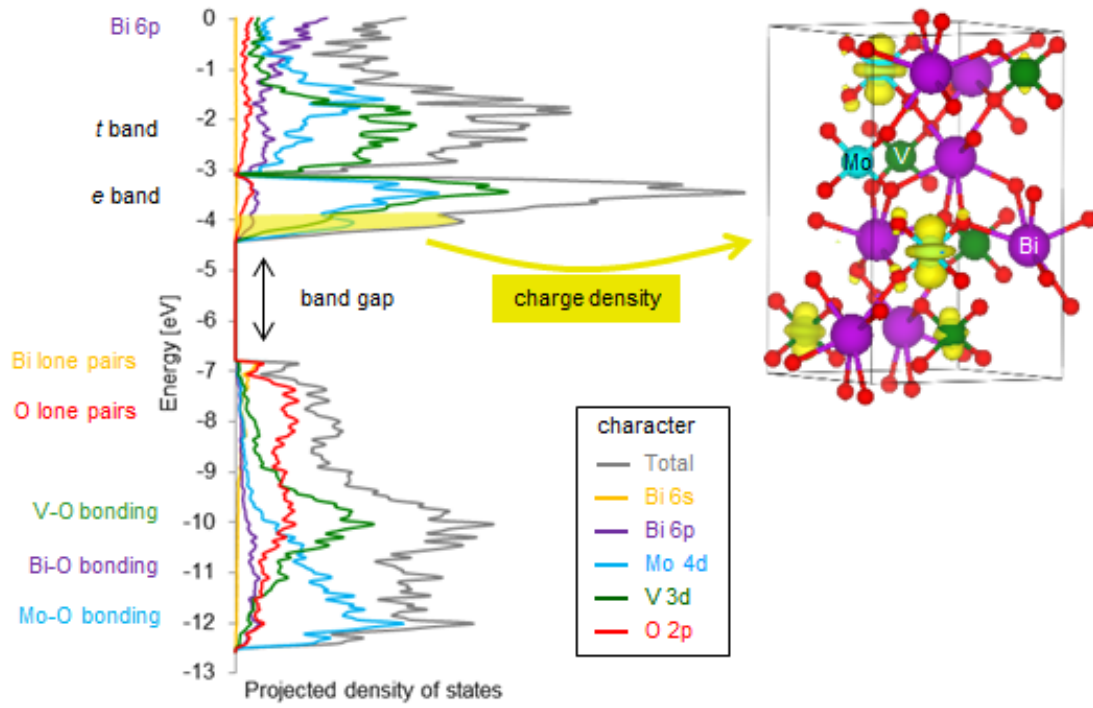
Figure 3.10 Site-projected density of states for $Bi_3FeMo_2O_{12}$. The conduction band states between -2.8 and -4.8 eV are shown in greater detail at center, with charge density maps provided for the mid-gap Fe d_{z^2} and $Fe_{x^2-y^2}$ states and first conduction band state.
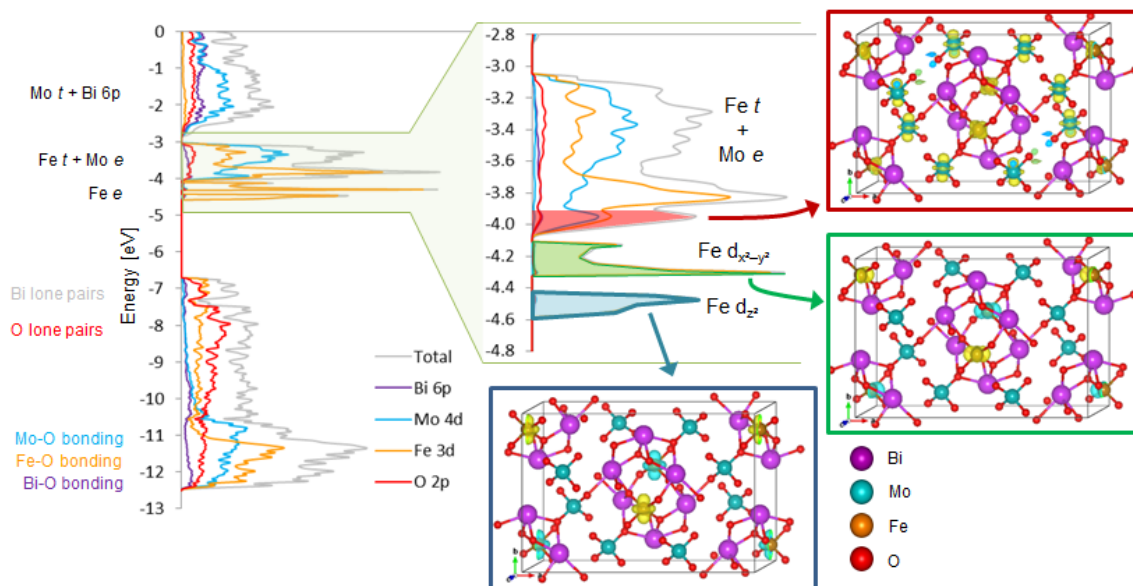
Scheme 3.1 Ligand-to-metal charge transfer excitation.
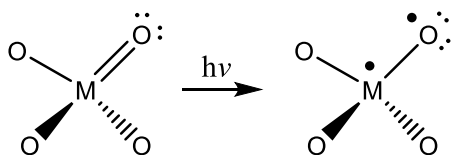
Table 3.1 Rate parameters for propene oxidation to acrolein.

$$rate = k_{app}P_{C3H6}^{m}P_{O2}^{n} = A_{app}\exp\left(-E_{app}/RT\right)P_{C3H6}^{m}P_{O2}^{n}$$

	k_{app}*	A_{app}**	E_{app}***	m	n
$BiVO_4$	1.74	9	14.5	1.0	0.0
$Bi_{0.95}V_{0.85}Mo_{0.15}O_4$	2.36	22	15.3	1.0	0.0
$Bi_{0.90}V_{0.70}Mo_{0.30}O_4$	3.28	30	15.3	1.0	0.0
$Bi_{0.85}V_{0.55}Mo_{0.45}O_4$	3.54	55	16.0	0.9	0.1
$Bi_3FeMo_2O_{12}$	0.36	39	18.6	1.0	0.0
$Bi_2Mo_3O_{12}$	0.67	195	19.9	1.0	0.0
$Bi_2Mo_{2.5}W_{0.5}O_{12}$	0.38	216	20.8	1.0	0.0

* apparent rate constant at 673K, in *10^{-5} mol/(min m^2-cat atm).
** apparent pre-exponential constant in *10^{-4} mol/(min m^2-cat atm).
*** apparent activation energy in kcal/mol

Table 3.2 Band-gap energies (eV) measured at 298K and 673K and calculated.

	E_G (298K)	E_G (673K)	E_G (DFT)
$BiVO_4$	2.34	2.06	2.28
$Bi_{0.950}V_{0.850}Mo_{0.150}O_4$	2.42	2.20	**
$Bi_{0.900}V_{0.700}Mo_{0.300}O_4$	2.43	2.24	**
$Bi_{0.875}V_{0.625}Mo_{0.375}O_4$	*	*	2.38
$Bi_{0.850}V_{0.550}Mo_{0.450}O_4$	2.47	2.32	**
$Bi_3FeMo_2O_{12}$	2.57	2.45	2.64
$Bi_2Mo_3O_{12}$	2.97	2.70	2.80
$Bi_2Mo_{2.5}W_{0.5}O_{12}$	2.99	2.72	2.84

* not measured experimentally. ** not calculated within DFT.

Table 3.3 Measured and calculated band-gap energies (E_G) and calculated values for E_{strech}, E_{hyb}, and E_{OH}.

	$BiVO_4$	$Bi_2Mo_3O_{12}$
E_G from DRUVS at 673K	2.06 eV	2.70 eV
E_G from DFT	2.28 eV	2.80 eV
$E_{stretch}$	20.9 kcal/mol	23.0 kcal/mol
E_{hyb}	30.1 kcal/mol	39.0 kcal/mol
E_{OH}	-115.8 kcal/mol	-117.9 kcal/mol

Table 3.4 Calulcated d-orbital energies.

Orbital	Energy (eV)
W 5d	-4.02
Mo 4d	-4.48
V 3d	-5.02
Fe 3d	-6.66

Table 3.5 Calculated values of band-gap energies and energies of e-band bottom, center, top, and width (eV).

	$BiVO_4$	$Bi_7V_5Mo_3O_{32}$	$Bi_3FeMo_2O_{12}$	$Bi_2Mo_3O_{12}$	$Bi_2Mo_{2.5}W_{0.5}O_{12}$
Band gap	**2.28**	**2.38**	**2.64**	**2.80**	**2.84**
e band bottom	-4.29	-4.42	-4.09	-3.95	-3.88
e band center	-3.64	-3.60	-3.54	-3.30	-3.26
e band top	-3.11	-3.08	-3.07	-2.65	-2.60
e band width	1.18	1.34	1.02	1.30	1.28

Figure 3.S1 Plot of $(\alpha h\nu)^2$ vs. $h\nu$ from the diffuse reflectance spectrum of $BiVO_4$ in air at 673K. The sigmoid fit (red) concurs with the data (blue) for energies below ~ 2.5 eV. Above this energy, additional electronic transitions give rise to further increases in absorption not captured by the sigmoid fit. The calculated band gap energy is E_g = 2.06 eV.
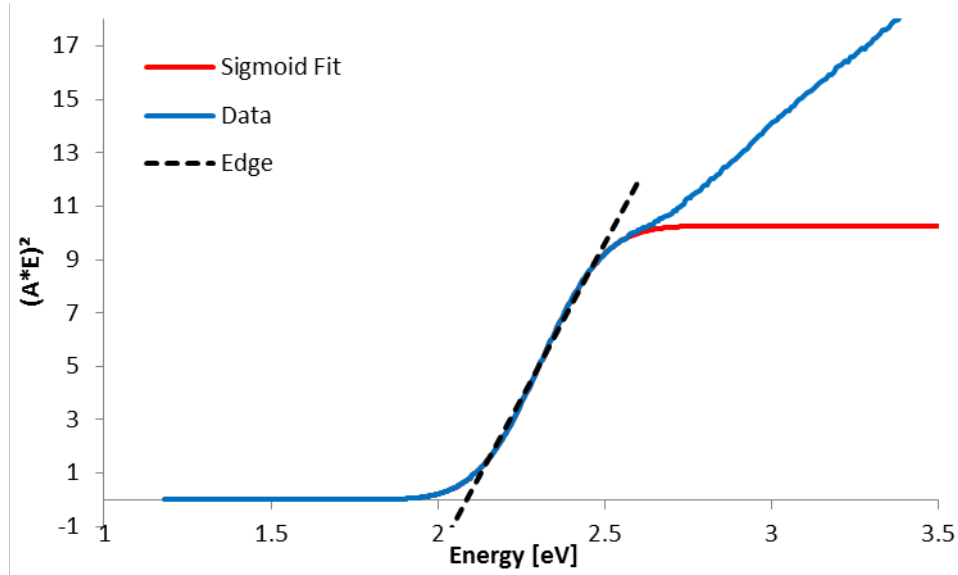
Figure 3. S2 Procedure used to align the calculated densities of states to the vacuum energy reference. Bottom (black): energy levels of orbitals in propene in a 13 Å x 14 Å x 15 Å box. Middle (blue): Density of states calculation for propene adsorbed on a $Bi_8V_8O_{32}$ surface. States identified as having predominantly carbon and hydrogen character are identified in darker blue. The energies of these states were aligned to the propene states below. Top (purple): Density of states in bulk $Bi_4V_4O_{16}$. These states were aligned with the corresponding states in the slab calculation.
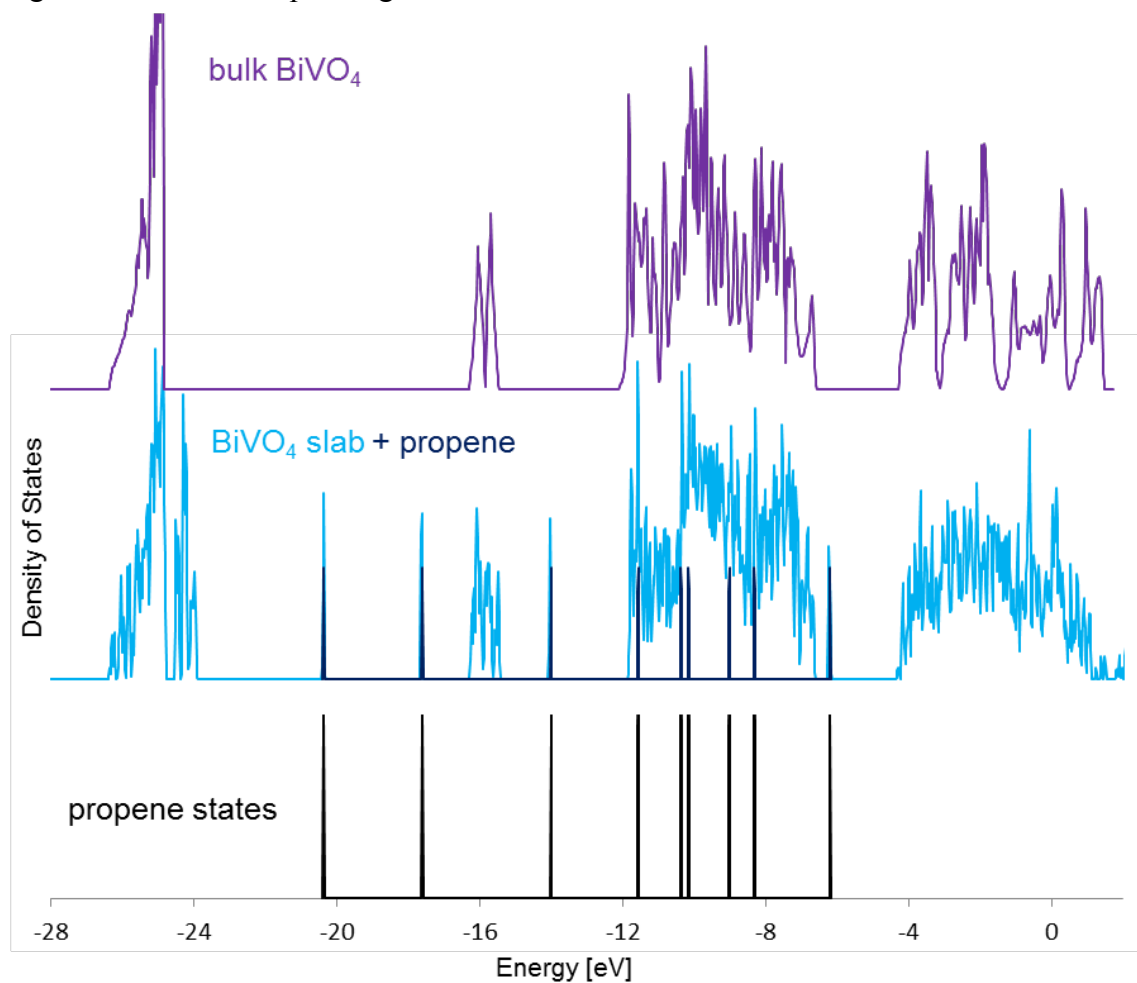
Figure 3.S3

    (i)   Variation in the acrolein production rate at 673 K and $P_{C3H6} = P_{O2} = 0.167$ atm measured as a function of propene conversion.
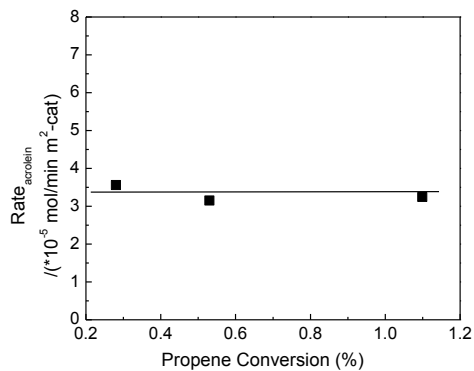
a) $BiVO_4$
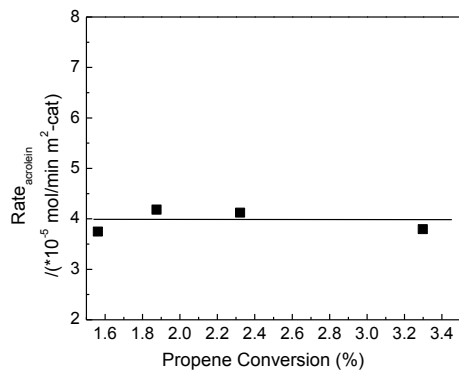
b) $Bi_{0.95}V_{0.85}Mo_{0.15}O_4$
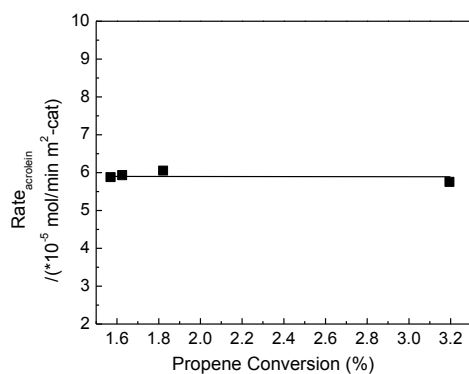
c) $Bi_{0.90}V_{0.70}Mo_{0.30}O_4$
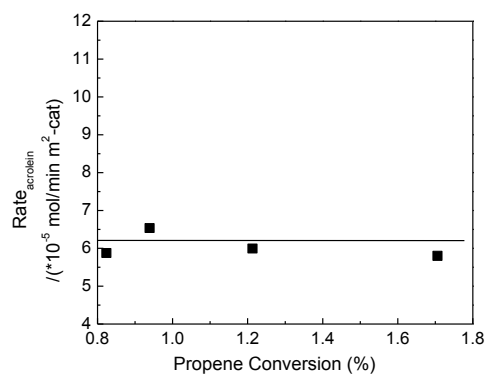
d) $Bi_{0.85}V_{0.55}Mo_{0.45}O_4$
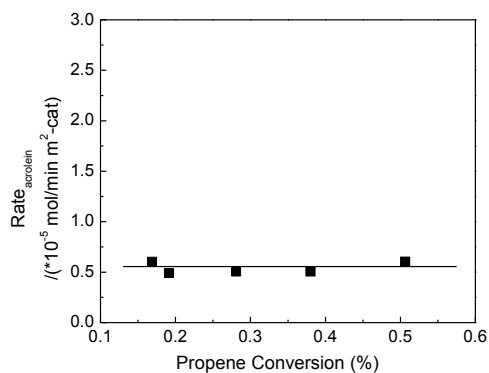
e) $Bi_3FeMo_2O_{12}$
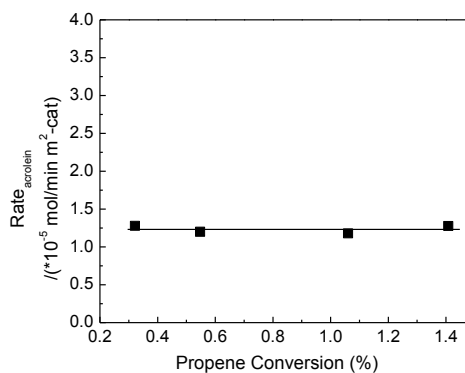
f) $Bi_2Mo_3O_{12}$
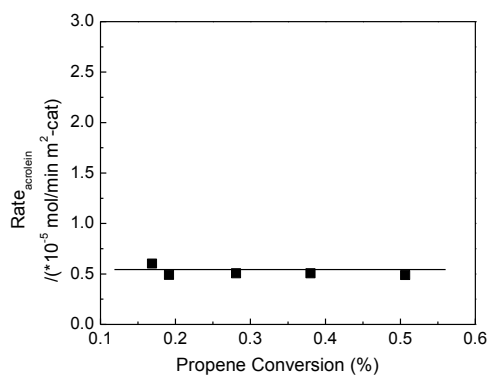
g) $Bi_2Mo_{2.5}W_{0.5}O_{12}$

(ii)   Reaction orders in propene and oxygen measured at 673 K for propene oxidation to acrolein. The partial pressures of propene or oxygen were fixed at 0.067 or 0.167 atm, respectively, while the other one was varied.

a) BiVO₄

y = 1.0222x - 8.7842
R² = 0.9698

y = -0.0529x - 11.401
R² = 0.9662
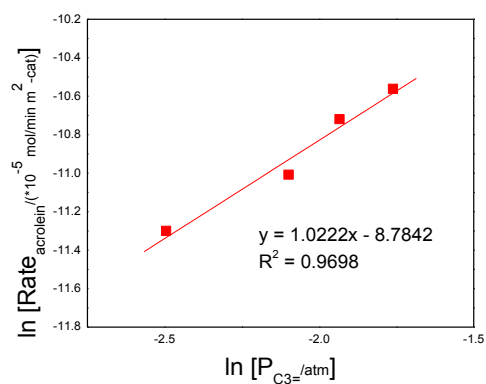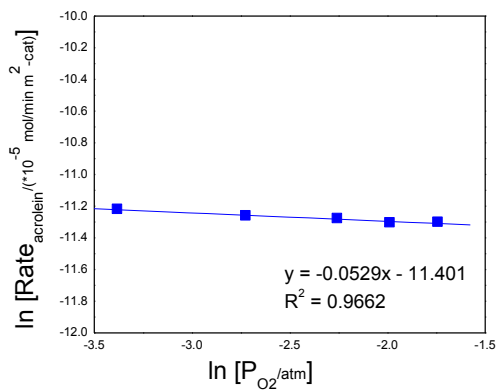
i) Propene Order   ii) Oxygen Order

b) Bi₀.₉₅V₀.₈₅Mo₀.₁₅O₄
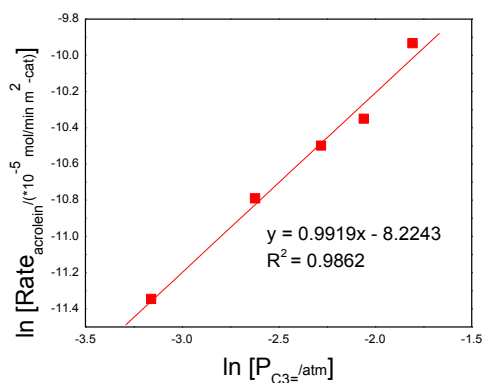
i) Propene Order
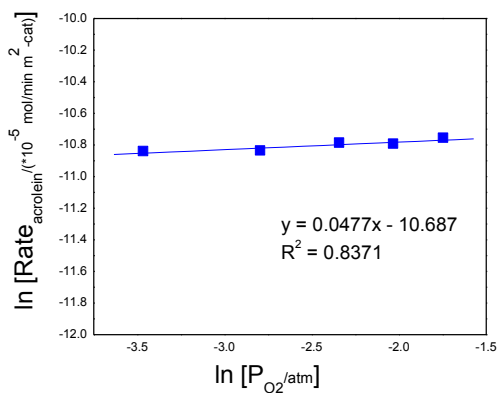
ii) Oxygen Order

c) Bi$_{0.90}$V$_{0.70}$Mo$_{0.30}$O$_4$
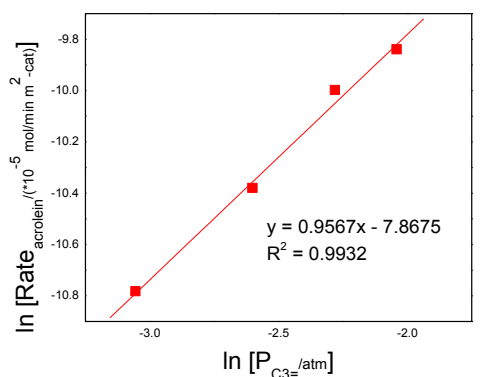
i) Propene Order
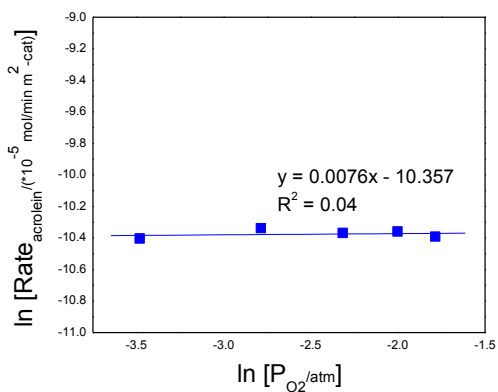
ii) Oxygen Order

d) Bi$_{0.85}$V$_{0.55}$Mo$_{0.45}$O$_4$
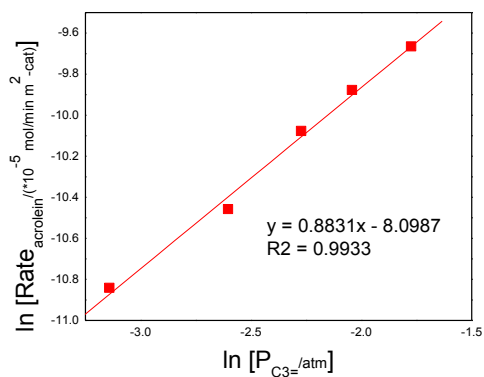
i) Propene Order
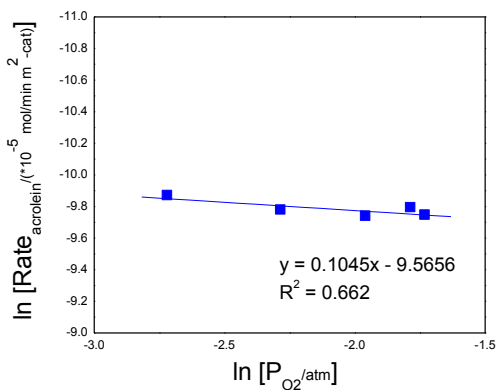
ii) Oxygen Order

e) Bi₃FeMo₂O₁₂
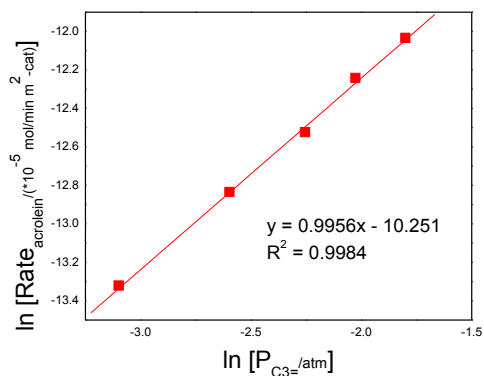
i) Propene Order
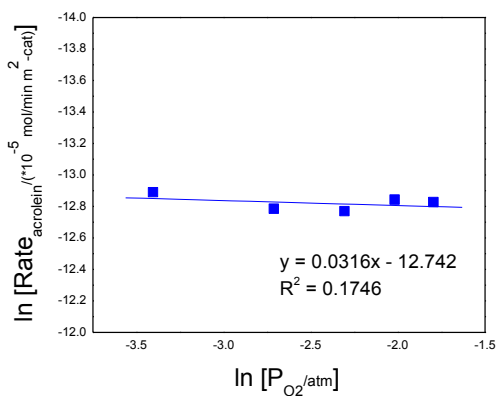
ii) Oxygen Order

f) Bi₂Mo₃O₁₂
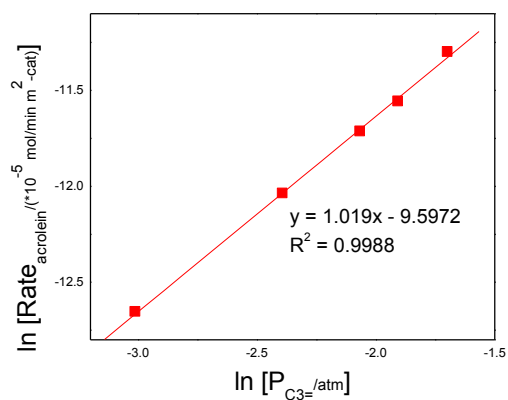
i) Propene Order
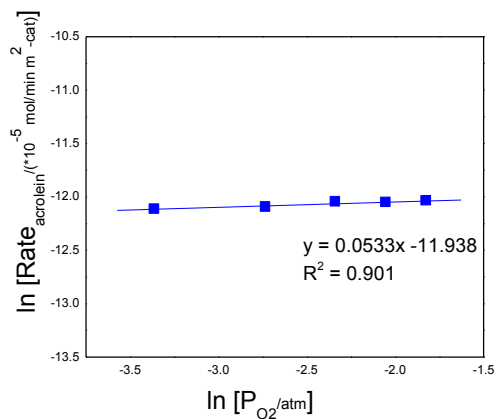
ii) Oxygen Order

g) Bi₂Mo₂.₅W₀.₅O₁₂
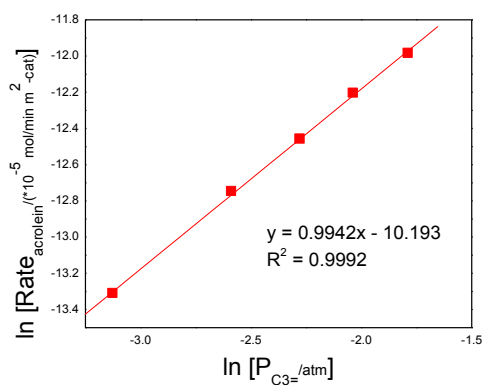
i) Propene Order
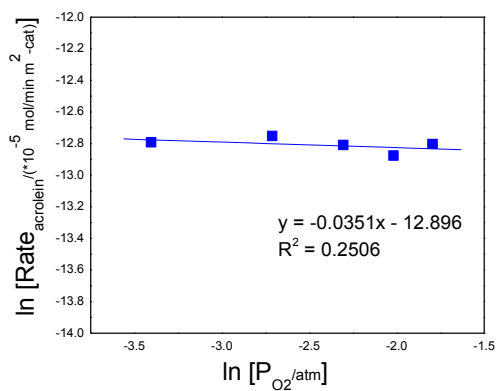
ii) Oxygen Order

Figure 3.S4 X-ray diffraction patterns for $Bi_2Mo_{2.5}W_{0.5}O_{12}$ (top, pink), $Bi_2Mo_3O_{12}$ (red), $BiVO_4$ (purple), and $Bi_3FeMo_2O_{12}$ (orange, bottom).
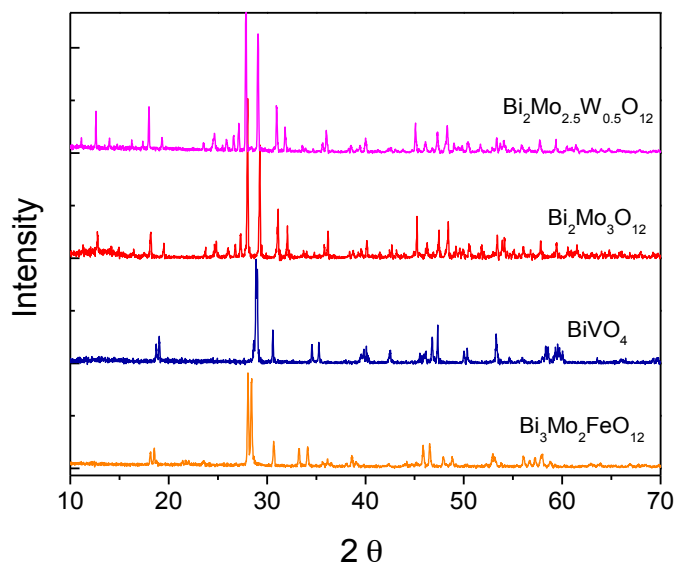
Figure 3.S5 Raman spectra of $Bi_{1-x/3}V_{1-x}Mo_xO_4$ catalysts prepared by citrate complexation. (a) The as-prepared catalysts. (b) Comparsion of the solid solution material with composition x = 0.45 to a physical mixture of $BiVO_4$ and $Bi_2Mo_3O_{12}$ with the same effective composition. (c) Close-up of the region between 800 and 1000 cm$^{-1.}$

(a)

(b)
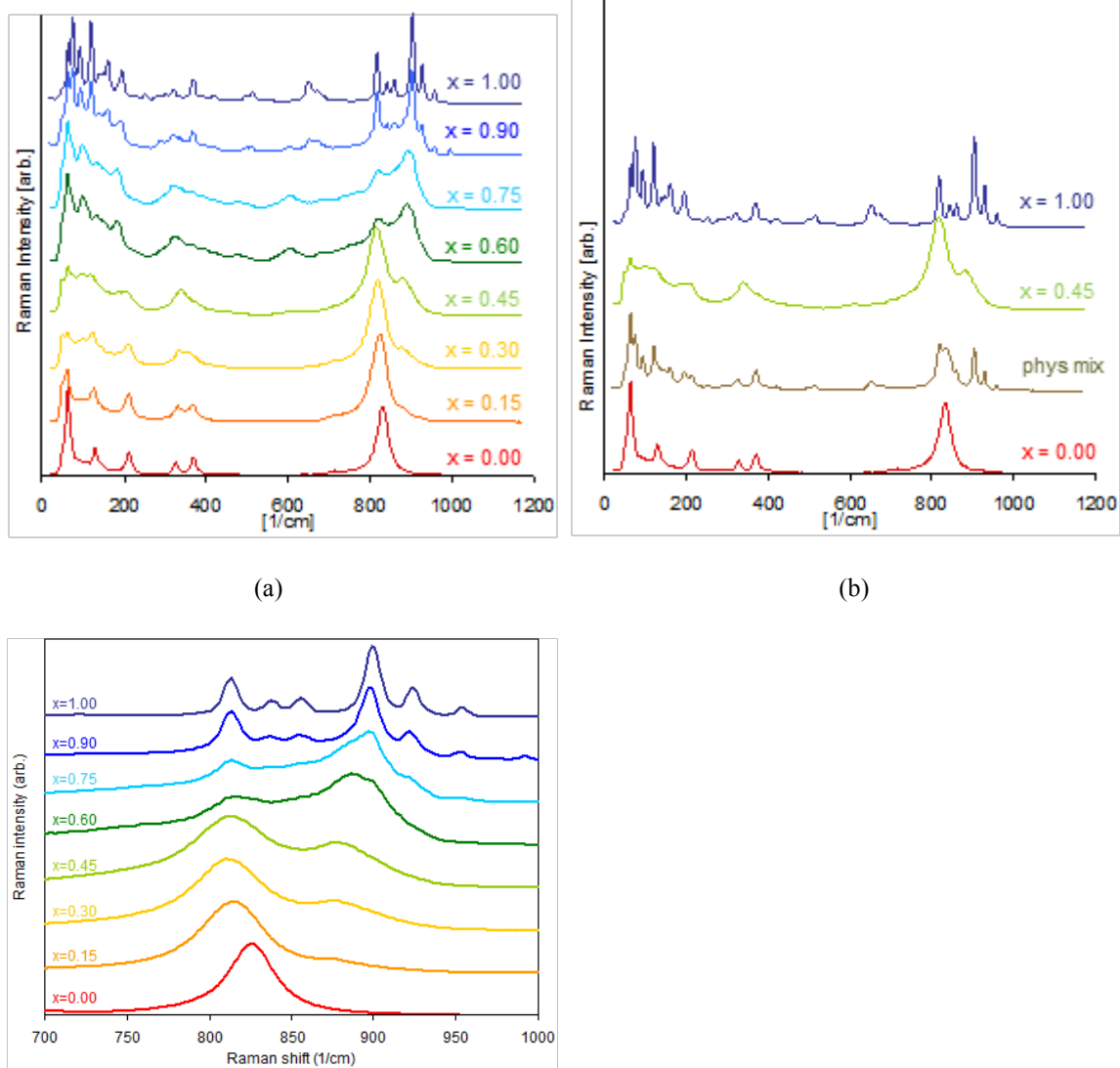
Figure 3.S6 Raman spectra of $Bi_2W_3O_{12}$ (top, navy), $Bi_2Mo_{2.5}W_{0.5}O_{12}$ (pink), $Bi_2Mo_3O_{12}$ (light blue), and $Bi_3FeMo_2O_{12}$ (dark red, bottom).
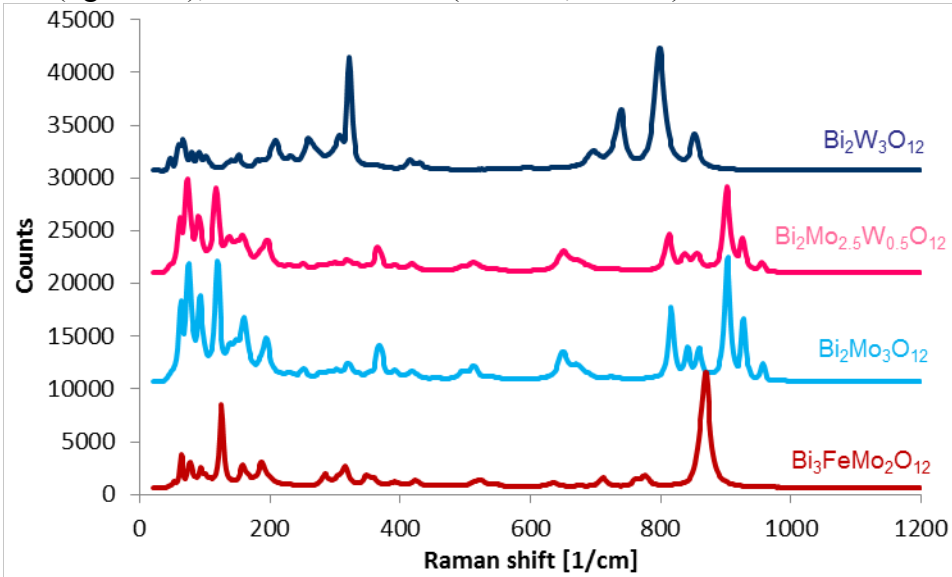
Figure 3.S7 Diffuse reflectance spectra of bismuth vanadate (blue), bismuth molybdate (red), and a physical mixture of the two (gray).
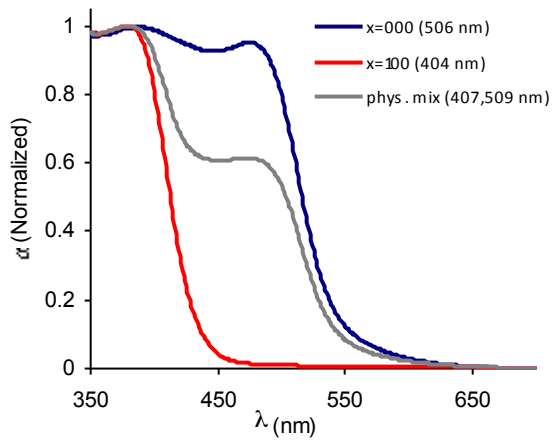
Figure 3.S8 (a) Diffuse reflectance spectra of $Bi_{0.85}V_{0.55}Mo_{0.45}O_4$ at temperatures between 298K – 713K. (b) Band gap of $Bi_{0.85}V_{0.55}Mo_{0.45}O_4$ as a function of temperature.

(a)

(b)
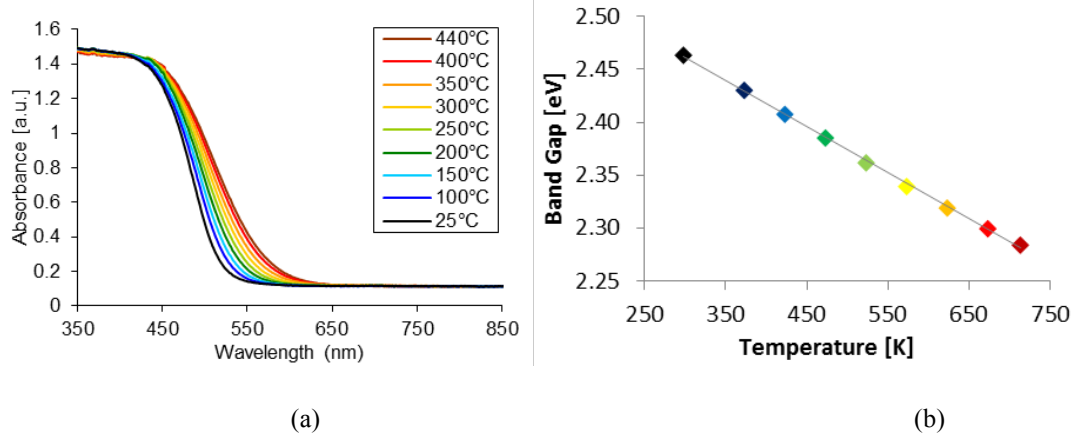
Figure 3.S9 Diffuse reflectance spectra of $BiVO_4$, $Bi_{0.85}V_{0.55}Mo_{0.45}O_4$, $Bi_3FeMo_2O_{12}$, $Bi_2Mo_3O_{12}$, and $Bi_2Mo_{2.5}W_{0.5}O_{12}$ under flowing oxygen at 673K.
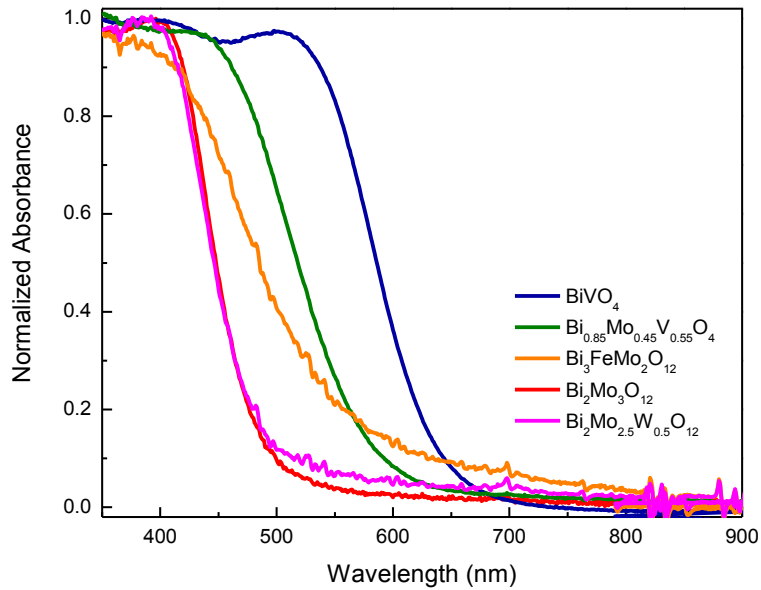
Figure 3.S10 Diffuse reflectance spectrum of $Bi_2Mo_3O_{12}$ at 673K exposed to 100 mL/min of 4% propene in helium. Scans are taken at 3 minute intervals over the course of 15 minutes.
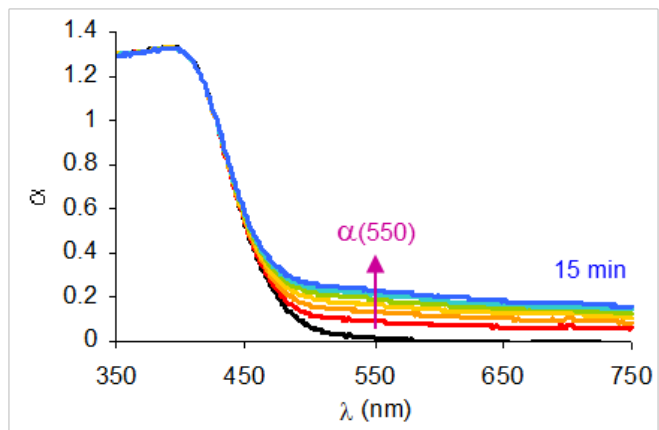
Figure 3.S11 Reaction coordinate diagram for initial C-H bond activation on $Bi_2Mo_3O_{12}$. After inclusion of spin-orbit coupling effects, the energy of the transition state (pictured in black) sits 32.3 kcal/mol above the energy of the initial state (pictured in blue).
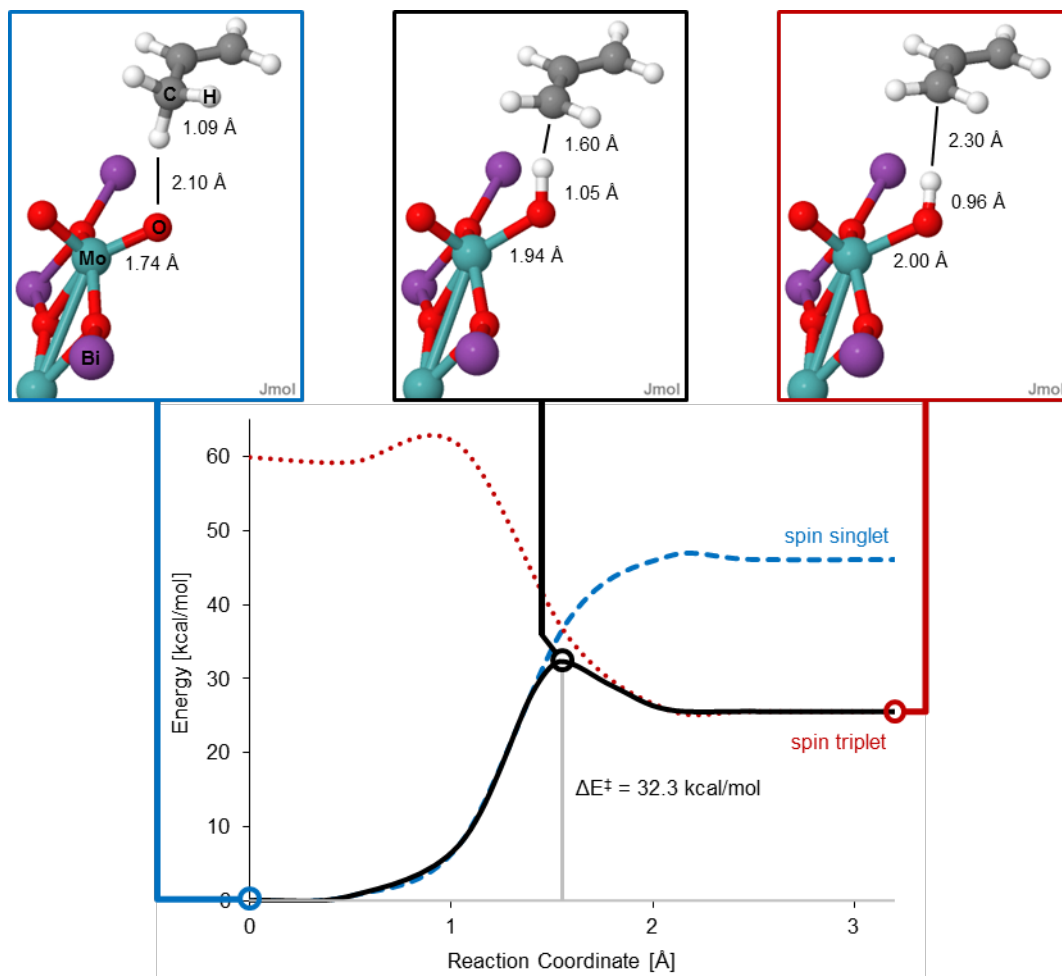
Figure 3.S12 Image of BiVO$_4$ acquired using transmission electron microscopy during the preparation of reference [20]. Edges of three particles have been highlighted in orange to illustrate the orthorhombic (nearly cubic) shape of the particles.
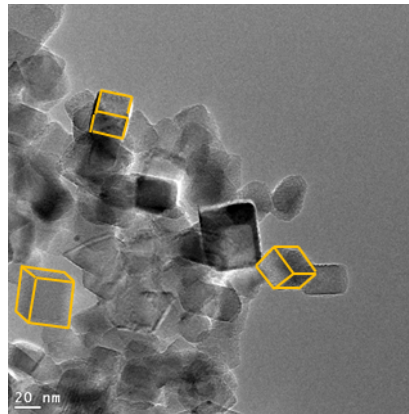
Figure 3.S13 (a) the BiVO$_4$(001) surface contains only lattice oxygen sites with Bi-O-V single bond character. (b) the BiVO$_4$(100) surface contains lattice oxygen sites with V=O double bond character as well as sites with Bi-O-V single bond character.
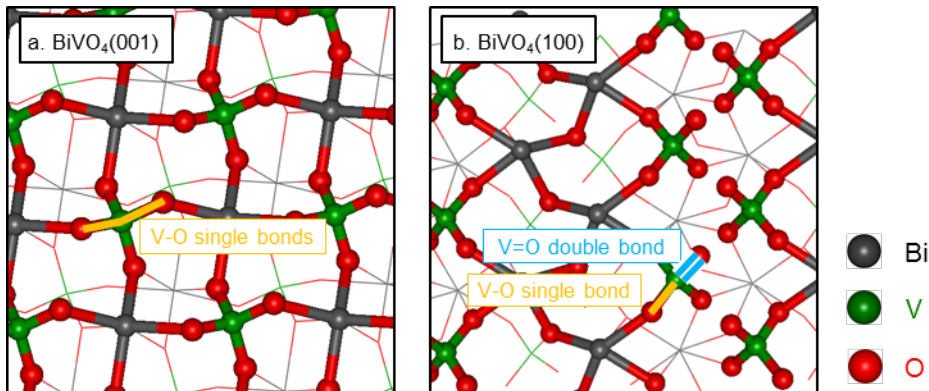
Figure 3.S14 Reaction path for C-H bond activation at a V=O site on the BiVO$_4$(100) surface.
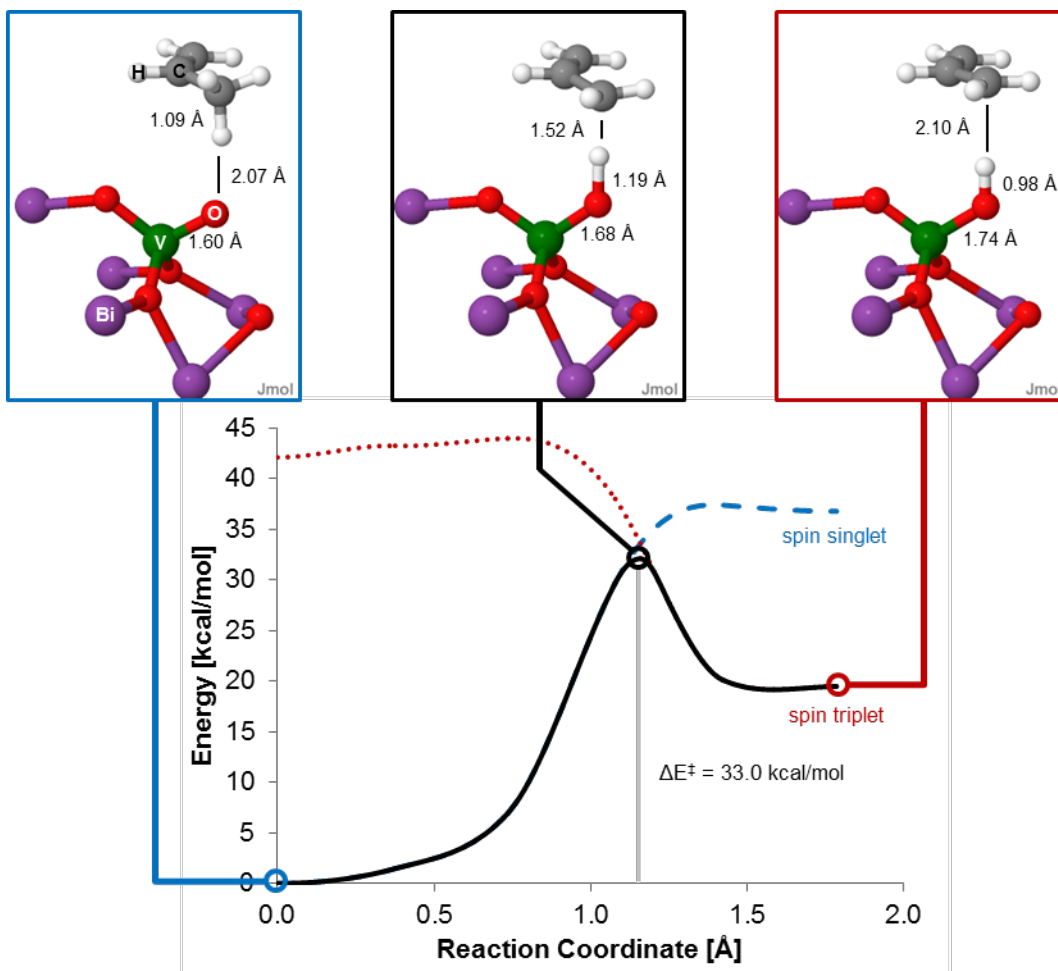
Chapter 4

Effects of Catalyst Crystal Structure on the Oxidation of Propene to Acrolein

Abstract

  Bismuth molybdate is known to be active for the oxidation of propene to acrolein and its activity can be altered by substitution of other elements (e.g., Fe, V, W) into the scheelite phase of α-$Bi_2Mo_3O_{12}$. This work has further revealed that the apparent activation energy for propene formation correlates with the band gap of the catalyst measured at reaction temperature. It is, therefore, of interest to establish to how the crystal structure of the catalyst affects the activation energy. We report here an investigation of propene oxidation conducted over Bi, Mo, V oxides having the aurivillius structure with the composition $Bi_4V_{2-x}Mo_xO_{11+x/2}$ (x = 0-1) and compare them to oxides having the scheelite structure with the composition $Bi_{2-x/3}Mo_xV_{1-x}O_{12}$ (x = 0-1). The aurivillius-phase catalysts again show a correlation between the apparent activation energy and the band gap of the oxide, and the only difference being that for a given band gap, the apparent activation energy for the aurivillius-phase catalysts is 1.5 kcal/mol higher than that for the scheelite-phase catalysts. This difference is attributed to the lower heat of propene adsorption on the aurivillius-phase catalysts. A further finding is that for catalysts with band gaps greater than ~ 2.1 eV, the acrolein selectivity is ~ 75% for the conditions used and independent of the propene conversion. When the band gap falls below ~ 2.1 eV, the intrinsic selectivity to acrolein decreases rapidly and then decreases further with increasing propene conversion. This pattern shows that when the activity of oxygen atoms at the catalyst surface becomes very high, two processes become more rapid - the oxidation of the intermediate from which acrolein is formed and the sequential combustion of acrolein to CO_2.

4.1 Introduction

  The oxidation of propene to acrolein has been widely studied because of the importance of acrolein as a monomer for acrylic polymers [1,2]. The principle catalysts used to promote this reaction are bismuth molybdates in which a part of the molybdenum is substituted by one or more other metals in order to enhance the catalyst activity and selectivity [3-10]. A number of groups have investigated the mechanism of propene oxidation on α-$Bi_2Mo_3O_{12}$ with the aim of understanding the elementary processes leading to acrolein and the influence of added elements on these processes [11-16]. These efforts have led to the following findings. On a fully oxidized catalyst, propene oxidation occurs via a Mars van Krevelen mechanism in which propene adsorbs reversibly and then reacts with an oxygen atom of the catalyst. This rate-limiting step leads to cleavage of one of the C-H bonds of the methyl group of the adsorbed propene and results in the formation of an adsorbed OH group and a loosely adsorbed allyl radical that is rapidly

stabilized as an adsorbed vinylalkoxide. Loss of an H atom from the later species leads to the formation of acrolein. Consistent with this mechanism and with the observed kinetics, the rate of acrolein formation is first order in the partial pressure of propene and zero order in the partial pressure of oxygen.

Several investigations have shown that the apparent activation energy for propene oxidation to acrolein can be reduced by the replacement of Mo by Fe or V for catalysts maintaining a scheelite structure over fully oxidized catalyst [17-21]. We have reported in previous sections that the activation barrier for the rate-limiting step is well described by the band-gap of such catalysts, the activation energy decreasing with the band gap [22]. What is not known, though, is how the correlation might be affected by the crystal structure of the catalyst. Therefore, the present study was undertaken in order to extend the exploration of the relationship between catalyst composition/structure and catalyst activity/selectivity to a different crystal structure.

The oxide phase chosen for study is the aurivillius structure [23]. This phase has the general stoichiometry of $Bi_2A_{n-1}B_nO_{3n+3}$ and consists of n perovskite-like layers ($A_{n-1}B_nO_{3n+1}$ sandwiched between bismuth-oxygen sheets $(Bi_2O_2)^{2+}$ [23]. The simplest crystal structure has n = 1 and corresponds to Bi_2MoO_6 (the gamma phase of the bismuth molybdate) or Bi_2WO_6. $Bi_4V_2O_{11}$ also corresponds to the first member of the family of aurivilius compounds but is oxygen deficient and can be expressed as $(Bi_2O_2)(VO_{3.5}\square_{0.5})$ [24]. Figure 4.1 shows the structure of $Bi_4V_2O_{11}$ and illustrates the $(Bi_2O_2)^{2+}$ layers alternating vanadium oxygen tetrahedra and oxygen-deficient octahedral [24,25]. Each bismuth atom is coordinated to four oxygen atoms of the $(Bi_2O_2)^{2+}$ layer and to two oxygen atoms (top or bottom oxygen of the octahedral) that are coordinated to the vanadium, and each vanadium is connected to eight oxygen. The work presented here reveals the similarities and differences between the mechanism and kinetics of propene oxidation to acrolein over oxides having an aurivillius structure with the stoichiometry $Bi_4V_{2-x}Mo_xO_{11+x/2}$ (x = 0-1) and oxides having a scheelite structure with the stoichiometry $Bi_{2-x/3}Mo_xV_{1-x}O_4$ (x = 0-1).

4.2 Methods

4.2.1 Catalyst Preparation

Molybdenum substituted bismuth vanadate catalysts ($Bi_4V_{2-x}Mo_xO_{11+x/2}$) were prepared by the complexation method, as described in more detail elsewhere [17]. Bismuth (III) nitrate pentahydrate ($Bi(NO_3)_3 \cdot 5H_2O$) (99.98% Sigma-Aldrich), ammonium metavanadate (NH_4VO_3) (99% Sigma-Aldrich) and ammonium molybdate tetrahydrate ($(NH_4)_6Mo_7O_{24} \cdot 5H_2O$) (99.98% Sigma-Aldrich) are used as precursors. These metal precursors were mixed to achieve atomic ratios of Bi:V:Mo = 4:(2-x):x in order to produce materials with the stoichiometry $Bi_4V_{2-x}Mo_xO_{11+x/2}$. The metal precursors were added 50 mL of water together with citric acid (1:1 molar ratio with metal precursors). The resulting solution was heated at 353 K for about 24 h in air to form a gel. The gel was then dried at 393 K and calcined in flowing air at 1023 K for 12 h. The material was then slowly cooled in air at 30 K/h to 573 K and then at 60 K/h to room temperature.

4.2.2 Catalyst Characterization

X-ray diffraction patterns were obtained with a Bruker-AXS D8 Discover GADDS diffractometer using Cu Kα radiation. Data were collected in the range of 10° < 2θ < 80° every 0.02°.

Diffuse reflectance UV-VIS-NIR spectra were acquired using a Fischer Scientific EVO 300 spectrometer equipped with a Praying Mantis reflectance chamber and an *in situ* high pressure cell (Harrick Scientific, Inc), fitted with quartz windows. Spectra were referenced to the diffuse reflectance spectrum of a Teflon reference tile. The procedure used to extract band gap energies from absorption edge data is given in the Supporting Information in Section 3.5.1.

4.2.3 Catalyst Activity and Selectivity

Measurements of reaction rates and product distributions were performed using a packed bed quartz tube reactor (10 mm in diameter) loaded with 100-800 mg of catalyst. The catalyst was preheated to the reaction temperature in air over night prior to starting a reaction. The operating temperature is between 623K and 713K and assures that no bulk phase changes occurred in the catalyst. All experiments were carried out at atmospheric pressure with 3.3-16.7% propene (99.9%, Praxair) and 3.3-16.7% oxygen (supplied from 20% oxygen in helium, Praxair), balanced as needed with additional helium (99.995%, Praxair). Organic products were analyzed using a gas chromatograph (GC) equipped with a 30 m HP-PLOT Q column and a flame ionization detector (FID). An Alltech Hayesep DB packed column and a thermal conductivity detector (TCD) were used to analyze for oxygen, CO and CO_2. Data were collected at steady-state. Conversion was calculated on the basis of products formed and product selectivity was defined as the moles of propene converted to the product over the sum of the moles of olefins converted to all products, based on a carbon balance. All selectivities reported in this study are intrinsic selectivity, extrapolated when the conversion is very low (< 1%).

4.3 Results

4.3.1 Catalyst Characterization

Powder X-ray diffraction patterns of $Bi_4V_{2-x}Mo_xO_{11+x/2}$ for x = 0, 0.05, 0.1, and 1.0 are shown in Figure 4.2. Comparison of these patterns with those in the literature shows that each material is a pure phase [26,27]. $Bi_4V_2O_{11}$ is stable in the α-phase polymorph for temperatures of below 723 K, and therefore the diffraction pattern for this material is assigned to α-$Bi_4V_2O_{11}$. For $Bi_4V_{2-x}Mo_xO_{11+x/2}$ where x = 0.5 and 0.1, the material is taken to be in the β-phase based on previous studies showing this phase to be stable for 0.05 < x < 0.225 [25,28].

The UV-Vis diffuse reflectance spectra of $Bi_4V_{2-x}Mo_xO_{11+x/2}$ are shown in Figure 4.3. $Bi_4V_2O_{11}$ has the lowest absorption edge, and γ-Bi_2MoO_6 has the highest absorption

edge. The absorption edge for $Bi_4V_{1.9}Mo_{0.1}O_{11.05}$ (x = 0.1) is lower relative to that for γ-Bi_2MoO_6, and exhibits only a single absorption edges. This result indicates that vanadate and molybdate ions are not electronically independent, and there is presumably coupling between Mo and V electronic states. Band gaps were determined from the UV-Vis absorption data for the fully oxidized catalyst at 673 K can be calculated using the method described in the Supporting Information in Section 3.5.1, and the results are listed in Table 4.1.

4.3.2 Measurements of Reaction Rates and Product Selectivities

The main products of propene oxidation over $Bi_4V_{2-x}Mo_xO_{11+x/2}$ are acrolein, CO_2, CO, acetic acid, and acetaldehyde. The rates of propene consumption at 673 K over $Bi_4V_2O_{11}$, $Bi_4V_{1.9}Mo_{0.1}O_{11.05}$, and γ-Bi_2MoO_6 are presented in Table 4.2 together with the product selectivities. In all cases, the data have been extrapolated to a propene conversion of zero. The overall activity for propene oxidation increases in the order $Bi_4V_2O_{11}$ < $Bi_4V_{1.9}Mo_{0.1}O_{11.05}$ < γ-Bi_2MoO_6, whereas the selectivity to acrolein increases in the reverse order and the selectivities to CO_2 and CO increase in the same order as the overall activity.

The effect of propene conversion on product selectivity was investigated by varying the space velocity of the feed. Figure 4.4 shows that while the product selectivity is almost constant with propene conversion for γ-Bi_2MoO_6, a very different pattern is observed for $Bi_4V_2O_{11}$ and $Bi_4V_{1.9}Mo_{0.1}O_{11.05}$. In both cases, the selectivity to acrolein decreases and the selectivities to CO_2 and CO increase with increasing propene conversion, indicating that acrolein undergoes secondary combustion to CO_x. Notably, though, the selectivities to acetaldehyde and acetic acid do not exhibit strong changes with the feed space velocity.

The dependence of the rate of acrolein formation on the partial pressures of propene and oxygen can be expressed in the form of a power-law model given by Eqn. 1.

$$rate_{acrolein} = k_{app}P_{C_3H_6}^m P_{O_2}^n \qquad (1)$$

Where k_{app} is the apparent rate coefficient, P_i is the partial pressure of reactant i, and m and n are the orders in propene and oxygen, respectively. Values for m and n at 673 K are given in Table 4.3 for propene oxidation to acrolein over $Bi_4V_{2-x}Mo_xO_{11+x/2}$ (x = 0, 0.1, and 1.0). The data show that the rate of propene oxidation to acrolein is nearly first-order with respect to the partial pressure of C_3H_6 and nearly zero-order with respect to the partial pressures of O_2.

Reaction orders for C_3H_6 and O_2 were also measured for the main byproduct produced over γ-Bi_2MoO_6, CO_2 and CO. The rates of CO_2 and CO production are both nearly first order in C_3H_6. The partial pressure dependence on O_2 is 0.4 for CO_2 and 0.9 for CO, which is consistent with our previous results from α-$Bi_2Mo_3O_{12}$ [17]. This suggests that the oxygen atoms in CO_2 come from both gas-phase oxygen and lattice oxygen, and mainly from the gas phase for the production of CO. This is a further

indication of the same mechanism for CO and CO_2 production compared with α-$Bi_2Mo_3O_{12}$.

Arrhenius plots for propene oxidation to acrolein over $Bi_4V_{2-x}Mo_xO_{11+x/2}$ are shown in Figure 4.5 for temperatures in the range of 623 K - 713 K. Values of the apparent activation energy are listed in Table 4.4. The apparent activation energy for $Bi_4V_{1.9}Mo_{0.1}O_{11.05}$ (x=0.1) is similar but higher to that for $Bi_4V_2O_{11}$. The apparent activation energy for acrolein production on γ-Bi_2MoO_6 is 18.8 kcal/mol, but smaller compared than that for α-$Bi_2Mo_3O_{12}$ 19.9 kcal/mol [17]. The values of these activation energies are comparable to those reported by Krenzke et al. for γ-Bi_2MoO_6 and α-$Bi_2Mo_3O_{12}$ 15 kcal/mol and 18 kcal/mol for temperatures above 693K [29].

4.4 Discussion

4.4.1 Mechanism of Propene Oxidation on γ-Bi_2MoO_6, $Bi_4V_2O_{11}$ and on $Bi_4V_{1.9}Mo_{0.1}O_{11.05}$ (x = 0.1)

4.4.1.1 Mechanism of Propene Oxidation on γ-Bi_2MoO_6

The kinetics of propene oxidation over γ-Bi_2MoO_6, which has an aurivillius structure, and α-$Bi_2Mo_3O_{12}$, which has a scheelite structure, are identical. For both catalysts, the rate is first order in the partial pressure of propene and zero order in the partial pressure of oxygen. Isotopic tracer studies for both catalysts show that the reaction proceeds by a Mars van Krevelen mechanism involving oxygen atoms of the lattice [30]. Moreover, the reaction kinetics suggests that the rate-limiting step involves cleavage of a C-H bond in the methyl group of propene [31]. There are also further similarities in the catalytic properties of γ-Bi_2MoO_6 and α-$Bi_2Mo_3O_{12}$. As noted in Table 4.5 both catalysts exhibit virtually the same activity per unit area and both have very similar activation energies 18.8 kcal/mol for γ-Bi_2MoO_6 and 19.9 kcal/mol for α-$Bi_2Mo_3O_{12}$.

The first question then is the whether the type of oxygen atoms involved in the oxidation of propene over α-$Bi_2Mo_3O_{12}$ and γ-Bi_2MoO_6 is the same? In situ XANES studies conducted on α-$Bi_2Mo_3O_{12}$ indicate that Bi remains in the 3+ state and does not undergo reduction, whereas Mo undergoes reduction from the 6+ to the 5+ oxidation state and then is rexodized in the course of propene oxidation [17]. This conclusion is supported by DFT studies, which reveal further that the most reactive O atoms are those in Mo=O bonds that interact with the lone pair of proximal Bi atoms (e.g., equatorial Mo=O bonds) [15,16]. This interaction destabilizes the HOMO and stabilizes the LUMO of the molybdate species, thereby facilitating the transfer of an electron into a Mo-O p* orbital.

By contrast to α-$Bi_2Mo_3O_{12}$, γ-Bi_2MoO_6 has a layered structure, as shown in Figure 4.6. Three different type of oxygen can be distinguished. The first, O1 is only coordinated to bismuth and is located in the $(Bi_2O_2)^{2+}$ layer. The second type of oxygen, O2 is in the $(MoO_2)^{2-}$ layer and is only coordinated to molybdenum. The third type of

oxygen, O3 is located at the top and bottom of the octahedron around the molybdenum and is coordinated to both bismuth and molybdenum [32].

Several attempts to identify the active form of oxygen in γ-Bi$_2$MoO$_6$ have been reported. Otsubo et al. [33] and Miura et al. [34] prepared γ-Bi$_2$MoO$_6$ by solid state reaction of Bi$_2$^{18}O$_3$•MoO$_3$ and Bi$_2$O$_3$•Mo^{18}O$_3$. While their results suggest that the formation of acrolein formation involves the O1 atoms of the (Bi$_2$O$_2$)$^{2+}$ layers rather than the oxygen atoms of the (MoO$_2$)$^{2-}$ layers, this conclusion is not definitive because at the high temperature required for the synthesis of γ-Bi$_2$MoO$_6$, oxygen migration occurs readily leading to complete scrambling of all oxygen atoms [35,36]. The likelihood that O1 is not the active form of oxygen is supported by the theoretical work of Dadyburjor et al. [37], who calculated the activation energies for removal of oxygen from γ-Bi$_2$MoO$_6$. This work revealed that the activation energies for removal of O1, O2, and O3 are 80 eV, 2eV, and 3 eV, respectively. These results suggest that O2 and O3 are much more likely to be the active form of O. XPS studies by Ono et al. [38] show that the Mo/Bi ratio at the surface of γ-Bi$_2$MoO$_6$ is 0.8, suggesting that O2 and O3 oxygen atoms should be present at the catalyst surface. The strong similarity of the activation energies for propene oxidation over α-Bi$_2$Mo$_3$O$_{12}$ and γ-Bi$_2$MoO$_6$, also suggests that the oxygen atom involved in the rate-limiting step is similar in both cases. As noted above, in the case of α-Bi$_2$Mo$_3$O$_{12}$ this is the equatorial oxygen, which interacts with the lone pair of Bi in a structure that that can be described as Bi$^{...}$O=Mo, in which the Bi-O distance is 2.7 Å. Figure 4.6 shows that O2 is located 2.5 Å from Bi so it is reasonable to expect that O2 interacts with Bi in a manner similar to that of the equatorial oxygen atom in α-Bi$_2$Mo$_3$O$_{12}$. Thus, we propose that the similarities in the activity of γ-Bi$_2$MoO$_6$ and α-Bi$_2$Mo$_3$O$_{12}$ are a consequence of the similarity in the active form of oxygen in both catalysts – O2 in the case of γ-Bi$_2$MoO$_6$ and equatorial O in the case of α-Bi$_2$Mo$_3$O$_{12}$.

The kinetics of propene oxidation to acrolein are identical for γ-Bi$_2$MoO$_6$ and α-Bi$_2$Mo$_3$O$_{12}$. The observed form of the rate expression can be rationalized on the basis of the reaction mechanism shown in Scheme 4.1 for α-Bi$_2$Mo$_3$O$_{12}$ [17]. As discussed previously, when the catalyst is fully oxidized and propene is weakly adsorbed on the catalyst surface, the rate of propene oxidation to acrolein is given by:

$$rate = K_1 k_2 P_{C_3H_6}[S] = k_{app} P_{C_3H_6} \qquad (2)$$

Here k_i is the rate coefficient of reaction i, K_i is the equilibrium constant for reaction i, and [S] is the concentration of activate site per unit BET surface area of the catalyst. In our view, the mechanism shown in Scheme 4.1 should also apply to propene oxidation over γ-Bi$_2$MoO$_6$.

4.4.1.2 Mechanism of Propene Oxidation on Bi$_4$V$_2$O$_{11}$ and on Bi$_4$V$_{1.9}$Mo$_{0.1}$O$_{11.05}$ (x = 0.1)

While there are similarities in the catalytic properties of Bi$_4$V$_2$O$_{11}$, which has an aurivillius structure, and BiVO$_4$, which has a scheelite structure, there are also notable differences. The similarity is in the reaction kinetics, which for both catalysts are first order in the partial pressure of propene and zero order in the partial pressure of oxygen.

The apparent activation energies are also nearly identical of the two catalysts – 14.5 kcal/mol for $BiVO_4$ and 14.4 kcal/mol for $Bi_4V_2O_{11}$. What is different, though, are the catalyst activity and selectivity. As can be seen in Table 4.5, the activity of $BiVO_4$ for propene oxidation to acrolein is more than 40 times larger than that for $Bi_4V_2O_{11}$ under identical reaction conditions. Table 4.2 also shows that the intrinsic selectivity to acrolein is significantly higher for $BiVO_4$ (76 %) than that for $Bi_4V_2O_{11}$ (39%). It is notable, though, that both catalysts show a monotonic decrease in the acrolein selectivity and corresponding rise in the selectivity to CO_2 with increasing propene conversion, whereas the selectivities to CO, CH_3COOH, and CH_3CHO remain constant with propene conversion. These trends indicate that acrolein readily undergoes combustion to CO_2 over both $BiVO_4$ and $Bi_4V_2O_{11}$ as the concentration of acrolein in contact with the catalyst increases. The differences in the activity and selectivity of $Bi_4V_2O_{11}$ and $BiVO_4$ are attributed to differences in the activity of the oxygen atoms present at the surface of the two materials. As discussed below the O atoms present at the surface of $Bi_4V_2O_{11}$ are significantly more active than those at the surface of $BiVO_4$. This difference can lead to higher rates of oxidation of the vinylalkoxide intermediate to acrolein (see Scheme 4.1) and consequently to a lower intrinsic selectivity to acrolein, as well as to a greater tendency for acrolein to combust as the acrolein concentration increases with increasing propene conversion. The points are discussed in more detail below.

For molybdenum-substituted $Bi_4V_2O_{11}$, $Bi_4V_{1.9}Mo_{0.1}O_{11.05}$ (x = 0.1), the activity and intrinsic selectivity of acrolein formation are higher than that of $Bi_4V_2O_{11}$ (Table 4.2) but still lower than that of $BiVO_4$. Figure 4.4 also shows that with increasing propene conversion, the selectivity to acrolein decreases and that to CO_2 increases. Further discussion of these trends is given below.

4.4.2 Band Gap Energy as a Descriptor of Activation Energy

We have recently shown that the apparent activation energy for propene oxidation to acrolein correlates with the band gap of catalyst of varying composition but all having a scheelite structure. This relationship has been rationalized on the basis of a Born-Haber cycle and the recognition that the largest contributor to this cycle is the band gap energy, which is also the component most dependent on catalyst composition [22]. The question that we now ask is whether a similar correlation holds for catalysts having the aurivillius structure.

Figure 4.7 shows that the apparent activation energy for propene oxidation correlates linearly with the band gap for catalyst of different composition having either the scheelite or aurivillius structure. The only difference is that for the same band gap, the apparent activation energies are about 1.5 kcal/mol higher for catalysts with the aurivillius than the scheelite structure. Since the apparent activation energy is the sum of the enthalpy of propene adsorption and the intrinsic activation energy, we propose that the slightly higher activation energies observed for catalysts with the aurivillius structure compared to the scheelite structure is due the slightly lower heat of adsorption for propene on the former structure. Unfortunately, to the best of our knowledge, the

difference in the heats of adsorption for the two types of structures has not been reported, and, therefore, we cannot verify this hypothesis.

The results presented in Figure 4.7 suggest that catalysts with low band gaps should be exhibit a higher activity for propene oxidation to acrolein per active site than those with higher band gaps. While this conclusion is true for catalysts with band gaps above about ~ 2.1 eV, it does not hold for catalyst with lower band gaps. As shown in this study for $Bi_4V_2O_{11}$ and $Bi_4V_{1.9}Mo_{0.1}O_{11.05}$, and reported earlier for $BiVO_4$, catalysts with band gaps below ~ 2.1 eV show both lower intrinsic selectivities to acrolein and higher activity for acrolein combustion. This pattern is nicely illustrated in Figure 4.8. Two factors can account for the loss of acrolein selectivity for catalysts with band gaps < 2.1 eV. Scheme 4.2 shows a possible pathway for the oxidation of the vinylalkoxide formed as an intermediate leading to acrolein [17]. Loss of an H atom from this intermediate initiates a cascade of steps leading to CO and CO_2. It is notable that the participation of an oxygen atom from O_2 adsorbed from the gas phase accounts for the observed positive order in oxygen partial pressure of the rate of CO_x formation. Clearly then, the more active the surface oxygen, the higher will be the rate of CO_x formation paralleling the rate of acrolein formation. A high chemical activity of surface oxygen could also be responsible for the secondary combustion of acrolein.

4.5 Conclusions

The oxidation of propene to acrolein has been investigated over aurivillius-structured mixed metal oxides, γ-Bi_2MoO_6, $Bi_4V_2O_{11}$, and Mo-substituted $Bi_4V_2O_{11}$, and the activity and selectivity of these materials are compared to those for similar catalysts prepared with the scheelite structure. All of the catalysts exhibit similar kinetics – the rate of acrolein formation is first order in the partial pressure of propene and zero order in the partial pressure of oxygen. These kinetics can be rationalized on the basis of the mechanism shown in Scheme 4.1. Both sets of catalysts show a linear correlation in the apparent activation energy with the band gap of the catalyst measured at the reaction conditions (see Figure 4.7). However, for the same band gap, the apparent activation energy for propene oxidation to acrolein is about 1.5 kcal/mol higher for catalysts having the aurivillius structure. This difference is attributed to the lower heat of propene adsorption on the aurivillius structure. The results of this study also reveal another interesting feature. As seen in Figure 4.8, catalysts with band gaps of above ~ 2.1 eV exhibit high intrinsic acrolein selectivities, $\sim 75\%$, whereas catalysts with band gaps below ~ 2.1 eV exhibit significant lower intrinsic acrolein selectivities. It is also observed that the acrolein selectivity is independent of propene conversion for catalysts with band gaps above ~ 2.1 eV, whereas catalysts with band gaps below ~ 2.1 eV exhibit a strong decrease in acrolein selectivity with increasing propene conversion as a consequence of acrolein combustion. These findings clearly indicate that there is no advantage to developing propene oxidation catalysts with band gaps below ~ 2.1 eV.

4.6 References

[1] G.W. Keulks, L.D. Krenzke, T. M. Notermann, Adv. Catal. 27 (1978) 183-225.

[2] G. Ertl, H. Knozinger, F. Schuth, J. Weitkamp (Eds.) Handbook of Heterogeneous Catalysis, Wiley- VCH, Weinheim, 2008, pp. 3481.

[3] Y. Moro-Oka, W. Ueda, Adv. Catal. 40 (1994) 233-273.

[4] J.M.M. Millet, H. Ponceblanc, G. Coudurier, J.M. Herrmann, J.C. Vedrine, J. Catal. 142 (1993) 381-391.

[5] D. Carson, G. Coudurier, M. Forissier, J.C. Vedrine, J. Chem. Soc. Faraday Trans. I. 79 (1983) 1921-1929.

[6] H.H. Voge, C.D. Wagner, D.P. Setvenson, J. Catal. 2 (1963) 58-62.

[7] W.M.H. Sachtler. Rec. Trav. Chim. 82 (1963) 243-245.

[8] B. Grzybowska, J. Haber, J. Janas, J. Catal. 49 (1977) 150-163.

[9] W. Ueda, K. Asakawa, C.L. Chen, Y. Moro-Oka, T. Ikawa, J. Catal. 101 (1986) 360-368.

[10] G.W. Keulks, J. Catal. 19 (1970) 232- 235.

[11] J. Haber, W. Turek, J. Catal. 190 (2000) 320-326.

[12] R.K. Grasselli, Top. Catal. 21 (2001) 79-88.

[13] R.K. Grasselli, J. Chem. Educ. 63 (1986) 216-221.

[14] L.C. Glaeser, J.F. Brazdil, M.A. Hazle, M. Mehicic, R.K. Grasselli, J. Chem. Soc., Faraday Trans. I 81 (1985) 2903-2912.

[15] A. Getsoian, V. Shapovalov, A. T. Bell, J. Phys. Chem. C 117 (2013) 7123-7137.

[16] A. Getsoian, A. T. Bell, J. Phys. Chem. C 117(2013), 25562-25578.

[17] Z. Zhai, A. Getsoian, A. T. Bell, J. Catal. 308 (2013) 25-36.

[18] Y. Moro-Oka, W. Ueda, Adv. Catal. 40 (1994) 233-273.

[19] P.Porta, M.L. Jacono, M. Valigi, G. Minelli, A. Anichini, S.D. Rossi, D. Gazzoli. J. Catal. 100(1986) 86-94

[20] S.D. Rossi, M.L. Jacono, P.Porta, M. Valigi, D. Gazzoli, G. Minelli, A. Anichini, J. Catal. 100(1986) 95-102

[21] D. Cordischi, M.L. Jacono, , D. Gazzoli, G. Minelli, P.Porta. J. Catal. 102(1986) 1-9

[22] A. Getsoian, Z. Zhai, A. T. Bell, J. Am. Chem. Soc. 136 (2014) 13684−13697.

[23] K. R. Kendall, C. Navas, J. K. Thomas, and H. Loye, "Recent Developments in Oxide Ion Conductors : Aurivillius Phases," no. 15, pp. 642–649, 1996.

[24] G. Mairesse, P. Roussel, R. N. Vannier, M. Anne, G. Nowogrocki, Solid State Sci. 5 (2003) 861–869.

[25] R. N. Vannier, G. Mairesse, F. Abraham, J. Solid State Chem., 103 (1993) 441–446

[26] A. Phuruangrat, P. Jitrou, P. Dumrongrojthanath, N. Ekthammathat, B. Kuntalue, S. Thongtem, T. Thongtem, J. Nanomater. 2013(2013) 1-8.

[27] A. M. Cruz and S. O. Alfaro, J. Mol. Catal. A Chem., 320 (2010) 85-91.

[28] S. J. Patwe, A. Patra, R. Dey, A. Roy, R. M. Kadam, S. N. Achary, and A. K. Tyagi, J. Am. Ceram. Soc., 96 (2013) 3448–3456.

[29] L.D. Krenzke, G.W. Keulks, J. Catal. 64 (1980) 295-302.

[30] L.D. Krenzke, G.W. Keulks, J. Catal. 61 (1980) 316-325.

[31] C.R. Adams, T.J. Jennings, J. Catal. 3 (1964) 549-558.

[32] R.G. Teller, J. F. Brazdel, R. K. Grasselli, Acta. Cryst., C40 (1984) 2001–2005.

[33] T.-T. Otsubo, H. Miura, Y. Morikawa, T. Shirasaki, J. Catal. 36 (1975) 240–243.

[34] H. Miura, T.-T. Otsubo, T. Shirasaki, Y. Morikawa, J. Catal.,56 (1979) 84–87.

[35] E.V. Hoefs, J.R. Monnier, G.W. Keulks. J. Catal. 57(1979) 331-337.

[36] L. T. Sim, C. K. Lee, A. R. West, J. Mater. Chem. 12 (2002) 17–19.

[37] B. Dadyburjor, J. Catal. 388 (1980) 383–388.

[38] T. Ono, K. Utsumi, S. Tsukamoto, H. Tamaru, M. Kataoka, F. Noguchi, J. Mol. Catal. A Chem., 318 (2010) 94–100.

Figure 4.1 Ideal crystal structure of $Bi_4V_2O_{11}$ as a representative of aurivilius structure [24].
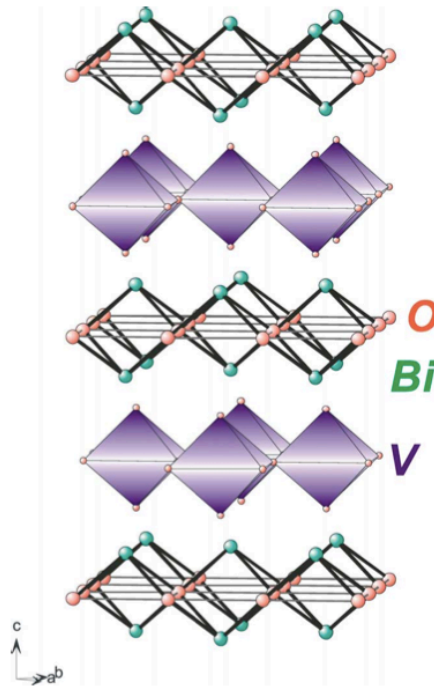
Figure 4.2 XRD patterns of $Bi_4V_{2-x}Mo_xO_{11+x/2}$ catalysts.
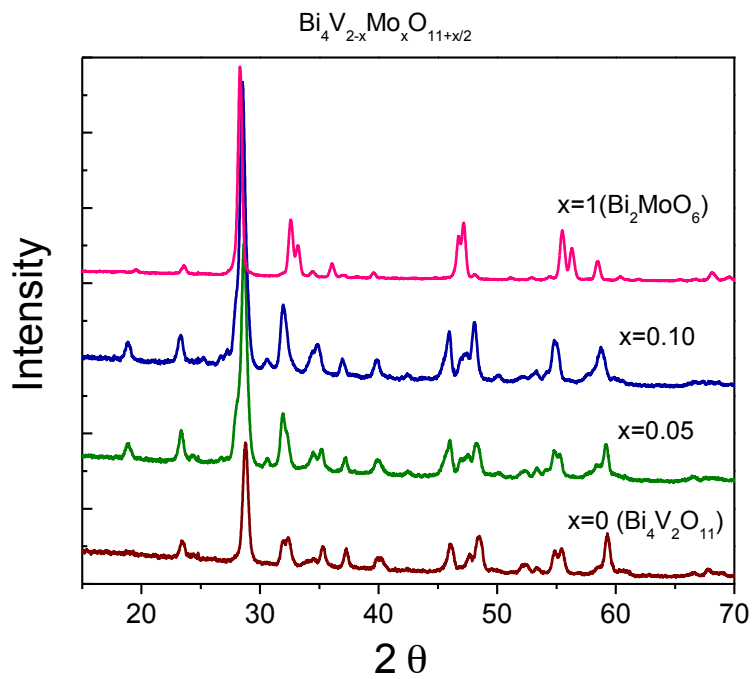
Figure 4.3 Diffuse reflectance UV-Visible absorption spectrum of $Bi_4V_{2-x}Mo_xO_{11+x/2}$ measured at 673K. Labels mark the principal LMCT absorption edge.
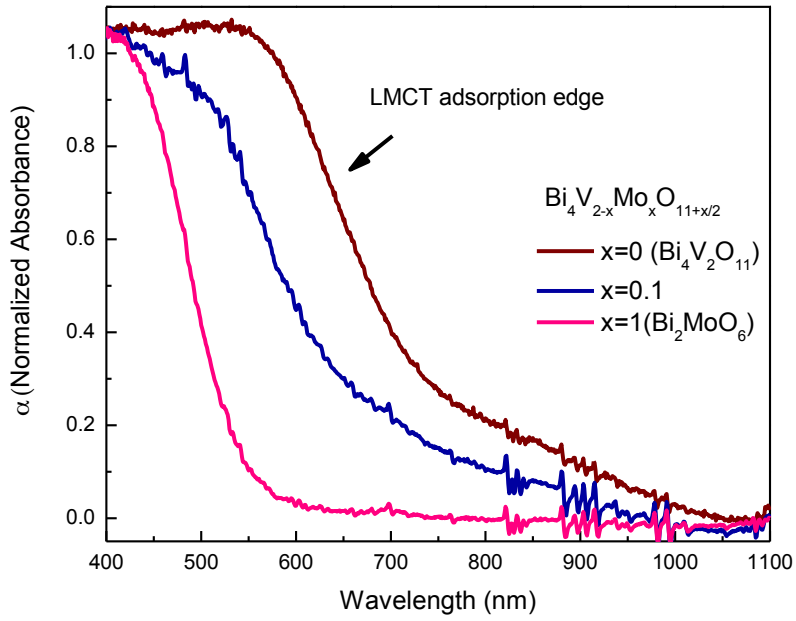
Figure 4.4 Variation in the selectivity of $Bi_4V_{2-x}Mo_xO_{11+x/2}$ for propene oxidation to acrolein at 673 K and $P_{C3H6} = P_{O2} = 0.167$ atm measured as a function of propene conversion.
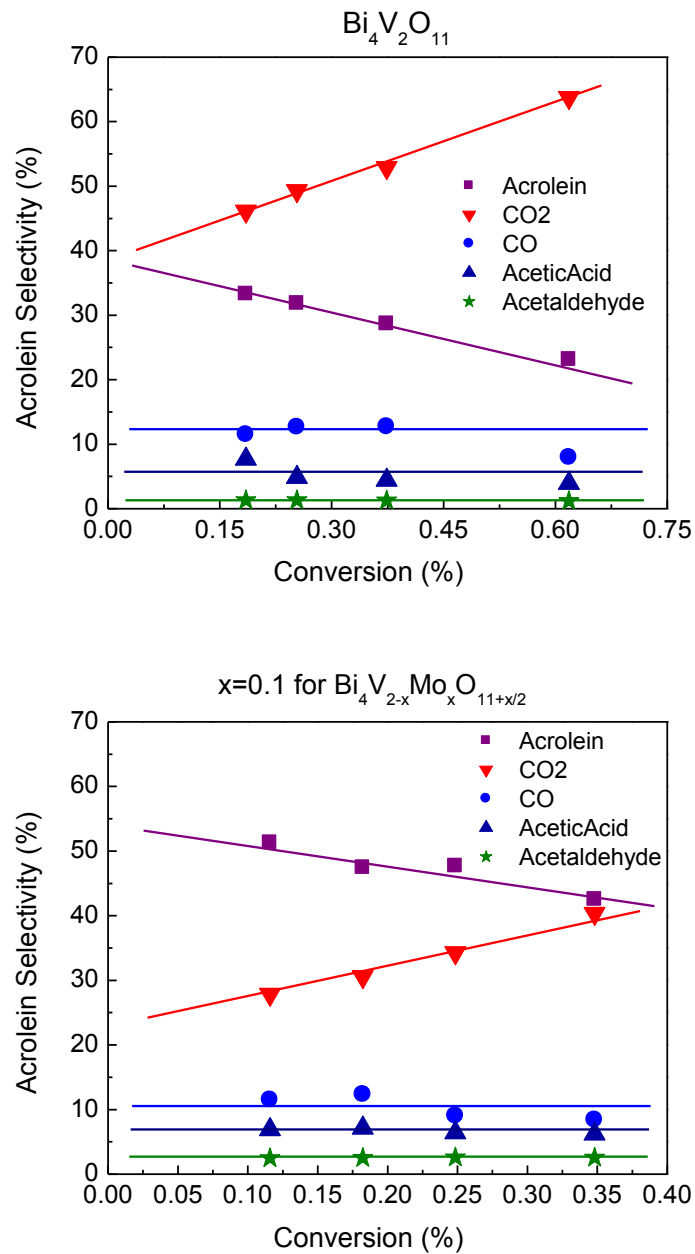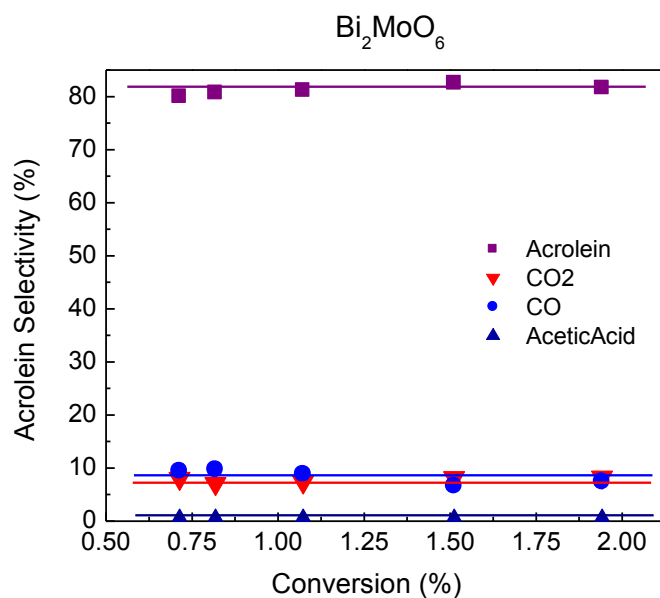
Figure 4.5 Arrhenius plots for propene oxidation to acrolein over $Bi_4V_{2-x}Mo_xO_{11+x/2}$ catalysts. Reaction conditions: T = 623 K - 713 K and $P_{C3H6} = P_{O2} = 0.167$ atm.
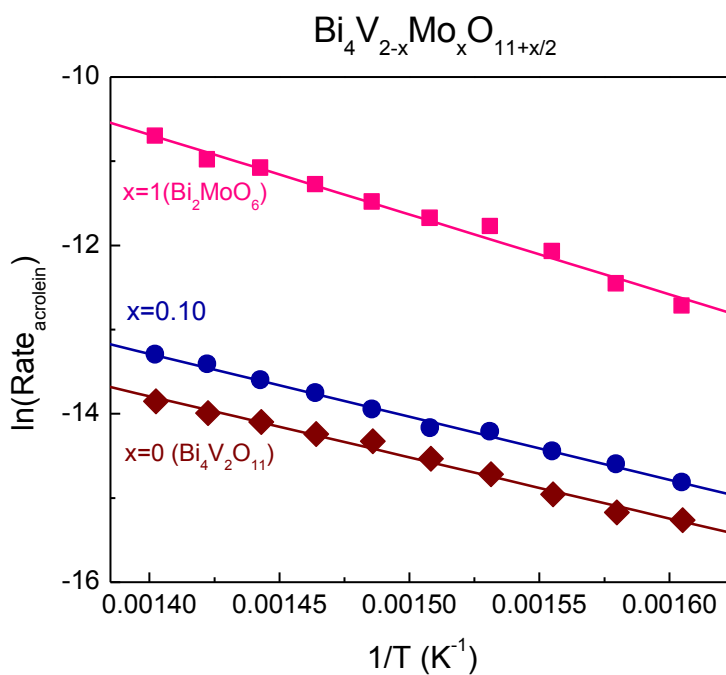
Figure 4.6 γ-Bi$_2$MoO$_6$ structure. Red: oxygen; Purple: bismuth; Green: molybdenum. O1, O2 and O3 refers to three different types of oxygen.
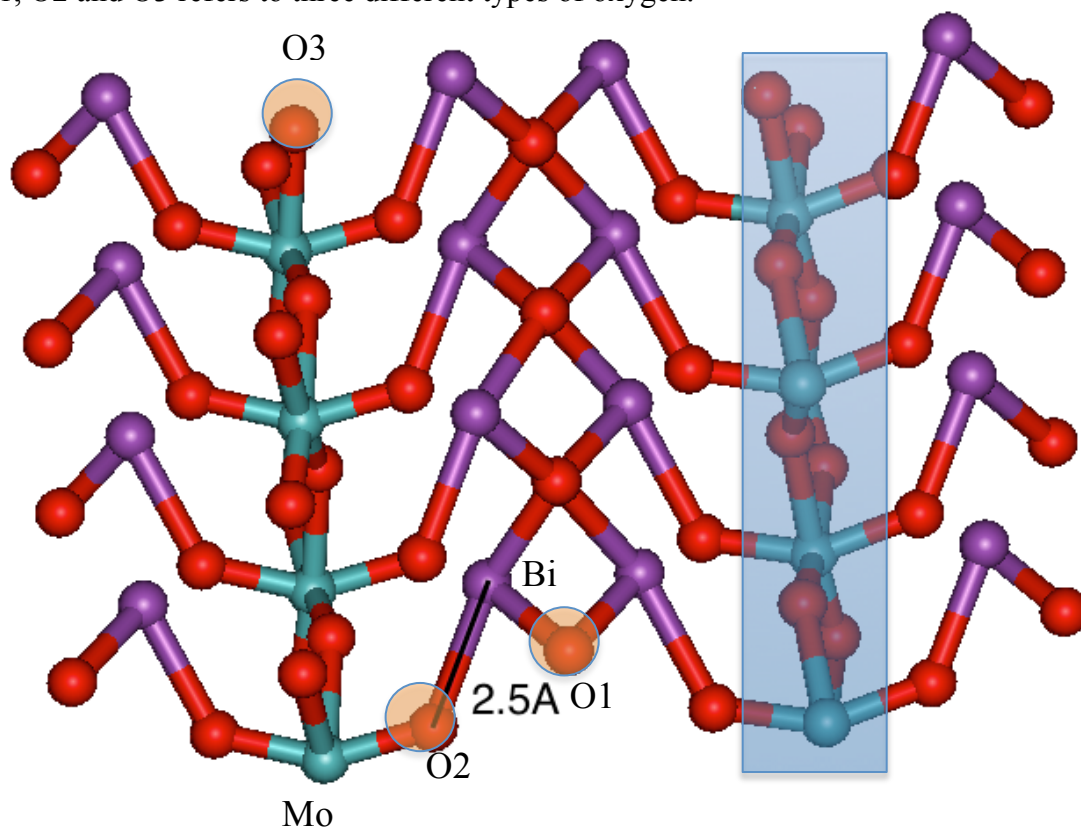
Figure 4.7 Apparent activation energies for oxidation of propene to acrolein versus the band gap measured at 673K for catalysts having the scheelite (lower line) and aurivilius (upperline) structures. Reaction conditions: T = 673K and $P_{C3H6} = P_{O2} = 0.167$ atm.
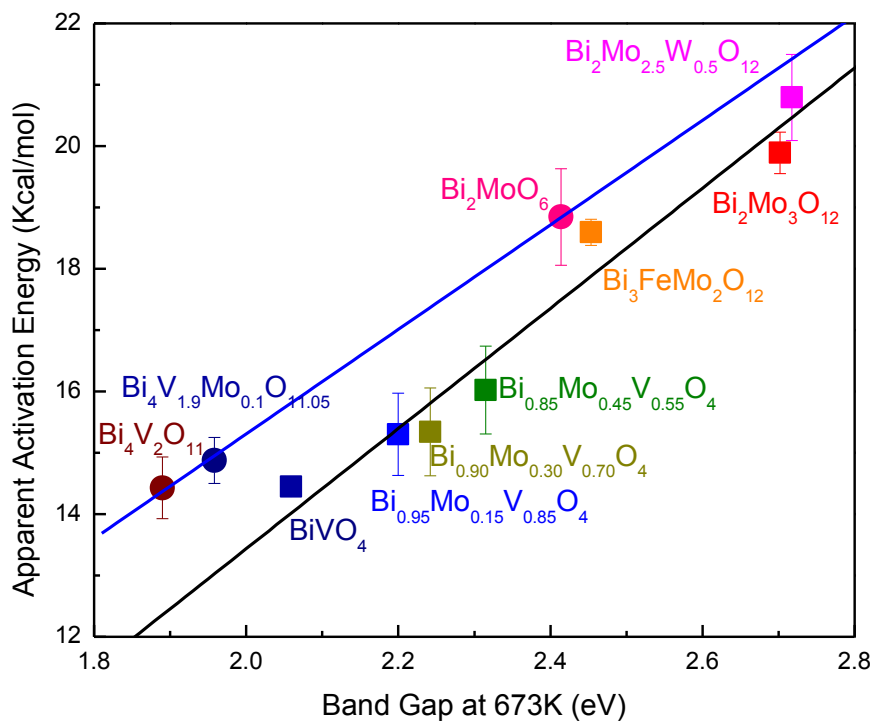
Figure 4.8 Intrinsic selectivity to acrolein versus the band gap measure at 673K.
Reaction conditions: T = 673K and $P_{C3H6} = P_{O2} = 0.167$ atm.
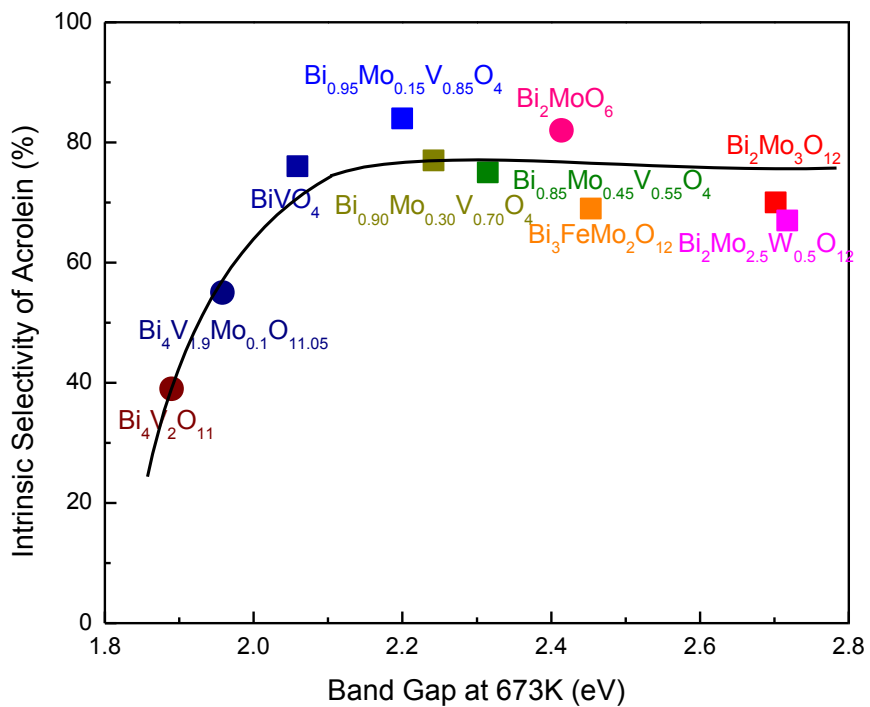
Scheme 4.1 The mechanism for the oxidation of propene to acrolein over $Bi_2Mo_3O_{12}$ proposed on the basis of data reported in this study [17].
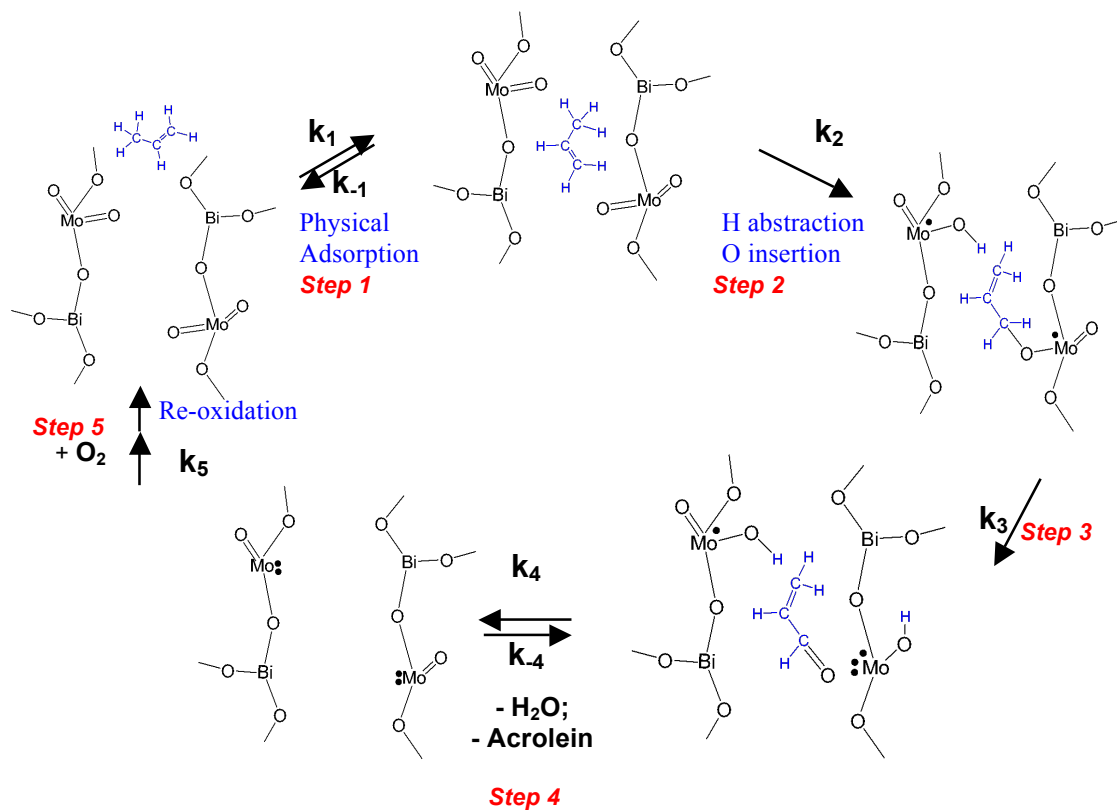
Scheme 4.2 Possible pathway for CO and CO_2 formation on Bi_2MoO_6 during the oxidation of propene [17].
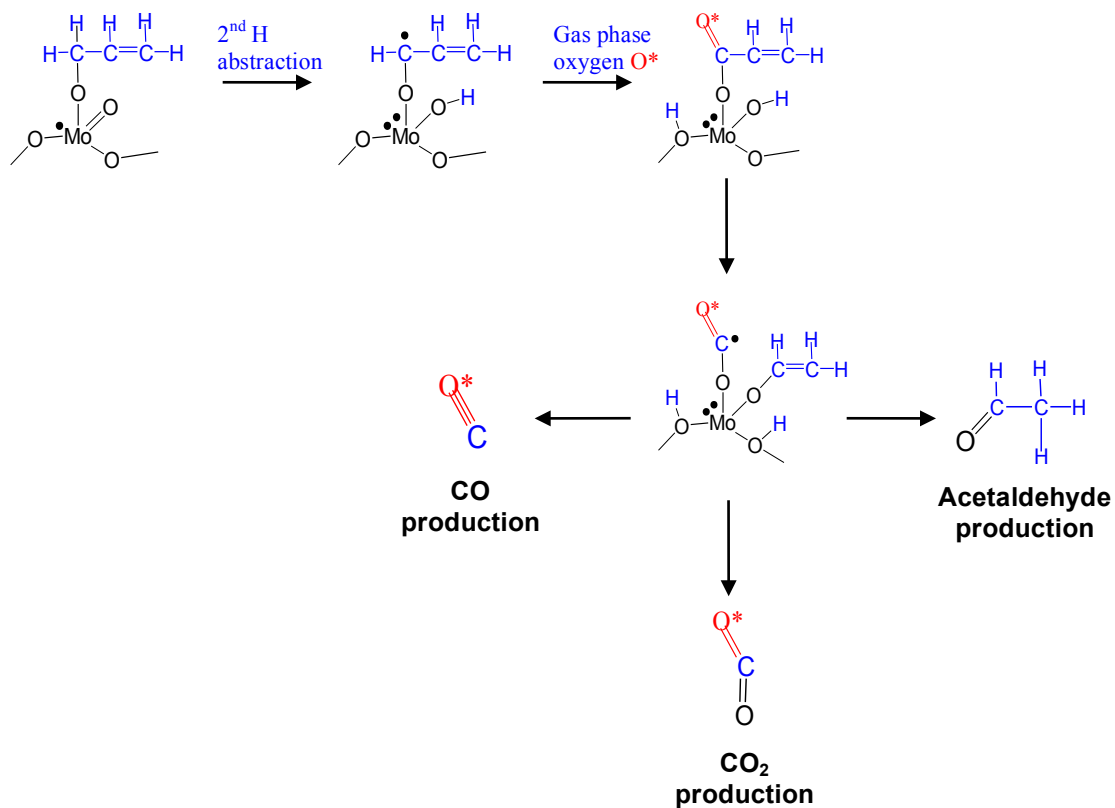
Table 4.1 Band-gap energies (eV) measured at 673K.

Catalyst	E_G (673K)
$Bi_4V_2O_{11}$	1.89
$Bi_4V_{1.9}Mo_{0.1}O_{11.05}$	1.96
Bi_2MoO_6	2.41

Table 4.2 Reaction rate of propene consumption and intrinsic selectivity on $Bi_4V_{2-x}Mo_xO_{11+x/2}$ for the oxidation of propene at 673 K and $P_{C3H6} = P_{O2} = 0.167$ atm.

Catalyst	Reaction rate of propene consumption ($*10^{-6}$ mol/min m^2/cat)	Selectivity (%)				
		Acrolein	CO	CO_2	Acetic Acid	Acetalde-hyde
$Bi_4V_2O_{11}$	1.6	39	15	40	5	1
$Bi_4V_{1.9}Mo_{0.1}O_{11.05}$	1.9	55	12.5	23	7	2.5
Bi_2MoO_6	12.4	82	7.5	8	0	2.5

Table 4.3 Reaction orders in propene and oxygen measure at 673 K for propene oxidation to acrolein on $Bi_4V_{2-x}Mo_xO_{11+x/2}$. The partial pressures of propene or oxygen were fixed at 0.067 or 0.167 atm, respectively, while the other one was varied.

Catalyst	673 K	
	Propene (m)	Oxygen (n)
$Bi_4V_2O_{11}$	1.0±0.1	0.1±0.1
$Bi_4V_{1.9}Mo_{0.1}O_{11.05}$	1.0±0.0	0.0±0.0
Bi_2MoO_6	1.0±0.0	0.1±0.1

Table 4.4 Apparent activation energies for propene oxidation to acrolein in the temperarure ranges of 623 - 713 K on $Bi_4V_{2-x}Mo_xO_{11+x/2}$. $P_{C3H6} = P_{O2} = 0.167$ atm.

Catalyst	E_{app} (kcal/mol)
$Bi_4V_2O_{11}$	14.4
$Bi_4V_{1.9}Mo_{0.1}O_{11.05}$	14.9
Bi_2MoO_6	18.8

Table 4.5 Apparent rate constant k_{app} for acrolein production on scheelite catalysts ($BiVO_4$ and $Bi_2Mo_3O_{12}$) and aurivilius catalysts ($Bi_4V_2O_{11}$ and Bi_2MoO_6). $P_{C3H6} = P_{O2} = 0.167$ atm, 673 K.

Catalyst	k_{app} ($*10^{-5}$ mol/min m^2/cat atm)	Catalyst	k_{app} ($*10^{-5}$ mol/min m^2/cat atm)
$BiVO_4$	17.4	$Bi_4V_2O_{11}$	0.4
$Bi_2Mo_3O_{12}$	6.7	Bi_2MoO_6	6.4

Chapter 5

Selective Oxidation and Oxidative Dehydrogenation of Hydrocarbons on Bismuth Vanadium Molybdenum Oxide

Abstract

A systematic investigation of the oxidative dehydrogenation of propane to propene and 1- and 2-butene to 1,3-butadiene, and the selective oxidation of isobutene to methacrolein was carried out over $Bi_{1-x/3}V_{1-x}Mo_xO_4$ (x = 0-1) with the aim of defining the effects of catalyst and reactant composition on the reaction kinetics. This work has revealed that the reaction kinetics can differ significantly depending on the state of catalyst oxidation, which in turn depends on the catalyst composition and the reaction conditions. Under conditions where the catalyst is fully oxidized, the kinetics for the oxidation of propene to acrolein and isobutene to methacrolein, and the oxidative dehydrogenation of propane to propene, 1-butene and trans-2-butene to butadiene are very similar - first order in the partial pressure of the alkane or alkene and zero order in the partial pressure of oxygen. These observations, together with XANES and UV-Vis data suggest that all these reactions proceed via a Mars van Krevelen mechanism involving oxygen atoms in the catalysts and that the rate-limiting step involves cleavage of the weakest C-H bond in the reactant. Consistent with these findings, the apparent activation energy and preexponential factor for both oxidative dehydrogenation and selective oxidation correlate with the dissociation energy of the weakest C-H bond in the reactant. As the reaction temperature is lowered, catalyst reoxidation can become rate-limiting, the transition to this regime depending on ease of catalyst reduction and effectiveness of the reacting hydrocarbons as a reducing agent. A third regime is observed for isobutene oxidation at lower temperatures, in which the catalyst is more severely reduced and oxidation now proceeds via reaction of molecular oxygen, rather than catalyst lattice oxygen, with the reactant.

5.1 Introduction

The oxidation of propene to acrolein and isobutene to methacrolein and the oxidative dehydrogentation of n-butene to 1,3-butadiene are used to produce commodity chemicals and monomers for a variety of polymers. Most of the catalysts used to promote these reactions are based on bismuth molybdate to which other metals are added to enhance activity and product selectivity [1-22]. For this reason there is considerable interest in understanding the influence of catalyst composition on catalyst activity and selectivity during the reaction process, and the effects of reactant composition on rate of product formation and the distribution of products formed. Surprisingly, though, there have been relatively few in depth investigations conducted on this subject.

Of the several systems of interest, the one that has been investigated most extensively is the oxidation of propene to acrolein over bismuth molybdate. This reaction has been shown to proceed via a Mars van Krevelen mechanism [23]. The rate-limiting

step has been shown to involve the abstraction of an H atom from the methyl group of propene to form an allyl intermediate, which is then stabilized on the catalyst surface as a vinyl alkoxide. Acrolein is then produced by the abstraction of a second H atom from the alkoxide species [24,25]. Much less is known, though, about the reactions of other hydorcarbons over bismuth molybdate-based catalysts. Studies of the oxidative dehydrogenation of n-butenes to butadiene over bismuth molybdate have been carried out and mechanism for this reaction is thought to resemble that for the oxidation of propene [26-31]. On the other hand, several different mechanisms have been proposed for the oxidation of isobutene to methacrolein, including a Langmuir-Hinshelwood mechanism and a redox model [32-34].

It is notable that previous studies of reaction mechanism and kinetics have tended to be reactant specific, and very few have involved a systematic investigation of the effects of catalyst and reactant composition. A notable exception has been the case of propene oxidation to acrolein over $Bi_{1-x/3}V_{1-x}Mo_xO_4$ (x = 0-1) [35] prepared with a scheelite structure. Ueda et al. [12] and Sleight et al. [36,37] have reported that $Bi_{1-x/3}V_{1-x}Mo_xO_4$ is more active for the oxidation of propene than either bismuth molybdate (x = 1) or bismuth vanadate (x = 0). Our work in Chapter 2 proposed a generalized model for the kinetics of propene oxidation over $Bi_{1-x/3}V_{1-x}Mo_xO_4$, and explained the exact roles of Bi, Mo and V in affecting the activity and selectivity of $Bi_{1-x/3}V_{1-x}Mo_xO_4$ [38-40]. By contrast, very little is known about the oxidation and oxidative dehydrogenation of butene isomers over vanadium-substituted bismuth molybdate. Therefore, many questions are still open. For example, will both reactions follow a mechanism similar to that propene oxidation for all catalyst compositions, and how does the composition and structure of the reactant affect reactant reactivity? Another question not fully understood is whether the reaction kinetics are the same independent of reaction conditions and if different for different reaction conditions, what are the mechanistic implications?

The work reported here was undertaken in order to determine catalyst and reactant composition, as well as reaction conditions affect the kinetics for the oxidative dehydrogenation of propane and 1- and 2-butene, and the selective oxidation of propene and isobutene over $Bi_{1-x/3}V_{1-x}Mo_xO_4$. The oxidation state of the catalyst reduction was probed by in situ XANES and UV-Vis spectroscopy. The results of this work demonstrate that $Bi_{1-x/3}V_{1-x}Mo_xO_4$ can operate in one of three regimes depending on the reactant and catalyst composition, the reaction temperature, and the partial pressure of the reactants. Under conditions where the catalyst is maintained in its fully oxidized state, all reactions follow a Mars van Krevelen mechanism. Under these conditions the reaction kinetics are first order in the partial pressure of the reactant and zero order in oxygen, and both the apparent activation energy and the apparent preexponential factor increase with the strength of the weakest C-H bond of the reactant involved in the rate-limiting step. When the rate of catalyst reoxidation cannot keep up with the rate of catalyst reduction, the reaction becomes zero order in reactant and fractional order in oxygen partial pressure. In this case the apparent activation energy and preexponential factor become independent of the reactant composition and reflective of the activation energy for catalyst reoxidation. When the catalyst is more severely reduced, reaction kinetics become inverse order in reactant and first order in oxygen partial pressure. Under these conditions, the apparent activation energy is very high and the reaction is thought to proceed via the reaction of adsorbed molecular O_2 and the reactant.

5.2 Methods

5.2.1 Catalyst Preparation

Catalysts were prepared by the complexation procedure [38]. The metal precursors, ammonium molybdate tetrahydrate (99.98%, Sigma-Aldrich), bismuth(III) nitrate pentahydrate (99.98%, Sigma-Aldrich), and ammonium metavanadate (99%, Sigma-Aldrich), at the atomic ratios of Bi:V:Mo = $(1-x/3):(1-x):x$, $(x = 0$ to $1.0)$ were mixed with citric acid (1:1 molar ratio with metal precursors) to produce materials with the stoichiometry $Bi_{1-x/3}V_{1-x}Mo_xO_4$. Metal precursors with citric acid were dissolved separately and then mixed together slowly. 2M HNO_3 was used in place of water to dissolve bismuth nitrate to the prevent precipitation of bismuth hydroxides. The resulting solution was dried at 60 °C for about 24 h in air to form a gel, which was then dried at 120 °C and calcined in flowing air at 600°C for 6 h.

5.2.2 Catalyst Characterization

X-Ray absorption spectroscopy (XAS) measurements were performed at the Advanced Photon Source at Argonne National Laboratory (ANL) on beam line 10BM. Measurement were performed as described previously [38]. Data were acquired at the Bi L_3-edge, and at the Mo and V K-edges before and after exposure to reactant at 713 K. Additional data were acquired in situ at the Mo K-edge under steady-state reaction conditions. These experiments were carried out in a controlled-atmosphere cell that could be heated up to 743K in the presence of flowing gas [41].

Diffuse reflectance UV-VIS-NIR spectra were acquired using a Fischer Scientific EVO 300 spectrometer equipped with a Praying Mantis reflectance chamber and an in-situ high pressure cell (Harrick Scientific, Inc). Spectra were referenced to the diffuse reflectance spectrum of a Teflon reference.

5.2.3 Catalyst Activity and Selectivity

Measurements of reaction rates and product distributions were performed using a packed bed quartz tube reactor (10 mm in diameter) loaded with 50-200 mg of catalyst. Prior to reaction, the catalyst was preheated to the reaction temperature in air. All experiments were carried out at atmospheric pressure with 3.3-16.7% propene (99.9%, Praxair), 1-butene (99%, Praxair), trans-2-butene (99%, Praxair), isobutene (99%, Praxair), propane (99%, Praxair), and 3.3-16.7% oxygen (supplied from 20% oxygen in helium, Praxair), balanced as needed with additional helium (99.995%, Praxair). Data were collected at steady-state between 573 K and 713 K. Products were analyzed using a gas chromatograph (Agilent 6890A) equipped with a 30 m HP-PLOT Q column and a flame ionization detector (FID), for analyzing hydrocarbons. An Alltech Hayesep DB packed column connected to a thermal conductivity detector (TCD) was used to analyze for oxygen, carbon mono- and di-oxides. Reactant conversion was calculated on the basis of products formed. Product selectivity was defined as the moles of reactant converted to the product over the sum of the moles of reactant converted to all products, based on a

carbon balance. All selectivities reported in this study are intrinsic selectivities, extrapolated to a conversion of < 1%.

5.3 Results

5.3.1 Kinetics

5.3.1.1 Product Distribution

The main product of 1-butene and trans-2-butene oxidation over $Bi_{1-x/3}V_{1-x}Mo_xO_4$ is 1,3-butadiene, and the principle byproducts are trans-, cis-2-butene and 1-butene. The influence of vanadium content on catalyst activity for 1,3-butadiene formation from 1-butene and trans-2-butene are presented in Figure 5.1. In both cases, the activity passes through a maximum at $x = 0.45$ in a manner similar to that observed for propene oxidation to acrolein production over the same catalysts [38].

The selectivities to products formed from 1-butene and trans-2-butene are presented in Figure 5.2. For both 1-butene or trans-2-butene, the product selectivities are similar and in each case the main product is 1,3-butadiene. However, the selectivity to 1,3-butadiene is higher starting from 1-butene than from trans-2-butene. For both isomers of butene, the selectivity to 1,3-butadiene passes through a shallow minimum at $x = 0.45$ with increasing value of x. By contrast, the selectivity to isomers of the reactant passes through a maximum at the same value of x.

The main product of isobutene oxidation is methacrolein and the principle byproducts are CO, CO_2 and ethene. As shown in Figure 5.3, the activity for methacrolein formation at 703K increases with the value of x, and then reaches a maximum for $Bi_{0.85}Mo_{0.45}V_{0.55}O_4$ ($x = 0.45$). Product selectivities are also presented in Figure 5.3. The selectivity to methacrolein is 55% for $x = 0$, rises slightly to 60% for $x = 0.45$, and then decreases to 48% for $x = 1.0$. CO_2 and CO (CO_x) are the primary byproducts, and selectivity to CO_x follows a trend with catalyst composition that is opposite to that for methacrolein. The selectivity to methacrolein observed for isobutene oxidation is about 10% lower than that to acrolein for propene reported for identical reaction conditions and catalysts [38]. It is notable, though, that the rate of methacrolein formation at a lower temperature (673K) and a higher partial pressure of isobutene (0.067 atm) is nearly independent of the value of x (Figure 5.4). The product selectivities for $BiVO_4$ are identical those observed at 703K and a propene partial pressure of 0.0167 atm (Figure 5.3). However, for Bi_2MoO_{12} and $Bi_{0.85}V_{0.55}Mo_{0.45}O_4$, the selectivity to methacrolein (40%) is about 10% lower and the selectivity to CO_2 is 10% higher than those observed at 703K and a propene partial pressure of 0.167 atm.

Figure 5.5 illustrate the effects of catalyst composition on the activity and product selectivities for the oxidative dehydrogenation of propane over $Bi_{1-x/3}V_{1-x}Mo_xO_4$. The main product in this case is propene, and the activity at 753K is shown in Figure 5.5. The main byproducts are acrolein and CO_2. The product selectivities are also shown in Figure 5.5. The selectivities to propene and CO_2 pass through shallow minima near $x = 0.45$, whereas the selectivity to acrolein passes through a weak maximum at the same value of x.

5.3.1.2 Partial Pressure Dependences

The rate of 1,3-butadiene formation from both 1-butene and trans-2-butene can be represented by:

$$rate_{1,3-butadiene} = k_{app}P_{1,2-C_4H_8}^m P_{O_2}^n \tag{1}$$

where m and n are the apparent reaction orders of the partial pressure of butenes and oxygen. Values of m and n are given in Tables 5.1 and 5.2 at temperatures of 673 K and 693 K (the high temperature range) and 633 K (the low temperature range) for values of x = 0, 0.45, and 1.0.

For $BiVO_4$ and $Bi_2Mo_3O_{12}$, the data show that for both the high and low temperature regimes, the rate of 1-butene (and trans-2-butene) oxidation to 1,3-butadiene is nearly first-order with respect to the partial pressure of the alkene and nearly zero-order with respect to the partial pressures of O_2, regardless of temperature. The observed reaction orders are identical to those reported by Keizer et al. [42] for the oxidative dehydrogenation of 1-butene over $Bi_2Mo_3O_{12}$ at temperatures between 541K and 688K.

For $Bi_{0.85}Mo_{0.45}V_{0.55}O_4$, the reaction orders were observed to vary with temperature for both reactants. The alkene partial pressure dependence increased from nearly zero order at low temperature (633 K) to close to first order at high temperature (673 and 693 K), whereas the oxygen partial pressure dependence decreased from a positive fractional order at lower temperatures to zero order at higher temperatures.

The rate of isobutene oxidation to methacrolein can be represented by:

$$rate_{methacrolein} = k_{app}P_{iso-C_4H_8}^m P_{O_2}^n \tag{2}$$

Table 5.3 lists the apparent reaction orders for methacrolein production. At both 673 K and 703 K, the isobutene partial pressure dependence over $BiVO_4$ is close to unity and the oxygen partial pressure dependence is nearly zero order. For $Bi_2Mo_3O_{12}$ and $Bi_{0.85}Mo_{0.45}V_{0.55}O_4$, the reactant partial pressure dependences at 703K are again first order in isobutene and zero order in oxygen. However, at 673 K the dependence on isobutene partial pressure becomes negative first order and the oxygen partial pressure dependence becomes nearly first order for both $Bi_2Mo_3O_{12}$ and $Bi_{0.85}Mo_{0.45}V_{0.55}O_4$.

Table 5.4 shows the reaction orders for propane dehydrogenation to propene at 773K. As expected, the rate of propene formation is first order in propane and zero order in oxygen for all values of x.

5.3.1.3 Temperature Dependences

Arrhenius plots for the oxidative dehydrogentation of 1-butene and trans-2-butene to 1,3-butadiene, the oxidation of isobutene to methacrolein, and the oxidative dehydrogenation of propane to propene over $Bi_{1-x/3}V_{1-x}Mo_xO_4$, are shown in Figure 5.6 - 5.8 for temperature in the range of 613 K - 773 K. Values of the apparent activation energies data are listed in Table 5.5 - 5.8.

For temperatures above 663 K, the apparent activation energies for 1-butene and trans-2-butene oxidative dehydrogenation to 1,3-butadiene increases slightly with x, from 6.5 to 9.2 kcal/mol for 1-butene oxidation, and from 14.0 to 17.4 kcal/mol for trans-2-butene oxidation. The activation energy for 1-butene oxidation to 1,3-butadiene obtained on bismuth molybdate (x = 1.0) is similar to that reported by Keizer et al. [42], 11 kcal/mol.

While the apparent activation energies for 1-butene and trans-2-butene oxidative dehydrogenation over $Bi_2Mo_3O_{12}$ and $BiVO_4$ are the same for temperatures below 663 K as they are for higher temperatures, for $Bi_{0.85}Mo_{0.45}V_{0.55}O_4$ the apparent activation energies below 663 K are higher than those measured at high temperatures, 24.3 kcal/mol in the case of 1-butene, 24.7 kcal/mol in the case of trans-2-butene. A similar pattern has been reported by Linn and Sleight [16] for 1-butene oxidation on bismuth molybdate, 14 kcal/mol for temperatures above 663K, and 38 kcal/mol for temperatures below 663K.

The apparent activation energy for the oxidation of isobutene to methacrolein exhibits a complex dependence upon the catalyst composition, the temperature regime, and the partial pressure of isobutene. For $BiVO_4$, the apparent activation energy is the same, 14.7 kcal/mol, independent of temperature or isobutene partial pressure in the feed (0.067 atm or 0.0167 atm). For $Bi_2Mo_3O_{12}$, the apparent activation energy is 21.6 kcal/mol when the isobutene partial pressure is 0.0167 atm and increases to 44.0 kcal/mol when the isobutene partial pressure is 0.067 atm, and for both isobutene partial pressures the apparent activation energy is independent of the temperature. In the case of $Bi_{0.85}Mo_{0.45}V_{0.55}O_4$ the apparent activation energy is found to depend on both the isobutene partial pressure and the reaction temperature. For an isobutene partial pressure of 0.0167 atm, the apparent activation energy is 17 kcal/mol for temperatures above 703 K and it is 44.0 kcal/mol for temperatures below 703 K. However, when the isobutene partial pressure is raised to 0.067 atm, the apparent activation energy becomes 44.0 kcal/mol independent of the reaction temperature (Figure 5.7).

5.3.2 Catalyst Characterization

XANES spectra were acquired in order to establish which elements are reduced at elevated temperature in the presence of different alkenes on $Bi_2Mo_3O_{12}$, $BiVO_4$ and $Bi_{0.85}Mo_{0.45}V_{0.55}O_4$. Measurements were taken before and after exposure to 1-butene, trans-2-butene, isobutene, and propene at 713 K for 2 h. All the spectra are shown in the Supplementary Information.

The position of the Bi L_3-edge did not change with time and remained identical to that for Bi_2O_3 independent of the composition of the reducing agent or the catalyst compositions. After exposure to propene, 1-butene, trans-2-butene, and isobutene the Mo K-edge shifted to lower energy, and the height of the pre-edge feature decreased. Similar trends were observed for the V K-edge. After reduction, the edge shifts and the pre-edge feature height decreased indicating a reduction of V. For both the Mo and V K-edges, a larger shift in the edge position and a smaller pre-edge feature were observed after reduction with all butene isomers than with propene, indicating that butenes are better

reducing agents than propene. It is also noted that the reported changes in the Mo and V K-edge spectra were larger for $Bi_{0.85}V_{0.55}Mo_{0.45}O_4$ than for $BiVO_4$ or $Bi_2Mo_3O_{12}$.

Diffuse reflectance UV-VIS spectra were acquired in order to further characterize the reducing power of different butenes. When the catalyst is heated to 673 K and exposed to a reducing agent, the absorbance of the baseline at a wavenumber below the adsorption edge increased as a function of time, due to catalyst reduction. The absorbance at 800 nm was plotted a function of time of exposure to reducing conditions, and the initial reduction rate was calculated (Supplementary Information). The correlation of the apparent rate coefficient k_{app} for different butene isomers with the initial rate of reduction measured by UV-VIS on $Bi_{0.85}V_{0.55}Mo_{0.45}O_4$ is shown in Figure 5.9. The observed linear correlation suggests that the oxidation of alkenes proceeds via a Mars van Krevelen mechanism involving catalyst oxygen atoms. The more readily the reactant can be reduced, the higher is the reaction rate. The reducibility of isobutene and trans-2-butene is lower than that of 1-butene, but greater than that of propene.

5.4 Discussion

5.4.1 Mechanism and Kinetics of the Oxidative Dehydrogenation of Propane, 1-butene, and Trans-2-butene and Oxidation of Isobutene

Tables 5.1 and 5.2 show that the kinetics for the oxidative dehydrogenation of propane to propene and of 1-butene and trans-2-butene to butadiene are very similar – essentially first order in the partial pressure of the alkane or alkene and zero order in the partial pressure of oxygen – for $BiVO_4$ and Bi_2MoO_{12}, and for $Bi_{0.85}V_{0.55}Mo_{0.45}O_4$ at temperatures above 663 K. Taken together, the UV-Vis and XANES data presented in Figure 5.9 and Figure 5.S1 – 5.S5 (Supplementary Information) suggest that in all cases oxidative dehydrogenation proceeds via a Mars van Krevelen mechanism involving oxygen atoms of the catalysts. The observed kinetics can be rationalized on the basis of the mechanism shown in Scheme 5.1, which is illustrated for the oxidative dehydrogenation of 1-butene on Bi_2MoO_{12} and is similar to that developed to explain the kinetics of propene oxidation to acrolein [38]. Reaction begin with the physical adsorption of 1-butene (Step 1) followed by hydrogen abstraction from the $-CH_2-$ group of 1-butene by one of the Mo=O bonds of the catalyst and concurrent reduction of Mo^{6+} to Mo^{5+} (Step 2). As in the case for propene oxidation, Step 2 is taken to be the rate-limiting step. Hydrogen abstraction is taken to occur from the $-CH_2-$ group of 1-butene because the strength of this C-H bond is weaker than that of other C-H bonds in the reactant. As discussed below, this assumption is supported by the observation that the apparent activation energy for the oxidative dehydrogenation of propane, 1-butene, and trans-2-butene correlates with the strength of the weakest C-H bond of the reactant. Getsoian et al. [39, 40] have demonstrated that of the three types of Mo=O bonds present on the surface of Bi_2MoO_{12}, the one that weakly interacts with the lone pair on Bi (e.g., Bi···O=Mo) is the most active for activating the C-H bond in the methyl group of propene. We, therefore, assume that this will also be the most active form of oxygen in the present system. The next step following C-H bond cleavage of the reactant involves abstraction of a hydrogen atom from the methyl group of the methyl-allyl radical (Step 3), which reduces the adjacent Mo=O to Mo^{5+} and produces 1,3-butadiene. In the final two steps of

the cycle, water is formed and desorbed reversibly producing an oxygen vacancy (Step 4) and the catalyst is then reoxidized by oxygen.

A rate expression for the rate of 1-butene consumption shown in Eqn. 3 can be derived under the assumption that Step 2 is rate-limiting and that the pseudo-steady-state assumption is valid for intermediates [38]:

$$rate = \frac{k_1 k_2 P_{C_4H_8}[S]}{(k_2 + k_{-1})\left[1 + \frac{k_1 P_{C_4H_8}}{k_2 + k_{-1}} + \frac{k_1 k_2 P_{C_4H_8}}{k_3(k_2 + k_{-1})} + \left(\frac{k_1 k_2 P_{C_4H_8}}{k_4(k_2 + k_{-1})} + \frac{k_1 k_2 k_{-4} P_{C_4H_8} P_{H_2O}}{k_4 k_5 P_{O_2}(k_2 + k_{-1})}\right) + \frac{k_1 k_2 P_{C_4H_8}}{k_5 P_{O_2}(k_2 + k_{-1})}\right]} \quad (3)$$

In Eqn. 3, k_i and k_{-i} represent the rate coefficients for reaction i in the forward and reverse directions, respectively, K_i represents the equilibrium constant for reaction i, P_j represents the partial pressure of reactant or product j, and [S] is the number of active sites per unit BET catalyst surface area.

When the rate of catalyst reoxidation is rapid relative to the rate of catalyst reduction, catalyst surface is fully oxidized, and if it is assumed that $k_{-1} \gg k_2$, Eqn. 3 simplifies to:

$$rate = \frac{k_1 k_2 [S]}{(k_{-1} + k_2)} P_{C_4H_8} \cong K_1 k_2 P_{C_4H_8}[S] = k_{app} P_{C_4H_8} \quad (4)$$

and the apparent rate constant k_{app} is now given by $K_1 k_2 [S]$. The form of Eqn. 4 is completely consistent with the kinetics observed for the oxidative dehydrogenation of 1-butene and trans-2-butene on $BiVO_4$ and Bi_2MoO_{12} at all temperatures and for $Bi_{0.85}V_{0.55}Mo_{0.45}O_4$ at temperatures above 663 K. It is also noted that Eqn. 4 also holds for the oxidative dehydrogenation of propane at all temperature for all three catalysts ($BiVO_4$, $Bi_{0.85}V_{0.55}Mo_{0.45}O_4$, and Bi_2MoO_{12}).

Tables 5.1 and 5.2 show that for $Bi_{0.85}V_{0.55}Mo_{0.45}O_4$ the orders in 1-butene and trans-2-butene change significantly for temperatures below 663 K. Thus, at 633 K the order in alkene decreases to nearly zero and the order in oxygen rises to 0.3. We also note that the apparent activation energy increases for both isomers of butene. Notably, though, changes in reaction order in alkene and oxygen, and the apparent activation energy, do not change for the oxidative dehydrogenation of propane to propene over $Bi_{0.85}V_{0.55}Mo_{0.45}O_4$. We attribute the changes in the reaction orders and the apparent activation energy to a transition of the catalyst from a state in which the catalyst surface is fully saturated with oxygen to one in which the catalyst is partially reduced. Under the latter circumstance the rate of catalyst reoxidation becomes rate limiting. The reason that the transition in kinetic regimes is not observed for the oxidative dehydrogenation of propane is that the rate of this reaction is two orders of magnitude lower than that for oxidative dehydrogenation of either 1-butene or 2-butene. Reference to Eqn. 3 shows that in the limit that the ratio of k_2/k_5 becomes very large, the last term in the denominator becomes dominant and the rate expression reduces to:

$$rate = k_5 P_{O_2} \quad (5)$$

116

The kinetics for isobutene oxidation to methacrolein for temperatures above 663 K are very similar to those reported earlier for the oxidation of propene to acrolein, to the kinetics reported here for the oxidative dehydrogenation of 1-butene and trans-2-butene to 1,3-butadiene and the kinetics for the oxidative dehydrogenation of propane to propene. For $BiVO_4$, the kinetics are first order in isobutene and zero order in oxygen independent of the isobutene partial pressure (0.0167 atm or 0.067 atm) and for Bi_2MoO_{12} and $Bi_{0.85}V_{0.55}Mo_{0.45}O_4$ only for isobutene partial pressures below 0.0167 atm. We note that under these constraints the apparent activation energies for isobutene oxidation are 14.7 kcal/mol for $BiVO_4$, 17.0 kcal/mol for Bi_2MoO_{12}, and 21.6 kcal/mol for $Bi_{0.85}V_{0.55}Mo_{0.45}O_4$.
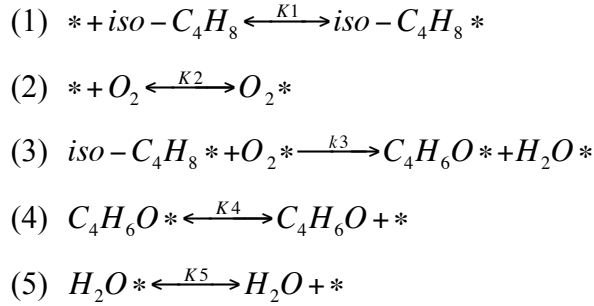
The kinetics of isobutene oxidation have been discussed to only a limited degree, with very different conclusions drawn by different authors [32-34]. Mann and Ko [32] considered 13 different mechanisms, and concluded rate of reaction on copper-promoted bismuth molybdate is described best by a mechanism in which the rate-controlling step is assumed to be the surface reaction between charged absorbed 2-methylpropene and oxygen molecules. By contrast, Benyahia and Mearns [33,34] found that fractional apparent orders with respect to isobutene and oxygen for isobutene oxidation over multicomponent bismuth molybdate, which they rationalized on the basis of a redox model. It should be noted though none of these studies reported sufficient rate data and catalyst characterization from which one could develop a compelling case for a particular reaction mechanism.

The kinetics of isobutene oxidation for the conditions noted above can be rationalized using the mechanism proposed in Scheme 5.2, which is very similar to that reported in our earlier work on the oxidation of propene to acrolein [38], as well as being similar to that shown in Scheme 5.1 for the oxidative dehydrogenation of alkenes and alkanes. The primary difference is that the 2-methyl-allyl radical formed in Step 2 is now trapped by reaction with a molybdenyl oxygen atom. This step, in turn leads to the formation of methacrolein. By contrast the 1-methyl-allyl radical formed by from 1-butene or trans-2-butene is not stabilized and, instead loses an H atom to form 1,3-butadiene. Moro-oka has noted that oxygen addition is only observed when the intermediate formed upon cleavage of the weakest C-H bond of the reactant does not have a weak C-H bond that can be easily cleaved [43]. In accord with Moro-oka's statement, we note that the C-H bond in the methyl group of 1-methyl-allyl will cleave easily leading to the formation of 1,3-butadiene. However, the C-H bond in the methyl group of 2-methyl-allyl is harder to cleave, and consequently is not possible to form a stable product. As a result, 2-methyl-allyl (from isobutene) will undergo oxygen insertion to form methacrolein, but 1-methyl-allyl (from 1-butene and trans-2-butene) will form 1,3-butadiene directly after dehydrogenation.

As noted earlier, the kinetics of isobutene are significantly different for Bi_2MoO_{12} and $Bi_{0.85}V_{0.55}Mo_{0.45}O_4$ for high isobutene partial pressures, and in the case of $Bi_{0.85}V_{0.55}Mo_{0.45}O_4$ at temperatures below 703 K. Under these conditions, the isobutene partial pressure becomes inverse first order and the oxygen partial pressure becomes first order, and the apparent activation energy increases to 44 kcal/mol for both catalysts. In situ UV-Vis spectra (see Supporting Information) also show more significant reduction of $Bi_{0.85}V_{0.55}Mo_{0.45}O_4$ at 673 K particularly for an isobutene partial pressure of 0.067 atm

than is observed the same experiment is carried out in 1-butene. Visual inspection of the catalyst after operation under steady-state reaction conditions also confirms that isobutene reduces both Bi_2MoO_{12} and $Bi_{0.85}V_{0.55}Mo_{0.45}O_4$ to a greater extent than does 1-butene. After reaction in 0.067 atm of isobutene and 0.167 atm of oxygen, the color of Bi_2MoO_{12} changes from white for the fully oxidized catalyst to grey, and $Bi_{0.85}V_{0.55}Mo_{0.45}O_4$ changes from bright yellow to dark yellow.

The kinetics of isobutene oxidation observed on the reduced forms of Bi_2MoO_{12} and $Bi_{0.85}V_{0.55}Mo_{0.45}O_4$ can be rationalized in terms of the following reactions sequence:

(1) $* + iso - C_4H_8 \xleftrightarrow{K_1} iso - C_4H_8*$

(2) $* + O_2 \xleftrightarrow{K_2} O_2*$

(3) $iso - C_4H_8 * + O_2* \xrightarrow{k_3} C_4H_6O * + H_2O*$

(4) $C_4H_6O* \xleftrightarrow{K_4} C_4H_6O + *$

(5) $H_2O* \xleftrightarrow{K_5} H_2O + *$

where " $*$ " represents an active site. In contrast to the mechanism presented in Scheme 5.2, is assumed here that oxidation occurs via reaction with adsorbed O_2. Implicit in the development of this pathway is that the reduction of the catalyst is much more rapid than its reoxidation. Step 1 and step 2 of the proposed sequence represent the adsorption of isobutene and oxygen onto active sites. Step 3 is the bimolecular reaction of the adsorbed molecules. Step 4 and 5 are desorption of methacrolein and water. If step 1, 2, 4 and 5 are assumed to be quasi-equilibrated and step 3 is the irreversible, rate-determining step, then the rate of methacrolein formation is given by the following relation:

$$rate_{methacrolein} = \frac{k_3 K_1 K_2 P_{iso-C_4H_8} P_{O_2}[S]}{\left(1 + K_1 P_{iso-C_4H_8} + K_2 P_{O_2} + \frac{P_{C_4H_6O}}{K_4} + \frac{P_{H_2O}}{K_5}\right)^2} \tag{6}$$

Since the conversion of isobutene was always below 5%, we assume that $P_{C_4H_6O}$ and P_{H_2O} are negligible. If we assume that at higher isobutene partial pressures, isobutene is strongly adsorbed onto the catalyst surface, so that adsorbed isobutene is the most abundant surface intermediate, then

$$rate_{methacrolein} = \frac{k_3 K_2 P_{O_2}[S]}{P_{iso-C_4H_8}} \tag{7}$$

Eqn.7 is consistent with the observed kinetics shown in Table 5.3, in which the rate of isobutene oxidation to methacrolein is negative first order in isobutene and positive first order in oxygen. This rate expression suggests that the high apparent activation energy measure for reduced Bi_2MoO_{12} and $Bi_{0.85}V_{0.55}Mo_{0.45}O_4$ is attributable to an even higher activation barrier for Step 3.

To this point, we have only discussed the mechanism and kinetics for formation of primary products. Therefore, we turn next to a discussion of the mechanism by which byproducts are formed. The byproducts of 1-butene and trans-2-butene over $Bi_{1-x/3}V_{1-}$

$_x$Mo$_x$O$_4$ catalysts are other butene isomers, but the byproducts of isobutene are mainly CO, CO$_2$ and ethene.

For the oxidative dehydrogenation of 1-butene and trans-2-butene, once the 1-methyl-allyl intermediate is formed following H abstraction, the intermediate can undergo further hydrogen abstraction, yielding 1,3-butadiene, or reinsertion of the first abstracted hydrogen at the end of the allylic moiety to yield other isomers. One might expect this process to lead to the same product distribution regardless of the starting alkene. However, our experimental data show that the product distributions resulting from the allylic intermediates produced from 1-butene and trans-2-butene are different (Figure 5.2). The selectivity to 1,3-butadiene is higher than that for 1-butene compared to trans-2-butene, indicating oxidative dehydrogenation is favored for 1-butene, but isomerization is favored for trans-2-butene. Similar results have been observed by Portela [8], and the reason can be explained as follows. For 1-butene, once 1-methyl-allyl intermediate is formed, the insertion must occur at the end of the intermediate. However, the position of the first abstracted hydrogen is not at the end of the intermediate. For trans-2-butene, the position of the first abstracted hydrogen is at the end of the intermediate, so it becomes much easier to form an isomerization product, cis-2-butene. This difference is illustrated in Scheme 5.3. The proposed pathways also help to explain the higher selectivity to cis-2-butene than 1-butene from trans-2-butene.

The byproduct formation occurring during the oxidation of isobutene differs from that observed for 1- and trans-2-butene. Isobutene does not undergo isomerization because the structure of the 2-methyl-allyl intermediate does not lend itself to isomerization, and thus only CO and CO$_2$ are formed as byproducts. The partial pressure dependence on O$_2$ for CO$_2$ formation is 0.4 on Bi$_2$Mo$_3$O$_{12}$, and is first order for CO formation, which is the same as for propene oxidation [38]. This suggests that the oxygen atoms in CO$_2$ come from both gas phase oxygen and lattice oxygen; however, the oxygen atom in CO only comes from gas phase oxygen. Possible pathways to these products are shown in Scheme 5.4. We still assume that CO and CO$_2$ originate from the precursor to methacrolein, in a manner similar to what we proposed earlier for CO and CO$_2$ formation from propene. However, since the selectivity of methacrolein from isobutene is lower (~50%, Figure 5.3) than the selectivity of acrolein from propene (~70%) [38] on bismuth molybdate, the selectivities to CO and CO$_2$ are higher for isobutene than for propene. As is shown in Scheme 5.4, for isobutene, the reaction sequence begins with the 2-methyl-allyl species formed in the rate-limiting step. Reaction of adsorbed O$_2$ with this species is proposed to form an intermediate leading to CO and CO$_2$. After re-oxidization, a new intermediate is formed, which can also produce CO and CO$_2$. This intermediate is exactly the same as the starting point of the allyl species formed in the RDS for propene to acrolein [38]. As a result, one isobutene molecule can produce more CO and CO$_2$ than propene, leading to a higher selectivity to CO$_x$. It should be noted that in Scheme 5.4, the oxygen in CO comes from O$_2$, whereas one of the oxygen atoms in CO$_2$ comes from O$_2$ and the other from lattice oxygen.

5.4.2 Correlation of the Apparent Activation Energies and Preexponential Factors with the Molecular Structure of the Reactants

The discussion of the mechanism and kinetics for the oxidative dehydrogenation of propane, 1-butene, and tran-2-butene and for the oxidation of isobutene are very similar at temperatures above 673 K, for which the catalyst is saturated with oxygen and the rate-limiting step is assumed to involve cleavage of the weakest C-H bond in the reactant. As noted earlier, under these circumstances, the rate of alkane of alkene consumption can be described by Eqn. 4. This expression can now be written to identify the significance of the apparent preexponential factor and the apparent activation barrier. Thus:

$$k_{app} = K_1 k_2 [S] = \sigma A_{app} \exp(\frac{-E_{app}}{RT})[S] = \sigma A_{app} \exp(\frac{-\Delta H_{ads} - E_{int}}{RT})[S] \qquad (8)$$

in σ is the symmetry number (i.e., how many equivalent C-H bonds could participate in the rate-limiting step). The symmetry number for different reactants is shown in Table 5.9. The apparent activation energy is the sum of the change in enthalpy of the adsorbate upon adsorption of a hydrocarbon molecule onto the surface, ΔH_{ads}, and the intrinsic activation energy of the C-H bond breaking, E_{int}. If we assume that the heat of adsorption is similar for all the butene isomers, and the difference between propene and 1-butene on bismuth molybdate is ~ 3 kcal/mol [44], we can expect a similar positive correlation between the intrinsic activation energy and the weakest C-H bond dissociation energy. The stronger the C-H bond, the more energy is needed to break it. We, therefore, conclude that a plausible descriptor for relating reactant activity is the strength of the weakest C-H bond.

Based on the preceding discussion, we plot the apparent activation energy versus the weakest C-H bond dissociation energy measure for the oxidative dehydrogenation of propane, 1-butene, and trans-2-butene, and for the oxidation of propene [38] and isobutene carried out over $Bi_2Mo_3O_{12}$, $Bi_{0.85}V_{0.55}Mo_{0.45}O_4$ and on $BiVO_4$. Figure 5.10 shows that for reactions over a given metal oxide, the apparent activation energy correlates with the strength of the weakest C-H bond. We note that the observed correlation is consistent with the theoretical interpretation of the intrinsic activation energy developed by Getsoian et al. for the oxidation of propene to acrolein [45]. The authors of this study reported that the intrinsic activation energy (E_{int}) determined from density functional theory can be interpreted in terms of the following sum:

$$E_{int} = E_{C-H} + E_G + E_{O-H} \qquad (9)$$

in which E_{C-H}, E_{O-H}, and E_G refers to the energy required for dissociation of a C-H bond, formation of an O-H bond, and the band gap of the catalyst, respectively.

For a given reactant, the bond dissociation energy of the C-H bond involved in the rate-limiting step is the same and independent of catalyst composition. The DFT calculations suggest that the O-H bond formation energy does not depend strongly on the identity of the nearest neighbor to oxygen, leading to the conclusion that the principle term in Eqn. 9 depending on catalyst composition is E_G, and hence, that for a given value of E_{C-H}, the apparent activation energy should increase with this parameter. A correlation of E_{int} with E_G for propene oxidation to acrolein was reported by Getsoian et al. [45] A similar trend can be deduced from Figure 5.10, consistent with the decrease in the

measured band gap in the order $Bi_2Mo_3O_{12}$ (2.70 eV) $>$ $Bi_{0.85}V_{0.55}Mo_{0.45}O_4$ (2.32 eV) $>$ $BiVO_4$ (2.06 eV).

The next question is whether the apparent preexponential factor, A_{app}, correlates with the apparent activation energy. This question is difficult to address unambiguously because it is not known whether the number of active sites, [S], is constant with changes in catalyst composition. For this reason, Figure 5.11 shows plots of $\ln(A_{app}[S])$ versus E_{app} for three representative catalysts, since it is reasonable to assume that the number of active sites for a given catalyst composition is independent of the composition of the reactant. It is evident from Figure 5.11 that for each catalyst there is a positive correlation between $\ln(A_{app}[S])$ and E_{app}. It is notable that the data points for isobutene oxidation lie farthest from the trend line and always above this line. Although the reason for this deviation is not known, we hypothesize that nature of the deviation suggests that the isobutene may access a larger number of surface oxygen atoms than that can any of the other reactants. This interpretation is certainly qualitatively consistent with the observation that isobutene is a more effective reducing agent than 1-butene or trans-2-butene.

The positive correlation of A_{app} with E_{app} indicates that the product of the preexponential factor for k_2 and entropy term of adsorption for K_1 in Eqn. 8 increases with the activation energy for this reaction. While it is possible that changes in the entropy of adsorption also contribute to changes in the magnitude of A_{app}, this seems unlikely, since the values for E_{app} and A_{app} are very similar for both propene oxidation and butene oxidative dehydrogenation. We, therefore, suggest that the principle cause of the increases in A_{app} is attributable to increase in the activation entropy for Step 2. This trend is what would be expected for a looser transition state involving a higher activation barrier.

5.5 Conclusions

The oxidative dehydrogenation of 1-butene and trans-2-butene to 1,3-butadiene, the oxidative dehydrogenation of propane to propene, and the oxidation of isobutene to methacrolein were investigated over $Bi_{1-x/3}V_{1-x}Mo_xO_4$ for a range of temperatures and reactant partial pressures. These investigations were complemented by characterization of the oxidation state of the catalyst by XANES and UV-Vis spectroscopy. These studies show that the reaction kinetics are strongly dependent on the state of catalyst reduction, which in turn depends on the catalyst and reactant composition, and on the reaction temperature and reactant partial pressures.

For conditions where the catalyst is fully oxidized, the kinetics of all reactions are nearly identical. The rate of reaction is linearly dependent on the alkane or alkene partial pressure and independent of the oxygen partial pressure, and the apparent activation energy ranges from 6.5 kcal/mol to 31.5 kcal/mol depending on the reactant composition. The kinetics for oxidative dehydrogenation and oxidation over fully oxidized catalysts can be interpreted in terms of a Mars van Krevelen mechanism in which the reactant adsorbs reversibly on the catalyst surface and then undergoes cleavage of the weakest C-H bond in the rate-limiting step. In the case of 1-butene and trans-2-butene, the allyl radical formed contains a relatively weak C-H bond which can undergo cleavage leading

to 1,3-butadiene. By contrast the allyl radical formed from isobutene does not contain such a C-H bond, and instead is first stabilized by addition to an oxygen atom on the catalyst surface. Subsequent cleavage of an H atom from the α-carbon atom of the vinyl alkoxide intermediate leads to the formation of methacrolein. This pattern of reaction is similar to that observed previously for the oxidation of propene to acrolein [38]. The apparent activation energy and preexponential factors for both the oxidative dehydrogenation of propane, 1-butene, and trans-2-butene, and the oxidation of propene and isobutene increase with the strength of the weakest C-H bond of the reactant involved in the rate-limiting step. A correlation of the apparent preexponential factor with the apparent activation energy, and hence the weakest C-H bond of the reactant is also observed. It is proposed that this trend is attributable to a transition state structure that is more strongly bound to the catalyst surface and is more negative in entropy change the stronger the C-H bond that must be cleaved. For a given reactant, it is also observed that the apparent activation energy is lower the lower the band gap of the catalyst, and hence the ease of undergoing reduction.

A second regime is observed when the catalyst cannot be maintained in a fully oxidized state and the rate of reaction becomes rate-limited by the reoxidation of the catalysts. This is the case for the oxidative dehydrogenation of 1- and trans-2-butene over $Bi_{0.85}V_{0.55}Mo_{0.45}O_4$ at low temperature regime. In this case the rate of oxidative dehydrogenation becomes zero order in alkene partial pressure and fractional oxygen partial pressure, and the apparent activation energy becomes independent of reactant composition.

A third reaction regime is observed for isobutene oxidation under conditions that result in a substantial degree of catalyst reduction. For $Bi_2Mo_3O_{12}$ and $Bi_{0.85}Mo_{0.45}V_{0.55}O_4$ the activation energy is 44.0 kcal/mol at all temperatures when the isobutene partial pressure is raised to 0.067 atm. This same apparent activation energy is also observed for $Bi_{0.85}Mo_{0.45}V_{0.55}O_4$ at temperatures below 703K when the isobutene partial pressure is 0.0167 atm.

5.6 Supplemental Information

5.6.1 Measurement of Catalyst Reduction by XANES

For $Bi_{0.85}Mo_{0.45}V_{0.55}O_4$ (x=0.45), XANES spectra for the L_3-edge of Bi, K-edge of Mo and V before and after exposure to propene and 1-butene for 2 hours are shown in Figure 5.S1. For both propene and 1-butene, the Bi L_3-edge (13429 ev) does not change with time and remains identical to that for Bi_2O_3, indicating that Bi remains in the 3+ state and is not reduced. For Mo K-edge, two standards are used. The Mo in the 6+ state in $CaMoO_4$ exists as isolated tetrahedral molybdate. The strong pre-edge feature is due to the high degree of p-d hybridization in tetrahedral coordination environments. For MoO_2, Mo^{4+} cations occur as nearly octahedral molybdate units, so no pre-edge feature due to no p-d hybridization. After reduction under propene and 1-butene, Mo K-edge position shifts to lower energy, and the height of pre-edge feature decreases. Similar trend is observed on V K-edge. After reduction, the edge shifts and pre-edge feature height decreases indicating a reduction of V to almost 4+ oxidation state. For both Mo K-edge and V K-edge, a larger shift of edge position and lower pre-edge feature after reduction of 1-

butene compared with propene means that 1-butene is a better reducing agents than propene.

Similar behavior is observed when use trans-2-butene and isobutene as reducing agents. Figure 5.S2 and 5.S3 show XANES spectra for the L_3-edge of Bi, the K-edge of Mo, and the K-edge of V before and after exposure of $Bi_{0.85}V_{0.55}Mo_{0.45}O_4$ (x = 0.45) to trans-2-butene and isobutene, respectively. Bismuth is not reduced, molybdenum is reduced from Mo^{6+} to almost Mo^{4+} and vanadium is reduced from 5+ to 4+ oxidation state. Both trans-2-butene and isobutene show stronger reduction ability than propene.

Figure 5.S4 and 5.S5 show XANES spectra before and after exposure of 1-butene on $Bi_2Mo_3O_{12}$ and $BiVO_4$. Bi^{3+} states remain Bi^{3+}, but molybdenum and vanadium are reduced. All changes are consistent with reduction using trans-2-butene and isobutene (not shown here). To summarize, for all compositions of $Bi_{1-x/3}V_{1-x}Mo_xO_4$, only molybdenum and vanadium are reduced by 1-butene, trans-2-butene and isobutene. This phenomenon is identical to propene. All butenes are better reducing agents than propene.

5.6.2 Determination of the Reduction Rate from UV-VIS Spectra

Exposure of catalysts heated to 673K in a non-reducing atmosphere to reducing conditions results in a time-dependent increase in absorbance at energies below the edge. This effect is illustrated in Figure 5.S6. The increase in absorbance of the catalyst at energies below the absorption edge is indicative of reduction of the catalyst.

5.6.3 Reduced State of Catalysts for Isobutene Oxidation

The kinetics of isobutene are significantly different for Bi_2MoO_{12} and $Bi_{0.85}V_{0.55}Mo_{0.45}O_4$ at high isobutene partial pressures, and in the case of $Bi_{0.85}V_{0.55}Mo_{0.45}O_4$ at temperatures below 703 K. In situ UV-Vis spectra show more significant reduction at steady state of $Bi_{0.85}V_{0.55}Mo_{0.45}O_4$ at 673 K particularly for an isobutene partial pressure of 0.067 atm than is observed the same experiment is carried out in 1-butene (Figure 5.S7). The edge position shifts, which is an indication of a structural change due to substantial degree of catalyst reduction.

5.7 References

[1] J.D. Idol. U.S. Patent 2, 904, 580, 1959.
[2] G.W. Hearne, M.L. Adams, U.S. Patent 2, 451, 485 1948.
[3] PH. A. Batist, J.F.H. Bouwens, G.C.A. Schuit, J. Catal. 25 (1972) 1-11.
[4] J. M. Lopez Nieto, E. A. Burga, G. Kremenic, Ind. Eng. Chem. Res. 29 (1990) 337-342.
[5] S. Breiter, H.-G. Lintz, Chem. Eng. Sci. 50 (1995) 785 -791.
[6] H. Lee, J.C. Jung, H. Kim, Y.-M. Chung, T.J. Kim, S.J. Lee, S.-H. Oh, Y.S. Kim, I.K. Song, Catal. Commun., 9 (2008) 1137-1172.
[7] D.A.G. van Oeffelen, J.H.C. van Hooff, G.C.A. Schuit, J. Catal. 95 (1985) 84-100.
[8] M. Farinha Portela, Top. Catal., 15 (2001) 241-243.

[9] H.H. Voge, C.D. Wagner, D.P. Setvenson, J. Catal. 2 (1963) 58-62.

[10] W.M.H. Sachtler, Rec. Trav. Chim. 82 (1963) 243-245.

[11] L.D. Krenzke, G.W. Keulks, J. Catal. 61 (1980) 316-325.

[12] W. Ueda, K. Asakawa, C.L. Chen, Y. Moro-Oka, T. Ikawa, J. Catal. 101 (1986) 360-368.

[13] G.W. Keulks, J. Catal. 19 (1970) 232- 235.

[14] B. Grzybowska, J. Haber, J. Janas, J. Catal. 49 (1977) 150-163.

[15] J. Haber, W. Turek, J. Catal. 190 (2000) 320-326.

[16] W.J. Linn, A.W. Sleight, J. Catal. 41 (1976) 134-139.

[17] I. Matsuura, G.C.A. Schuit, J. Catal. 20 (1971) 19-39.

[18] M. Oliveira, M.F. Portela, M. J. Pires, F.R. Riebeiro. Can. J. Chem. Eng. 61 (1983) 87-92.

[19] J.C. Jung, H. Kim, A.S. Choi, Y-M. Chung, T.J. Kim, S.J. Lee, S-H. Oh, I.K. Song, J. Mol. Catal. A 259 (2006) 166-170.

[20] B. Grzybowska, J. Haber, J. Komorek, J. Catal. 25 (1972) 25-32.

[21] E.V. Hoefs, J.R. Monnier, G.W. Keulks, J. Catal. 57 (1979) 331-337.

[22] M.W.J. Wolfs, PH.A. Bastist, J. Catal. 32 (1974) 25-36.

[23] P. Mars, D.W. van Krevelen, Chem. Eng. Sci. 3 (1954) 41-59.

[24] R.K. Grasselli, Top. Catal. 21 (2001) 79-88.

[25] R.K. Grasselli, J. Chem. Educ. 63 (1986) 216-221.

[26] C.R. Adams, H.H. Voge, C.Z. Zorgan., W. E. Armstrong, J. Catal. 3 (1964) 379-386.

[27] PH. A. Batist, C.J. Kapteijns, B.C. Lippens, G.C.A. Schuit, J. Catal. 7(1967) 33-49.

[28] C.R. Adams, T. T. J. Jennings, J. Catal. 2 (1963) 63-68

[29] A. C. A. M. Bleijenberg, B.C. Lippens, G.C.A. Schuit, J. Catal. 4(1965) 581-585.

[30] PH. A. Batist, C.J. Kapteijns, B.C. Lippens, G.C.A. Schuit. J. Catal. 7(1967) 33-49.

[31] PH. A. Batist, A.H.W.M. Der Kinderen, Y. Leeuwenburgh, F.A.M.G. Mets, G.C.A. Schuit, J. Catal. 12(1968) 45-60.

[32] R. S. Mann, D.W. Ko, J. Catal. 30 (1973) 276-282.

[33] F. Benyahia, A.M. Mearns, Appl. Catal. 66 (1990) 383-393.

[34] F. Benyahia, A.M. Mearns. Appl. Catal. 70 (1991) 149-159.

[35] M. Cesari, G. Perego, A. Zazzetta, G. Manara, G. Notari, J. Inorg. Nucl. Chem. 33 (1971) 3595-3597.

[36] A.W. Sleight, K. Aykan, D.B. Rogers, J. Solid State Chem. 13 (1975) 231-236.

[37] A.W. Sleight, W. J. Linn, Ann. N. Y. Acad. Sci. 272 (1976) 22-44.

[38] Z. Zhai, A. Getsoian, A. T. Bell, J. Catal. 308 (2013) 25-36.

[39] A. Getsoian, V. Shapovalov, A. T. Bell, J. Phys. Chem. C 117 (2013) 7123-7137.

[40] A. Getsoian, A. T. Bell, J. Phys. Chem. C 117(2013), 25562-25578.

[41] R.E. Jentoft, S.E. Deutsch, B.C. Gates, Rev. Sci. Instrum. 67 (1996) 2111–2112.

[42] K. Keizer, PH.A. Batist, G.C. Schuit, J. Catal. 1969(15) 256-266.

[43] Y. Moro-oka, Catal. Today. 45 (1998) 3-12.

[44] M. Krivanek, P. Jiri, J. Strnad, J. Catal. 23 (1971) 259-269.

[45] A. Getsoian, Z. Zhai, A. T. Bell, J. Am. Chem. Soc. 136 (2014) 13684−13697.

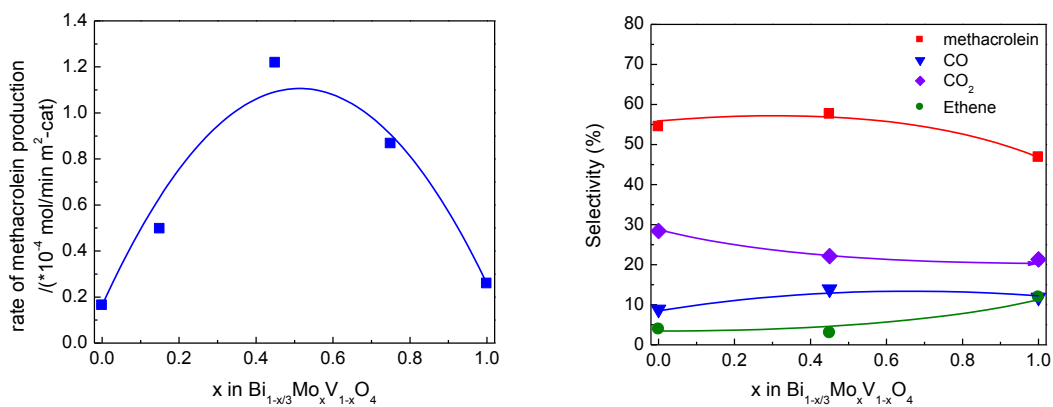**Figure 5.1** Variation in the rate of the oxidative dehydrogenation of 1-butene and trans-2-butene to 1,3-butadiene on $Bi_{1-x/3}V_{1-x}Mo_xO_4$ with x at 673 K. Left: 1-butene, $P_{1-C4H8} = 0.067$ atm, $P_{O2} = 0.167$ atm. Right: trans-2-butene, $P_{trans-2-C4H8} = 0.067$ atm, $P_{O2} = 0.167$ atm.
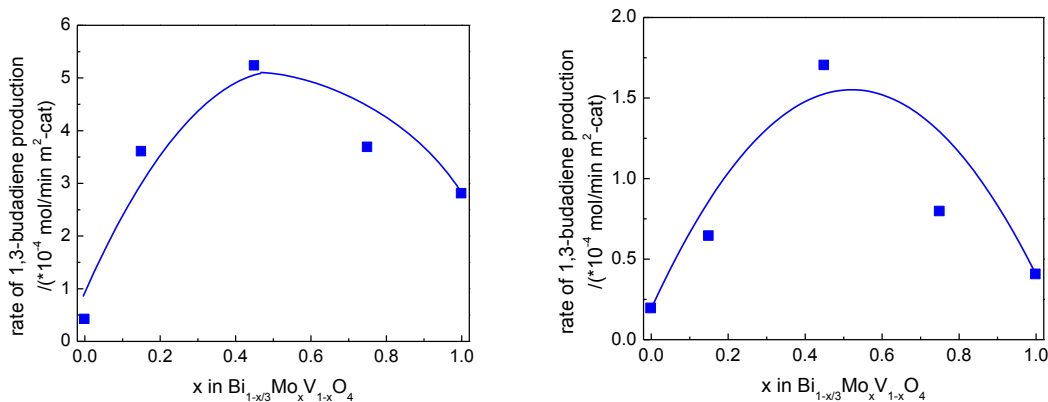

Figure 5.2 Dependence of the selectivity of $Bi_{1-x/3}V_{1-x}Mo_xO_4$ for the oxidative dehydrogenation of 1-butene and trans-2-butene at 673 K. Left: 1-butene, $P_{1-C4H8} = 0.067$ atm, $P_{O2} = 0.167$ atm. Right: trans-2-butene, $P_{trans-2-C4H8} = 0.067$ atm, $P_{O2} = 0.167$ atm.
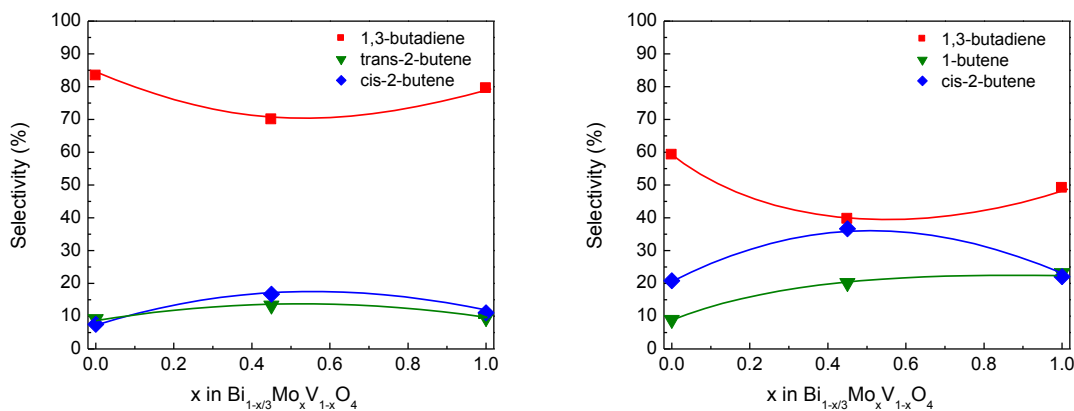
Figure 5.3 Variation in the rate and selectivity of iso-butene oxidation to methacrolein on $Bi_{1-x/3}V_{1-x}Mo_xO_4$ with x. $P_{iso-C4H8} = 0.0167$ atm, $P_{O2} = 0.167$ atm, 703 K.

Figure 5.4 Variation in the rate and selectivity of iso-butene oxidation to methacrolein on $Bi_{1-x/3}V_{1-x}Mo_xO_4$ with x. $P_{iso-C4H8} = 0.067$ atm, $P_{O2} = 0.167$ atm, 673K.
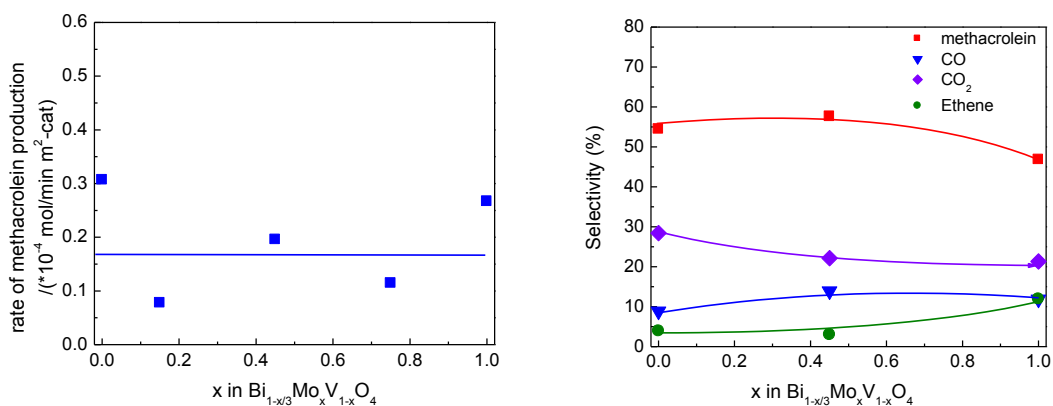
Figure 5.5 Variation in the rate and selectivity of the oxidative dehydrogenation of propane to propene on $Bi_{1-x/3}V_{1-x}Mo_xO_4$ with x. P_{C3H8} = 0.067 atm, P_{O2} = 0.167 atm, 753 K.
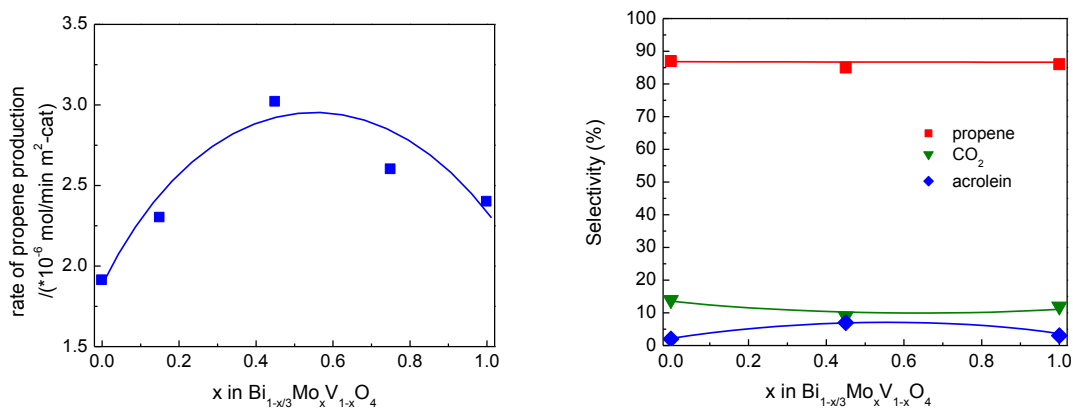
Figure 5.6 Arrhenius plot of the oxidative dehydrogenation of 1-butene and trans-2-butene oxidation to 1,3-butadiene over $Bi_{1-x/3}V_{1-x}Mo_xO_4$ catalysts at 613 K - 733 K and P_{C4H8} = 0.067 atm, P_{O2} = 0.167 atm.
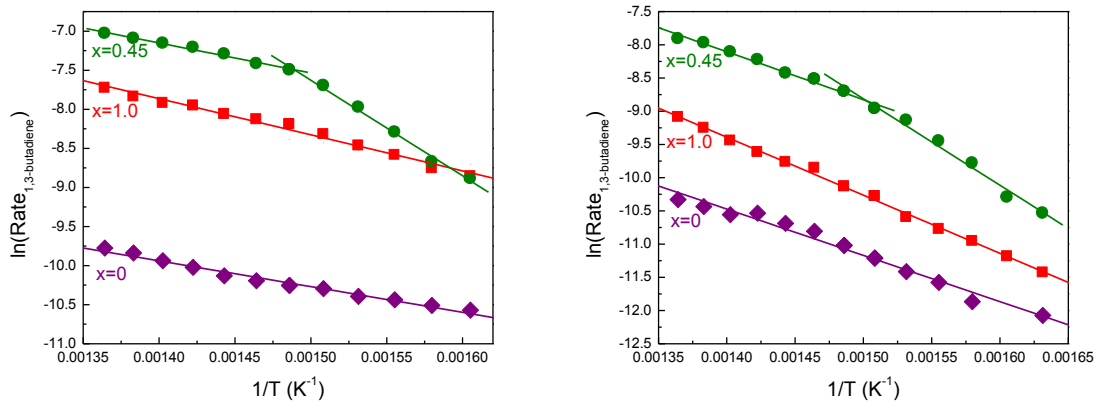
Figure 5.7 Arrhenius plot of the isobutene oxidation to methacrolein over $Bi_{1-x/3}V_{1-x}Mo_xO_4$ catalysts at 613 K - 733 K. Left: $P_{iso-C4H8}$ = 0.0167 atm, P_{O2} = 0.167 atm. Right: $P_{iso-C4H8}$ = 0.067 atm, P_{O2} = 0.167 atm.
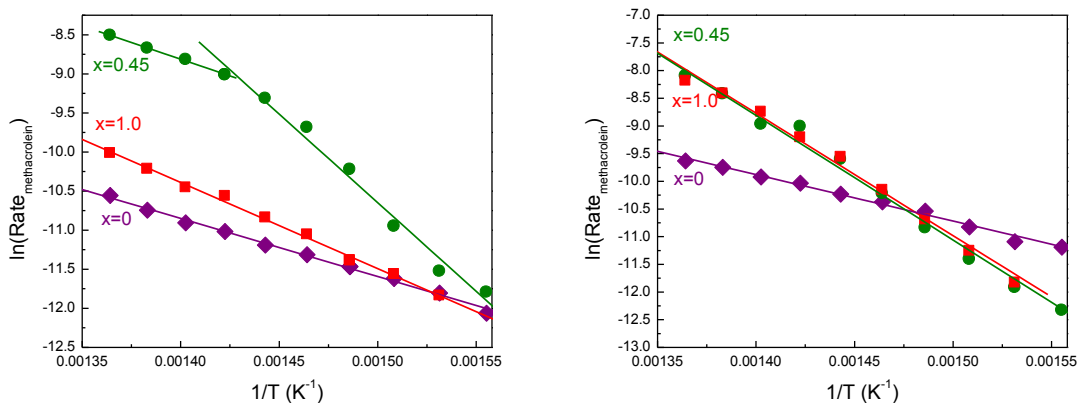


Figure 5.8 Arrhenius plot of the oxidative dehydrogenation of propane to propene over $Bi_{1-x/3}V_{1-x}Mo_xO_4$ catalysts at 703 K - 773 K and P_{C3H8} = 0.067 atm, P_{O2} = 0.167 atm.
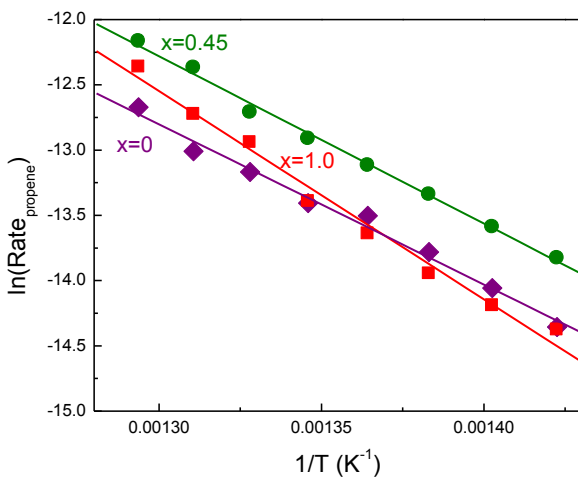
Figure 5.9 Correlation of the apparent rate coefficient for the production of the principle product, k_{app}, at 703 K for different butene isomers ($P_{C4H8} = 0.0167$, $P_{O2} = 0.167$ atm) and initial rate of reduction measured using UV-VIS at 703 K ($P_{C4H8} = 0.0167$ atm) on $Bi_{0.85}V_{0.55}Mo_{0.45}O_4$
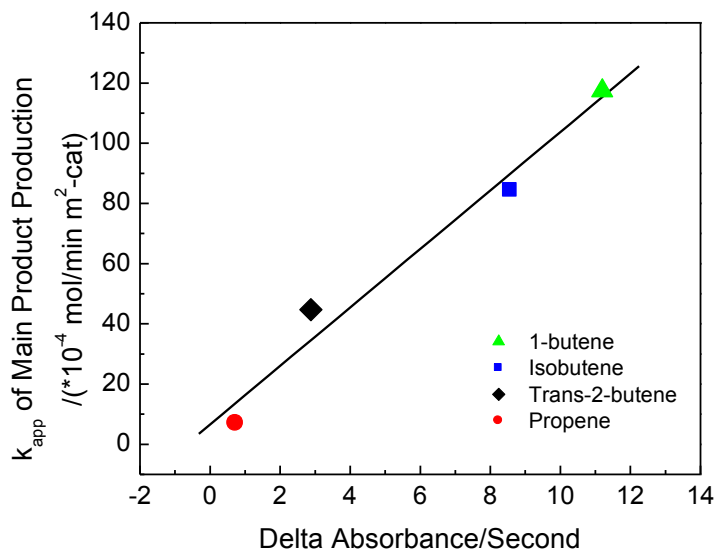
Figure 5.10 Correlation of the apparent activation energy for formation of the principle product with the dissociation energy of the weakest C-H bond involved in the rate-determining step occurring on $Bi_2Mo_3O_{12}$ (top), $BiVO_4$ (bottom left) and $Bi_{0.85}V_{0.55}Mo_{0.45}O_4$ (bottom right). All bond dissociation energy data come from: Handbook of bond dissociation energies in organic compounds. Yu-Ran Luo. CRC Press, 2003.
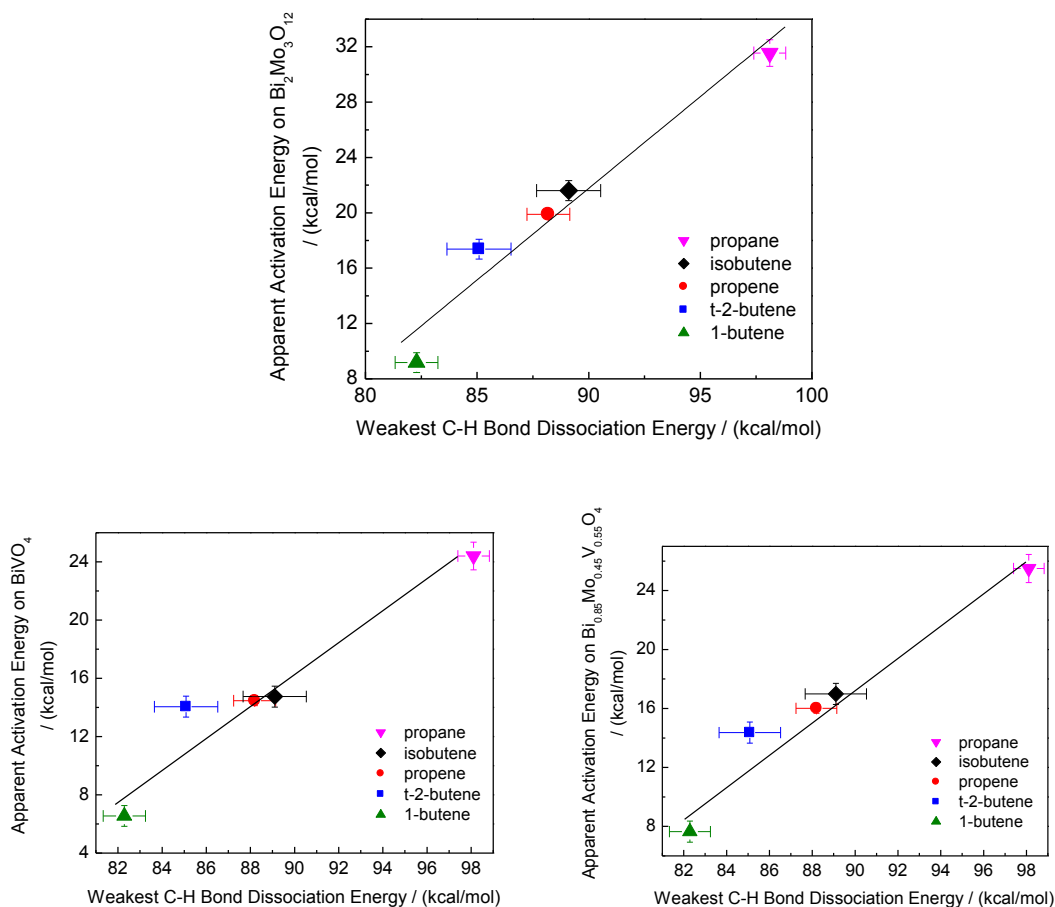
Figure 5.11 Correlation of the natural log of apparent pre-exponential factor with the apparent activation energy for formation of the principle products occurring over $Bi_2Mo_3O_{12}$ (top), $BiVO_4$ (bottom left) and $Bi_{0.85}V_{0.55}Mo_{0.45}O_4$ (bottom right).
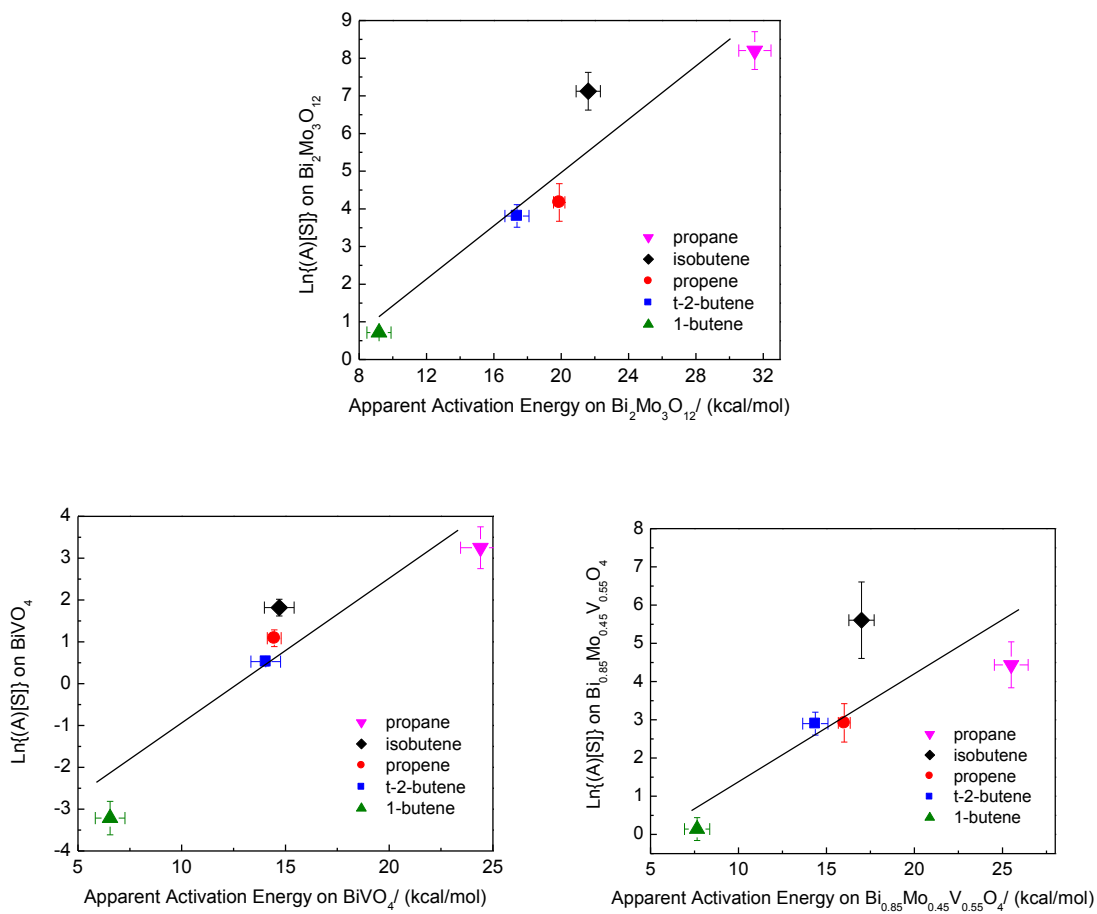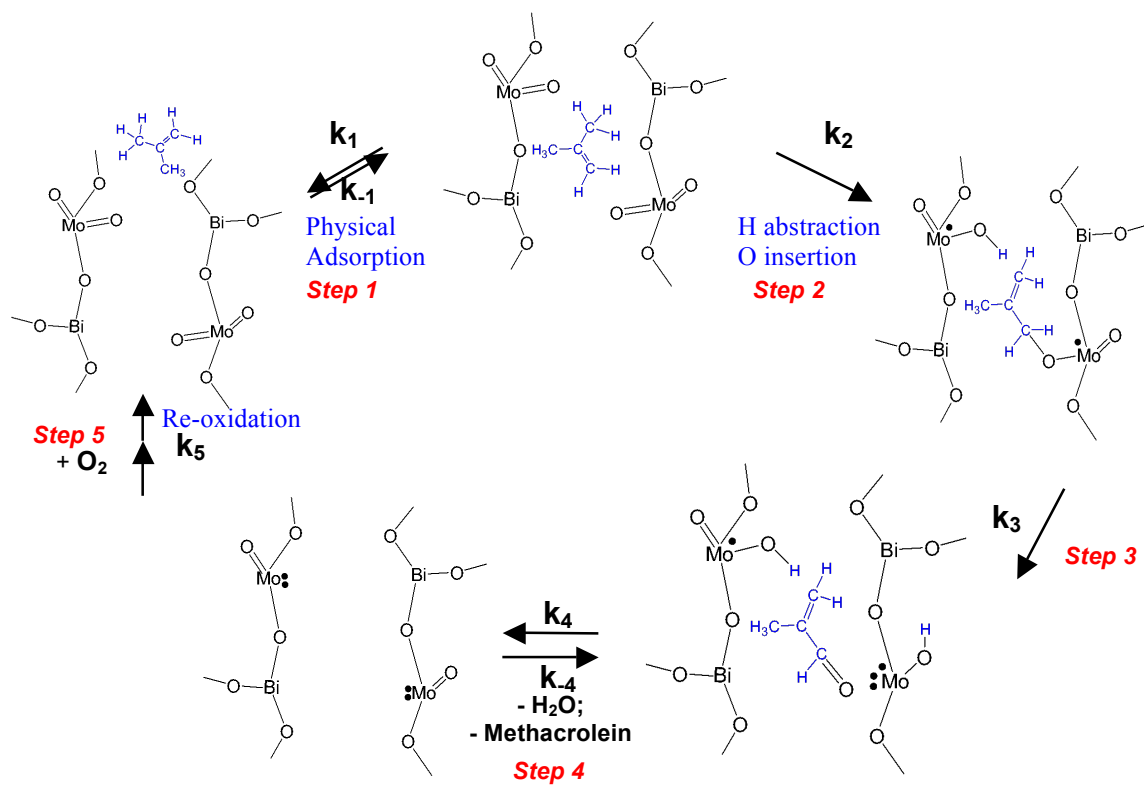
Scheme 5.1 The mechanism of the oxidative dehydrogenation of 1-butene to 1,3-butadiene over $Bi_2Mo_3O_{12}$ proposed on the basis of data reported in this study.
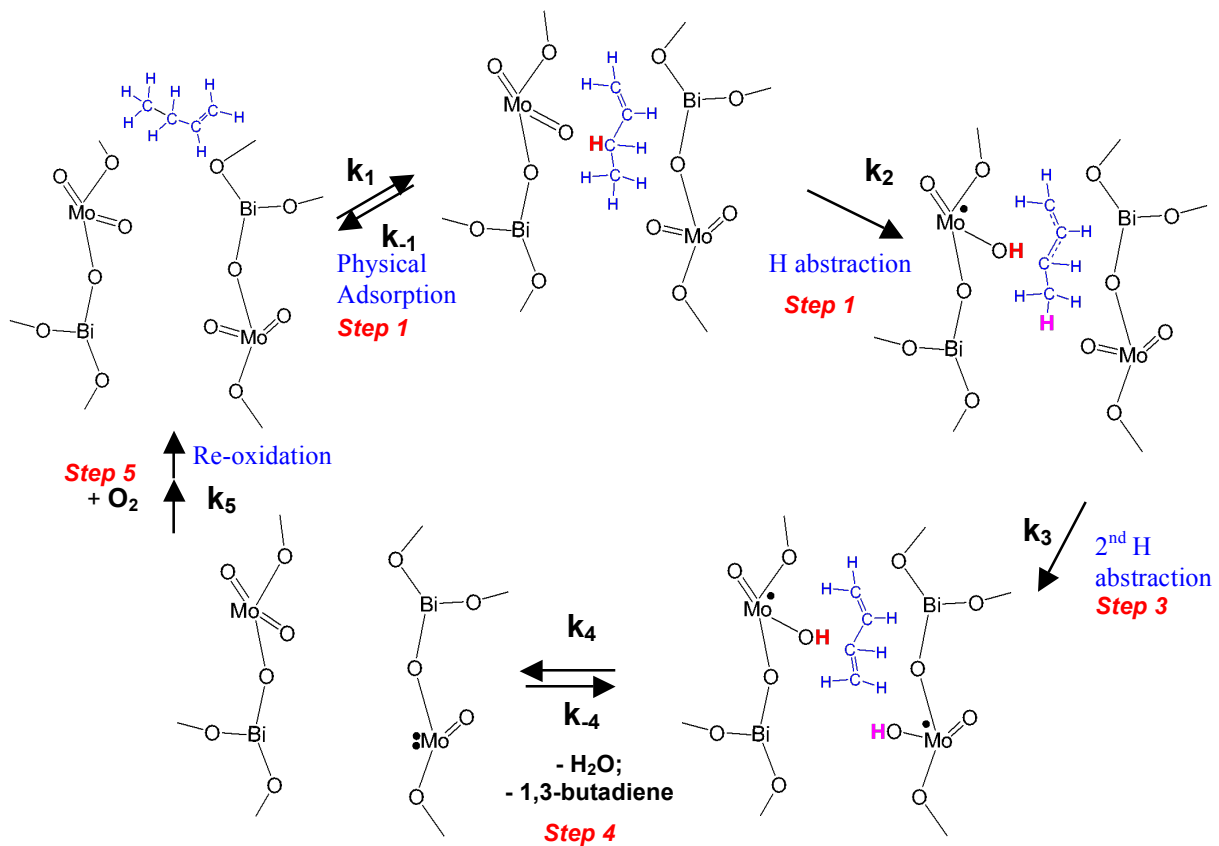
Scheme 5.2 The mechanism of the oxidation isobutene to methacrolein over $Bi_2Mo_3O_{12}$ under lower partial pressure of isobutene proposed on the basis of data reported in this study.

k_1

k_{-1}

Physical
Adsorption
Step 1

k_2

H abstraction
O insertion
Step 2

Re-oxidation

Step 5
$+ O_2$

k_5

k_3

Step 3

k_4

k_{-4}
$- H_2O$;
$-$ Methacrolein

Step 4

Scheme 5.3 Differences in the mechanisms of isomers formation from 1-butene and trans-2-butene.

1-butene:

Trans-2-butene:
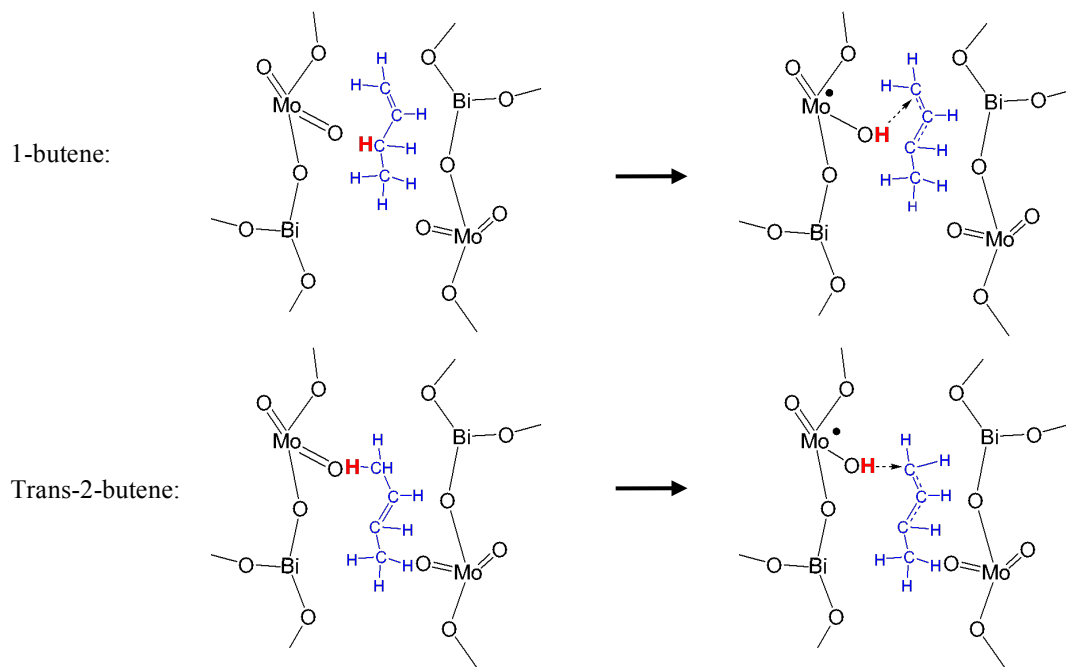
Scheme 5.4 Possible pathway for CO and CO_2 formation on $Bi_2Mo_3O_{12}$ during isobutene oxidation.
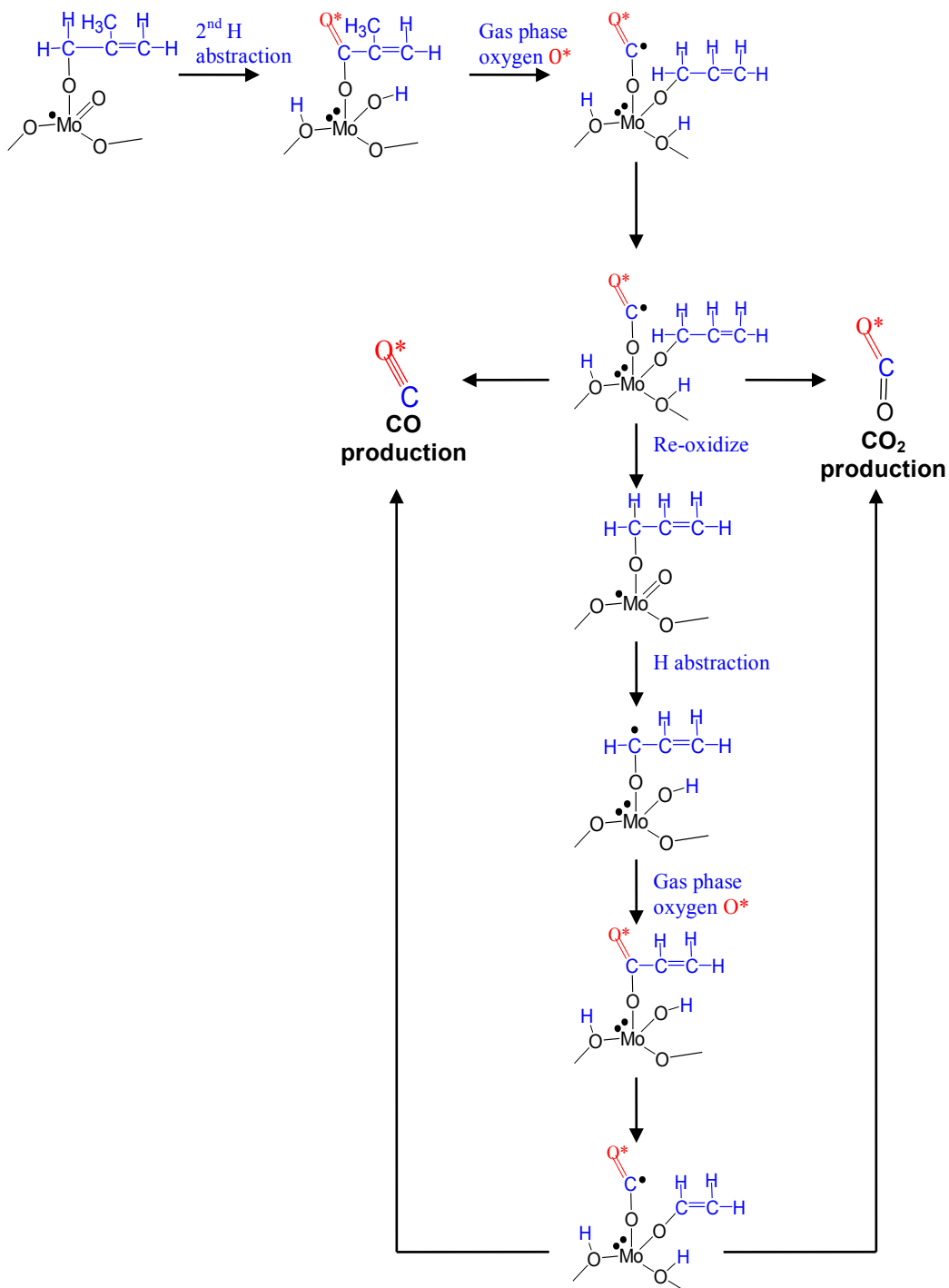
Table 5.1 Reaction orders at different temperatures for 1-butene and oxygen to produce 1,3-butadiene on $Bi_{1-x/3}V_{1-x}Mo_xO_4$. The partial pressures of 1-butene and oxygen were fixed at 0.067 and 0.167 atm when varying the other one.

Composition	633K		673K		693K	
	1-butene	Oxygen	1-butene	Oxygen	1-butene	Oxygen
0	0.9±0.0	0.0±0.0	1.0±0.0	-0.1±0.1	0.9±0.0	0.0±0.0
0.45	0.1±0.0	0.3±0.0	0.9±0.1	0.0±0.1	1.0±0.0	0.0±0.1
1	0.8±0.0	-0.1±0.1	1.0±0.0	-0.1±0.1	0.9±0.0	0.0±0.0

Table 5.2 Reaction orders at different temperatures for trans-2-butene and oxygen to produce 1,3-butadiene on $Bi_{1-x/3}V_{1-x}Mo_xO_4$. The partial pressures of trans-2-butene and oxygen were fixed at 0.067 and 0.167 atm when varying the other one.

Composition (x)	633K		673K		693K	
	Trans-2-butene	Oxygen	Trans-2-butene	Oxygen	Trans-2-butene	Oxygen
0	0.8±0.1	0.2±0.1	0.8±0.1	0.2±0.1	0.8±0.1	0.3±0.0
0.45	0.0±0.1	0.3±0.0	0.9±0.0	0.1±0.0	0.9±0.1	0.1±0.1
1	0.9±0.0	0.0±0.1	1.0±0.1	0.0±0.0	1.0±0.0	0.2±0.0

Table 5.3 Reaction orders at different temperatures for isobutene and oxygen to produce methacrolein on $Bi_{1-x/3}V_{1-x}Mo_xO_4$. The partial pressures of isobutene and oxygen were fixed at 0.067 and 0.167 atm when varying the other one at 673K (left). The partial pressures of isobutene and oxygen were fixed at 0.0167 atm and 0.167 atm when varying the other one at 703K (right).

Composition (x)	673K		703K	
	Isobutene (0.05~0.15atm)	Oxygen (0.067~0.167atm)	Isobutene (<0.0167atm)	Oxygen (0.067~0.167atm)
0	0.9±0.1	0.0±0.1	1.0±0.1	0.0±0.1
0.45	-0.8±0.1	0.8±0.1	0.9±0.2	0.0±0.0
1	-0.9±0.0	1.1±0.1	0.9±0.1	0.0±0.0

Table 5.4 Reaction orders at different temperatures for propane and oxygen to produce propene on $Bi_{1-x/3}V_{1-x}Mo_xO_4$. The partial pressures of propane and oxygen were fixed at 0.067 and 0.167 atm when varying the other one at 773K.

Composition (x)	773K	
	Propane	Oxygen
0	1.0±0.1	0.0±0.0
0.45	1.1±0.2	0.0±0.1
1	1.0±0.1	0.0±0.0

Table 5.5 Apparent activation energies under different temperature ranges for 1-butene and oxygen to produce 1,3-butadiene on $Bi_{1-x/3}V_{1-x}Mo_xO_4$. P_{1-C4H8} = 0.067atm, P_{O2} = 0.167 atm.

Composition(x)	E_{app}(kcal/mol)	
	663~713K	613~663K
0	6.5	
0.45	7.6	24.3
1	9.2	

Table 5.6. Apparent activation energies under different temperature ranges for trans-2-butene and oxygen to produce 1,3-butadiene on $Bi_{1-x/3}V_{1-x}Mo_xO_4$. $P_{trans-2-C4H8}$ = 0.067atm, P_{O2} = 0.167 atm.

Composition(x)	E_{app}(kcal/mol)	
	663~713K	613~663K
0	14.0	
0.45	14.4	24.7
1	17.4	

Table 5.7 Apparent activation energies under different temperature ranges for isobutene and oxygen to produce methacrolein on $Bi_{1-x/3}V_{1-x}Mo_xO_4$. $P_{iso-C4H8}$ = 0.0167atm, P_{O2} = 0.167 atm.

| Composition(x)	E_{app}(kcal/mol)	
	703~733K	643~703K
0	14.7	
0.45	17.0	44.8
1	21.6	

Table 5.8 Apparent activation energies for propane and oxygen to produce propene on $Bi_{1-x/3}V_{1-x}Mo_xO_4$. $P_{C3H8} = 0.167$atm, $P_{O2} = 0.167$ atm.

Composition(x)	E_{app}(kcal/mol)
	703~773K
0	24.4
0.45	25.5
1	31.5

Table 5.9 Symmetry number (σ) for different reactants.

Reactant	Symmetry number (σ)
propene	3
1-butene	2
trans-2-butene	6
isobutene	6
propane	6

Figure 5.S1 Normalized Bi L_3-edge, Mo K-edge and V K-edge XANES spectra of $Bi_{0.85}Mo_{0.45}V_{0.55}O_4$. Samples were treated in air to 713 K for oxidized sample and in propylene and 1-butene for 2 hours for reduced samples.
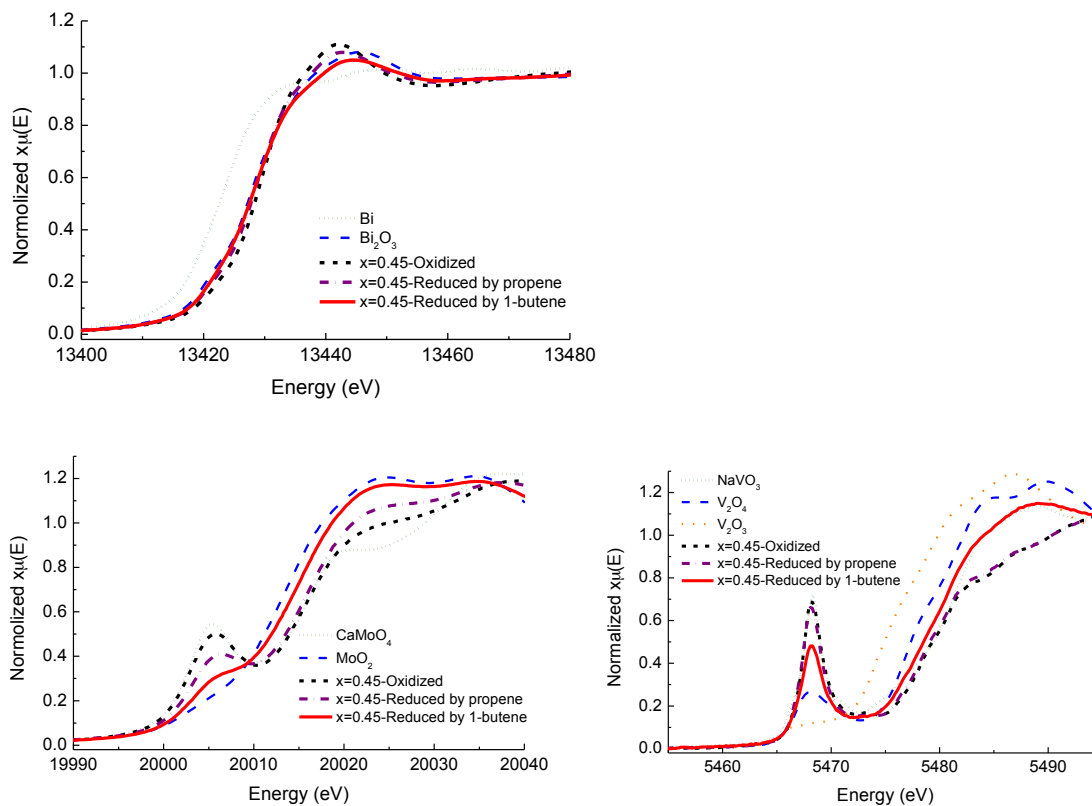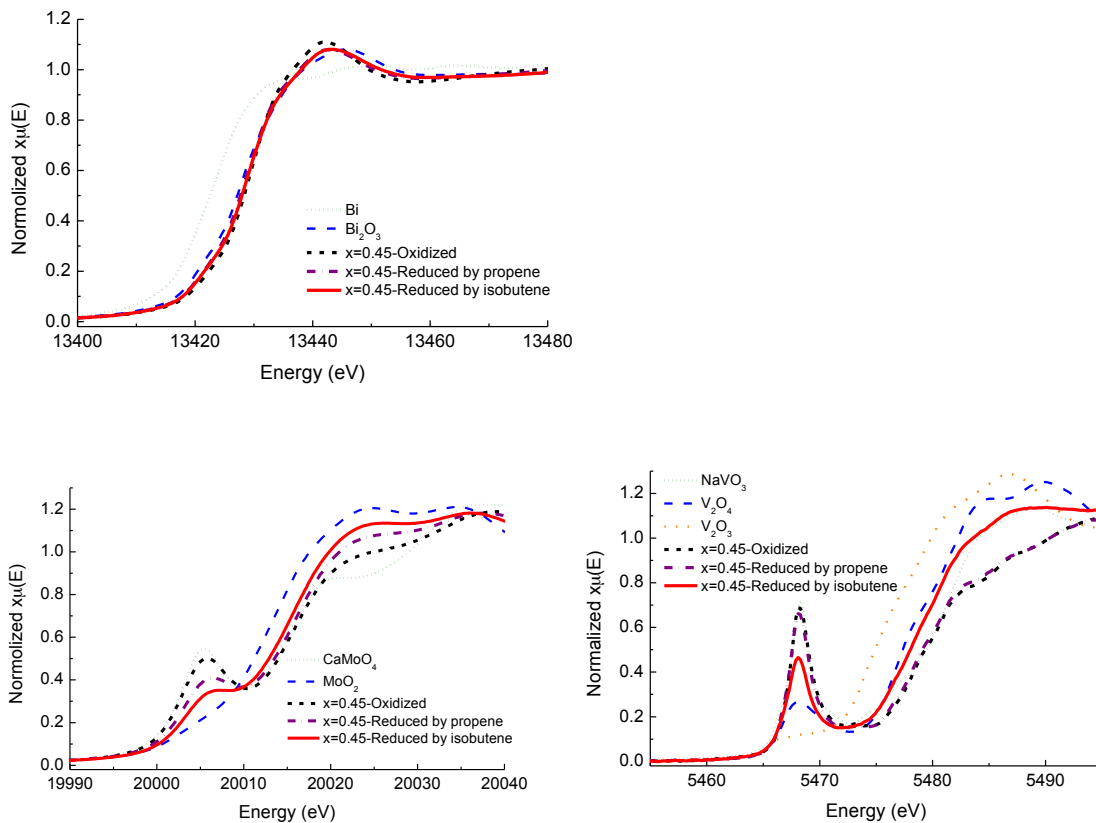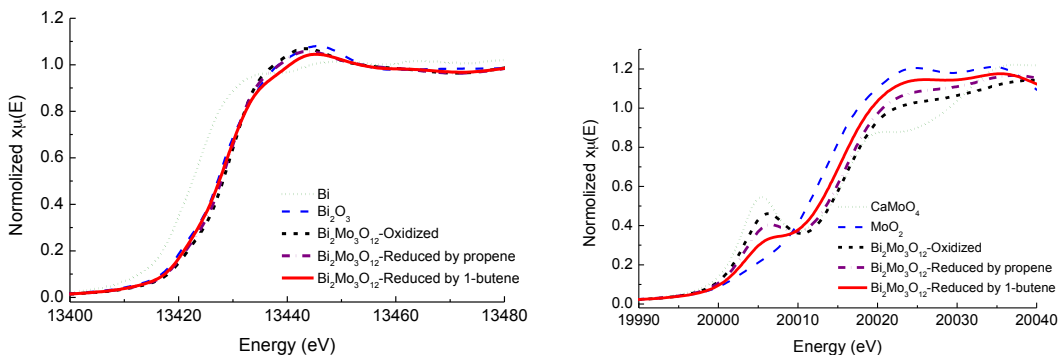
Figure 5.S2 Normalized Bi L_3-edge, Mo K-edge and V K-edge XANES spectra of $Bi_{0.85}Mo_{0.45}V_{0.55}O_4$. Samples were treated in air to 713 K for oxidized sample and in propylene and trans-2-butene for 2 hours for reduced samples.
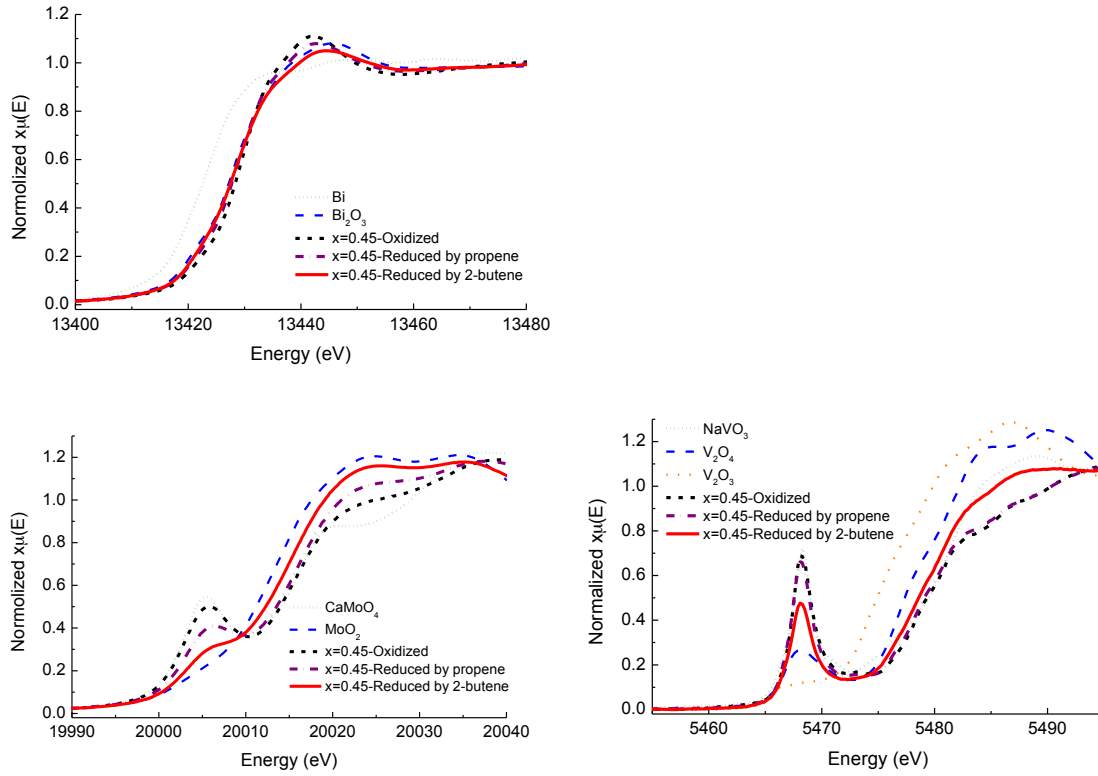
Figure 5.S3 Normalized Bi L₃-edge, Mo K-edge and V K-edge XANES spectra of Bi$_{0.85}$Mo$_{0.45}$V$_{0.55}$O$_4$. Samples were treated in air to 713 K for oxidized sample and in propylene and isobutene for 2 hours for reduced samples.


Figure 5.S4 Normalized Bi L₃-edge and Mo K-edge XANES scans of Bi$_2$Mo$_3$O$_{12}$. Samples were treated in air to 713 K for oxidized sample and in propylene and 1-butene for 2 hours for reduced samples.

Figure 5.S5 Normalized Bi L$_3$-edge and V K-edge XANES scans of BiVO$_4$. Samples were treated in air to 713 K for oxidized sample and in propylene and 1-butene for 2 hours for reduced samples.
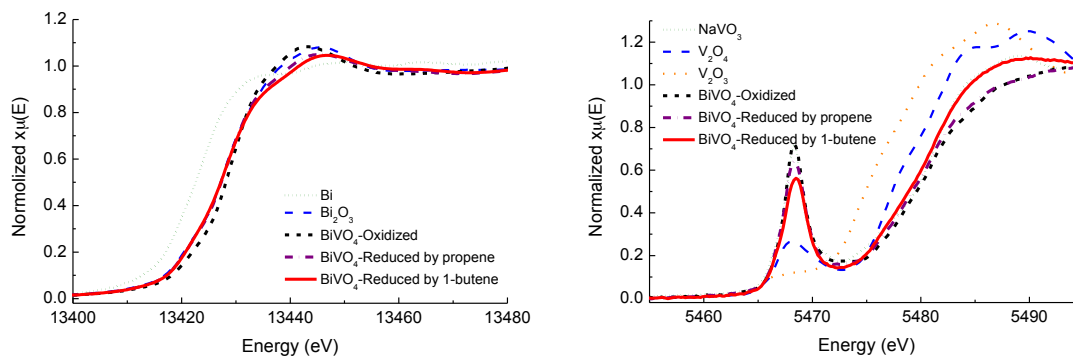
Figure 5.S6 Left: Diffuse reflectance UV-VIS-NIR spectra of catalysts during *in situ* reduction at 673K. Right: Absorbance at 800 nm as a function of time exposed to reducing conditions. The initial rate of reduction is extracted as shown.
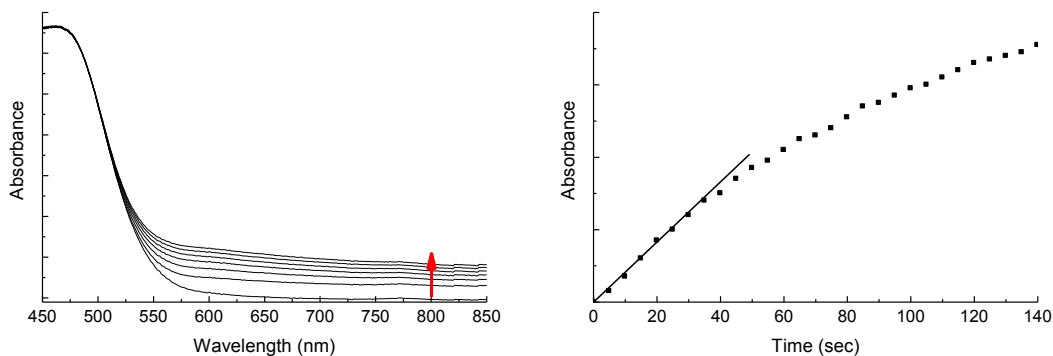
Figure 5.S7 Left: 1-butene as reactant, UV-Vis spectra of $Bi_{0.85}V_{0.55}Mo_{0.45}O_4$ at 673 K before reation, at steady state 1 (P_{1-C4H8} = 0.0167 atm, P_{O2} = 0.167 atm) and at steady state 2 (P_{1-C4H8} = 0.067 atm, P_{O2} = 0.167 atm). Right: Isobutene as reactant, UV-Vis spectra of $Bi_{0.85}V_{0.55}Mo_{0.45}O_4$ at 673 K before reation, at steady state 1 ($P_{iso-C4H8}$ = 0.0167 atm, P_{O2} = 0.167 atm) and at steady state 2 ($P_{iso-C4H8}$ = 0.067 atm, P_{O2} = 0.167 atm).